

NON-EQUILIBRIUM TOPOLOGICAL PHASES WITH PERIODICALLY DRIVEN MOLECULES AND QUANTUM ROTORS

by

Volker Karle

February, 2025

*A thesis submitted to the
Graduate School
of the
Institute of Science and Technology Austria
in partial fulfillment of the requirements
for the degree of
Doctor of Philosophy*

Committee in charge:

Prof. Scott Waitukaitis, Chair
Prof. Mikhail Lemeshko
Ass. Prof. Denitsa Baykusheva
Prof. Olga Smirnova



The thesis of Volker Karle, titled *NON-EQUILIBRIUM TOPOLOGICAL PHASES WITH PERIODICALLY DRIVEN MOLECULES AND QUANTUM ROTORS*, is approved by:

Supervisor: Prof. Mikhail Lemeshko, ISTA, Klosterneuburg, Austria

Signature: _____

Committee Member: Ass. Prof. Denitsa Baykusheva, ISTA, Klosterneuburg, Austria

Signature: _____

Committee Member: Prof. Olga Smirnova, Max Born Institute, Berlin, Germany

Signature: _____

Defense Chair: Prof. Scott Waitukaitis, ISTA, Klosterneuburg, Austria

Signature: _____

Signed page is on file

© by Volker Karle, February, 2025

CC BY-NC-ND 4.0 The copyright of this thesis rests with the author. Unless otherwise indicated, its contents are licensed under a [Creative Commons Attribution-NonCommercial-NoDerivatives 4.0 International License](https://creativecommons.org/licenses/by-nc-nd/4.0/). Under this license, you may copy and redistribute the material in any medium or format. This is on the condition that: you credit the author, do not use it for commercial purposes and do not distribute modified versions of the work.

ISTA Thesis, ISSN: 2663-337X

I hereby declare that this thesis is my own work and that it does not contain other people's work without this being so stated; this thesis does not contain my previous work without this being stated, and the bibliography contains all the literature that I used in writing the dissertation.

I accept full responsibility for the content and factual accuracy of this work, including the data and their analysis and presentation, and the text and citation of other work.

I declare that this is a true copy of my thesis, including any final revisions, as approved by my thesis committee, and that this thesis has not been submitted for a higher degree to any other university or institution.

I certify that any republication of materials presented in this thesis has been approved by the relevant publishers and co-authors.

Signature: _____

Volker Karle
February, 2025

Signed page is on file

Abstract

Rotations constitute one of the fundamental symmetries in physics, characterized by their intricate group structure and infinite dimensional representations. In contrast to classical rotations, quantum mechanics unveils the $SO(3)$ symmetry group structure, manifesting in phenomena without classical counterparts, from angular momentum quantization to non-trivial addition of angular momenta. While most studies of topological physics have focused on two-band systems, the $SO(3)$ symmetry group of quantum rotors offers an inherently more complex platform with unprecedented possibilities for exploring topological phenomena. Despite their ubiquity in nature— from molecules to nanorotors— their potential for hosting topological phases has remained largely unexamined.

In this thesis, we mainly focus on periodically driven linear molecules as a prototype for studying topological phenomena in quantum rotors. Recent technological advances in coherent control of molecules, particularly through precisely shaped laser pulses, have made it possible to investigate linear rotors in the context of topology. While planar rotors have received some attention in recent years, three-dimensional rotors—particularly linear molecules—harbor substantially richer topological phenomena due to their non-abelian nature and their additional angular degrees of freedom. We demonstrate that these systems can host novel edge states and topological features fundamentally impossible in planar systems.

We begin by establishing a theoretical bridge between periodically

kicked rotors and "crystalline" lattices in angular momentum space. Using non-interacting linear molecules as our primary example, we show how quantum interference and revival patterns lead to the possibility to simulate band models with arbitrary number of bands N . While our framework applies to various quantum rotors, including nanorotors and kicked Bose-Einstein condensates, linear molecules provide an ideal experimental platform due to their above-mentioned precise controllability.

The core of this work examines adiabatic dynamics of 3D quantum rotors, establishing a geometric framework based on the Euler class to characterize its non-abelian topology. The non-Hermitian nature of the system enables novel braiding behaviors and topological transitions impossible in static systems, leading to an anomalous Dirac string phase with edge states in each gap, even though the Berry phases are all zero. These features can be directly observed through molecular alignment and rotational level populations.

These findings establish quantum rotors as an alternative platform for studying multi-band topological physics, while suggesting practical implementations for quantum computation where topological protection could offer natural resilience against decoherence. The rich structure of three-dimensional rotation groups, combined with the tunability of topological features through driving parameters, makes this platform particularly valuable for exploring fundamental physics and developing quantum technologies.

Acknowledgements

Looking back on this academic journey, I am grateful for the constellation of people who helped shape these years into something truly remarkable. First and foremost, I want to express my deepest gratitude to Misha Lemeshko, whose trust enabled me to establish, together with him, an entirely new research direction. His support proved invaluable during the challenges of the pandemic, particularly after my recovery from a severe case of COVID-19. Even through these difficult times, his continued belief in my work and generous support made it possible for me to develop new theoretical models and share them at conferences and schools across Europe and the United States. His mentorship struck that perfect balance between guidance and independence, allowing our pioneering research to flourish while keeping me on track.

I want to express my sincere appreciation to my committee members who guided this thesis to completion. I want to thank Denitsa Baykusheva and Olga Smirnova – I am particularly inspired by Olga’s work on chirality with molecules, and I’m thankful for her warm hospitality during my visit to the Max Born Institute in Berlin. My appreciation extends to Maksym Serbyn, who provided valuable guidance during my rotation period, and to Ilya Averbukh – both offered insightful perspectives during my qualifying exam that helped establish my research direction.

During the early stages of my PhD, I was fortunate to work with two exceptional mentors who profoundly influenced my scientific devel-

opment: Areg Ghazaryan played an important role in the first part of my PhD journey, guiding me through the intricacies of topological physics with patience. His critical feedback and deep physical intuition were instrumental in developing our project into a successful publication. Equally formative was my collaboration with Alexios Michailidis during my first rotation with Maksym Serbyn. Through our work together I learned a lot about the numerical treatment of many-body quantum physics and tensor networks.

At the Chicago March Meeting, I was very fortunate to meet Nur Ünal, Robert-Jan Slager, and Adrien Bouhon, leading to an important collaboration during the second half of my PhD. They taught me the intricacies of multi-gap topology and helped me understand the deeper mathematical structure behind non-abelian braiding and the Euler class.

Over my years at ISTA, our research group was filled with wonderful colleagues who came and went at different times: Enderalp, Li, Artem, Giacomo, Igor, Katja, Wojciech, Mishka, Alberto, Georgios, Ragheed, Florian, Mateja, Jinglun, Baptiste, Palina, and Gulnaz: They made the workplace feel welcoming and intellectually stimulating. Together with Alberto, I organized regular arthouse movie nights at my apartment, where we've explored cinema from Fellini's classics to Park Chan-wook's contemporary masterpieces, often accompanied by great dinners. These evenings of film, cuisine, and discussion have added a wonderful personal dimension to our academic interactions.

I am grateful to Hossein Sadeghour for the opportunity to present my recent work at ITAMP, which led to a fantastic collaboration with Ceren Dag, Vasilis Rokaj, and Orianna Diessel during my stay in Cambridge. I want to thank Matthew Fishman for his welcome at the Flatiron Institute and for sharing his valuable insights into tensor networks. My special thanks go to Tilman Enss and Andreas Buchleitner, who have supported me since my Master's and Bachelor's studies respectively, and for their continued interest in my

work, hosting me in Heidelberg and Freiburg to present my recent research.

My travels revealed a dimension very different from the academic centers and megacities I saw in the US earlier – the vast expanses of the Southwest and the national parks, with its iconic Grand Canyon. I became completely captivated by these boundless landscapes. I'm particularly thankful to Rishabh for sharing this 1000-kilometer journey around the Grand Canyon with me after the APS meeting.

For their meticulous proofreading, I thank Fabian, Fred, Andreas, Joey, Philippe, Georgios, and Florian.

Working alongside Andrea and later Sofia as student representatives in the Graduate School Association (2022-2024) was one of the most rewarding experiences of my PhD. Their extraordinary dedication and tireless commitment transformed our student community after the pandemic. Together, we established initiatives that went far beyond what we initially imagined – from organizing "Wine and Whine" events to scientific trips to Budapest. I was particularly delighted when we discovered what would become our PhD retreat venue in a Slovak castle, which created a unique atmosphere for scientific discussions within historic surroundings. I hope it will continue to serve future generations of PhD students as a place for both academic exchange and community building. Furthermore, I want to acknowledge the Vienna Quantum Center (VCQ) and their student representatives for creating a vibrant scientific community through talks, retreats, summer schools, and christmas parties.

My scientific journey began when I participated in 'Jugend forscht', Germany's premier youth science competition, which opened my first window to the vast world of research. Now, years later, teaching at the Deutsche Schülerakademie and Quantenakademie in Jülich feels like coming full circle. I want to express my heartfelt thanks to Kathi, Lisa and Dane, from whom I learned so much about the art of teaching, and to the dedicated organizers of both academies

who create these transformative experiences for young students. I'm honored to have these opportunities to give back – to support and encourage young minds in their journey of independent scientific thinking, just as others once supported me.

I'm deeply indebted to additional friends who provided balance and joy - Manas, Lukas, and Tobias for chess and board game nights; Gökhan, Sasha, Raimel, Yunet, Deniz, Ayub, Andrea, Liliann, Daniel, David, Adrian and Sarath – your friendship has been invaluable.

To my parents, who carved out a path of freedom different from their own, your sacrifices and support made this journey possible. Your life's work became the foundation of my choices.

And to my partner Joey – for illuminating this scientific journey with your unique perspective on human experience. Your talent for introspection and psychological insight guided me through academic ivory tower labyrinths. During the isolation of the pandemic, through paper rejections and thesis writing, you created moments where physics merged with artistic expression, where scientific setbacks gave rise to musical inspirations, and where your grasp of human complexity lent clarity to my own personal academic challenges.

About the Author

After studies in physics at the Universities of Freiburg (BSc) and Heidelberg (MSc), he worked on tipping elements at the Potsdam Institute for Climate Impact Research (PIK) and developed predictive analytics for renewable energies at a startup in Berlin. His path then led him to join ISTA in 2019 to pursue research in quantum physics.

His research focuses on molecular quantum physics and driven topological phenomena. His doctoral work began with investigating non-equilibrium many-body states with Maksym Serbyn, before working on periodically driven molecules as a novel platform for topological physics. He presented his research at various venues, including APS March Meetings in Chicago (2022) and Las Vegas (2023), the JuliaCon at MIT (2023) and gave invited talks at Harvard University, Heidelberg University, Max Born Institute Berlin, and Max Planck Institute for Complex Systems Dresden. During a research stay at ITAMP (Harvard) in late 2023, he investigated topological edge states in cavity systems.

Alongside his research, he taught at the Deutsche SchülerAkademie (DSA), covering topics from the philosophy of science fiction to the historical foundations of quantum mechanics. As president of the Graduate School Association (2022-2024), he organized PhD retreats, coordinated student-faculty panels, and led a scientific exchange to Budapest. When not exploring quantum phenomena, he enjoys philosophical discussions and brings people together for music jam sessions.

List of Collaborators and Publications

This thesis builds upon several research projects I conducted under the supervision of Mikhail Lemeshko. While the results presented here stem from published work, I independently created all figures and wrote the main text.

During my first rotation project with Maksym Serbyn, I studied the failure of the *eigenstate thermalization hypothesis* in chaotic and non-integrable models with symmetries. Our investigation revealed zero-modes with area-law scaling in their von-Neumann entropy [1]. In my main doctoral project, working with Mikhail Lemeshko and Areg Ghazaryan, I investigated periodically-driven molecules. The discovery of topological charges in this system constitute the central theme of this thesis and were published in [2, 3].

A referee’s observation regarding the sudden approximation led to a new research direction, resulting in [4]. This work provides the foundation for Chapter 2. For my final project, I collaborated with F. Nur Ünal, Adrien Bouhon, and Robert-Jan Slager at Cambridge University to study non-abelian charges and their braiding process. This work, presented in [5] (under review), forms the core of Chapter 5.

During the course of my PhD, we produced the following works:

- [1] Volker Karle, Maksym Serbyn, and Alexios A. Michailidis. “Area-Law Entangled Eigenstates from Nullspaces of Local Hamiltonians”. In: *Physical Review Letters* 127 (2021), p. 060602. DOI: [10.1103/PhysRevLett.127.060602](https://doi.org/10.1103/PhysRevLett.127.060602).

- [2] Volker Karle, Areg Ghazaryan, and Mikhail Lemeshko. “Topological charges of periodically kicked molecules”. In: *Physical Review Letters* 130.10 (2023), p. 103202. doi: [10.1103/PhysRevLett.130.103202](https://doi.org/10.1103/PhysRevLett.130.103202).
- [3] Volker Karle and Mikhail Lemeshko. “Die faszinierende Topologie rotierender Quanten: Rotierende Moleküle in starken Feldern”. In: *Physik in unserer Zeit* 55.1 (2024), pp. 28–33. doi: [10.1002/piuz.202301690](https://doi.org/10.1002/piuz.202301690).
- [4] Volker Karle and Mikhail Lemeshko. “Modeling laser pulses as δ kicks: Reevaluating the impulsive limit in molecular rotational dynamics”. In: *Physical Review A* 109 (2024), p. 023101. doi: [10.1103/PhysRevA.109.023101](https://doi.org/10.1103/PhysRevA.109.023101).
- [5] Volker Karle, Mikhail Lemeshko, Adrien Bouhon, Robert-Jan Slager, and F. Nur Ünal. *Anomalous multi-gap topological phases in periodically driven quantum rotors*. 2024. arXiv: [2408.16848](https://arxiv.org/abs/2408.16848).

Table of Contents

Abstract	vii
Acknowledgements	ix
About the Author	xiii
List of Collaborators and Publications	xiv
Table of Contents	xvii
1 Introduction	1
1.1 Motivation	1
1.2 Topological physics	8
1.3 Non-equilibrium Floquet physics	13
1.4 Organization of the thesis	16
2 Rotating molecules with ultrashort pulses	19
2.1 Overview	19
2.2 Laser induced rotation of molecules	21
2.3 The sudden approximation	29
2.4 Exact time-evolution of rotational wavepackets	45
2.5 Outlook	51
3 Lattices of angular momentum	53
3.1 Overview	53
3.2 Floquet theory	55

3.3	Quantum resonance of rotors	62
3.4	Dynamical localization	81
3.5	Periodically driven 3D rotors	86
3.6	Outlook	99
4	Geometric phases of driven rotors	101
4.1	Overview	101
4.2	Geometric phases	103
4.3	Dirac cones and topological charges	116
4.4	Experimental signatures of Dirac cones	122
4.5	Outlook	127
5	Non-abelian topological phases	129
5.1	Overview	129
5.2	Non-Orientability and Dirac-strings	132
5.3	The triple-kicked rotor	140
5.4	Anomalous Dirac-String phase	146
5.5	Outlook	148
6	Conclusion	149
6.1	Summary	149
6.2	Future directions	151
	Bibliography	153
	Appendix	185
	Integrals	185
	Periodicity proofs	186
	List of Figures	191

CHAPTER 1

Introduction

It has long been an axiom of mine that the little things are infinitely the most important.

– Arthur Conan Doyle, A Case of Identity

1.1 Motivation

Amidst the enormous variety of physical phenomena, few concepts appear as deceptively simple, yet prove as profoundly deep as the notion of rotations. Indeed, the Hamiltonian that governs quantum rotations – while arising from one of the most elementary non-trivial Lie groups, $SO(3)$ – unveils mathematical structures of astonishing intricacy.

In this thesis, we shall embark on an odyssey through the quantum mechanics of rotation. We will uncover synergies between molecular and chemical physics, condensed matter theory, and the abstract mathematics of geometry and topology – all emerging from the infinite-dimensional representations of $SO(3)$ and the delicate interplay between continuous and discrete symmetries that shape our cosmos. Our analysis reveals that the study of molecular rotations leads to an understanding that discloses new complexities born from

the interplay between the mathematical formalism, the peculiarities of the quantum mechanical treatment, and the physical properties of molecules.

Our experimental advances in controlling quantum systems have largely focused on transitions of two-level systems [6]. When we attempt to reduce complex phenomena such as molecular rotations to such two level systems, we essentially restrict ourselves in exploring a minuscule corner of available Hilbert spaces. The full structure of $SO(3)$ quantum rotations offers a vastly more opulent playground. While the classical theory of angular momentum has been known for centuries, its quantum control applications remain largely unexplored.

We begin with a historical perspective on quantum rotations, followed by recent developments that motivate our research objectives and guide the structure of this thesis.

1.1.1 A short history of rotations

The study of rotational motion has its roots in ancient astronomy. Babylonian astronomers were among the first to systematically record celestial events, noting the periodic nature of celestial motions. Their meticulous observations of the Moon, including deviations from uniform circular motion, laid the early groundwork for understanding rotational dynamics [7]. The Babylonians excelled at identifying patterns in the heavens and recognized that celestial bodies did not always follow simple circular paths. This realization prompted them to develop early geometrical models to explain these behaviors¹.

¹As Aaboe highlights [7], "*Thus the astronomical tradition in the West is linked to Babylonian astronomy. Mathematical astronomy was, however, not only the principal carrier and generator of certain mathematical techniques, but it became the model for the new exact sciences which learned from it their principal goal: to give a mathematical description of a particular class of natural phenomena capable of yielding numerical predictions that can be tested against observations.*" Furthermore, Aaboe underlines the Babylonian contributions to the foundations of

Although Ptolemy's geocentric model of the solar system with its rotating spheres was incorrect, it required a basic understanding of how angular velocity relates to radius². Later, in the medieval period, Islamic scholars like Ibn al-Shatir improved upon the Ptolemaic system³, hence indirectly contributing to the theory of rotations. European scholars, such as Jean Buridan, challenged the classical Aristotelian physics, which, at its core, was unable to explain rotations [11]. These scholars introduced concepts that would later lead to the understanding of inertia and momentum. However, understanding the moment of inertia without a framework of differential calculus proved to be a formidable challenge.

It was only in the 17th century that Newton and Leibniz provided the mathematical foundation to describe continuously rotating bodies with changing angular momenta and dynamic torques through differential calculus. Although they attempted to write down the equations for angular momentum, they did not achieve what reached its pinnacle through the work of Euler in 1765 [12]. He derived the

scientific thought, suggesting that their qualitative models of celestial motion inspired later advancements in astronomy. Although their methods did not achieve the precision of later astronomical models, the qualitative insights they provided were instrumental in shaping subsequent theories. Therein, it is also noted that the idea of representing celestial motions through geometric constructs might have paved the way for future scholars, such as Hipparchus and Ptolemy.

²The Ptolemaic system (developed in 150 CE) used an intricate arrangement of deferents (large circles) and epicycles (smaller circles) to explain planetary motion. While mathematically powerful, its use of an equant point—which allowed for non-uniform circular motion—faced objections from Islamic astronomers and later from Copernicus. For philosophical rather than astronomical reasons, Copernicus rejected the equant and instead added more circles to his heliocentric model to achieve the same result [8].

³Ibn al-Shatir was an Arab astronomer, mathematician, and engineer who lived from 1304 to 1375 in Damascus, Syria. He served as a muwaqqit (timekeeper) at the Umayyad Mosque, where he was responsible for regulating the astronomically defined times of prayer [9]. Ibn al-Shatir made significant contributions to astronomical instrumentation and planetary theory. Most notably, he developed a geocentric model of planetary motion that was mathematically identical to Copernicus' later heliocentric model, raising questions about the possible transmission of his ideas to Europe [10].

rotation of rigid bodies, which in modern notation reads

$$\dot{\mathbf{L}} = \mathbf{L} \times \boldsymbol{\Omega} \quad (1.1)$$

with the angular momentum vector \mathbf{L} and the angular velocity vector $\boldsymbol{\Omega}$ with components J_k/I_k , where I_k are the principal moments of inertia⁴. These seemingly simple equations give rise to remarkably diverse physical phenomena, ranging from the regular precession of a spinning top to the chaotic motion of asymmetric rotors, where the ratio of moments of inertia dictates the system behavior [13]. Moreover, the non-linear nature of these equations leads to fascinating phenomena such as the *tennis racket instability*, where rotation around the intermediate axis becomes unstable [14–16]. This instability manifests dramatically in the *Dzhanibekov effect*⁵, where objects flip when rotating around their intermediate axis.

The scientific revolution of quantum mechanics transformed not just our understanding of nature, but the very language we use to describe it. Planck’s *quantum hypothesis* in 1900 [18] marked only the beginning of this transformation – the mathematical framework needed to capture quantum phenomena remained elusive for decades [19]. Heisenberg’s breakthrough on the island of Helgoland in 1925 [20], followed by Born and Jordan [21], provided the first rigorous mathematical framework through the so-called *matrix mechanics*. Von Neumann’s work in 1927 [22] finally revealed self-adjointed operators as the natural language of quantum phenomena, ensuring two crucial properties: the reality of eigenvalues and the conservation of probability [19].⁶

⁴This will be explained in much more detail in Section 2.2.

⁵The Dzhanibekov effect, discovered by astronaut Vladimir Dzhanibekov during his 1985 mission aboard the Salyut Orbital Station, demonstrates how the tennis racket instability manifests in free-floating objects. When rotating around their intermediate principal axis of inertia, objects undergo periodic flips without any external forces, a behavior fully explained by Euler’s equations. This effect also offers exciting potential applications in inertial navigation, where altering the distribution of spacecraft components can effectively manipulate moments of inertia [17].

⁶The philosophical implications of quantum mechanics have generated intense debate

The machinery of angular momentum operators developed by Pauli, Dirac, Uhlenbeck, Goudsmit, and others became the basis of our understanding of atomic structure, from elementary spin to molecular rotations to collective electronic excitations in materials⁷. This quantum mechanical perspective unveiled a myriad of new phenomena, where the quantization of angular momentum and the inherent symmetries of the system dictate its behavior [25, 26].

Today, it has become clear that the Hamiltonian of quantum rotors spans a remarkable range of physical systems. They show up in driven Bose-Einstein condensates, manifest in rotating molecules, and appear in systems as diverse as nanorotors or the rotational behavior of non-spherical nuclei [27–32]. Perhaps even more intriguing is their manifestation as quasiparticles – rotational states of excitons, polaritons, the newly-discovered Angulons, or Laughlin quasi-holes [33–37]. Each incarnation offers a new window into fundamental physics, revealing the connections between seemingly disparate phenomena through the unifying concept of angular momentum.

since the 1920s. While the *'Copenhagen interpretation'* emerged as dominant after the 1927 Como and Solvay conferences, where Bohr presented his concept of complementarity, its precise meaning remains contested. As Camilleri demonstrates [23], the interpretation spans diverse philosophical perspectives, from logical positivism to neo-Kantianism. Even among its principal architects, there was significant disagreement: von Neumann, Dirac, and Wigner either ignored or explicitly criticized Bohr's notion of complementarity. The term *'Copenhagen interpretation'* thus represents not a unified philosophical framework, but rather a collection of related viewpoints addressing the fundamental nature of measurement, reality, and human knowledge in quantum mechanics. This philosophical tension between mathematical formalism and physical interpretation continues to generate discussion today [23].

⁷For a historical account of quantum mechanics and the spin in particular, see Weinberg [24], p.5. Notably, Weinberg emphasizes how attempts to resolve the relativistic spin corrections led Schrödinger to his wave equation.

1.1.2 Modern developments in rotational physics

In recent years, a series of experiments have transformed our understanding of molecular structure and quantum rotations through the use of high-intensity pulsed laser sources [38–42]. These tools have revolutionized our ability to control and image molecular rotational dynamics, enabling us to achieve molecular alignment in both one and three dimensions with control over angular distributions [27, 43]. Quantum state tomography of rotational wavefunctions, once considered cumbersome, has become possible through techniques such as Coulomb explosion imaging and time-resolved x-ray diffraction [44, 45].

What makes this development fascinating is how it connects seemingly disparate areas of physics. A linear molecule subjected to a train of identical linearly polarized pulses exhibits behavior similar to Anderson localization, a phenomenon first discovered in condensed matter physics [46–48]. This is not merely an analogy; it is a physical correspondence that reveals fundamental aspects about quantum mechanics itself. The angular momentum lattice becomes a synthetic dimension, where localization occurs in angular momentum space rather than real space, yet still follows the same universal principles. This parallel illustrates how the lattice-like structure of pulse trains can serve as a powerful tool for simulating condensed matter systems [47, 49].

For quantum information science, quantum rotors provide a third fundamental quantum state space, different from the widely studied qudits and harmonic oscillators [50]. Recent experimental advances in ion systems [51, 52], superconducting circuits [53, 54] and ultra-cold molecules [55, 56] have made quantum rotor control increasingly feasible. The $SO(3)$ structure inherent to three-dimensional rotors offers both naturally protected quantum gates through non-abelian geometric phases and high-dimensional quantum encoding in their infinite-dimensional Hilbert space [50, 57, 58]. Moreover,

polyatomic molecules extend these possibilities by accessing higher symmetry groups. These non-abelian geometric phases that come together with these groups enable novel schemes for topological quantum error correction.

Perhaps the most remarkable aspect of molecular rotors is their ability to exhibit quantum phenomena at room temperature [27]. This is not just experimentally convenient; it represents a fundamental advantage for quantum simulation. The physics we observe in these driven systems is diverse, encompassing Anderson Walls, Bloch oscillations, topological edge states, and angular momentum transport [59, 60]. Surprisingly, band theory, a cornerstone of solid-state physics, describes these quantum rotors with unexpected effectiveness [61]. This effectiveness hints at deeper principles we are only beginning to understand. The periodic structure in angular momentum space, induced by periodic driving, creates a synthetic crystal structure where, as we will see, topology and geometry interplay in novel ways.

Central to our approach is the manipulation of molecular rotation using ultrashort, high-intensity laser pulses via off-resonant Raman transitions. Previous studies of periodically driven three-dimensional molecular rotors focused on quantum resonances [62], dynamical localization [59, 60, 63–66], and zero-angular momentum edge states [67, 68]. Moreover, recent advances in imaging molecular rotational dynamics [38, 39, 41] and controlling their angular degrees of freedom open new possibilities to probe kicked rotor physics. Now, the time has come to redirect our focus in atomic and molecular physics toward a paradigm that has already revolutionized condensed matter physics.

1.2 Topological physics

The emergence of topological physics in the last decades has fundamentally transformed our understanding of quantum matter [69–71]. While the field gained wide recognition with the Nobel Prize in Physics awarded to Thouless, Haldane, and Kosterlitz in 2016 [72], its foundations were established through various seemingly unrelated discoveries throughout the 20th century. The central insight – that geometric and topological properties of wavefunctions fundamentally shape their characteristics – has revolutionized materials research (see Fig. 1.1). This paradigm came into existence from precise experimental observations of the quantum Hall effect by von Klitzing in 1980 [73], where the Hall conductance of a material subjected to strong magnetic fields exhibited exact quantization in units of e^2/h .⁸

The theory of topological physics evolved as follows: Thouless demonstrated that the quantized Hall conductance corresponds to a topological invariant – the first Chern number of the electronic Bloch states [77]. Haldane later established that topological phases can exist without external magnetic fields, first in antiferromagnetic chains [78] and subsequently in two-dimensional electronic systems [79]. These seminal works established topological phases as a fundamental phenomenon in quantum systems [70].

The ubiquity of topological phenomena in material science naturally raises the question of their universality across different areas of physics, and science in general. Indeed, the underlying mathematical structures have a long historical tradition. Classical manifestations of so-called geometric phases appeared as early as 1851 in Foucault’s

⁸The precision of his measurements was so remarkable that when first presented, many physicists expressed skepticism as the quantization exceeded their best resistance standards at the time by many orders of magnitude [74]. Von Klitzing received the Nobel Prize in 1985, just five years after his discovery – an unusually rapid recognition that shows the importance of the discovery. Today, the quantum Hall resistance serves as a resistance standard, with h/e^2 known as the von Klitzing constant (RK).



Figure 1.1: Illustration of topology. A ball, a ring and a pretzel represent distinct topological classes, characterized by their genus - the number of holes in the surface (0, 1, and 2, respectively). These objects cannot be continuously deformed into one another while preserving their topology, just as electronic states in topological insulators remain robust against continuous perturbations. This geometric intuition underlies modern condensed matter physics, where topological protection guarantees the stability of edge states and quantum phenomena even in the presence of disorder [72, 75, 76].

pendulum [80], where parallel transport on a curved manifold results in observable precession⁹. Also in chemical physics, the concept of geometric phases—without calling it by that name—was discovered as early as 1958 by Robert A. Sack and other quantum chemists investigating molecules with vibrations and rotations [82]. In their model, the wavefunction is treated in the Born-Oppenheimer approximation, where the nuclear coordinates vary slowly and give rise to an effective potential for the electronic wavefunction. As we will lay out in more detail later, the symmetries of the effective Hamiltonian can give rise to degeneracies in the energy landscape. Crucially, it was noted that “encircling” these degeneracies leads to a sign change of the wavefunction, giving rise to measurable differences in, for example, chemical reactions. This led to the creation of the field of conical intersections in 1963, as the phenomenon was understood by Gerhard Herzberg and Longuet-Higgins [83].

⁹The phase shift per rotation is given by $\alpha = -2\pi \sin(\lambda)$ at latitude λ , providing a direct measurement of Earth’s rotation [81].

At that time not connected, this phenomenon was also found in the Ehrenberg-Siday-Aharonov-Bohm effect¹⁰. It occurs when electrons acquire a geometric phase when encircling a magnetic flux, even though their wavefunction is negligible within the magnetic field directly [84]. This demonstrates that electromagnetic potentials can influence quantum particles through their topological nature alone.

Meanwhile, in high-energy physics and statistical physics, the concept was reinvented in terms of quantum field theoretical language as the *Wegner-Wilson loop*¹¹. This provided a gauge-invariant measure when studying gauge theories [87]. This geometric perspective culminated in the Berry phase¹², in which Berry recognized the universal nature of this geometric phase while studying the adiabatic evolution of quantum states [88]. Finally, in 1989, Joshua Zak recognized the importance of the Berry phase in solids and reintroduced it as the Zak phase [89].

Interestingly, it turns out that the perspective of the Wegner-Wilson loop is very general, and many of the problems can be cast back to the problem of a charged particle in a gauge field [87]. While physicists

¹⁰The Aharonov-Bohm effect has a fascinating history of multiple discoveries. While commonly attributed to Aharonov and Bohm's 1959 paper, it was first predicted by Ehrenberg and Siday in 1949. The effect remained largely unknown until its rediscovery, prompting Weisskopf's famous observation [84]: "The first reaction to this work is that it is wrong; the second is that it is obvious."

¹¹The term *Wegner-Wilson loop* reflects a convergence of discoveries in different contexts of theoretical physics. Kenneth Wilson introduced these loops in 1974 as part of his work on quantum chromodynamics (QCD) [85], for which he was awarded the 1982 Nobel Prize. He used them to formulate gauge theories on a discrete lattice, providing a non-perturbative approach to QCD. Independently, Franz Wegner from Heidelberg had developed similar ideas in 1971 while studying lattice gauge theories in the context of statistical mechanics, particularly in relation to duality transformations [86]. Wegner's formulation, which preceded Wilson's work and had an equally if not more important impact on the topological physics community, focused on the discrete version of these loops on a lattice.

¹²The history of this concept, again, reflects the circuitous nature of scientific discovery. Shivaramakrishnan Pancharatnam first identified this phase in 1956. Decades later, Michael Berry independently rediscovered the same phenomenon in 1984.

are not necessarily acquainted with differential geometry, they very often have an intuitive understanding of Maxwell's equations, which can give rise to surprisingly intuitive pictures of basic aspects of algebraic topology. As an example, Gauss's law states that a surface integral of the electric field around a sphere is proportional to the number of charges inside. However, this result can be understood also from the aforementioned deep connection between topology and geometry, which has been generalized in mathematics and worked out through a series of very interesting developments over the last centuries [70].

In particular, the mathematical foundations underlying geometric phases emerged from profound developments in differential geometry and topology [87]. Central to this development is the mathematics of fiber bundles and connections, which provides an elegant structure for understanding geometric phases in quantum systems. A fiber bundle represents a concept where a space manifests locally as a product of two simpler spaces while potentially exhibiting global twisting [76]. The Möbius strip serves as the canonical example¹³, beautifully illustrating these concepts: its base space consists of the central circle, while the *fiber* is represented by the perpendicular line at each point. As one traverses the base circle, the fiber undergoes a twist, completing a 180-degree rotation upon returning to the starting point. Within this framework, a *connection* provides a mathematical prescription for comparing points along different fibers. This abstraction finds profound applications in physics: the fibers encode phase information, while the base space—obtained by abstracting away the phase—corresponds to the physical ray space [90].

These geometric insights were further developed by Chern's theory of characteristic classes in 1946 [91], which provided essential tools for classifying the topology of complex vector bundles – the natural

¹³We will go into more detail when discussing topology, see Fig. 4.1 for an example of Möbius strip.

setting for quantum states¹⁴. The subsequent Atiyah-Singer index theorem in 1963 established the fundamental relationship between analytical and topological invariants of manifolds [94], providing the mathematical foundation for *bulk-boundary correspondence* in topological phases [71]. This mathematical framework catalyzed numerous breakthrough discoveries, beginning with the quantum spin Hall effect predicted through topological band theory. These developments ultimately led to the theoretical prediction and experimental observation of three-dimensional topological insulators, Weyl semimetals, and topological superconductors [95–97].

The implications of these results extend far beyond condensed matter systems. The *bulk-boundary correspondence* guarantees the existence of topologically protected boundary modes. This fundamental principle shows up across a physical systems, from electronic states in quantum materials to photonic edge modes in electromagnetic structures [71]. The universality of these phenomena establishes topology as a unifying framework in quantum physics, with profound consequences for atomic and molecular systems.

The discovery of topological phases of matter exemplifies the connection between abstract mathematical concepts and fundamental physical phenomena. While the initial classification of topological insulators relied on static systems, subsequent research revealed that driving the systems out of equilibrium introduces novel possibilities for controlling topological properties. These driven systems can exhibit phases of matter with no static analogue, leading to an entirely new direction in quantum engineering [98].

¹⁴Chern’s breakthrough in 1944-1945 provided the first intrinsic way to understand topological invariants in complex geometry [92]. His key insight was that curvature forms could be used to construct global topological invariants (now called Chern classes) that are quantized and independent of local geometric details. This mathematical framework proved fundamental for understanding quantum Hall effects, topological insulators, and gauge theories. The resulting Chern classes c_n appear naturally in physics as quantum numbers characterizing topological phases, while the related Chern-Simons forms describe three-dimensional topological field theories [93].

To analyze such periodically driven quantum systems, we resort to Floquet theory, a framework originally formulated in the late 19th century for classical differential equations, which can provide the mathematical foundation for this analysis. In the following chapter, we examine how this classical mathematical theory has become a substantial cornerstone for understanding periodically driven quantum matter far from equilibrium.

1.3 Non-equilibrium Floquet physics

In 1883, Gaston Floquet published his seminal work on linear differential equations with periodic coefficients, establishing what we now recognize as the Floquet theorem [99]. He demonstrated that solutions to periodic differential equations can be characterized by higher harmonics of the period, analogous to Fourier coefficients for waves and periodic signals¹⁵.

The developments of Floquet theory unified several important problems in classical physics. Both the Mathieu equation, describing vibrating elliptical membranes, and Hill's equation [100], emerging from the analysis of the Moon's orbit, represent special cases of the Floquet equation¹⁶. The theory proved useful for analyzing mechanical systems, especially in understanding parametric resonance and stability conditions, and periodic phenomena in circuits and vibrations [103].

For quantum physicists, the Floquet theorem looks familiar, as it is based on a translation invariance similar to the Bloch theorem¹⁷.

¹⁵The technical details are presented in Section 3.2 of Chapter 3.

¹⁶While Émile Léonard Mathieu (1868) and George William Hill (1877) developed their formalism independently from Floquet, both equations can be cast into Floquet form [101, 102].

¹⁷Felix Bloch developed this theorem during his doctoral work as Werner Heisenberg's first graduate student [104]. Curiously, many papers incorrectly cite Bohm's 1949 paper on superconductivity [105]—a misattribution that seems to have propagated through the literature.

The theory was generalized to the Floquet-Bloch theorem¹⁸ in the 1950s [107, 108]. The 1970s and 1980s witnessed the application of the Floquet theorem in solid-state physics, for example for magnetic resonance experiments. Researchers recognized that the response properties of electrons in solids, driven periodically by electromagnetic radiation, could be described using the Floquet formalism [109]. This period also saw significant developments in computational techniques for solving Floquet problems, notably through the work of Peter Hänggi and colleagues [110, 111].

During the late 1970s the field of *quantum chaos* emerged¹⁹ and while classical driven systems can exhibit deterministic chaos [113], the quantum behavior of such systems revealed unexpected features. In 1979, Casati and colleagues discovered *dynamical localization* in periodically kicked quantum rotors [46], demonstrating that quantum interference effects can suppress classical chaos. Fishman later provided a theoretical framework through Floquet theory by connecting dynamical localization to Anderson localization²⁰ in disordered systems [114]. The quantum kicked rotor became a central model for quantum chaos studies, as its simple structure permits direct analysis through Floquet theory while capturing fundamental aspects of the quantum-classical correspondence [115]. These advances in Floquet engineering naturally lead us to consider an exciting frontier: the manipulation of synthetic dimensions through periodic driv-

¹⁸While Jon Shirley’s 1965 paper [106] is often credited as the first application of Floquet theory in quantum mechanics, this work appeared more than a decade after Herman Haken and Léon Brillouin’s contributions. However, Shirley’s work proved more influential in the field.

¹⁹The notion of chaos in quantum mechanics requires careful analysis. The linearity of the Schrödinger equation prevents quantum systems from exhibiting the exponential sensitivity to initial conditions characteristic of classical chaos. This fundamental distinction led Berry to introduce the term “quantum chaology” [112] for studying quantum systems whose classical counterparts display chaos.

²⁰As we will show in Section 3.4, the quasi-energy spectrum of the kicked rotor maps onto the energy spectrum of an Anderson model, which implies that temporal disorder in driven systems corresponds to spatial disorder [60].

ing, where time-dependent protocols create and control additional effective spatial dimensions.

1.3.1 Synthetic dimensions in time

As we are arguing in this thesis, periodically-driven molecular systems offer a particularly promising area for exploring topological physics due to their rich and highly controllable Hilbert space [27, 116]. While our focus here primarily concerns rotational degrees of freedom, other quantum numbers such as vibrational or electronic modes present equally compelling avenues for investigation. As mentioned earlier, unlike the translational motion of electrons in crystalline lattices, rotations of molecular rigid rotors are governed by the non-abelian $SO(3)$ group. Although free rotations trace trivial paths on this manifold [117, 118], we will demonstrate that precisely designed laser pulses can guide molecules along topologically non-trivial trajectories, enabling the observation of non-trivial Berry-phases and related phenomena. Historically, the connection between molecular physics and topology has centered on conical intersections of potential energy surfaces [83, 119], including light-induced variants [120, 121]. Our work extends this approach by establishing a direct bridge between symmetry-protected topological phases in condensed matter physics and periodically driven molecular systems.

The continuous modulation of kick strengths introduces an effective synthetic dimension in time, a concept that proved fundamental in realizing topological phase transitions [75, 95]. This temporal synthetic dimension manifests in a different way than spatial dimensions, yet maintains the essential geometric properties necessary for topological classification. The ability to engineer such synthetic dimensions opened novel possibilities for quantum state manipulation and control. Our research reveals that this temporal dimension serves a dual purpose: beyond enabling topological transitions, it

provides a mechanism for quantum state preparation through the geometric properties of Floquet states. While this approach shares conceptual similarities with established protocols, it goes way beyond conventional static equilibrium frameworks. The power of Floquet theory in this context lies in its capacity to provide an exact treatment of the driving, effectively summing all orders in the driving strength rather than relying on perturbative expansions.

Previous investigations of double-kicked planar rotors have revealed rich topological phase diagrams, including spectra reminiscent of the celebrated Hofstadter butterfly and associated Chern numbers [61, 122, 123]. We extend these ideas to rotating molecules in terms of the 3D rotor. These discoveries could have implications for chemical reactions and molecular control [124, 125]. We demonstrate the engineering of an effective topological semimetal with topological edge states, and suggest pathways toward realizing more complex topological phases. The exceptional degree of control available in molecular systems, combined with their inherent multi-band nature, opens new possibilities for exploring non-abelian topological phases and non-equilibrium quench dynamics that depend on the topology of the system. These topics form the core of this thesis, whose organization we now outline.

1.4 Organization of the thesis

The thesis is structured as follows:

Chapter 2 explores how ultrashort and strong laser pulses can address the rotational degrees of freedom of molecules, developing a novel platform for quantum simulation. This platform leverages the high degree of control and flexibility afforded by laser pulses to create a versatile testbed for studying multi-band lattice models and localization phenomena. We show that the so-called sudden approximation greatly simplifies the calculation of the full Floquet

operator, which is necessary for subsequent chapters. We justify this approximation, delineating the circumstances under which it holds and its implications for the accuracy and validity of the simulations.

Chapter 3 demonstrates how periodically driven angular momentum states can serve as a synthetic dimension, forming a lattice of angular momentum. We analyze this for 2D and 3D rigid rotors, showcasing the universality of the approach. We elucidate the emergence of quantum resonances and the contrasting regime of dynamical localization. We discuss the limitations for real molecules, such as centrifugal distortion, and their impact on the observed phenomena. Notably, the restriction of angular momentum to $l > 0$ in 3D leads to the appearance of edge states, which we later show to be of topological origin.

Chapter 4 explores the role of topology, providing an introduction to topological aspects in physics. We demonstrate how band degeneracies of periodically driven rotors can lead to symmetry-protected topological charges. These charges manifest as topologically protected edge states, observed for a wide range of model parameters, underscoring the robustness and universality of the topological phenomena. We conclude by outlining an experimental protocol to measure these states, discussing potential challenges and strategies to overcome them.

Chapter 5 investigates novel multi-band topologies in periodically driven quantum rotors, focusing on systems with three or more bands. We demonstrate how symmetry-protected band degeneracies acquire non-abelian characteristics, leading to braiding phenomena impossible in single-gap systems. The chapter establishes how \mathcal{PT} symmetry generates real Hamiltonians whose band singularities carry non-abelian frame charges. We analyze the Euler class and its role in characterizing topologically protected nodes, revealing how periodic driving enables the manipulation of these non-abelian charges through controlled band crossings. The emer-

gence of an anomalous Dirac string phase, unique to Floquet systems, demonstrates the rich interplay between multi-gap topology and non-equilibrium dynamics. We conclude by showing how these phenomena manifest in experimentally observable zero-angular-momentum edge states, providing clear signatures of the underlying topological structure.

Throughout the thesis, we try to maintain a clear progression of ideas, with each chapter building upon the concepts introduced in the previous ones. By the end, readers will hopefully understand how the interplay between ultrafast laser pulses, angular momentum, and topology can lead to the emergence of new quantum phases and phenomena in molecular systems.

CHAPTER 2

Rotating molecules with ultrashort pulses

Science is an essentially anarchic enterprise.

– Paul Feyerabend

2.1 Overview

In the preceding chapter, we introduced the idea of using molecules as a novel platform for exploring non-equilibrium topological phenomena. While previous studies have examined topological aspects of two-dimensional rotors, our research takes a significant leap forward by focusing on three-dimensional molecular rotation. This idea closely aligns with recent experimental advancements as outlined in Section 1.1.2, which have demonstrated the feasibility of controlling three-dimensional molecular rotations [27, 126], providing the basis for our theoretical explorations. This chapter will examine the practical aspects of molecular physics that form the backbone of our work, before transitioning to the more mathematically involved topological physics in subsequent chapters.

We will demonstrate how molecules can serve as versatile platforms for quantum simulation, starting with the fundamental case: a three-dimensional linear molecule subjected to off-resonant, linearly polarized laser pulses¹. In Section 2.2, we will explore the rotational degrees of freedom in molecules and methods to manipulate them using strong fields. While the primary focus of this thesis is on the total angular momentum of linear molecules, one could also consider the potential of more complex rotors, such as symmetric tops or even asymmetric tops. These systems possess the additional quantum number K , potentially expanding the usable Hilbert space. Furthermore, by incorporating the laser polarization as an additional degree of freedom, one can utilize the full rotational sphere $SO(3)$ as the synthetic manifold. As we will demonstrate in subsequent sections, the linear rotor alone provides sufficient complexity to observe fascinating topological physics. Nevertheless, we will outline how harnessing these additional degrees of freedom presents significant potential for expanding our synthetic dimensions.

To arrive at the one-dimensional kicked rotor model, we must assume that the pulse train consists of infinitely short pulses, known as the impulsive limit (or "sudden approximation"), effectively establishing a lattice in time. This approximation has been widely used to accurately describe the interaction between molecules and short, far-off-resonant laser pulses. It posits that the timescale of the laser-molecule interaction is significantly shorter than the internal rotational period of the molecule, effectively "freezing" the rotational motion during the interaction. This simplified model of laser-molecule interaction is incorporated into various theoretical frameworks predicting the rotational dynamics of molecules driven by short laser pulses.

To assess the validity of this approximation, we have developed an effective theory for ultrashort laser pulses, which represents a novel

¹This chapter follows closely our work [4], Copyright © 2024 American Physical Society.

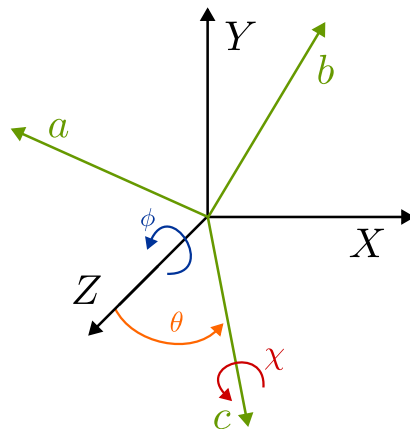
contribution to the field. In Section 2.3, we will undertake a comprehensive analysis of the full time-evolution operator and solve the time-dependent Schrödinger equation at the operator level. Our investigation will show that there is a critical angular momentum, l_{\max} , which marks the point at which the impulsive limit ceases to be valid. This finding underscores that the applicability of the sudden approximation is not solely dependent on pulse duration, but also on pulse intensity, as the latter determines the extent of angular momentum state population. We will examine this for both ultrashort multi-cycle (Gaussian) pulses and the less frequently studied half-cycle pulses, each giving rise to distinct effective potentials. Subsequently, we will critically assess the constraints of the impulsive limit and introduce a novel approach that involves rescaling the effective matrix elements. This method aims to provide a more refined and accurate portrayal of rotational laser-molecule interactions. Afterwards, we will investigate the time-evolution to gain a more nuanced understanding of the dynamics at play during strong laser-molecule interactions. Surprisingly, we uncover curious behaviors of the wavefunction that have not been observed before, either in theory or experiments. It remains unclear whether these behaviors have a deeper significance or are merely intriguing phenomena. They may potentially have applications in non-equilibrium quench dynamics with molecules.

2.2 Laser induced rotation of molecules

Let us recapitulate what is the most generic expression for a (3D²) asymmetric top molecule within a circular/elliptically polarized light. Within the Born-Oppenheimer approximation [127] we can neglect the vibrational and electronic degrees of freedom, which can be considered as fast fluctuations on top of the rotation of the molecule

²The arguments of the 2D rotor are analogous to this discussion and will not be given here; we will look into them more closely in the next chapter when discussing the periodically driven rotor.

Figure 2.1: Euler angles of the rotating molecule. The two coordinate systems are shown in black (laboratory frame) and green (body-fixed molecular frame). The rotation is described by three angles: $\phi \in [0, 2\pi)$ represents rotations around the laboratory Z -axis, $\chi \in [0, 2\pi)$ describes rotations around the molecular c -axis, and $\theta \in [0, \pi)$ defines the angle between the Z - and c -axes.



as long as the rotational energy is much smaller than the former. The coupling between vibration and rotation can be taken into account ad-hoc, as long as the vibrational level does not change during the considered time window. This is also why it is important to use off-resonant laser pulses. They do not leverage transitions between different vibronic levels. Hence, for our purposes and the kind of molecules we consider here it is sufficient to model the molecules as *rigid rotors*³.

We describe the quantum mechanical rotation of a molecule using two coordinate frames: the laboratory frame (X, Y, Z) and the molecule-fixed frame (a, b, c) (see Fig. 2.1). The body-fixed axes are assigned according to the principal moments of inertia $I_a \leq I_b \leq I_c$ (see Table 2.1 for the rotational classification of molecules). The rotational motion is governed by the Hamiltonian

$$H = AL_a^2 + BL_b^2 + CL_c^2, \quad (2.1)$$

where L_i are the components of the angular momentum operator in the body-fixed frame and $A = 1/(2I_a)$, $B = 1/(2I_b)$, and $C = 1/(2I_c)$ are the rotational constants [19].

³Non-rigidity may play a role when considering very strong electric field strengths, in particular for linear molecules [128]. In that case one has to include the deformation terms in the Hamiltonian. We will discuss the effects of centrifugal distortion in Section 3.5.2.

2.2. Laser induced rotation of molecules

The orientation of the molecule is specified by three Euler angles (ϕ, θ, χ) . These angles define successive rotations: first by ϕ around the space-fixed Z axis, then by θ around the new Y axis (defining the angle between the space-fixed Z and body-fixed c axes), and finally by χ around the body-fixed c axis [128]. The quantum mechanical rotation operator $R(\phi, \theta, \chi)$ implements these rotations in sequence

$$R(\phi, \theta, \chi) = e^{-i\phi\hat{L}_Z} e^{-i\theta\hat{L}_y} e^{-i\chi\hat{L}_c}. \quad (2.2)$$

The rotational wavefunctions are expressed through Wigner D-matrices

$$D_{mk}^l(\phi, \theta, \chi) = \langle lm | R(\phi, \theta, \chi) | lk \rangle = e^{-im\phi} d_{mk}^l(\theta) e^{-ik\chi}, \quad (2.3)$$

where $d_{mk}^l(\theta) = \langle lm | e^{-i\theta\hat{L}_y} | lk \rangle$ represents Wigner's d-matrix element, with quantum numbers $l \in \mathbb{N}_0$ and $|m|, |k| \leq l$. A pure rotational state is hence fully characterized by these complete set of basis states

$$\langle \theta, \phi, \chi | lmk \rangle = \sqrt{\frac{2l+1}{8\pi^2}} D_{mk}^{l*}(\phi, \theta, \chi) \quad (2.4)$$

with the normalization

$$\begin{aligned} \int D_{m'k'}^{l'*}(\Omega) D_{mk}^l(\Omega) d\Omega &= \frac{8\pi^2}{2l+1} \delta_{mm'} \delta_{kk'} \delta_{ll'}, \\ \sum_k D_{mk}^{l'*}(\Omega) D_{m'k}^l(\Omega) &= \sum_k D_{km}^{l'*}(\Omega) D_{km'}^l(\Omega) = \delta_{mm'}. \end{aligned} \quad (2.5)$$

With these definitions of the relative angles, the angular momentum operators become

$$\hat{L}_Z = -i \frac{\partial}{\partial \phi}, \quad \hat{L}_c = -i \frac{\partial}{\partial \chi}. \quad (2.6)$$

Angular momentum operators satisfy $[\hat{L}_i, \hat{L}_j] = i\epsilon_{ijk}\hat{L}_k$ and the Casimir operator $\hat{L}^2 = \sum_i \hat{L}_i^2$ with the eigenvalues

$$\begin{aligned} \hat{L}^2 |lmk\rangle &= l(l+1) |lmk\rangle, \\ \hat{L}_c |lmk\rangle &= k |lmk\rangle, \\ \hat{L}_Z |lmk\rangle &= m |lmk\rangle. \end{aligned} \quad (2.7)$$

The rotational energies of the symmetric tops become

$$E_{\text{rot}} = \frac{l(l+1)}{2I_a} + k^2 \left(\frac{1}{2I_c} - \frac{1}{2I_a} \right). \quad (2.8)$$

For the linear and spherical top the k -dependent term vanishes. The asymmetric top gives rise to eigenstates with a superposition of different k (either even or odd, depending on the parity of the asymmetric top eigenstate [43]) and is generally not integrable.

Class	Moments of inertia	Examples
Spherical top	$I_c = I_b = I_a$	$\text{CH}_4, \text{P}_4, \text{CCl}_4$
Linear top	$I_c = I_b \gg I_a \approx 0$	$\text{O}_2, \text{CO}, \text{H}_2\text{C}_2$
Prolate symmetric top	$I_c = I_b > I_a$	$\text{CH}_3\text{I}, \text{CHCl}_3$
Oblate symmetric top	$I_c > I_b = I_a$	$\text{C}_6\text{H}_6, \text{C}_4\text{H}_4, \text{NH}_3$
Asymmetric top	$I_c > I_b > I_a$	$\text{NO}_2, \text{HO}_2, \text{H}_2\text{O}_2, \text{C}_{14}\text{H}_{10}$

Table 2.1: Moments of inertia for molecular rotation.

2.2.1 Molecule-laser interaction

Next, we examine the interaction with a laser. A non-resonant laser⁴ leaves a molecule in its vibronic state and excites only rotational eigenstates via Raman-type transitions⁵. We choose the laser coordinates as the lab coordinates with the Z -axis as the direction of propagation. The potential energy of a polar rotor in an electromagnetic field is given by

$$V(t) = -\boldsymbol{\mu} \cdot \boldsymbol{\mathcal{E}}(t) \quad (2.9)$$

with (total) dipole moment $\boldsymbol{\mu}$ and laser field amplitude $\boldsymbol{\mathcal{E}}(t)$. This electric field, which leads to an induced dipole moment⁶ through a

⁴We consider a laser with frequency $\omega_l \gg \omega_v, \omega_e$, where ω_v are the molecular vibrational and ω_e electronic frequencies of the molecule [129].

⁵This subsection is rephrasing the argument in [129].

⁶Higher orders such as quadrupole moments etc. can be included using higher polarizability tensors such as the hyperpolarizability tensor $\beta(\omega)$ [27]. However, since the

temporary Stark shift of the relevant energy levels and a hybridization of the energy levels, can be modeled by the effective polarizability $\alpha(\omega)$ of the molecule⁷. In the long wavelength regime of interest the dynamical polarizability has converged to its dc limit $\alpha(\omega) \rightarrow \alpha$ [129]. The total dipole moment then takes the form

$$\mu_i = (\mu_0)_i + \frac{1}{2} \sum_j \alpha_{ij} \mathcal{E}_j(t) + \mathcal{O}[\mathcal{E}^2(t)], \quad (2.10)$$

with the permanent dipole moment of the molecule μ_0 and the polarizability tensor α_{ij} . For now, let us drop the permanent dipole moment; then, we can express the interaction potential between the laser and the molecule as following [43]

$$V = -\frac{1}{2} \sum_{i,j=1}^3 \mathcal{E}_i(t) \alpha_{ij}^{\text{lab}} \mathcal{E}_j(t) = -\frac{1}{2} \text{tr}[\alpha^{\text{lab}} F(t)] \quad (2.11)$$

with electric field with electric field tensor $F_{ij}(t) = \mathcal{E}_i(t)\mathcal{E}_j(t)$. In molecular coordinates, we can assume that the polarizability tensor is diagonal in the principal axes of the molecule $\alpha_{ij}^{\text{mol}} = \alpha_{ii}\delta_{ij}$ and it is therefore a spherical tensor of rank 2. The non-zero components in the molecular frame read

$$\alpha_{00}^{\text{mol}} = \frac{1}{3}(\alpha_{xx} + \alpha_{yy} + \alpha_{zz}) \equiv \bar{\alpha}, \quad (2.12)$$

$$\alpha_{20}^{\text{mol}} = \sqrt{\frac{3}{2}}(\alpha_{zz} - \bar{\alpha}), \quad (2.13)$$

$$\alpha_{2,\pm 2}^{\text{mol}} = \alpha_{2,2}^{\text{mol}} = \frac{2}{2}(\alpha_{xx} - \alpha_{yy}). \quad (2.14)$$

Henceforth, the rotation of the tensor from the lab frame to the molecular frame reads

$$\alpha_{lm}^{\text{lab}} = \sum_k D_{mk}^l(\phi, \theta, \chi) \alpha_{lk}^{\text{mol}} = \sum_k D_{mk}^l(\Omega) \alpha_{lk}^{\text{mol}} \quad (2.15)$$

size of a molecule is small compared to the wavelength of the electric field, they can be neglected as a first approximation.

⁷See Chapter 8 of [130] for a derivation.

2. ROTATING MOLECULES WITH ULTRASHORT PULSES

with components (we abbreviate $D_{mk}^l \equiv D_{mk}^l(\phi, \theta, \chi)$)

$$\alpha_{00}^{\text{lab}} = \bar{\alpha} \quad (2.16)$$

$$\alpha_{20}^{\text{lab}} = D_{00}^2 \alpha_{20}^{\text{mol}} + (D_{02}^2 + D_{0,-2}^2) \alpha_{22}^{\text{mol}} \quad (2.17)$$

$$\alpha_{2\pm 1}^{\text{lab}} = D_{\pm 10}^2 \alpha_{20}^{\text{mol}} + D_{\pm 12}^2 \alpha_{22}^{\text{mol}} \quad (2.18)$$

$$\alpha_{2\pm 2}^{\text{lab}} = D_{\pm 20}^2 \alpha_{20}^{\text{mol}} + (D_{\pm 22}^2 + D_{\pm 2,-2}^2) \alpha_{22}^{\text{mol}}. \quad (2.19)$$

Likewise, the dyadic field tensor $F_{ij}(t)$ is a rank 2 spherical tensor and can be written as

$$F_{00}(t) = \frac{1}{2} |\mathcal{E}(t)|^2, \quad (2.20)$$

$$F_{20}(t) = \sqrt{\frac{3}{2}} (\mathcal{E}_z^2(t) - \frac{1}{3} |\mathcal{E}(t)|^2), \quad (2.21)$$

$$F_{2\pm 1}(t) = \mp (\mathcal{E}_x(t) \mathcal{E}_z(t) \pm i \mathcal{E}_y(t) \mathcal{E}_z(t)) \quad (2.22)$$

$$F_{2,\pm 2}(t) = \frac{1}{2} (\mathcal{E}_x^2(t) - \mathcal{E}_y^2(t) \pm 2i \mathcal{E}_x(t) \mathcal{E}_y(t)). \quad (2.23)$$

The potential (2.11) then becomes

$$\begin{aligned} V &= -\frac{1}{2} \sum_{lm} \alpha_{lm}^{\text{lab}} F_{lm}(t) = -\frac{1}{2} (\alpha_{00}^{\text{lab}} F_{00}(t) + \alpha_{20}^{\text{lab}} F_{20}(t) \\ &\quad + F_{21}(t) \alpha_{21}^{\text{lab}} + F_{2,-1}(t) \alpha_{2,-1}^{\text{lab}} + \alpha_{22}^{\text{lab}} F_{22}(t) + \alpha_{2,-2}^{\text{lab}} F_{2,-2}(t)) \\ &= -\frac{1}{2} \left(\frac{1}{2} \bar{\alpha} |\mathcal{E}(t)|^2 + (D_{00}^2 \alpha_{20}^{\text{mol}} + (D_{02}^2 + D_{0,-2}^2) \alpha_{22}^{\text{mol}}) \sqrt{\frac{3}{2}} (\mathcal{E}_z^2(t) - \frac{1}{3} |\mathcal{E}(t)|^2) \right. \\ &\quad - (\mathcal{E}_x(t) \mathcal{E}_z(t) + i \mathcal{E}_y(t) \mathcal{E}_z(t)) (D_{10}^2 \alpha_{20}^{\text{mol}} + D_{12}^2 \alpha_{22}^{\text{mol}}) \\ &\quad + (\mathcal{E}_x(t) \mathcal{E}_z(t) - i \mathcal{E}_y(t) \mathcal{E}_z(t)) (D_{-10}^2 \alpha_{20}^{\text{mol}} + D_{-12}^2 \alpha_{22}^{\text{mol}}) \\ &\quad + (D_{20}^2 \alpha_{20}^{\text{mol}} + (D_{22}^2 + D_{2,-2}^2) \alpha_{22}^{\text{mol}}) \frac{1}{2} (\mathcal{E}_x^2(t) - \mathcal{E}_y^2(t) + 2i \mathcal{E}_x(t) \mathcal{E}_y(t)) \\ &\quad \left. + (D_{-20}^2 \alpha_{20}^{\text{mol}} + (D_{-22}^2 + D_{-2,-2}^2) \alpha_{22}^{\text{mol}}) \frac{1}{2} (\mathcal{E}_x^2(t) - \mathcal{E}_y^2(t) - 2i \mathcal{E}_x(t) \mathcal{E}_y(t)) \right) \\ &= -\frac{1}{2} \left(\frac{1}{2} \bar{\alpha} |\mathcal{E}(t)|^2 + \alpha_{20}^{\text{mol}} B_{20}(t) + \alpha_{22}^{\text{mol}} B_{22}(t) \right) \end{aligned} \quad (2.24)$$

with coefficients

$$\begin{aligned}
 B_{20}(t) &= D_{00}^2 \sqrt{\frac{3}{2}} (\mathcal{E}_z^2(t) - \frac{1}{3} |\mathcal{E}(t)|^2) + \mathcal{E}_x(t) \mathcal{E}_z(t) (D_{-10}^2 - D_{10}^2) \\
 &\quad - i \mathcal{E}_y(t) \mathcal{E}_z(t) (D_{10}^2 + D_{-10}^2) + \frac{1}{2} (D_{20}^2 + D_{-20}^2) (\mathcal{E}_x^2(t) - \mathcal{E}_y^2(t)) \\
 &\quad + i \mathcal{E}_x(t) \mathcal{E}_y(t) (D_{2,0}^2 - D_{-2,0}^2), \\
 B_{22}(t) &= (D_{02}^2 + D_{0,-2}^2) \sqrt{\frac{3}{2}} (\mathcal{E}_z^2(t) - \frac{1}{3} |\mathcal{E}(t)|^2) + \mathcal{E}_x(t) \mathcal{E}_z(t) (D_{-1,2}^2 - D_{1,2}^2) \\
 &\quad - i \mathcal{E}_y(t) \mathcal{E}_z(t) (D_{12}^2 + D_{-1,2}^2) \\
 &\quad + (\mathcal{E}_x^2(t) - \mathcal{E}_y^2(t)) \cdot (D_{22}^2 + D_{2,-2}^2 + D_{-2,2}^2 + D_{-2,-2}^2) \\
 &\quad + 2i \mathcal{E}_x(t) \mathcal{E}_y(t) \cdot (D_{22}^2 + D_{2,-2}^2 - D_{-2,2}^2 - D_{-2,-2}^2).
 \end{aligned} \tag{2.25}$$

When assuming some laser frequency $\omega \gg \tau_B^{-1}$ with the rotation time of the molecule $\tau_B = \frac{\hbar\pi}{B}$, we can integrate out the time-dependency of the laser⁸ and all the mixed terms $\mathcal{E}_x(t)\mathcal{E}_y(t)$, $\mathcal{E}_x(t)\mathcal{E}_z(t)$, \dots etc. vanish. For symmetric tops $\alpha_{xx} = \alpha_{yy}$ and hence $\alpha_{22}^{\text{mol}} = 0$. In that case, let us consider only $B_{20}(t)$. It turns out that the force which is applied on the molecule depends on the effective field direction of the laser pulse, which is different for circular and linearly polarized light. For linear polarized light, the axis should be $\langle \mathcal{E} \rangle_t \propto \mathbf{e}_Z$, since the angle θ measures exactly the angle between the space-fixed Z and body-fixed c axes (a linearly polarized pulse whose polarization axis is aligned with the principal axis of the molecule does not exert any force) and the $D_{\pm 20}^2$ terms vanish. For circular polarized light with X-Y plane as the polarization plane, the effective direction is again the Z-axis. In that case, $\mathcal{E}_z(t) = 0$, $\langle \mathcal{E}_x \rangle = \langle \mathcal{E}_y(t) \rangle$ and again the $D_{\pm 2,0}^2$ terms vanish; both cases lead to an effective potential $V \propto \cos^2(\theta)$. A non-exhaustive representation of the laser with the x,z-axis defined as the polarization plane and y-axis as the propagation axis is given by [43]

$$\mathcal{E}(t) = \mathcal{E}_0(t) [\epsilon_x \cos(\omega t) \mathbf{e}_x + \epsilon_z \sin(\omega t) \mathbf{e}_z], \tag{2.26}$$

⁸For a pulse with $\lambda = 800\text{nm}$ the cycle time is few femtoseconds, while the rotational time scale is in the picosecond regime [128].

2. ROTATING MOLECULES WITH ULTRASHORT PULSES

with the electric field envelope $\mathcal{E}_0(t)$, the polarization eccentricities ϵ_x, ϵ_z and the unit vectors $\mathbf{e}_x, \mathbf{e}_z$. Note that the eccentricities satisfy $\epsilon_x^2 + \epsilon_z^2 = 1$. For $\epsilon_z = 0$ (or $\epsilon_x = 0$) we recover a linearly polarized field, for $\epsilon_x = \epsilon_z$ a circular polarized field, and for $0 \leq \epsilon_x < \epsilon_z$ an elliptically polarized field. As mentioned earlier, after integration only few elements are non-zero. For the above parametrization, only the following three spherical components of the field tensor are non-zero (we also omit the $F_{0,0}$ term which introduces a constant shift in all energies) [43]

$$F_{2,0}(t) = \frac{2}{\sqrt{6}}(2 - 3\epsilon_x^2)\mathcal{E}_0^2(t), \quad F_{2,\pm 2}(t) = \epsilon_x^2\mathcal{E}_0^2(t). \quad (2.27)$$

The matrix element of the $H_{\text{ind}}(t)$ in (2.31) becomes [43]

$$\begin{aligned} \langle lkm | H_{\text{ind}} | l'k'm' \rangle &= -\frac{1}{2} \sqrt{\frac{2l+1}{2l'+1}} \left(\alpha_{20}^{\text{mol}} C_{lk2,0}^{l'k'} + \alpha_{2,2}^{\text{mol}} \left(C_{lk2,2}^{l'k'} + C_{lk2,-2}^{l'k'} \right) \right) \\ &\quad \times \left(F_{2,0}(t) C_{lm2,0}^{l'm'} + F_{2,2}(t) \left(C_{lm2,-2}^{l'm'} + C_{lm2,2}^{l'm'} \right) \right), \end{aligned} \quad (2.28)$$

where $C_{l_1 m_1 l_2 m_2}^{l m} = \langle l_1 m_1 l_2 m_2 | l m \rangle$ are the usual Clebsch-Gordan coefficients. The interaction with a linearly polarized laser field depends only on the angle θ , the angle between the polarization vector of the field (defining the z-axis) and the molecular axis, which corresponds to the case $\epsilon_x = 0$, i. e. only $F_{2,0}(t)$ is non-zero. If we further consider the case of a linear molecule, the only non-zero component in the polarizability is

$$\alpha_{2,0}^{\text{lin.}} = \sqrt{\frac{2}{3}}(\alpha_{cc} - \alpha_{bb}) \equiv \sqrt{\frac{2}{3}}(\alpha_{\parallel} - \alpha_{\perp}) \equiv \sqrt{\frac{2}{3}}\Delta\alpha, \quad (2.29)$$

while (2.31) becomes

$$\langle lkm | H_{\text{ind}}^{\text{lin.,lin.}} | l'k'm' \rangle = -\frac{1}{6} \cdot \Delta\alpha \cdot \mathcal{E}_0^2(t) \sqrt{\frac{2l+1}{2l'+1}} C_{lk2,0}^{l'k'} C_{lm2,0}^{l'm'}. \quad (2.30)$$

Since for angular momentum addition we require $m = m_1 + m_2$ it follows that these elements are zero unless $m = m'$ and $k = k'$.

Hence, for a linear molecule with linearly-polarized laser pulses the molecule-laser interaction becomes

$$\hat{H}(t) = -\frac{1}{4}\mathcal{E}^2(t)\Delta\alpha\cos^2(\hat{\theta}) \quad (2.31)$$

with electric field envelope $\mathcal{E}(t)$, where we drop the underscore zero from now. This concludes the derivation of the laser-molecule interaction. In the next section we will take a closer look at pulses that are much shorter in duration than the typical rotational time of the molecule.

2.3 The sudden approximation

2.3.1 Overview

The following section is based on a recent paper of ours [4]. For off-resonant ultrashort laser pulses (usually with infrared frequencies far detuned from any transitions, as mentioned earlier), the rotational motion is generally considered to be slow compared to the laser modes, leading to the “frozen” rotational motion assumption during the laser–molecule interaction [116, 131–137]. This justifies the impulsive limit, which adapts a semi-classical approach by neglecting the accumulation of quantum phases during the pulse duration. One has to take into account however, that for linear quantum rotors, the energy splittings grow linearly with the angular momentum l ,

$$E_{l+1} - E_l \propto 2l + 3, \quad (2.32)$$

which causes the corresponding change of the relevant timescales. Therefore the applicability of the sudden approximation does not solely rely on the duration of the laser pulse, but also on its intensity which determines how many l -states are populated during the laser excitation. For example, for a molecule with a rotational period $\tau_{\text{rot}}(l)$, for the impulsive limit to be valid, only states with l satisfying

$\tau_{\text{rot}}(l) \gg \tau_L$ should be occupied, where τ_L represents the pulse duration of the laser. Additionally, the specific shape of the laser pulse is an important factor to consider. It is not immediately evident which values of $\tau_{\text{rot}}(l)$ are large enough or how different laser shapes affect this relationship. Despite the widespread adoption of the impulsive limit as a theoretical framework to describe molecular rotational response to a laser pulse, a comprehensive analysis of the specific states for which this approximation is valid remains unexplored. Here, we develop an effective theory for ultrashort laser pulses by analyzing the full time evolution of linear rotors during and after an off-resonant, linearly polarized laser pulse illumination. A lot of work has been done during the last decades employing the impulsive limit for very short pulses, providing analytic expressions in the $\tau_L \rightarrow 0$ limit with applications to molecular alignment and orientation [131–133, 138–140], controlling molecular vibrational states [141, 142], as well as studying the dynamics of atoms [143], semiconductor nanostructures [144], and low-dimensional electronic systems driven by pulses [145]. Our approach goes beyond these efforts by illustrating how deviations occur from the sudden approximation, providing some understanding of the specific conditions that cause these deviations. Our approach can be extended to more complex molecules with higher order polarizability terms and other laser polarization schemes. While the sudden limit for multi-cycle pulses is well-established [63, 65, 146], we also investigate the effects of half-cycle pulses, which can generate unipolar fields [147–150]. Using a theoretical method accounting for the full time-evolution operator, we demonstrate that the validity of the sudden limit can be understood in terms of a critical angular momentum threshold l_{crit} . We propose a new method involving rescaling of matrix elements, resulting in an effective theory that accounts for deviations from the standard impulsive limit when encountering extended pulse durations. Our findings hold significant implications for experimentalists working with ultrashort lasers and theorists who employ the sudden limit within their models.

Here we focus on time-dependence of the full time-evolution operator instead of time-evolving a single initial state with respect to a given laser envelope, as commonly used to describe the dynamics of rotational wavepackets. The advantage is that we do not only learn about the time-evolution of a particular initial state, but also of all possible superpositions. Following (2.31), the interaction of a linear molecule with $H_0 = B\hat{\mathbf{L}}^2$ with an ultrashort, off-resonant linearly polarized laser pulse takes the form

$$\hat{H}(t) = \hat{H}_0 - \mu_0 \mathcal{E}(t) \cos(\hat{\theta}) - \frac{1}{4} \mathcal{E}^2(t) \Delta\alpha \cos^2(\hat{\theta}) \quad (2.33)$$

with angle between field polarization and molecular axis $\theta \in [0, \pi]$, the electric field in the Z -direction $\mathcal{E}(t)$ and the difference between parallel and perpendicular polarizability $\Delta\alpha$. Molecular rotation sets the timescale of the Hamiltonian, thereby justifying the representation of time in units of the rotational revival time $\tau_B = \pi\hbar/B$, denoted as $\tilde{t} = t/\tau_B$. In an effort to render the Hamiltonian dimensionless, we can conveniently incorporate the \hbar^{-1} prefactor of the time evolution into the coupling constants, resulting in the following expression⁹

$$\tilde{H}(\tilde{t}) = \pi\hat{\mathbf{L}}^2 - \mathcal{E}(\tilde{t})/\mathcal{E}_\mu \cos(\hat{\theta}) - \mathcal{E}^2(\tilde{t})/\mathcal{E}_{\Delta\alpha}^2 \cos^2(\hat{\theta}). \quad (2.34)$$

This includes the constants

$$\mathcal{E}_\mu = \frac{B}{\pi\mu}, \quad \mathcal{E}_{\Delta\alpha} = \sqrt{\frac{4B}{\pi\Delta\alpha}}, \quad (2.35)$$

which depend on the particular molecule under study. Moving forward, we will omit the tilde on t and H , keeping in mind that all expressions are now unitless.

In order to study the validity of the sudden approximation, we numerically integrated the differential equation of the time-evolution

⁹Note that we do not employ the common units of H/B , since we are interested in expressing time in units of τ_B , which leads to an additional factor of π in front of $\hat{\mathbf{L}}^2$.

2. ROTATING MOLECULES WITH ULTRASHORT PULSES

operator $\hat{U}_{\text{full}}(t)$,

$$i\partial_t \hat{U}_{\text{full}}(t) = \hat{H}(t)\hat{U}_{\text{full}}(t) \quad (2.36)$$

for a reasonable cutoff $l < l_{\text{max}}$ and various parameters¹⁰. As mentioned earlier, each angular momentum eigenstate $|l, m\rangle$ oscillates with the frequency

$$\omega_{\text{rot}}(l) = \pi \cdot l(l + 1)/\tau_B \quad (2.37)$$

corresponding to the rotational periods

$$\tau_{\text{rot}}(l) = \tau_B/(l(l + 1)) \quad (2.38)$$

which provides a natural cutoff scale; the approximation can only succeed for states with $\langle l|\psi\rangle \approx 0$ for l with $\tau_L > \tau_{\text{rot}}(l)$. The eigenstates l with $\tau_L > \tau_{\text{rot}}(l)$ oscillate with a frequency equal or higher than the pulse duration and a separation of timescales is not possible. The matrix elements for the potentials are

$$\langle l'm' | \cos(\theta) | lm \rangle = -\delta_{mm'} C_{lm10}^{l'm} C_{l'010}^{l0} \quad (2.39)$$

$$\langle l'm' | \cos^2(\theta) | lm \rangle = +\delta_{mm'} \left(\frac{2}{3} C_{lm20}^{l'm} C_{l'020}^{l0} + \frac{1}{3} \delta_{ll'} \right). \quad (2.40)$$

Henceforth, our analysis will concentrate exclusively on linearly polarized laser fields that drive molecules at low temperatures for which different m -sectors are independent¹¹ and we can assume $m = 0$. Following the definitions for the sudden limit in Eqs. (2.50)

¹⁰For each calculation we increase the cutoff scale until the results we are interested in are converged. This typically depends on the timescale (since high l correspond to high frequency) and the field strength (which determines how many l states are occupied).

¹¹It is important to note that when $m = 0$, molecular rotations occur within the plane of the electric field. This characteristic simplifies the rationale for comparing the field's duration to the rotational period, given the changing relative angle as the molecule rotates. Conversely, for situations where $|m| \approx l$ and l is significantly large, the molecular orientation tends to be nearly orthogonal to the electric field. In such cases, the angle between the molecule's axis and the field's polarization remains relatively unchanged throughout its rotational phase. Thus, in such extreme scenarios, there's potential for deviations from the findings presented in our analysis.

and (2.59), the effective potential of the full time evolution can be calculated as

$$\hat{V}_{\text{eff}}(t) = -i \log[e^{+i\hat{H}_0(t-t_0)} \hat{U}_{\text{full}}(t) e^{+i\hat{H}_0 t_0}] \quad (2.41)$$

where one has to use the correct branch cut of the logarithm¹². For times $t \gg t_0$ it converges to a constant, time-independent potential $\hat{V}_{\text{eff}} \equiv \hat{V}_{\text{eff}}(t = \infty)$. This is the potential an instantaneous laser pulse at t_0 exerts upon the molecule, after the full time evolution. We want to know if the effective matrix elements resemble the ones given in (2.39) and (2.40). For perfect agreement the off-diagonal matrix elements

$$v_l^{(s)} = \langle l \pm s | \hat{V}_{\text{eff}} | l \rangle \quad \text{with } s \in \{1, 2\} \quad (2.42)$$

should resemble $P_s \cdot \langle l \pm s | \cos^s(\hat{\theta}) | l \rangle$ where P_s depends on the field $\mathcal{E}(t)$. In that case, we can find the strength by $P_s = v_l^{(s)} / \langle l \pm s | \cos^s(\hat{\theta}) | l \rangle$ which should be the same for all l . However, in a realistic case the matrix elements deviate from that obtained in the sudden limit. This implies that the kick strength coefficients

$$p_l^{(s)} \equiv v_l^{(s)} / \langle l \pm s | \cos^s(\hat{\theta}) | l \rangle \quad (2.43)$$

depend on l . In many cases, we are only interested in the convergence up to some experimentally relevant l_{av} . We define the average of a matrix element A_l as $\bar{A} \equiv \frac{1}{l_{\text{av}}+1} \sum_{l=0}^{l_{\text{av}}} A_l$ and estimate the strength $P_{s,\text{eff}}$ and its error by

$$P_{s,\text{eff}} \equiv \overline{p^{(s)}}, \quad \delta P_{s,\text{eff}} \equiv \sqrt{(\overline{p^{(s)}})^2 - \overline{p^{(s)2}}}. \quad (2.44)$$

Clearly, if the sudden approximation was exact we would find $\delta P_{s,\text{eff}} = 0$. For the case, where the sudden approximation is applicable, this value should be sufficiently small. However, for small kick strengths,

¹²For values of the effective kick strength smaller than $P \approx \pi$ the logarithm is straightforward to calculate. For larger values one has to resort an algorithm that guarantees a smooth transition of the operator eigenvalues in order to choose the correct branch cut.

this error becomes small as well, therefore, it is necessary to consider the relative error

$$r_s \equiv \delta P_{s,\text{eff}} / P_{s,\text{eff}}. \quad (2.45)$$

Only the size of r_s poses a sufficient criterion whether the sudden limit approximation is valid or not. Until now we have assumed that we are looking at the impulsive limit in the form of Eqs. (2.50) and (2.59). However, there is a more generic possibility of

$$\hat{U}_{\text{sudd,generic}} = e^{-i\hat{H}_0(t-t_0)} e^{+i\hat{V}_{\text{eff}}} e^{-i\hat{H}_0 t_0} \quad (2.46)$$

with \hat{V}_{eff} as defined in Eq. (2.41). In that case, since \hat{V}_{eff} is derived from the full Schrödinger equation, $\hat{U}_{\text{sudd,generic}} = \hat{U}_{\text{full}}$. However, in many cases one is interested in situations where \hat{V}_{eff} assumes a simpler form or when we can suitably approximate the effective potential. In particular, as we will see later, the numerically estimated effective potentials will often have the same off-diagonal structure as the generating potentials $\hat{V}(t)$. Therefore, it is possible to use *rescaled* matrix-elements $v_l^{(s)}$ that originate from finite time pulses or pulses that are not Gaussian, such as half-cycle pulse. A rescaled potential will have the form $v_l^{(s)} \rightarrow v_l^{(s)} f_l^{(s)}$ with some function $f_l^{(s)}$ that depends on the laser shape. We introduce the usual interaction picture of a Hermitian operator \hat{A} by

$$\hat{A}_I(t) = e^{+i\hat{H}_0 t} \hat{A} e^{-i\hat{H}_0 t} \quad (2.47)$$

and the time-evolution operator (with $t_0 = 0$) with $U_I(t) = e^{+i\hat{H}_0 t} \hat{U}(t)$. The Schrödinger equation then reads

$$i\partial_t \hat{U}_I(t) = \hat{V}_I(t) \hat{U}_I(t). \quad (2.48)$$

In the following we resort to numerical integration of (2.48) and use (2.41) to calculate the effective potential directly. The scaling functions exhibit a continuous behavior over a wide regime and offer a more streamlined approach compared to managing the entire potential. Admittedly, while obtaining these functions requires solving

the Schrödinger equation, one can envisage scenarios where exploring a comprehensive parameter set is of interest. In such situations, interpolating coefficients of the scaling function across a grid might be more efficient than interpolating the entire potential. Thus, while this method doesn't entirely replace the simplicity of the conventional sudden approximation, it provides an alternative strategy to navigate the intricacies associated with finite-width pulses.

2.3.2 Gaussian pulses

In the far-field limit¹³ the electric field of the laser pulse has to integrate to zero [151, 153, 154]

$$\int_{-\infty}^{\infty} \mathcal{E}(t) dt = 0. \quad (2.49)$$

For a laser pulse with many cycles one often assumes that only the part with $\mathcal{E}(t)^2$ is relevant, since the linear term averages out. In that case, one can assume a purely positive Gaussian envelope¹⁴ for the laser field amplitude with kick strength P_2 , peak position t_0 and width σ_t . In the sudden approximation, the time-evolution propagator (for $t \gg t_0$) takes the simple form

$$\hat{U}_{\text{sudd,gaussian}} = e^{-i\hat{H}_0(t-t_0)/\hbar} e^{+iP_2 \cos^2(\hat{\theta})} e^{-i\hat{H}_0 t_0/\hbar}. \quad (2.50)$$

Note that the kick strength is dimensionless. In first order of the Magnus expansion we find

$$P_2 = -\frac{\Delta\alpha}{4\hbar} \int_{-\infty}^{\infty} \mathcal{E}^2(t) dt \quad (2.51)$$

which leads straightforwardly to

$$f_l^{(2)} = p_l^{(2)} / P_2 \quad (2.52)$$

¹³In the broader context, and not strictly in the far-field limit, this condition may not always hold true, as demonstrated, e.g., by [151, 152].

¹⁴Typically, for fast optical oscillations the slow envelope approximation is used.

with the error factor

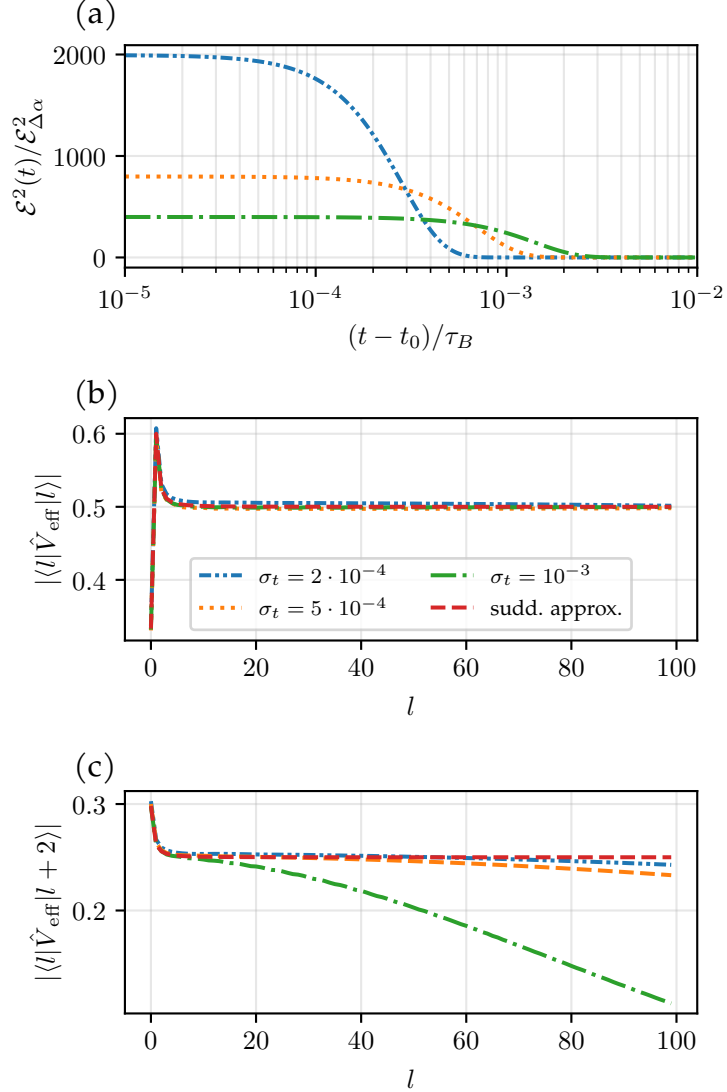
$$\delta_l = 1 - f_l^{(2)} \quad (2.53)$$

that gives a good indication how much rescaling is necessary. Let us now analyze the impact of pulses with a defined width that significantly exceeds the duration of a single optical cycle. By leveraging the slow-envelope approximation, we bypass the complexities of each cycle, focusing primarily on the Gaussian envelope. Consequently, our representation of multi-cycle pulses is based on the Gaussian functions,

$$\mathcal{E}^2(t)/\mathcal{E}_{\Delta\alpha}^2 = e^{-(t-t_0)^2/2\sigma_t^2}/(\sigma_t\sqrt{2\pi}) \quad (2.54)$$

with the squared field strength $\mathcal{E}^2(t)$, $\mu_0 = 0$, and $P_2 = 1$, which we will denote *Gaussian pulses* in what follows. Hence, the pulse width of the laser can be directly inferred from $\tau_L \approx \sigma_t$, depending on the definition of τ_L . Figure 2.2 provides an illustration of the results calculated for a range of σ_t . As one would intuitively expect we observe that as the ratio σ_t/τ_B becomes increasingly small, the results aligns more closely with the sudden limit. However, with an increase in the value of σ_t , the effective potential begins to display noticeable deviations from the sudden limit. This divergence is prominently displayed in the off-diagonal matrix elements. A detailed look at these matrix elements reveals a significant decrease for larger values of l . This contrasts with the matrix elements of the pure sudden pulse, which remains constant. One of the primary features of the perfect delta kick is its ability to transfer angular momentum even for states with high l values. However, this feature is absent in the case of pulses of finite width. Here, the transfer of angular momentum may cease altogether for large l . This can occur when the rotational periods $\tau_{\text{rot}}(l)$, are comparable or smaller than the laser pulse duration τ_L . We assume that such parity leads to destructive interference, inhibiting the laser's capacity to transfer energy to the molecule coherently. The phenomenon is more clearly depicted in Figure 2.3, where the scaling factor, f_l , and its error, $\delta_l \equiv 1 - f_l$, are showcased for different values of σ_t . When the values of f_l or δ_l are equal to 1 or

Figure 2.2: Results for a Gaussian pulse. The full time evolution was integrated numerically and \hat{V}_{eff} was calculated using Eq. (2.41). In (a) the field strength squared after the peak, in (b) the diagonal matrix element and in (c) the second off-diagonal matrix element. Other matrix elements are close to zero. We observe that the diagonal matrix elements (b) coincide perfectly with the sudden limit (red dashed line), but the second off-diagonal matrix elements (c) show large deviations. For increasing σ_t , the deviations set in for lower l . It becomes clear that there only for $l < l_{\text{crit}}$ with some $l_{\text{crit}}(P, \sigma_t)$ the sudden limit with $V_{\text{eff}} = P \cos^2(\hat{\theta})$ is a valid approximation.



0 respectively, it indicates an agreement with a delta kick. However, if δ_l diverges from 0, it signals a deviation from a delta kick. As per our findings, the sudden limit holds true until a certain critical value, $l_{\text{crit}} \propto \sigma_t^{-1}$. Once this point is surpassed, the sudden limit no longer applies, leading to decay in matrix elements and rapid growth in deviations. However, the relative error in Figure 2.4 shows that the approximation is insensitive to P_2 . Henceforth, the time-evolution of

2. ROTATING MOLECULES WITH ULTRASHORT PULSES

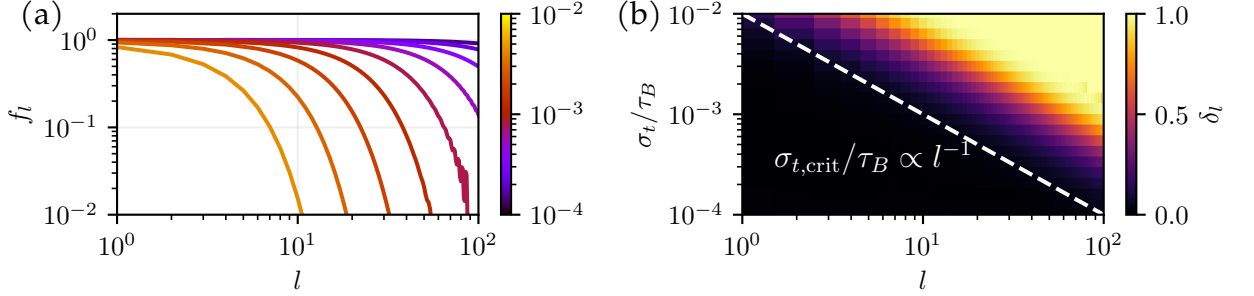
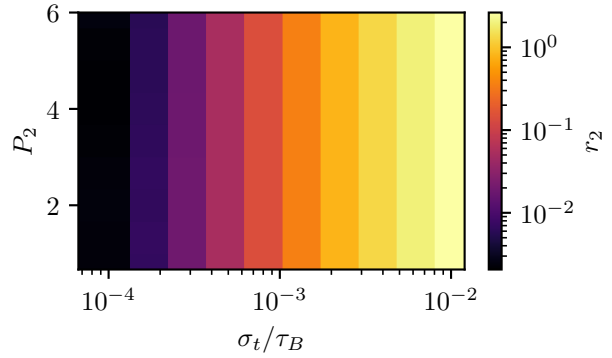


Figure 2.3: Sudden approximation for Gaussian pulses. (a) The scaling factor f_l , Eq. (2.52), for different pulse widths σ_t as indicated by the color; (b) the deviation δ_l , Eq. (3.3), for a Gaussian pulse with $P_2 = 1$. In the region with $f_l \approx 1$ or low error δ_l (black) the sudden limit is a good approximation, i. e. for $l \ll l_{\text{crit}}$. Approximately above the dashed white line (i. e. the non-black region) with $\sigma_t \propto l^{-1}$, there are large deviations from a delta $\cos^2(\theta)$ potential, see Fig. 2.2 for examples.

Figure 2.4: Relative error r_2 . Following (2.44), this figure demonstrates that the goodness of the approximation is independent of P_2 , i. e. the integral of the pulse: it is only sensitive to the width σ_t .



a wavepacket that is driven by a Gaussian-shaped pulse can be captured by the sudden approximation when the wavepacket has only occupations for $l < l_{\text{crit}}(\sigma_t)$. In that case, the sudden approximation is valid and it is not necessary to integrate the Schrödinger equation fully. Another possibility is to rescale the effective potential to

$$\langle l'm' | \hat{V}_{\text{rescaled}} | lm \rangle = \delta_{mm'} \left(f_l^{(2)} \frac{2}{3} C_{lm20}^{l'm} C_{l'020}^{l0} + \frac{1}{3} \delta_{ll'} \right) \quad (2.55)$$

with the rescaling function f_l . This way we can capture the deviations that arise due to the non-zero pulse width. However, this rescaling is

not possible in all cases, as we will demonstrate in Section 2.4. These findings are expected to be useful in understanding the behavior of half-cycle pulses, which we will be exploring in our subsequent analysis.

2.3.3 Few-cycle pulses

Although it is possible to replace pulses with kicks, for few- and half-cycle pulses one has to take into account the full spatial dependence of the laser field. Here, we analyze the half-cycle pulse as an exemplary and experimentally important case, but this analysis can be extended straightforwardly to few-cycle pulses. We consider the following parametrization from Ref. [154]:

$$\mathcal{E}(t) = \begin{cases} 0 & (t \leq 0) \\ \mathcal{E}_1 \cos^2(\omega_L(t - t_p)/2) \sin(\omega_L(t - t_p)) & (0 \leq t < t_p) \\ \mathcal{E}_2 (1 - e^{-(t-t_p)/\tau_1}) e^{-(t-t_p)/\tau_2} & (t \geq t_p), \end{cases} \quad (2.56)$$

with electric field amplitudes $\mathcal{E}_1, \mathcal{E}_2 > 0$, the laser frequency ω_L , the pulse duration of the first part of the laser pulse $t_p = \pi/\omega_L$ (in the following referred to as positive pulse duration), the switch-on and switch-off times τ_1, τ_2 . The ratio

$$\xi \equiv \mathcal{E}_2/\mathcal{E}_1 \quad (2.57)$$

determines the width of the first peak relatively to the negative tail. The pulse defined by Eq. (2.56) satisfies the condition (2.49) and is shown in Fig. 2.5 for various values of ξ (note the logarithmic time-axis). The condition that the electric field is smooth at $t = t_p$ further leads to $\tau_1 = \frac{\mathcal{E}_2}{\omega_L \mathcal{E}_1} = \xi/\omega_L$ and Eq. (2.49) leads to

$$\begin{aligned} \tau_2 &= (2\omega_L^2 \tau_1)^{-1} + \sqrt{(2\omega_L \tau_1)^{-2} + (\omega_L)^{-2}} \\ &= (2\omega_L \xi)^{-1} + \sqrt{(2\xi)^{-2} + (\omega_L)^{-2}}, \end{aligned} \quad (2.58)$$

2. ROTATING MOLECULES WITH ULTRASHORT PULSES

see Ref. [154]. The decay time is determined by τ_2 . The sudden limit for this potential follows as

$$\hat{U}_{\text{sudd,half-cycle}} = e^{-i\hat{H}_0(t-t_0)/\hbar} e^{+iP_1 \cos(\hat{\theta})} e^{-i\hat{H}_0 t_0/\hbar} \quad (2.59)$$

with estimated peak position t_0 and kick strength P_1 . Observe that t_0 does not have to match with t_p , as the pulse's peak (i. e. the pulse position) occurs for $t_0 < t_p$. Furthermore, the duration t_p might not align with the laser duration τ_L based on the value of ξ , since it would disregard the negative tail of the pulse. Still P_1 is frequently approximated in the literature as [134]

$$P_1 \approx \frac{\mu_0}{\hbar} \int_{-\infty}^{t_p} \mathcal{E}(t) dt, \quad (2.60)$$

i. e. by the integral over the positive part of the field amplitude. This is a good approximation when the half-cycle pulse looks similar to a Gaussian pulse, which we demonstrate below. Approximately, the integral over the positive peak scales as $P_1 \propto \mathcal{E}_1 \cdot t_p$ (the negative tail compensates for exactly this value). For half-cycle pulses a simple expression for the rescaling function as for Gaussian pulses

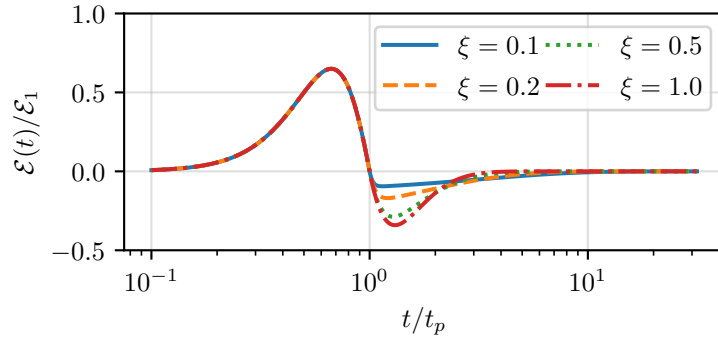


Figure 2.5: Parametrization of a half-cycle pulse. Following (2.56) in units of the pulse position t_p . \mathcal{E}_1 determines the pulse maximum, \mathcal{E}_2 the minimum and the ratio $\xi = \mathcal{E}_2/\mathcal{E}_1$ the decay time (see the text). The laser pulse duration τ_L includes the negative tail up to some degree depending on the field strength. In the Gaussian approximation, the pulse width is approximately given by $\tau_L \approx t_p$.

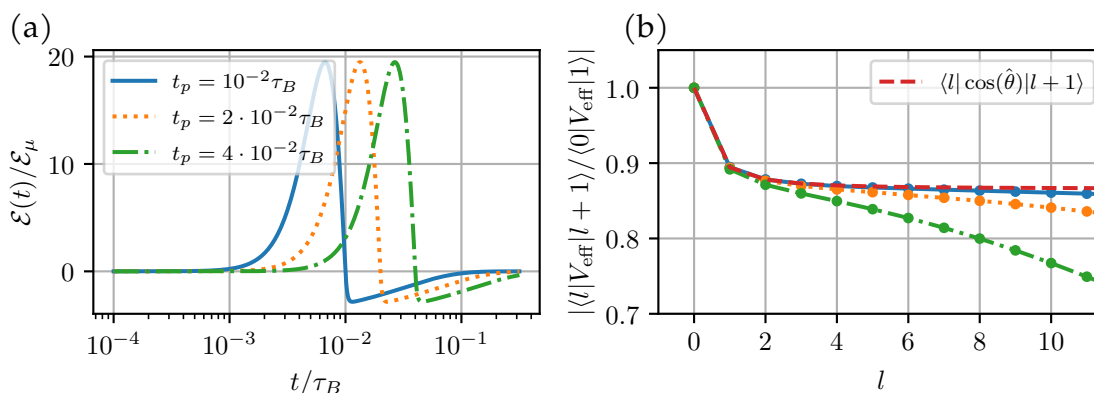
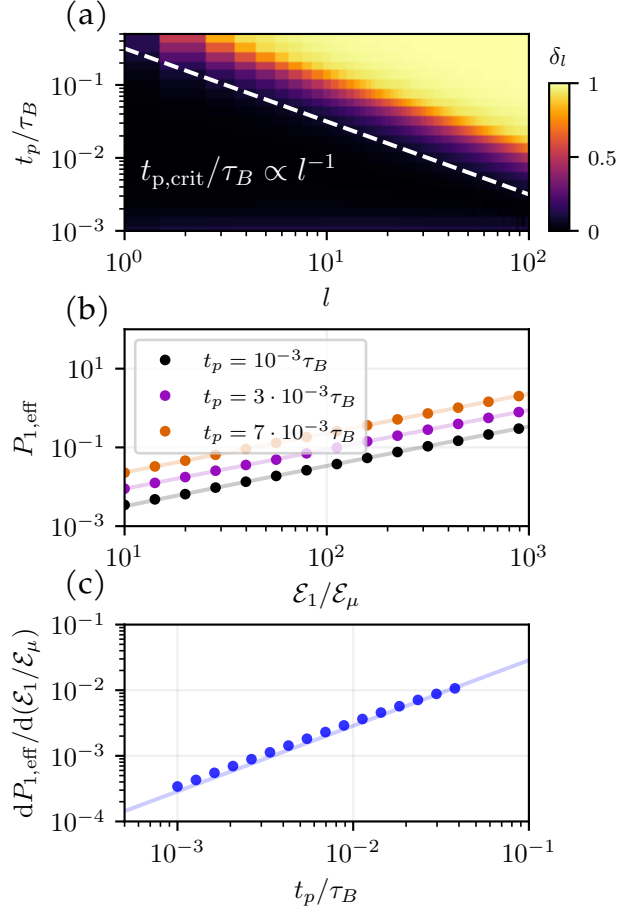


Figure 2.6: Behavior of a finite-width half-cycle pulse. Following (2.56), for different positive pulse durations $t_p = \pi/\omega_L$, where t_p also controls the peak width and hence also the strength P_1 . (a) The field strength $\mathcal{E}(t)/\mathcal{E}_\mu$ for $\mathcal{E}_1/\mathcal{E}_\mu = 30$ and $\mathcal{E}_2/\mathcal{E}_\mu = 0.03$. (b) The first off-diagonal matrix element of the effective potential defined in Eq. (2.41). Note that we divide by $\langle 0|V_{\text{eff}}|1\rangle$ to bring the potentials on top of each other since each potential corresponds to a different P_1 . Similar to the multicycle pulses of Fig. 2.2 we observe that for small t_p the matrix elements coincide perfectly with the sudden limit (red dashed line).

as in (2.52) is not possible, since one has to infer additionally the effective strength P_1 . In this section, we shift our focus to half-cycle pulses. For simplicity we focus only on the dominant term, the permanent dipole term with finite $\mu_0 > 0$. For many linear molecules this is a good approximation since the specific constants (2.35) satisfy $\mathcal{E}_\mu \ll \mathcal{E}_{\Delta\alpha}$. As previously mentioned, in the case of half-cycle pulses, there is a positive peak followed by a potentially long negative tail. While it is possible to fine-tune the sudden pulse position t_0 , we choose for simplicity $t_0 \equiv t_p$ from now on and note that fine-tuning this parameter only leads to minor improvements (which could be important in specific situations which are not considering here). The $\langle l|\cos(\hat{\theta})|l'\rangle$ matrix element is only non-zero for $l = l' \pm 1$. In many cases, this is also true for \hat{V}_{eff} . Specifically, in the limit where the ratio $\xi \rightarrow 0$ from (2.57), which we will refer to as the *Gaussian limit*, the behavior converges to the Gaussian pulse discussed earlier, since the depth of the negative tail is minimal and

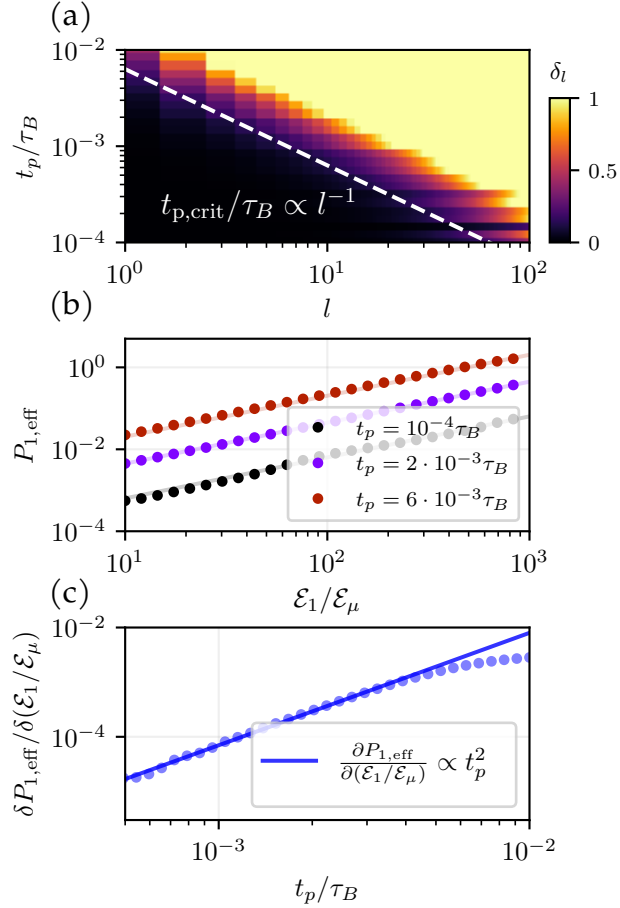
2. ROTATING MOLECULES WITH ULTRASHORT PULSES

Figure 2.7: Outcomes for half-cycle pulses in the Gaussian limit. (a) The deviation error, denoted as $\delta_l = |1 - p_l^{(2)}/p_{l=0}^{(2)}|$, for a half-cycle pulse where $\xi = 10^{-3}$ (corresponding to the Gaussian limit) and $l_{\max} = 250$. Similar to the Gaussian pulse (refer to Fig. 2.3), a power-law dependence on the critical pulse width is observed (indicated by the dashed white line, estimated visually). (b) The effective kick strength, $P_{1,\text{eff}}$ evaluated up to $l_{\text{av}} = 50$, as a function of field strength $\mathcal{E}_1/\mathcal{E}_\mu$ for three distinct t_p . (c) Confirms the anticipated linear relationship, $P_{1,\text{eff}} \propto t_p \cdot \mathcal{E}_1$, with $\frac{d^2 P_{1,\text{eff}}}{d\mathcal{E}_1 dt_p} \approx 0.287$.



it requires an infinite amount of time to satisfy Equation (2.49). In Fig. 2.6, we illustrate the shape of the potential for very small values of ξ . As expected, the effective potential matrix elements diverge from the $\cos(\theta)$ potential for increasing t_p , exhibiting similar behavior to that of Gaussian pulses (cf. Fig. 2.3). For half-cycle pulses, the positive pulse duration t_p plays a role analogous to the width σ_t for Gaussian pulses. In Fig. 2.7 we find that the critical positive pulse width scales as $t_{p,\text{crit}}/\tau_B \propto l^{-1}$, which is similar to the critical pulse width for Gaussian pulses in Fig. 2.3. The primary difference arises from the fact that $t_p = \pi/\omega_L$ (only for half-cycle pulses) with the laser frequency ω_L , corresponding to exactly half a cycle, while the variable σ_t of the Gaussian pulses corresponds to the width of one

Figure 2.8: Results for half-cycle pulses for the oscillating limit. With $\xi = \mathcal{E}_2/\mathcal{E}_1 = 1$ with the same parameters as in Fig. 2.7, i. e. $\delta_l = |1 - p_l^{(2)}/p_{l=0}^{(2)}|$ with $l_{\max} = 500$. Again, a power-law dependence on the critical pulse width is observed (indicated by the dashed white line, estimated visually). However, unlike for Gaussian pulses the break-down of the sudden limit occurs for smaller l_{crit} . In (b) the effective kick strength, $P_{1,\text{eff}}$ evaluated up to $l_{\text{av}} = 50$, as a function of field strength $\mathcal{E}_1/\mathcal{E}_\mu$ for three distinct t_p . In (c) we demonstrate that the slopes of (b) are related to t_p by $\partial P_{1,\text{eff}}/\partial(\mathcal{E}_1/\mathcal{E}_\mu) \propto t_p^2$ as long as t_p is not large enough (note that deviations for $t_p \sim 10^{-2}\tau_B$). This is a new result and originates from the non-Gaussian pulse shape, which does not allow for the simple estimation of P_1 , Eq. (2.60).

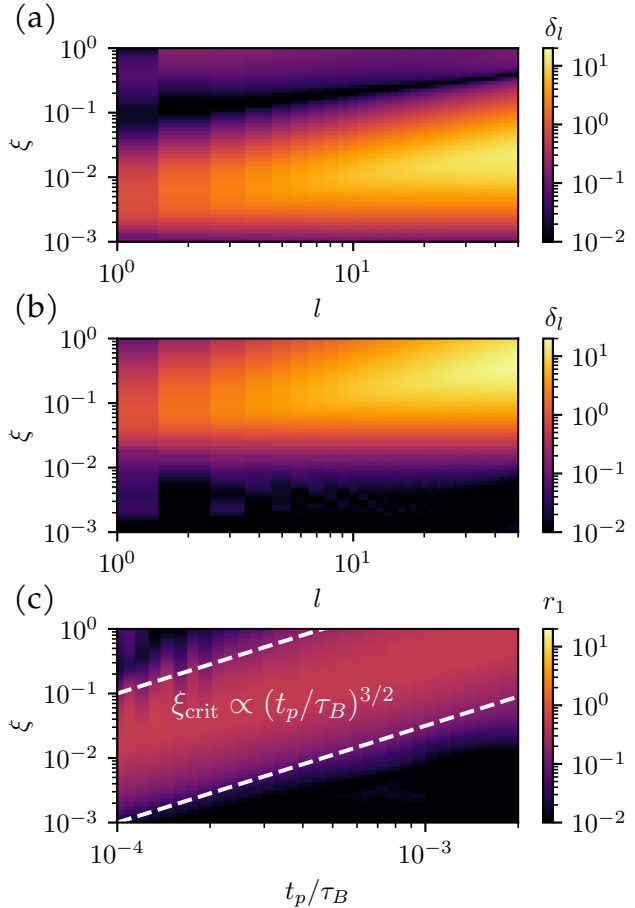


standard deviation, or approximately 68% of the nominal pulse area. We note that in the *Gaussian limit*, we do not observe a dependency of the relative error on the kick strength $P_{1,\text{eff}}$. However, when leaving the Gaussian limit, i. e. when ξ is not small, it plays an important role how the potential deviates from the impulsive limit. Now we look at the opposite limit $\xi = 1$, which we denote the *oscillating limit*, since the negative tail can not be integrated out, like we did effectively for the Gaussian limit. Also in that limit we find that it is

2. ROTATING MOLECULES WITH ULTRASHORT PULSES

possible to approximate the full time-evolution with the impulsive limit, see Fig. 2.8. The main difference is that for a given t_p , the sudden approximation breaks down for smaller l , which implies that one has to choose smaller widths t_p/τ_B than in the Gaussian limit to achieve the same accuracy. Further, it is important to note that unlike the Gaussian case the diagonal elements are not vanishing completely. While we confirm the relationship $P_{1,\text{eff}} \propto \mathcal{E}_1/\mathcal{E}_\mu$, the dependency on t_p is more complicated than in the $\xi \rightarrow 0$ case and we find $\partial P_{1,\text{eff}}/\partial(\mathcal{E}_1/\mathcal{E}_\mu) \propto t_p^2$, displaying a strong deviation from the generally accepted result (2.60). Finally, we turn our focus to the

Figure 2.9: Behavior for an arbitrary value of ξ . With $\mathcal{E}_1/\mathcal{E}_\mu = 10^3$. In (a) and (b) the relationship between angular momentum l and ξ for two positive pulse widths t_p that incorporate a large cutoff at $l_{\text{max}} = 500$. In (c) the dependency of the relative error r_1 , as defined in equation (2.45), on both t_p and ξ (where we averaged up to an value of $l_{\text{av}} = 20$). As ξ approaches either extreme of 1 or 0 for small t_p , we recover the behavior $\delta_l \rightarrow 0$ from previous figures. However, within these extremes, the error scaling is heavily influenced by the positive pulse width t_p . This makes sense as the specific timescale exerts a significant impact on how the rotational modes interact with the field.



case involving arbitrary ξ . Our compiled results are presented in Fig. 2.9. This consolidates our previous analyses for the two limiting

scenarios: $\xi \rightarrow 0$ and $\xi = 1$. Additionally, it provides an understanding of how the Gaussian and oscillating limits respectively cease to hold for mid-range values of ξ , where the error δ_l grows large already for small l . Evidently, in the scenario of $\xi \rightarrow 1$, a small t_p/τ_B ratio is necessary to maintain the sudden approximation, as has been demonstrated in Fig. 2.8. Contrarily, we discover that in the opposing extreme where $\xi \approx 0$, a larger t_p proves beneficial, at least for the relative error. We observe that when ξ approaches 1, the condition of $t_p \rightarrow 0$ becomes critical. Interestingly, an increase in t_p values not only allows, but also appears to encourage, higher ξ values when transitioning from the $\xi \approx 0$ limit. We have visually approximated this relationship as $\xi_{\text{crit}} \propto (t_p/\tau_B)^{3/2}$, although the actual dependence can be more complex. Nevertheless, it's noteworthy that increasing the ratio t_p/τ_B permits the use of a greater ξ value for fixed \mathcal{E}_1 .

2.4 Exact time-evolution of rotational wavepackets

We executed a series of numerical simulations, aiming to examine the dynamics of an OCS molecule's wave-packet under illumination of different half-cycle pulses. In Figs. 2.10, 2.11, 2.12, and 2.13, we present the results using $\tau_B \approx 80$ ps, $\Delta\alpha \approx 4.67 \text{ \AA}^3$, and $\mu \approx 0.66$ Debye [155]. By using rescaled units (2.34), we obtain the specific field constants $\mathcal{E}_\mu \approx 6$ kV/cm and $\mathcal{E}_{\Delta\alpha} \approx 1$ MV/cm. Since $\mathcal{E}_\mu \ll \mathcal{E}_{\Delta\alpha}$, we neglect the influence of the $\Delta\alpha$ term in what follows. In a study by Fleischer et al. [156], they reported the use of half-cycle pulses with an average field strength of approximately 22 kV/cm up to 1 MV/cm when applied to OCS molecules, which is the regime we are examining here. Note that as can be inferred from Fig. 2.7, the relative field strength $\mathcal{E}/\mathcal{E}_{\Delta\alpha}$ should be on the order of 100 – 1000 in order to see a visible effect on the molecule. The time-dependent

2. ROTATING MOLECULES WITH ULTRASHORT PULSES

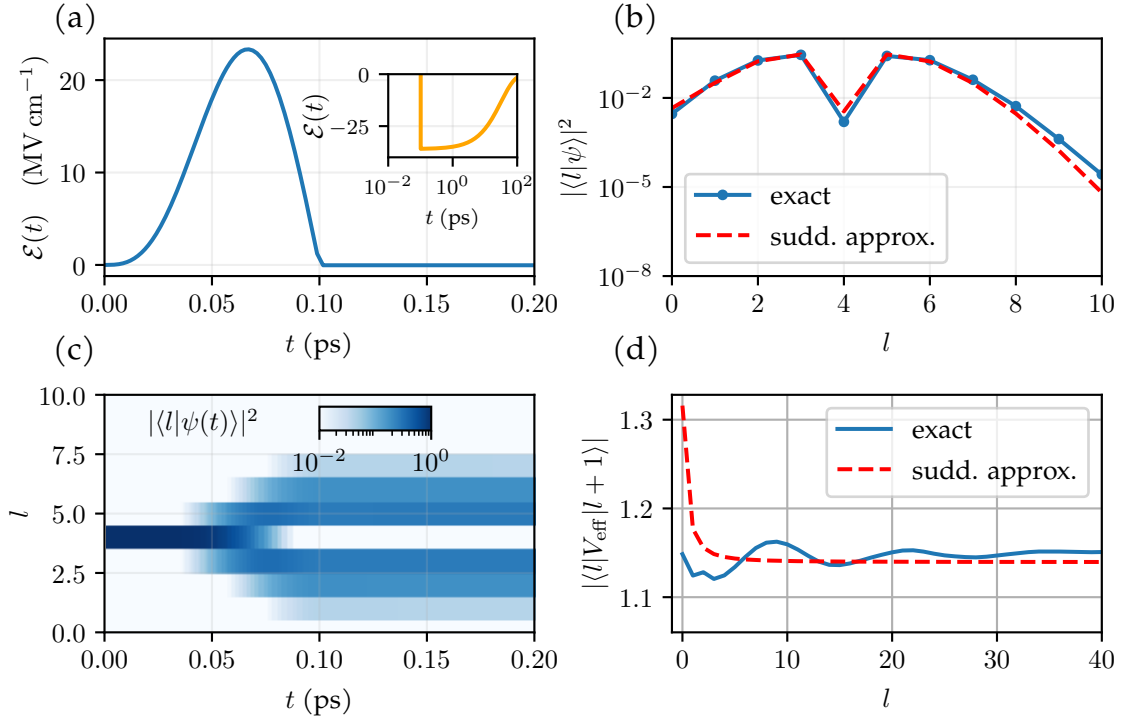


Figure 2.10: Numerical simulation of wave-packet time-evolution for an OCS molecule. The parameters characterizing the molecule [155] are $\tau_B \approx 80$ ps, $\Delta\alpha \approx 4.67 \text{ \AA}^3$, and $\mu \approx 0.66$ Debye. Field constants specific to OCS, Eq. (2.35), are used. (a) The field profile of the half-cycle laser pulse in the Gaussian regime, $\mathcal{E}_1 = 6000$, $\xi = 10^{-3}$, resulting in a peak intensity $\mathcal{E}_{\max} \approx 23$ MV/cm. The inset show the long-time behavior of the pulse. (b) The absolute value of the wavepacket components for a wavepacket initialized with $l = 4$. (c) The converged wavepacket long after the pulse. (d) The effective matrix elements from the full time-evolution and the sudden approximation for $P_{1,\text{eff}} \approx 2.28$, as determined by Eq. (2.44). The relative error for this potential, calculated using Eq. (2.45), is a modest $r_1 \approx 2\%$, indicating that the sudden approximation is effective in this context.

wave-packet evolution of a molecule (with $m = 0$) is controlled by

$$\partial_t C_l(t) = -i \sum_{l'=0} \langle l' | \hat{V}_I(t) | l \rangle C_{l'}(t), \quad (2.61)$$

2.4. Exact time-evolution of rotational wavepackets

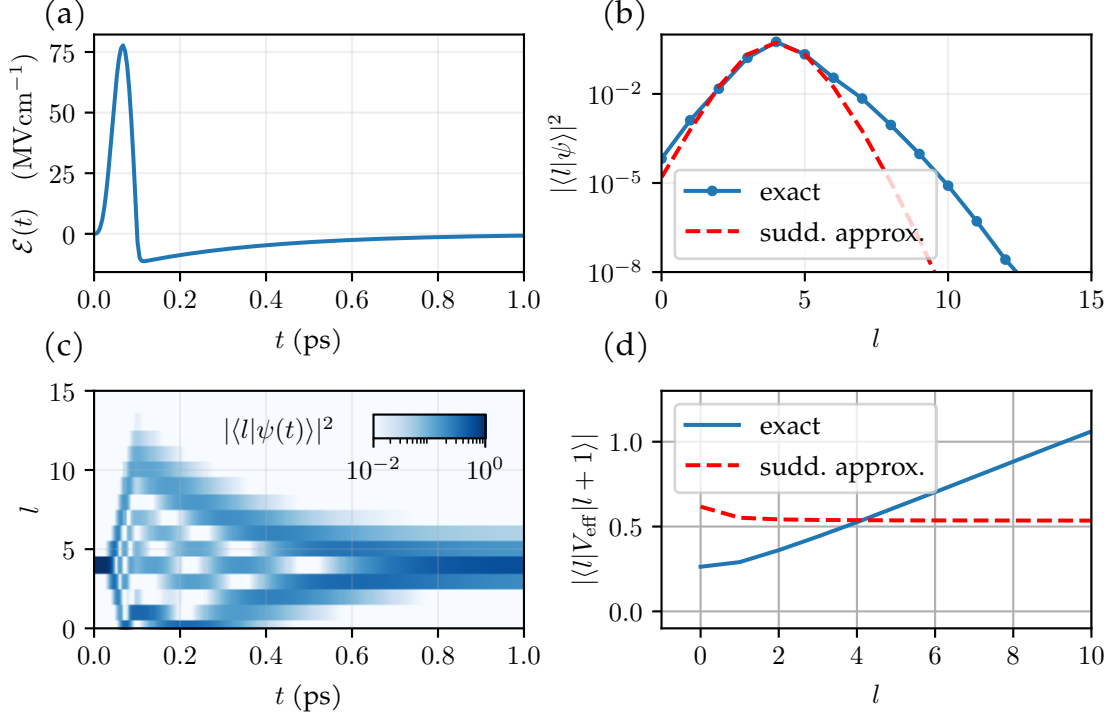


Figure 2.11: Similar parameters as in Fig. 2.10. (b) Shows that the negative tail now lowers the occupations at high l values and (c) demonstrates the deviation from the sudden approximation. (d) The effective matrix elements for $P_{1,\text{eff}} \approx 1.07$, calculated by Eq. (2.44) for matrix elements up to $l_{\text{av}} = 10$. The substantial relative error of $r_1 \approx 43\%$ indicates the inadequacy of the sudden approximation in this case.

with the potential in the interaction picture defined in (2.47), and the solution for the wavefunction

$$\langle l|\psi(t)\rangle = C_l(t)e^{-i\pi l(l+1)t} \quad (2.62)$$

in units of rotational time τ_B . In Fig. 2.10, the molecule is exposed to a half-cycle pulse in the Gaussian regime, with $\xi = 10^{-3}$, whose profile is shown in Fig. 2.10(a). The pulse has a width t_p , significantly shorter than the molecule's rotational period. The wavepacket in the initial condition is in a pure $l = 4$ angular momentum state¹⁵, i. e.

¹⁵We did not choose $l = 0$ as not to be influenced by the open boundary, which could lead to other effects not mentioned here.

2. ROTATING MOLECULES WITH ULTRASHORT PULSES

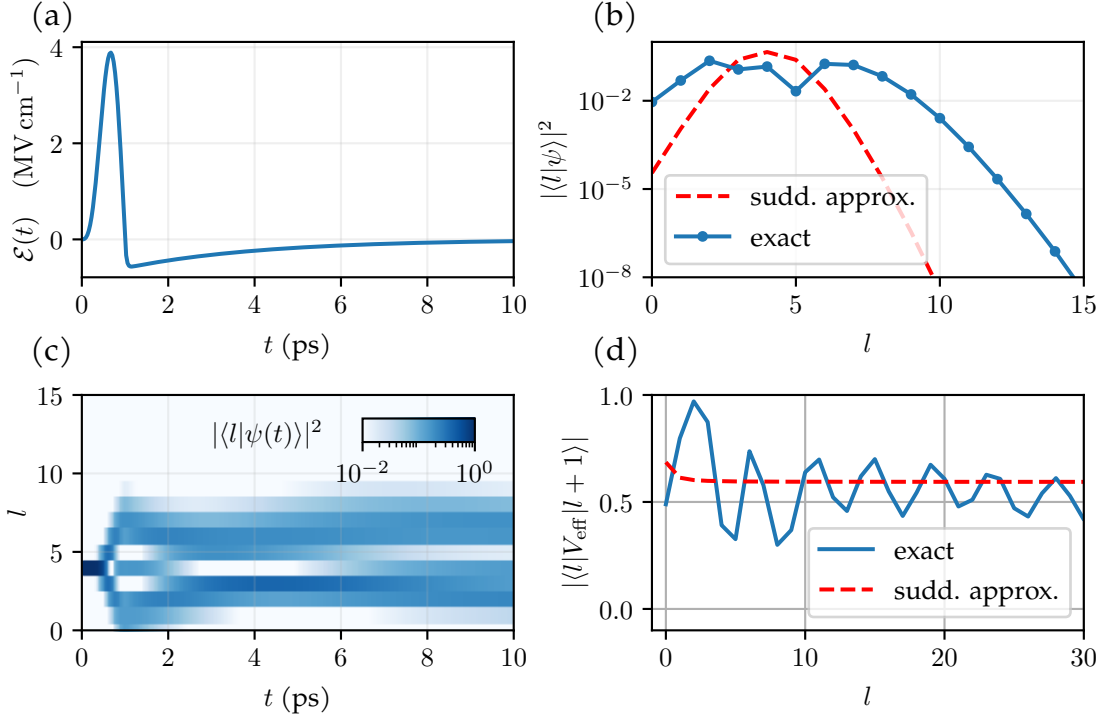


Figure 2.12: Same as in Fig. 2.10, but with a significantly extended pulse duration of $t_p = 1$ ps. (d) The effective matrix elements for $P_{1,\text{eff}} \approx 1.2$ as calculated by Eq. (2.44) for matrix elements up to $l_{\text{av}} = 10$. High relative error of 41% underscores the poor agreement with the sudden approximation. This discrepancy is attributed to oscillations in the effective potential induced by the pulse width, which is comparable to the rotational periods $\tau_{\text{rot}}(l)$ of some non-zero angular momentum states.

$\langle l|\psi\rangle = \delta_{l,4}$. During the pulse illumination, the pulse performs akin to a Gaussian pulse, with both lower and higher angular momentum states being occupied. Notably, the angular momentum states stay well below the critical value, which can be read off from Fig 2.7 (a) with $t_p/\tau_B \approx 1.25 \cdot 10^{-3}$. Post-illumination, a decrease in the occupation probability for state $l = 4$ is evident, possibly due to destructive interference. We use the sudden approximation, defined by (2.44), to estimate the effective kick strength of an instantaneous delta pulse. This approximation mirrors the final state of the wavepacket with high precision, demonstrating a fidelity of 97%, and it accurately

2.4. Exact time-evolution of rotational wavepackets

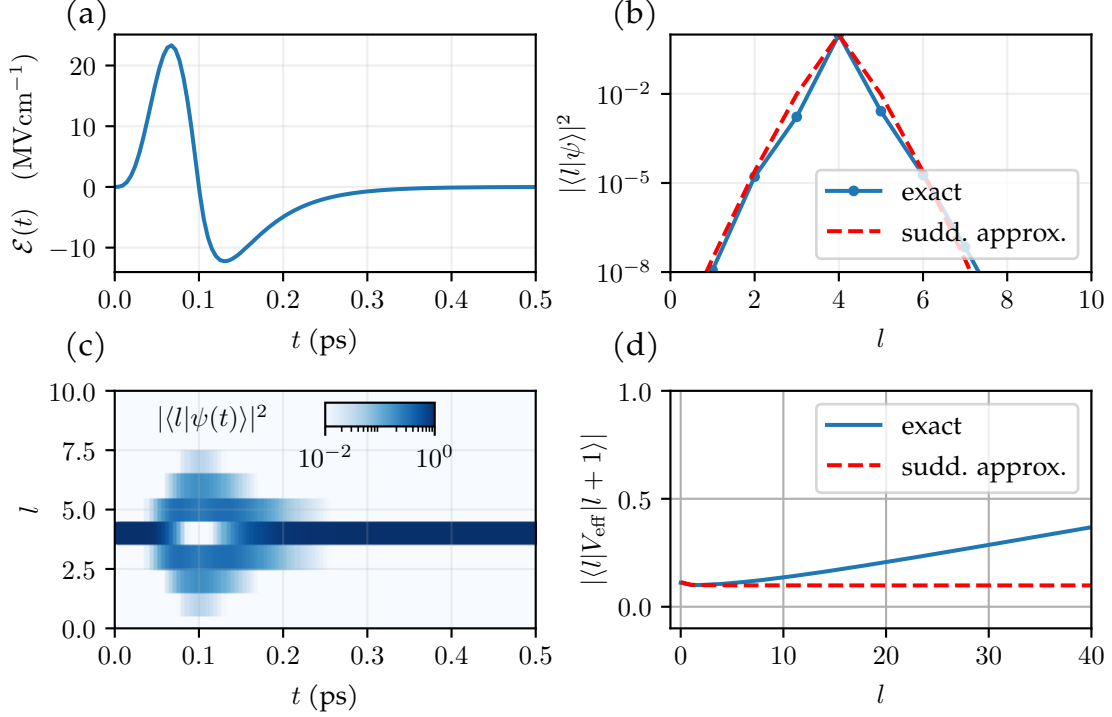


Figure 2.13: Same as in Fig. 2.10, but under oscillating conditions, $\xi = 1$. (b) highlights how the sharp the negative slope of the pulse counteracts the positive peak, leading to an almost complete negation of previously occupied angular momentum states. Despite this behavior, the agreement with the sudden approximation is very high, as seen in (c) with the long-time result of the wavepacket. (d) The effective matrix elements for $P_{1,\text{eff}} \approx 0.2$, as calculated by Eq. (2.44) for matrix elements up to $l = 5$ with a relative error of 3%.

predicts the dip in the $l = 4$ state. The sudden approximation's agreement with the full time-evolution is further confirmed by the effective matrix elements (2.41), see Fig. 2.10(d). The small relative error (2.45) of $r_1 \approx 2\%$ underscores the appropriateness of the sudden approximation in this context. Figures 2.11, 2.12, and 2.13 were created similarly to Fig. 2.10, albeit with varied pulse parameters and widths. In Fig. 2.11, the pulse is set in the intermediate regime $\xi = 0.1$. The sudden approximation proves challenging to apply in this scenario, as evident in the evolution of the representative wavepacket. The matrix elements of the effective potential begin to

diverge for large l , failing to plateau like in the case of the sudden approximation. Consequently, finding the correct kick strength that could reproduce the full time-evolution results is problematic. Therefore, we advise against using the sudden approximation in such a scenario due to the significant deviations. In Fig. 2.12, we adjust the pulse width to a longer duration ($t_p = 1$ ps), while staying within the same intermediate regime ($\xi = 0.1$). This modification leads to noticeable oscillations (see Fig. 2.12(d)) in the matrix elements of the effective potential, resulting from the compatibility of the pulse width with the rotational periods of certain angular momentum states. Evidently, in this regime, the laser's timescale overlaps with the molecule's rotational oscillations, causing interference. This interference hinders the application of the sudden approximation, corroborated by a poor agreement between the wavefunctions of the sudden approximation and the full time evolution (as low as 20%). An intriguing observation is the absence of a depopulation in high angular momentum states, likely attributable to the longer duration of the negative peak. In the final scenario, as illustrated in Fig. 2.13, we look into the oscillating limit by setting $\xi = 1$. We observe that the pulse's negative slope almost negates the positive peak, leading to a markedly reduced effective kick strength. Nevertheless, the agreement with the sudden approximation in this regime is remarkably high, presenting a fidelity of 98%, reinforcing our previous analysis of Fig. 2.8.

2.4.1 Validity of the sudden approximation

In summary, our analysis of the full time-evolution operator, solved at the operator level, establishes clear criteria for the validity of the impulsive limit. Both Gaussian and half-cycle pulses can be accurately approximated by delta kicks when three conditions are met: the angular momentum remains below l_{crit} , the pulse width (σ_t or t_p) is much shorter than the rotational period τ_B , and for half-cycle pulses, the shape parameter ξ approaches either the Gaussian

($\xi \rightarrow 0$) or oscillating ($\xi = 1$) limit.

These findings provide practical guidelines for experimental implementations, defining parameter regimes where delta kicks can be reliably realized. Within these constraints, the matrix elements of finite-width pulses become indistinguishable from those of delta pulses in the long-time limit. Outside this regime, however, significant deviations emerge due to non-negligible evolution during the pulse width.

Our approach, based on the effective potential (2.41), complements existing methods such as the Magnus expansion [157] and the techniques developed in Ref. [145]. While these earlier works focus on expanding the time-evolution operator in terms of τ_L , our method provides novel insights into rotational states and off-diagonal matrix elements specific to molecule-laser interactions. By quantifying deviations from the sudden approximation, we explicitly demonstrate how increasing pulse widths and laser strengths lead to behavior beyond the first-order Magnus expansion. This analysis not only defines the boundaries of the impulsive limit but also characterizes the nature of deviations beyond these boundaries. Future work could extend these investigations to more complex pulse shapes, including few-cycle pulses, and explore quantum numbers beyond angular momentum l .

2.5 Outlook

This concludes our analysis of single-pulse interactions. The following chapter extends our discussion to pulse trains, where the sudden approximation developed and justified here will significantly simplify the time-translation operator, enabling the study of more sophisticated driving protocols.

Lattices of angular momentum

Attention is the rarest and purest form of generosity.

– Simone Weil

3.1 Overview

In their seminal 1979 paper, Casati et al. [46] discovered an extraordinary manifestation of quantum interference: the localization of angular momentum distributions in driven quantum rotors. This phenomenon, while mathematically analogous to Anderson’s theory of electron localization in disordered solids, occurs in the space of angular momentum rather than physical position space. Although the theory in its pure form is simple, it has sparked extensive research in Quantum chaos, from quantum billiards and kicked tops to quantum graphs [115]. The universality of this effect has since been demonstrated across an impressive range of quantum systems—from atoms in microwave fields [158, 159] to highly excited Rydberg states [160]. Perhaps most intriguingly, when rigid linear molecules are subjected to linearly polarized electromagnetic radiation [66], they exhibit similar localization behavior [63, 65], despite their inherently three-dimensional nature. As we established in Section 2.2.1,

the cylindrical symmetry of this interaction preserves the magnetic quantum numbers (m, K) , effectively projecting the dynamics onto a planar rotor in the polar angle θ .

The hallmark of localization is the exponential decay of wavefunctions [48]:

$$\psi(r) \propto \exp(-|l - l_0|/\xi) \quad (3.1)$$

where ξ is the localization length. The dynamical localization phenomenon represents a striking breakdown of quantum-classical correspondence: while the classical kicked rotor exhibits chaotic behavior with unbounded energy growth, its quantum counterpart remains confined in angular momentum space. While dynamical localization occurs for a wide range of parameters, at so-called *quantum resonances* a different phenomenon emerges that depends intimately on the ratio between the driving period and the rotational revival time [161–163]. These resonances, far from being mere curiosities, reveal deep connections between the fractional revivals of the rotor and quantum transport.

Our theoretical framework begins with an introduction to the Floquet theory of the kicked rotor in Section 3.2, yielding an effective stroboscopic Hamiltonian whose structure we examine in Section 3.2.1. The rich interplay between fractional revivals and quantum resonances, detailed in Section 3.3, illuminates how the underlying time-lattice geometry gives rise to fundamental quasi-momentum symmetries, explored in Section 3.3.3. At perfect quantum resonance, addressed in Section 3.3.4, the system shows the exactly solvable case of unbounded growth—in stark contrast to the anti-resonant case examined in Section 3.3.5, where the dynamics freeze entirely. The exploration of higher resonances in Section 3.3.6 reveals a hierarchy of increasingly complex dynamical behaviors.

The extension to the 3D rotor, presented in Section 3.5, introduces remarkable new physics while preserving essential insights from the planar case. The convergence of matrix elements involving Clebsch-

Gordon coefficients, proven in Section 3.5.1, allows us to bridge the apparent complexity gap between 2D and 3D rotors. The emergence of the Anderson wall—a critical angular momentum beyond which quantum resonances dissolve—is analyzed in Section 3.5.2, while Section 3.5.4 reveals how the characteristic $l(l + 1)$ spectrum of 3D rotors gives rise unique revival patterns absent in planar systems.

Through careful examination of the interplay between dynamical localization and quantum resonances, we uncover how the delicate balance between strong pulses and quantum interference produces a rich phase space of dynamical behavior. This foundation proves essential for our subsequent exploration of topological phenomena in quantum rotors in the next Chapter. Let us now begin with the fundamental framework of Floquet theory.

3.2 Floquet theory

Finding solutions to the Schrödinger equation with a time-dependent potential often presents greater challenges than those encountered with static potentials. When energy is not conserved, energy eigenstates do not exist either. In this work, we focus on a special case where the potential is Hermitian¹ at any given moment—ensuring real energies—but varies over time. Furthermore, we consider potentials that are periodic in time, such as a train of laser pulses. This periodicity allows us to employ methods from condensed matter physics, including the Bloch theorem and related concepts.

In the time domain, this framework is encompassed by the Floquet theorem, or more broadly, Floquet theory. We can express such a Hamiltonian as $\hat{H}(t) = \hat{H}_0 + \hat{V}(t)$, where $\hat{V}(t + T) = \hat{V}(t)$. Consequently, the Hamiltonian commutes with the one-period time translation operator, $[\hat{H}(t), \hat{U}(t + T, t)] = 0$, allowing for simultane-

¹This implies that we neglect couplings to a bath or other dissipative processes.

3. LATTICES OF ANGULAR MOMENTUM

ous diagonalization² with $\hat{U}_T(t) \equiv \hat{U}(t + T, t)$. The periodicity in T also guarantees that the time-translation operator is periodic in both arguments $\hat{U}(t' + T, t) = \hat{U}(t', t)$ for $t' \geq t$ and $\hat{U}(t', t + T) = \hat{U}(t', t)$ for $t' \geq t + T$. Given that \hat{U} is unitary, its eigenvalues lie on the unit circle

$$\hat{U}(t + T, t) |\psi_j(t)\rangle = e^{-i\epsilon_j T} |\psi_j(t)\rangle = |\psi_j(t + T)\rangle \quad (3.2)$$

with $j \in \{1, \dots, N\}$ and the dimension³ of the Hilbert space $\dim[\mathcal{H}] = N$. The eigenstates $|\psi_j(t)\rangle$ are also known as *Floquet states*. These states form a complete basis for the Hilbert space and are periodic in time with period T . The corresponding eigenvalues $e^{-i\epsilon_j T}$ define the *quasienergies* ϵ_j , which play a role analogous to energy in time-independent systems. It is important to note that the quasienergies are only defined modulo $\Omega = 2\pi/T$, reflecting the discrete time translation symmetry of the system. Importantly, this introduces the possibility of having the so-called π -gap, an energy gap that arises due to the periodic nature of quasienergies. Hence, in Floquet systems, states that differ by $\epsilon_j \mapsto \epsilon_j + \pi/T$ become equivalent in the *folded* spectrum, so that an avoided crossing or band splitting about π/T can form a gap. This phenomenon is unique to periodically driven systems, since it relies exactly on this periodicity [164].

Let us define the 2π -remainder norm for two numbers $x, y \in \mathbb{R}$ with

$$|x - y|_{2\pi} = \min_{n \in \mathbb{Z}} |x - y + 2\pi n| \quad (3.3)$$

²Let us recall briefly the argument behind simultaneous diagonalization. Let us assume H is invariant with respect to a symmetry operator A (which according to Wigner's theorem [19], has to be either unitary or anti unitary), then

$$AHA^\dagger = H \Leftrightarrow [H, A] = 0, \quad H|\psi\rangle = E|\psi\rangle \Rightarrow AH|\psi\rangle = EA|\psi\rangle \Leftrightarrow HA|\psi\rangle = EA|\psi\rangle.$$

The last argument shows that $A|\psi\rangle$ is also an eigenfunction of the hamiltonian with the same eigenvalue. More important: We can *always* find simultaneous eigenfunctions if $[H, A] = 0$, but they do not necessarily have the same eigenvalues.

³Let us assume for now a finite Hilbert space. However, the discussion carries over to the infinite case with minor subtleties.

which gives the minimal distance on the circle between radiants x, y . Hence, we can define the gap between two quasi-energies by the difference $\Delta\epsilon \cdot T = |\epsilon_i T - \epsilon_j T|_{2\pi}$.

This property leads to a quasienergy Brillouin zone (similar to the concept in solid-state physics). The Floquet states can be expressed in the form

$$|\psi_j(t)\rangle = e^{-i\epsilon_j t} |u_j(t)\rangle \quad (3.4)$$

where $|u_j(t)\rangle$ are time-periodic states satisfying

$$|u_j(t+T)\rangle = e^{-i\epsilon_j(t+T)} |\psi(t+T)\rangle = e^{-i\epsilon_j t} |\psi(t)\rangle = |u_j(t)\rangle. \quad (3.5)$$

These modes encapsulate the micromotion of the system within each driving period. In the context of our study on kicked rotors and molecular systems, Floquet theory provides a powerful framework for understanding how the periodic application of laser pulses can manipulate and control quantum states.

The Floquet states form an orthonormal basis, characterized by $\langle \psi_i(t) | \psi_j(t) \rangle = \delta_{ij}$. This property enables us to express the general solution of the Schrödinger equation as a linear combination of these special solutions

$$|\phi(t)\rangle = \sum_j c_j(t) |\psi_j(t)\rangle, \quad (3.6)$$

with coefficients c_j determined by initial conditions

$$c_j = \langle \psi_j(t_0) | \phi(t_0) \rangle. \quad (3.7)$$

Expressing time as $t = t_0 + nT$, where $n \in \mathbb{N}_0$, we can rewrite the solution

$$|\phi(t)\rangle = \sum_j c_j e^{-i\epsilon_j(t-t_0)} |\psi_j(t_0)\rangle. \quad (3.8)$$

Note that $|u_j(t)\rangle = |u_j(t_0)\rangle$, implying that the full dynamics is captured by the phase factors $e^{-i\epsilon_j(t-t_0)}$. This allows us to express the

3. LATTICES OF ANGULAR MOMENTUM

time evolution operator as

$$U(t, t_0) = \sum_j e^{-i\epsilon_j(t-t_0)} |\psi_j(t_0)\rangle \langle \psi_j(t_0)|. \quad (3.9)$$

To illustrate, consider a time-independent Hamiltonian with stationary solutions $\hat{H}|\psi_j\rangle = E_j|\psi_j\rangle$. In this case

$$\hat{U}(t+T, t)|\psi_j(t)\rangle = e^{-iE_j T} |\psi_j(t)\rangle. \quad (3.10)$$

Clearly, all $|\psi_j(t)\rangle$ are Floquet states with quasienergies $\epsilon_j = E_j$, for any $T \in \mathbb{R}$. The energies are proportional to quasienergies modulo 2π . Returning to the time-dependent scenario, we substitute the Floquet ansatz into the Schrödinger equation:

$$\left[i\partial_t - \hat{H}(t) \right] \sum_j c_j |\psi_j(t)\rangle = 0. \quad (3.11)$$

The linear independence of Floquet states allows us to separate this into N equations. For each j we find

$$\left[i\partial_t - \hat{H}(t) \right] e^{-i\epsilon_j t} |u_j(t)\rangle = 0 \quad (3.12)$$

$$\Leftrightarrow \left[\hat{H}(t) - i\partial_t \right] |u_j(t)\rangle = \epsilon_j |u_j(t)\rangle \quad (3.13)$$

Given the periodicity of $|u_j(t)\rangle$ and $H(t)$, we can expand them into Fourier series

$$|u_j(t)\rangle = \sum_k |u_j(k)\rangle e^{ik\Omega t}, \quad |u_j(k)\rangle = \frac{1}{T} \int_0^T e^{-i\Omega kt} |u_j(t)\rangle dt, \quad (3.14)$$

$$\hat{H}(t) = \sum_k \hat{H}(k) e^{ik\Omega t}, \quad \hat{H}(k) = \frac{1}{T} \int_0^T e^{-i\Omega kt} \hat{H}(t) dt, \quad (3.15)$$

where $\Omega = \frac{2\pi}{T}$. Substituting these expansions yields

$$\sum_{k,q} \left(\hat{H}(q) e^{iq\Omega t} - k\Omega \right) e^{ik\Omega t} |u_j(k)\rangle = \sum_k \epsilon_j e^{ik\Omega t} |u_j(k)\rangle. \quad (3.16)$$

the frequency expansion. Specifically, since we are dealing with extremely strong but ultrashort kicks, far exceeding the weakly-driven regime, a high-frequency expansion would be inadequate, as a Dirac delta-shaped pulse has spectral components across all frequencies. Therefore, we need to directly compute the time-translation operator in order to understand the behavior of the system completely.

3.2.1 Stroboscopic Hamiltonian

While a driven Hamiltonian is not time-independent, we can find an effective time-independent Hamiltonian, following the same idea as in (2.40) when evaluating the effective potential for a pulse with finite duration. The effective, i. e. stroboscopic Hamiltonian⁴ is defined by

$$\hat{U}_T \equiv \exp[-i\hat{H}_{\text{eff}}T] \quad (3.22)$$

in dimensionless units with an hermitian operator \hat{H}_{eff} , which is not necessarily unique, which we will demonstrate in the following. Starting from the one-period time-translation operator U_T at $t = t_0$ with eigenvalues $\lambda_j = e^{-\epsilon_j T}$, We can construct one solution straightforwardly from the Floquet states (with a matching $t = t_0$) in (3.2). The ambiguity of the effective Hamiltonian arises from the ordering of the eigenstates, since quasi-energies can be degenerate, and the periodicity of the quasi-energies. Let us denote the subspace of the j -quasi-energy by \mathcal{M}_j , then

$$\hat{H}_{\text{eff}} = \sum_j \epsilon_j \mathcal{P}_j \quad (3.23)$$

with the projector $\mathcal{P}_j = \sum_{n \in \mathcal{M}_j} |\psi_n\rangle\langle\psi_n|$. Clearly, the effective Hamiltonian shares the eigenstates with the one-period time-translation operator

$$\hat{H}_{\text{eff}}|\psi_n\rangle = \epsilon_j|\psi_n\rangle \quad \forall n \in \mathcal{M}_j \quad (3.24)$$

⁴Stroboscopic refers here to the analysis of the system only at integer multiples of the period T , as in a stroboscopic camera.

and the quasi-energies as the phases of the eigenvalues⁵. Formally, we can define the logarithm by (3.23) and write

$$\hat{H}_{\text{eff}} = i \log[\hat{U}_T]/T \quad (3.26)$$

while keeping in mind that this mapping is not unique.

3.2.2 Time-slide symmetry

Intuitively it is evident that the asymptotic behavior of a periodic system remains invariant under shifts in the initial time t_0 , a property reflected in the invariance of quasienergies for the one-period time-translation operator. Consider an arbitrary partition $\hat{U} = \hat{U}_1\hat{U}_2$. The time-slide symmetry implies that the shifted operator $\hat{W} = \hat{U}_2\hat{U}_1$ has identical eigenvalues. Expressing $\hat{U}_1 = e^{-i\hat{A}_1}$ and $\hat{U}_2 = e^{-i\hat{A}_2}$ in terms of Hermitian operators A_1 and A_2 , we can relate these operators through a similarity transform

$$\hat{U}_1 = e^{i\hat{A}_2}\hat{W}e^{-i\hat{A}_2} \Leftrightarrow \hat{W} = e^{-i\hat{A}_1}\hat{U}_1e^{i\hat{A}_1}. \quad (3.27)$$

This transformation demonstrates the spectral equivalence of \hat{U} and \hat{W} . While their eigenvalues coincide, the eigenstates differ by a rotation⁶.

⁵We can construct infinitely other other effective Hamiltonians that have the same time-translation operator. Let us look at the exponential map

$$\hat{U}_T = \sum_j e^{-i\tilde{\epsilon}_j T} \mathcal{P}_j, \quad (3.25)$$

then we realize that any choice of $\tilde{\epsilon}_j = \epsilon_j + 2\pi q/T$, $q \in \mathbb{Z}$ leads to the same \hat{U}_T . This can even lead to the curious case that a pair of non-degenerate eigenvalues of the effective Hamiltonian are effectively degenerate, because their distance is a multiple of $2\pi/T$. Typically, we are interested in effective Hamiltonians that are smooth with respect to some external parameter, which constraints the choice of Energies of the effective Hamiltonian.

⁶To prove this, let \hat{V}_U diagonalize \hat{U} such that $\hat{U}\hat{V}_U = \hat{V}_U\hat{\Lambda}$, where $\hat{\Lambda}$ is diagonal. Similarly, let \hat{V}_W diagonalize \hat{W} . Applying (3.27), we obtain

$$\hat{W}e^{-i\hat{A}_2}\hat{V}_U = e^{-i\hat{A}_2}\hat{V}_U\hat{\Lambda} \Leftrightarrow \hat{V}_U = e^{-i\hat{A}_1}\hat{V}_W\Gamma \quad (3.28)$$

3.3 Quantum resonance of rotors

Let us now apply this theory to quantum rotors. We will first examine 2D rotors and subsequently extend these results to 3D rotors in Section 3.5. The 2D rotors can be derived as a limit of a 3D rotor when $l \rightarrow \infty$. In this scenario, the z-directional angular momentum takes any value $m \in \mathbb{Z}$ and is quantized through the relation $\hat{L}_z|m\rangle = m|m\rangle$, where $\hat{L}_z = -i\frac{\partial}{\partial\phi}$, and the eigenfunctions are given by $\langle m|\phi\rangle = \frac{1}{\sqrt{2\pi}}e^{-im\phi}$ with $\phi \in [0, \pi)$ (note that this leads by definition to anti-periodic boundary conditions for any wavepacket). The kicked rotor, expressed in dimensionless units, is given by

$$H_{\text{KR}}(t) = \hat{L}_z^2 + P \cos(\hat{\phi}) \sum_{n=0}^{\infty} \delta(t - nT) \quad (3.29)$$

where P is the kicking strength and T is the duration between kicks. Following the discussion in Chapter 2, the one-period time-translation operator is simplified to

$$\hat{U}_T = \exp[-iT\hat{L}_z^2] \exp[-iP \cos(\hat{\phi})]. \quad (3.30)$$

Note that even though angle ϕ is continuous, its compactness (which is reflected in the quantized momenta) guarantees the discretization of the eigenstates of \hat{U} . The matrix element of the potential is⁷

$$\begin{aligned} \langle m|e^{-iP \cos(\hat{\phi})}|m'\rangle &= \frac{1}{2\pi} \int_0^{2\pi} e^{-i(P \cos(\phi) + \phi(m-m'))} d\phi \\ &= (-i)^{m'-m} J_{m'-m}(P) \end{aligned} \quad (3.31)$$

with the Bessel function $J_n(x)$. Since the matrix elements only depend on the difference $m - m'$, the one-period time-translation operator inherits the periodicity of the free rotation.

where $\Gamma = \text{diag}[e^{-i\Phi}]$ accounts for the $U(1)$ gauge freedom of each eigenstate, with Φ being a vector of freely chosen phases.

⁷Using the expression [165] $e^{iP \cos(\phi)} = \sum_{n=-\infty}^{\infty} (-i)^n J_n(P) e^{in\phi}$. Additionally, $e^{iP \sin(\phi)} = \sum_{n=-\infty}^{\infty} J_n(P) e^{in\phi}$ is also true, which we will use later.

3.3.1 Fractional revivals and quantum resonances

Before looking into a complete pulse train, it is worthwhile to examine the revival structure of a 2D rotor following a single kick. This approach can provide some insights into the nature of rotational quantum resonances which will become important later. The revival pattern of a freely evolving wavepacket, described by $|\psi(t)\rangle = \sum_n e^{-itm^2} \langle m|\psi(0)\rangle$, can be interpreted as an extended version of the Talbot effect⁸. In this context, the rotational time of the rotor ($\tau_{\text{rot}} = 2\pi$ in our units) assumes the role of the Talbot time, during which periodic wavefronts experience regular revivals.

Rotational revivals manifest as fractional revivals, characterized by periodic sharpening and spreading of the wave packet's angular distribution. These phenomena bear resemblance to optical focusing effects, particularly the so-called catastrophes such as *rainbows* and *glories*. The concepts underlying these revivals are fundamental to applications in molecular alignment. While the topics of rotational revivals and quantum carpets have been extensively explored in the literature [167–170], we present here a novel perspective on quantum resonances.

The complexity of rotational revivals extends beyond the standard Talbot effect, as the overlap with the initial state (i. e. , the autocorrelation function) depends crucially on the initial state occupations

$$\mathcal{A}(t) = |\langle \psi(t)|\psi(0)\rangle|^2 = \left| \sum_{m=-\infty}^{\infty} |\langle m|\psi(0)\rangle|^2 e^{-itm^2} \right|^2 \quad (3.32)$$

where $\psi(0)$ for a single kick is given by (3.31) and the autocorrelation

⁸The Talbot effect, first observed by Henry Fox Talbot in 1836, is a near-field diffraction phenomenon where a periodic structure (such as a diffraction grating) creates repeated self-images at regular distances. When monochromatic light passes through a periodic grating, the wave field replicates the original pattern at integer multiples of a characteristic distance called the Talbot length ($z_T = 2a^2/\lambda$, where a is the grating period and λ is the wavelength), see [166] for a review.

3. LATTICES OF ANGULAR MOMENTUM

function $\mathcal{A}(t)$. In Fig. 3.1 we show the results for a gaussian state

$$\langle m|\psi_0\rangle = \mathcal{N}^{-1}(\beta)e^{-\beta m^2} \quad (3.33)$$

with a normalization $\mathcal{N}(\beta)$ ⁹ such that $|\langle\psi|\psi\rangle|^2 = 1$ and a parameter $\beta > 0$ which controls the width of the distribution. For $\beta \rightarrow 0$, the gaussian state has a orientation signal $\langle\cos(\hat{\phi})\rangle$ of one¹⁰. We observe that at the revival times $t = 2\pi n, n \in \mathbb{N}$ the wavepacket is revived exactly; this phenomenon is commonly known as *grand revival* [171]. Further, we find that at half-revival times $t = 2\pi n - \pi$ the overlap with the initial wavepacket goes to zero. Strikingly, this is a state that has negative orientation, which allows for a semi-classical interpretation of the angular momentum wavefunction.

Fig. 3.2 illustrates the autocorrelation function $\mathcal{A}(t)$ as a function of time for various kicking strengths P for an initial state $\phi_0 = \delta_{m,0}$. As P increases, a larger number of m states become occupied, each oscillating with frequency $\omega_{\text{rot}}(m) = 2\pi m^2$, as in (2.37). Over time t , these different modes dephase, leading to a decrease in $\mathcal{A}(t)$ due to destructive interference. This explains the inverse relationship between P and overall overlap for a given t .

However, fractional revivals occur when these modes constructively interfere. For large P , this is most pronounced at $t = \pi/2$, where all even m modes interfere constructively. At $t = \pi$, a phase inversion occurs. This is because the even nodes are becoming orthogonal to the initial wave packet. Additional revivals are observed at multiples

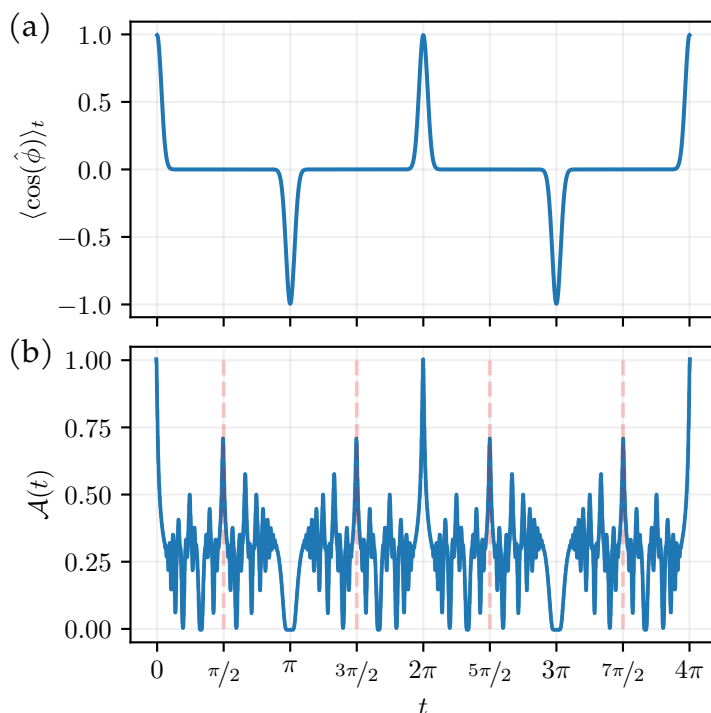
⁹ The normalization factor can be evaluated straight-forwardly by $\mathcal{N}^2(\beta) = \sum_m e^{-\beta m^2} = \Theta_3(0, e^{-\beta})$ with the Jacobi-Theta function $\Theta_3(z, q)$.

¹⁰We can evaluate the orientation signal at $t = 0$ exactly by

$$\begin{aligned} \langle\psi_0|\cos(\hat{\phi})|\psi_0\rangle &= \mathcal{N}^{-2}(\beta) \sum_{m=-\infty}^{\infty} \left(e^{-\beta(m+1)^2} + e^{-\beta(m-1)^2} \right) e^{-\beta m^2} = \mathcal{N}^{-2}(\beta) \sum_{m=-\infty}^{\infty} e^{-\beta(m+1)^2 - \beta m^2} \\ &= e^{\beta/2} \Theta_2(0, e^{-2\beta}) / \Theta_3(0, e^{-2\beta}) \end{aligned} \quad (3.34)$$

which for $\beta \rightarrow 0$ goes to 1 and for $\beta \rightarrow \infty$ goes to zero.

Figure 3.1: Revivals of the 2D rotor in a gaussian state. (a) Orientation signal for a gaussian state $\psi(t=0) \propto e^{-\beta m^2}$ with $\beta = 10^{-2}$. (b) Auto-correlation function $\mathcal{A}(t)$ of the same state. As expected, there is a *grand revival* at $t = 2\pi$ and minor revivals at fractions of the revival time (see main text). At $t = \pi$, we find the anti-revival, which can be interpreted when looking at the alignment, which flips to ≈ -1 .



of $\pi/3, \pi/4$, and consequently $\pi/12$, related to the commensurability of individual mode frequencies. The complexity of the revivals becomes clear in Fig. 3.2(b), which shows a non-linear pattern of minima and maxima in the autocorrelation function, interconnected by branches of a fractal revival tree. As P increases, leading to the occupation of more modes, we observe an increasing number of autocorrelation minima branchings. Remarkably, even at strong kicking strengths ($P \approx 10$), significant revivals persist, such as resonances that appear to be $t = \frac{15\pi}{16}$ and $t = \frac{23\pi}{24}$, but this is difficult to examine. Quantitative analysis of these revivals would make it necessary to consider all kinds of fractal interference effects and the analysis of the full non-linear revival manifold, going beyond simple commensurability arguments. This phenomenon, involving numerous participating modes, appears paradoxical from a classical perspective. While we cannot exhaustively explore all details here, it is evident that even the simple summation of oscillating terms e^{-im^2t}

3. LATTICES OF ANGULAR MOMENTUM

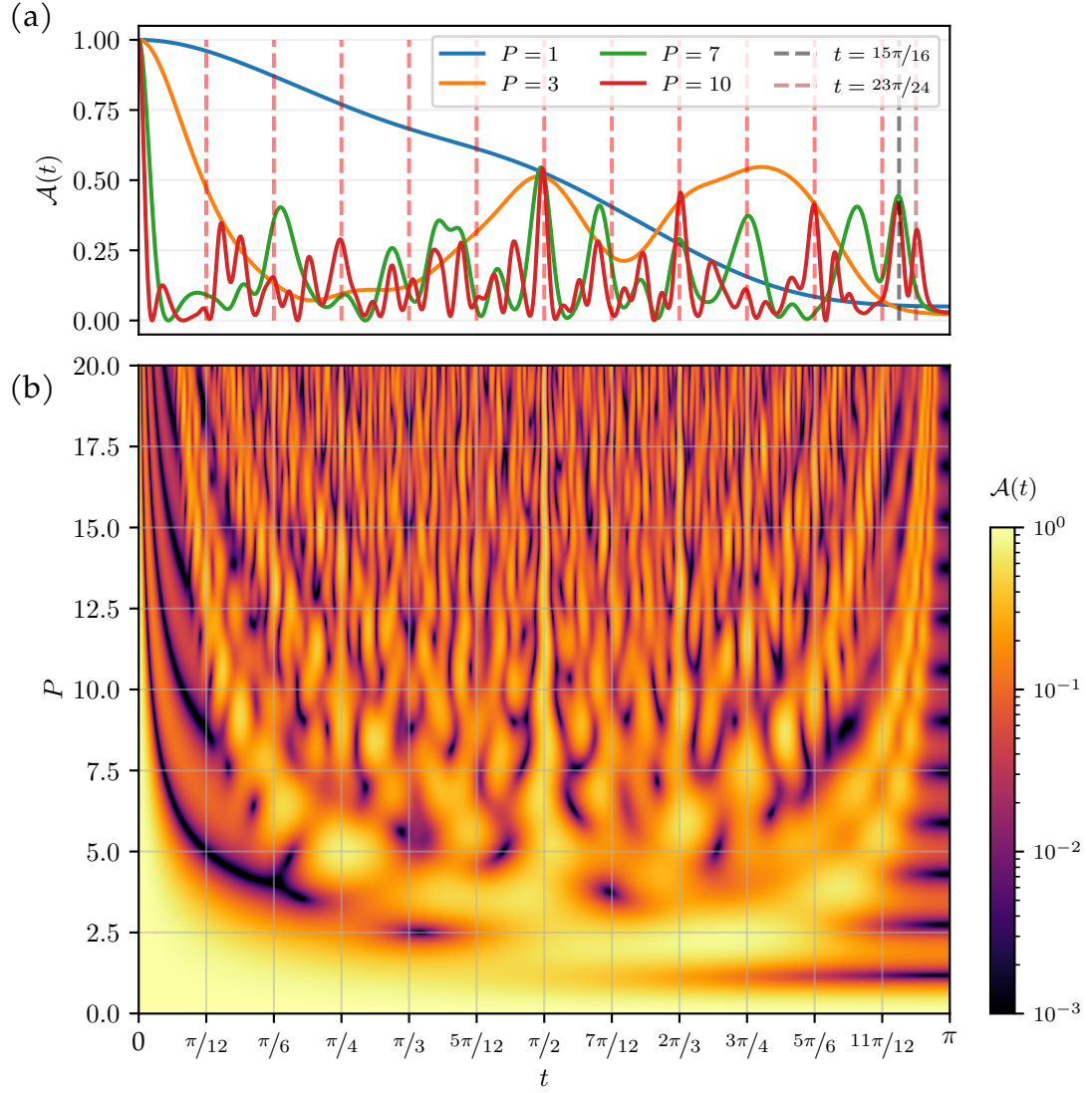


Figure 3.2: Fractional revival pattern for the 2D rotor following a single kick. (a) Autocorrelation function $\mathcal{A}(t) = |\langle \psi(t) | \psi(0) \rangle|^2$ between the evolved and initial wavepackets for various kicking strengths P . The plot is restricted to $0 \leq t \leq \pi$ due to symmetry around $t = \pi$. (b) Heatmap visualization of $\mathcal{A}(t)$ as a function of both time t and kicking strength P . Despite the complex revival structure, two consistent features are observed across all P values: a pronounced revival at $t = \pi/2$ and a characteristic low overlap at $t = \pi$ (for $P \gg 0$).

generates a complex pattern.

Let us now consider a series of kicks in the *quantum resonance regime*, defined by $T = 2\pi/N$ with $N \in \mathbb{N}$. In this regime, the free rotation operator is given by

$$\langle m | e^{-2\pi \hat{L}_z^2} | m' \rangle = \delta_{mm'} e^{-2\pi m^2/N}. \quad (3.35)$$

This operator is periodic with period N ¹¹. The interplay between the previously discussed Floquet theorem and the complex revival pattern we have observed in Fig. 3.2 gives rise to a new symmetry in m -space. This symmetry allows us to reformulate the time-evolution operator in terms of a new variable k , which we shall refer to as the quasi-momentum.

Intriguingly, this symmetry bears a resemblance to crystal symmetry, but manifests in the time domain and, consequently, in m -space. This results in a regular lattice structure in time, governed by the quantum resonance examined earlier. This temporal lattice structure facilitates the definition of a Fourier transform.

3.3.2 Floquet fourier transform

Any operator with the aforementioned periodicity is translation invariant in angular momentum space with period N , i.e.,

$$\langle m | \hat{A} | m' \rangle = \langle m + N | \hat{A} | m' + N \rangle \quad (3.36)$$

for all $m, m' \in \mathbb{Z}$. Let us parametrize each m', m by $m = n \cdot N + \sigma$ and $m' = n' \cdot N + \sigma'$ with $n, n' \in \mathbb{Z}$ and spinor variables¹² $\sigma, \sigma' \in \{0, 1, \dots, N - 1\}$.

¹¹If N is divisible by 4, an additional symmetry emerges, reducing the effective period to $N_{\text{eff}} = N/2$. However, we will primarily focus on cases where N is not divisible by 4. The period of N is proven in the Appendix 6.2. More generally, we could choose $T = 2\pi\tilde{M}/\tilde{N}$ with $\tilde{N}, \tilde{M} \in \mathbb{N}$. By dividing \tilde{N}, \tilde{M} by their greatest common divisor, we obtain $T = 2\pi M/N$, resulting in a period N equal to the least common multiple $N = \text{LCM}(\tilde{N}, \tilde{M})$.

¹²Analogous to condensed matter physics where the dimension N of the unit cell defines the pseudospin of the particle.

3. LATTICES OF ANGULAR MOMENTUM

Then,

$$A_{mm'} = A_{\sigma\sigma'}(n, n') = A_{\sigma\sigma'}(n - n') = A_{\sigma\sigma'}(\Delta n). \quad (3.37)$$

Evidently, \hat{A} only depends on the off-diagonal index Δn , due to the periodicity. This enables us to define a Fourier transform \mathcal{F} that maps from angular momentum space to quasi-momentum k -space with $k \in [0, 2\pi)$ and reads

$$\begin{aligned} A_{\sigma\sigma'}(k) &= \sum_{\Delta n=-\infty}^{\infty} e^{-i\Delta n \cdot k} A_{\sigma\sigma'}(\Delta n), \\ A_{\sigma\sigma'}(\Delta n) &= \frac{1}{2\pi} \int_0^{2\pi} e^{i\Delta n \cdot k} A_{\sigma\sigma'}(k) dk \end{aligned} \quad (3.38)$$

which is equivalent to the notion that the N -periodic operator \hat{A} conserves quasi-momentum k . Note that for $N = 1$, the quasi-momentum trivially becomes the angle ϕ , which makes sense because the m -quantum number is the Fourier transform of the angle. In that case, $\mathcal{F}[e^{iP \cos(\hat{\phi})}] = e^{iP \cos(k)}$. However, for a unit cell larger than one, the situation becomes more intricate. For a state $f(m) = \langle m | f \rangle \in \mathbb{C}$, the Fourier transform is defined by

$$\begin{aligned} f_{\sigma}(k) &= \sum_{\Delta n=-\infty}^{\infty} e^{-i\Delta n \cdot k} f(\sigma + N\Delta n), \\ f(\sigma + N\Delta n) &= \frac{1}{2\pi} \int_0^{2\pi} f_{\sigma}(k) e^{+i\Delta n \cdot k} dk. \end{aligned} \quad (3.39)$$

Similarly, the Fourier transforms of the cosine and cosine squared operators are given by

$$(\cos(\hat{\phi}))(k) = \frac{1}{2} \underbrace{\begin{pmatrix} 0 & 1 & & \dots & e^{-ik} \\ 1 & 0 & 1 & & \\ & 1 & 0 & & \\ \vdots & & & \ddots & \vdots \\ & & & & 1 \\ e^{+ik} & \dots & & 1 & 0 & 1 \\ & & & 1 & 0 \end{pmatrix}}_{N \times N \text{ Matrix}} \quad (3.40)$$

and

$$(\cos^2(\hat{\phi}))(k) = \frac{1}{2} \underbrace{\begin{pmatrix} 1 & 0 & 1/2 & & \dots & e^{-ik}/2 & 0 \\ 0 & 1 & 0 & 1/2 & & \dots & e^{-ik}/2 \\ 1/2 & 0 & 1 & 0 & 1/2 & & \\ & 1/2 & 0 & 1 & 0 & & \\ \vdots & & & \ddots & & & \vdots \\ e^{+ik}/2 & & & & & 1 & 0 & 1/2 \\ 0 & e^{+ik}/2 & \dots & & & 0 & 1 & 0 \\ & & & & & 1/2 & 0 & 1 \end{pmatrix}}_{N \times N \text{ Matrix}} \cdot \quad (3.41)$$

These expressions allow us to calculate the Fourier transform of the time-translation operator at arbitrary N and hence determine the exact time-evolution at all times.

3.3.3 Quasi-momentum Symmetries

Also for this system we have a time-slide symmetry as explained in Section 3.2.2. This implies that the position of the kick does not alter the model, as it represents merely a gauge freedom. Let's examine

3. LATTICES OF ANGULAR MOMENTUM

this symmetry in the case of a quantum resonance, i. e.

$$U(\beta) = e^{-2\pi i \hat{L}_z^2 (1-\beta)/N} e^{-i\hat{V}} e^{-2\pi i \hat{L}_z^2 \beta/N} \sim U = e^{-2\pi i \hat{L}_z^2/N} e^{-i\hat{V}} \quad (3.42)$$

where the symbol \sim indicates that the two operators share the same spectrum, albeit with a rotated set of eigenstates for any $0 \leq \beta \leq 1$. However, as noted earlier, a finite β results in a distinct N -periodicity. Let us express $\beta = \frac{a}{b}$ where $a, b \in \mathbb{N}$ and $a < b$. For incommensurable a and $b \cdot N$, the periodicity of the operator becomes $b \cdot N$ (conversely, for commensurable a and $N \cdot b$, it will be the least common multiple). The equivalence of the spectra consequently leads to bN bands replacing N bands, compensating for the larger unit cell. This phenomenon is well-known in solid-state physics as "band folding".

In addition to that, we find a *time-reversal symmetry* present for all models with one kick in the Floquet operator (where we use that our kicking potentials are real Hermitian $V^* = V = V^T$). More specifically, a second kick with different strength¹³ would break the time-reversal invariance. For Hamiltonians and hence also for our effective Hamiltonian, time-reversal symmetry is defined as [71]

$$\hat{\mathcal{T}} \hat{H} = \hat{H}^* \hat{\mathcal{T}} \Leftrightarrow \mathcal{T} H_k = H_{-k}^* \mathcal{T} \quad (3.43)$$

with an anti-unitary operator¹⁴ \mathcal{T} and conjugation $*$. Note that in the momentum space basis, we have to invert the momentum under time-reversal¹⁵. How the time-reflection operator acts on a time-translation operator is evident from its definition, but we can derive it¹⁶ to be sure from (3.26),

$$\hat{\mathcal{T}}(i \log[\hat{U}_T]/T) \stackrel{!}{=} \hat{\mathcal{T}}(i \log[\hat{U}_T]/T)^* \hat{\mathcal{T}} \Leftrightarrow \hat{\mathcal{T}} \hat{U} = \hat{U}^\dagger \hat{\mathcal{T}}. \quad (3.44)$$

¹³For example, $U_{2\text{-kick}} = e^{-2\pi i \hat{L}_z^2/N} e^{-i\hat{V}_1} e^{-2\pi i \hat{L}_z^2/N} e^{-i\hat{V}_2}$ with $\hat{V}_1 \neq \hat{V}_2$.

¹⁴According to Wigner's theorem symmetries in quantum mechanics are either unitary or anti-unitary [19]. Here, we can represent \mathcal{T} by a unitary matrix $U_{\mathcal{T}}$ and the conjugation operator \mathcal{K} such that $\mathcal{T} = U_{\mathcal{T}} \mathcal{K}$.

¹⁵Which, mathematically, follows straightforwardly from the definition of momentum space in (3.38), but can also be understood intuitively.

¹⁶We use $(-\log[\hat{U}]) = \log[\hat{U}^{-1}] = \log[\hat{U}^\dagger]$.

3. LATTICES OF ANGULAR MOMENTUM

with $\mathcal{P}^\dagger \mathcal{P} = \mathcal{P}^2 = \mathbb{I}$. Since it's a spatial symmetry and does not involve conjugation, it acts similarly on the time-translation operator $\mathcal{P}U = U\mathcal{P}$. In k -space we find

$$\mathcal{P} = \underbrace{\begin{pmatrix} & \dots & 0 & 1 \\ & & 1 & 0 \\ \vdots & & \ddots & \vdots \\ 0 & 1 & & \\ 1 & 0 & \dots & \end{pmatrix}}_{N \times N \text{ Matrix}} \quad (3.47)$$

including a k -inversion $k \rightarrow -k$. For effective Hamiltonian we find $\mathcal{P}H_k = H_{-k}\mathcal{P}$ and similarly for the time-translation $\mathcal{P}U_k = U_{-k}\mathcal{P}$. Note that since this operator obeys both time-reversal and inversion symmetry, we can always gauge it to a real form¹⁹. This holds true even when an auxiliary parameter is introduced, acting as a synthetic dimension that does not disrupt the existing symmetries. Importantly, the system's \mathcal{PT} symmetry remains intact along an adiabatic path $P(\alpha)$, where $\alpha \in \mathbb{R}$, irrespective of any changes to these synthetic dimensions (this will become important in Chapter 4).

3.3.4 Fully resonant case $N = 1$

As mentioned earlier, for $N = 1$, the free rotation is trivial with $e^{-2\pi im^2} = 1$. The one-period time-translation operator then reduces to the kick (3.31). After n kicks, a wave packet evolves as

$$U(t_0 + nT, t_0) = \underbrace{e^{-iP\hat{\phi}} \dots e^{-iP\hat{\phi}}}_n = e^{-inP\hat{\phi}} \quad (3.48)$$

¹⁹Let us define the eigenstates and eigenvalues of \mathcal{P} by $\mathcal{P}\mathcal{V} = \mathcal{V}\text{diag}[\lambda]$, then, in the time-reversal symmetric frame ($\beta = 1/2$) the operator $\mathcal{W} = \text{diag}[\sqrt{\lambda}]\mathcal{V}^\dagger$ defines a transformation that gauges the Hamiltonian to be real, i. e. $H_k \mapsto \tilde{H}_k = \mathcal{W}H_k\mathcal{W}^\dagger \in \mathbb{R}^{N \times N}$, since $\tilde{H}_k = \tilde{H}_k^* \Leftrightarrow \tilde{H} \in \mathbb{R}^{N \times N}$, which follows from $\tilde{H}_k = \tilde{H}_{-k}^*$ and inversion invariance.

3.3. Quantum resonance of rotors

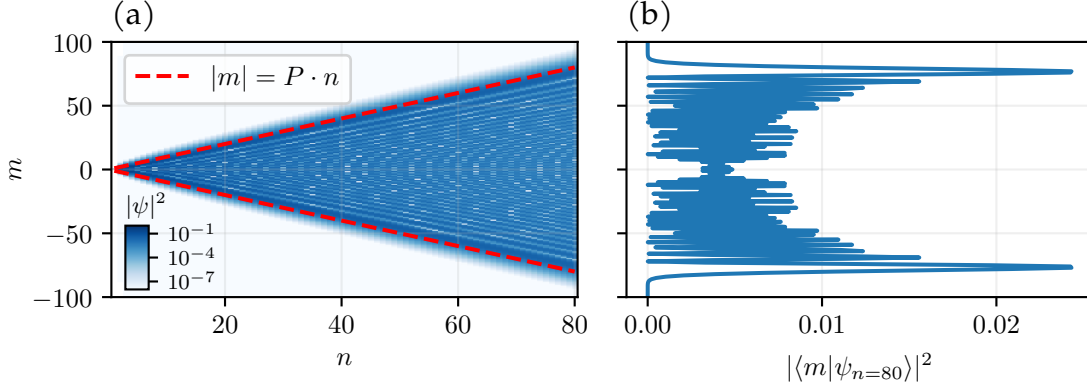


Figure 3.3: Dynamics of a quantum rotor at full resonance ($\mathbf{N=1}$) with $\mathbf{P=1}$. (a) Logarithmic color plot of $|\langle m|\psi(nT)\rangle|^2$, depicting the ballistic spread of a wave packet initially localized at $m = 0$. (b) Probability distribution $|\langle m|\psi(nT)\rangle|^2$ at $t = 80T$, showing the squared Bessel function $|J_m(nP)|^2$ (cf. (3.48)).

with rescaled matrix elements from the kick (3.31). For an initial state with $\langle m|\psi_0\rangle = \delta_{m,0}$, we can evaluate the kinetic energy exactly²⁰

$$\langle \hat{H}_0 \rangle_t = \langle \psi(t) | \hat{L}_z^2 | \psi(t) \rangle_{t=nT} = (Pt)^2/2 \quad (3.49)$$

which demonstrates a ballistic growth in energy (see Fig. 3.3). Likewise, one can straightforwardly show²¹ that the wave front of the

²⁰To evaluate the identity, let us first look at

$$\frac{\partial}{\partial \phi} e^{ix \sin(\phi)} = ix \cos(\phi) e^{ix \sin(\phi)} \stackrel{!}{=} \frac{\partial}{\partial \phi} \sum_{m=-\infty}^{\infty} J_m(x) e^{im\phi} = i \sum_{m=-\infty}^{\infty} m J_m(x) e^{im\phi}.$$

Then, let us take the modulo square and integrate over $\int_0^{2\pi} d\phi$,

$$\pi x^2 \stackrel{!}{=} \int_0^{2\pi} d\phi \sum_{mm'} J_m^*(x) J_{m'}(x) m^2 e^{i(m-m')\phi} = 2\pi \sum_m m^2 |J_m(x)|^2$$

which leads to the desired expression.

²¹First we show that the Bessel function $J_m(x)$ reaches its global minimum with respect to m at $m \approx x$. To this end, we can use the stationary phase approximation. Another integral representation is given by [165] $J_m(x) = \frac{1}{\pi} \int_0^\pi \cos(\gamma(u)) du$ with the phase $\gamma(u) = mu - x \sin(u)$. The stationary points occur where the derivative is zero,

wavepacket spreads like $m_{\max} \approx Pt$, which suggests a linear spread in angular momentum space. For other initial conditions than a pure state, the wave fronts and the energy growth will deviate from these exact results due to interference effects, but we still expect asymptotically a linear behavior in wave front spreading and a quadratic growth in energy.

3.3.5 Staggering case $N = 2$

This is a unique and somewhat unusual case compared to other resonances, as after two kicks, any initial wavefunction is precisely mapped back onto itself. This is noteworthy because it holds true for any kicking strength P or any initial state. This can be demonstrated straightforwardly using identities of the Bessel function²², but there is another argument that will be useful later, which is more illustrative and simpler. Specifically, we can perform the Fourier transform to gain insights into the spin model that naturally emerges from this mapping. For $N = 2$, the cosine in (3.40) becomes

$$\mathcal{F}[P \cos(\hat{\phi})](k) = \begin{pmatrix} 0 & 1 + e^{-ik} \\ 1 + e^{ik} & 0 \end{pmatrix} = (1 + \cos(k))\sigma_x + \sin(k)\sigma_y \quad (3.50)$$

$\gamma'(u) = m - x \cos(u) = 0$ i. e. $\cos(u) = \frac{m}{x}$. Solutions exist when $|m| \leq x$. The maximum contribution to $J_m(x)$ occurs when $u = 0$, leading to $m = x$. The maximum of the wave packet (with $\psi_0 = \delta_{0,m}$) with $|\langle m | \psi(t = nT) \rangle|^2 = |J_m(nP)|^2$ then occurs, likewise, at $m = Pn$.

²²Consider an initial wave function $|\psi_0\rangle$. The free rotation simply introduces a phase factor $(-1)^m$, while the kick results in the matrix elements (3.31). After two kicks, we have

$$\begin{aligned} \langle m | \psi \rangle &= (-1)^m \sum_{m_1=-\infty}^{\infty} (-i)^{m_1-m} J_{m_1-m}(P) (-1)^{m_1} \sum_{m_2=-\infty}^{\infty} (-i)^{m_2-m_1} J_{m_2-m_1} J_{m_2-m_1}(P) \langle m_2 | \psi_0 \rangle \\ &= \sum_{m_2=-\infty}^{\infty} (-i)^{m_2-m} \langle m_2 | \psi_0 \rangle \sum_{m_1=-\infty}^{\infty} (-1)^{m_1+m} J_{m_1-m}(P) J_{m_2-m_1}(P) = \langle m | \psi_0 \rangle. \end{aligned}$$

where in the last step we shifted the sum $m_1 \rightarrow m_1 + m$ and utilized the identities $J_{-m}(P) = (-1)^n J_m$ and $\sum_{m=-\infty}^{\infty} J_m(P) J_{m+q}(P) = J_q(0) = \delta_{q,0}$.

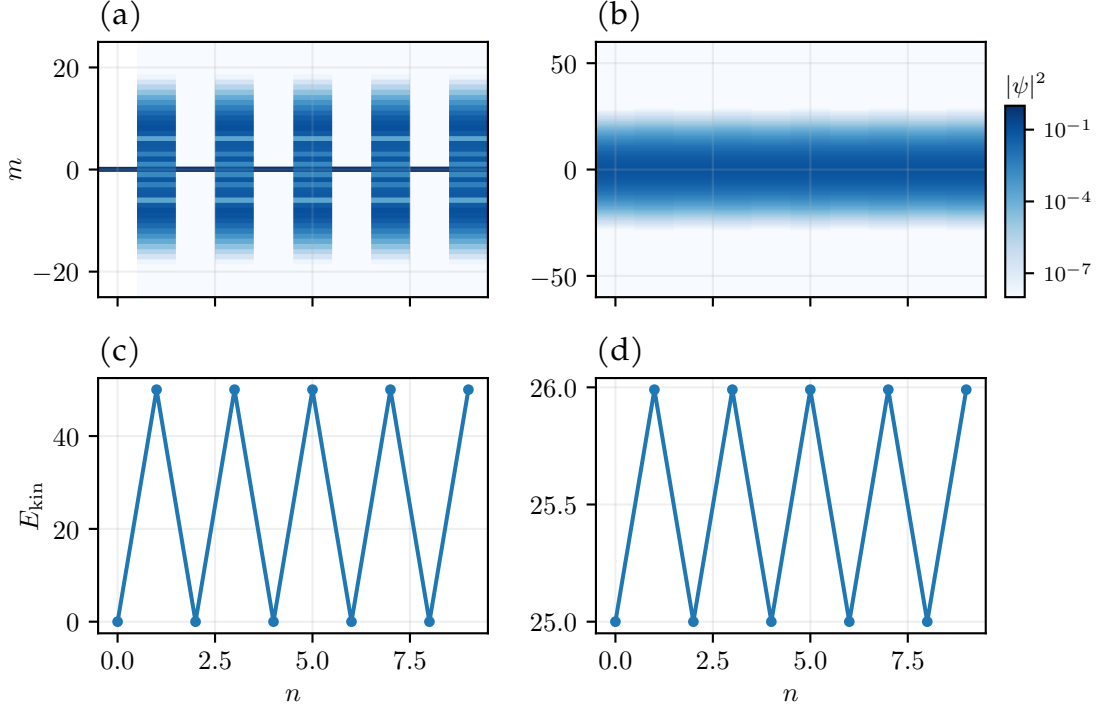


Figure 3.4: Dynamics of a quantum rotor at half resonance ($N=2$) with $P=10$. (a) Time evolution of the probability density $|\psi(t)|^2$ for an initially localized state $\langle m|\psi(0)\rangle = \delta_{m,0}$. (b) Temporal evolution of $|\psi(m,t)|^2$ for an initially Gaussian state $\langle m|\psi(0)\rangle \propto e^{-\beta|m|^2}$ with $\beta = 10^{-2}$. (c-d) Kinetic energy dynamics corresponding to (a-b). As demonstrated in the main text, the system exhibits perfect revival after two kicks, returning to its initial state with no net change. For a Gaussian state we do not see any change in population.

with the pauli matrices σ_i . They can be easily exponentiated using a variant of the Euler-Rodrigues' rotation formula [15]

$$e^{-i\mathbf{d}_k \cdot \boldsymbol{\sigma}} = \mathbb{I} \cos(\xi) + i(\mathbf{n} \cdot \boldsymbol{\sigma}) \sin(\xi) \quad (3.51)$$

where $\mathbf{d}_k = (P(1 + \cos(k)), P \sin(k), 0) \equiv \xi \mathbf{n}$ with $\mathbf{n}^2 = 1$. The free rotation simply becomes $\mathcal{F}[\delta_{mm'} e^{-\pi m^2}] = \sigma_z$, and thus the one-period translation operator takes the form

$$\hat{U}(k) = \sigma_z \cos(\xi) + i\sigma_z(\mathbf{n} \cdot \boldsymbol{\sigma}) \sin(\xi) \quad (3.52)$$

which clearly squares to one $\hat{U}^2(k) = \mathbb{I}$. Hence, after two kicks, the initial wavepacket is recovered.

3.3.6 Higher order quantum resonances

Let us now examine the case of the *triadic resonance* $N = 3$. In Fig. 3.5 we show the quasi-energy spectrum and time evolution. We observe that the spectrum branches from a single band at $P = 0$ into three bands with increasing width as P increases, consistent with the expected periodicity. Notably, at $P \approx 4$, there is a band touching, which will be investigated at a later stage. Similar to the $N = 1$ resonance case, we observe unobstructed ballistic growth for most initial eigenstates. While we derived an exact expression for the energy growth in the $N = 1$ case (see (3.49)), obtaining such expressions for the general case proves to be significantly more challenging. We can express the effective Hamiltonian in momentum space as

$$H_k = \mathbf{d}_k(P) \cdot \lambda \quad (3.53)$$

where $\lambda_i \in \{\lambda_1, \dots, \lambda_8, \mathbb{I}\}$ are the Gell-Mann matrices belonging to the Lie algebra of $SU(3)$, including the unity as the ninth matrix (see [76, 172]), and $\mathbf{d}_k(P) \in \mathbb{R}^{8+1}$ is the so-called winding vector, similar to the 2-band case in (3.51). This formulation allows us to use the properties of $SU(3)$ to understand the symmetries and structure of our system. Using (3.3) we can define the bandgap of the n -th band by of the model by

$$\delta_n = \min_{k \in [0, 2\pi]} |\epsilon_n(k) - \epsilon_{n+1}(k)|_{2\pi} \quad (3.54)$$

and the minimal band gap by $\min_n \delta_n$.

As outlined in Section 3.3.3, this Hamiltonian obeys the symmetries $\mathcal{T}H_k = H_{-k}^* \mathcal{T}$ and $\mathcal{P}H_k = H_{-k} \mathcal{P}$, which constrain the vector \mathbf{d}_k . For resonances with $N > 3$, we can generalize this approach using the $SU(N)$ generalized Gell-Mann matrices. When we look

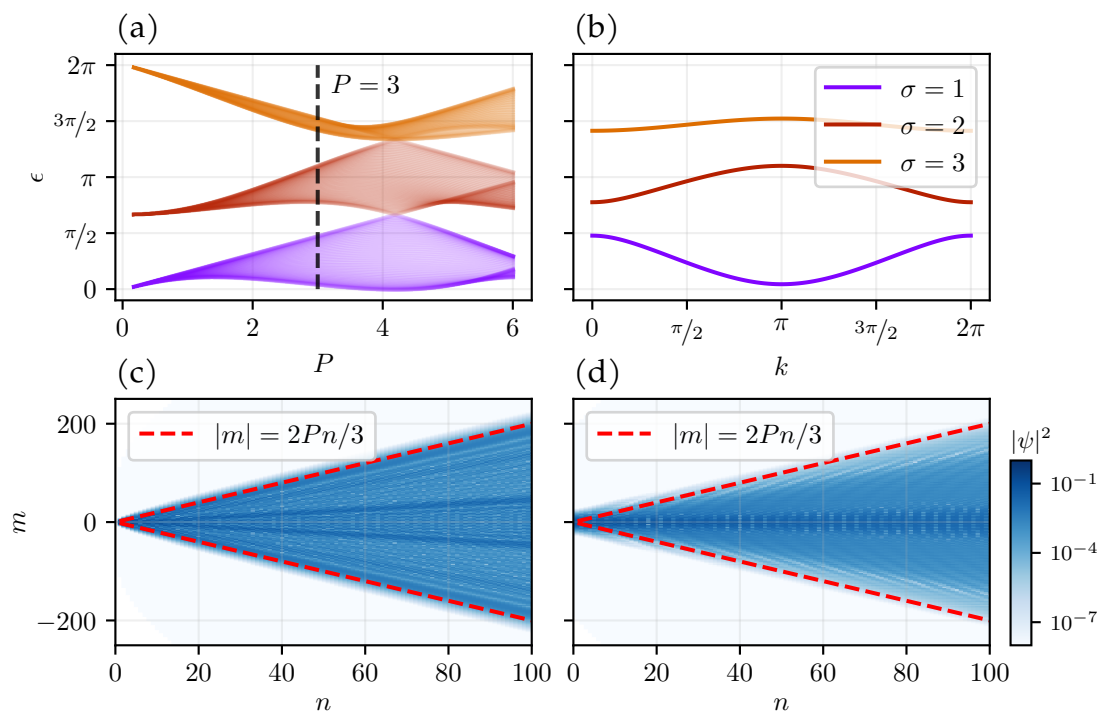


Figure 3.5: Quasi-energy spectrum at the triadic resonance $N = 3$. (a) Quasi-energy spectrum as a function of kicking strength P from exact diagonalization (see (3.29)). The spectrum exhibits branching from a single band at $P = 0$ into three bands with increasing width as P increases. (b) Quasi-energy spectrum as a function of quasi-momentum k at $P = 3$ (indicated in (a) by the dashed vertical line), demonstrating the inversion symmetry around $k \rightarrow -k$. (c)-(d) Time-evolution of the probability density $|\psi(t)|^2$ for the same states as in Fig. 3.4.

at higher quantum resonances $N > 3$, Fig. 3.6 demonstrates that these resonances also exhibit a linear spread of the wavefunction. However, determining the precise slope of the wavepacket spread for arbitrary N is challenging, since unlike the cases before, there is no known expression for the maxima of the wavefunction. As emphasized in Fig. 3.6, the spread in angular momentum is generally less pronounced the higher the quantum resonance N is. This is a phenomenon already outlined in [49], which provides a semi-empirical

3. LATTICES OF ANGULAR MOMENTUM

equation with

$$\langle \hat{H}_0 \rangle_t \approx Dt^2 \exp[-2N/D] \quad (3.55)$$

where $D = \frac{P^2}{T}$ is a semi-classical diffusion constant²³, noting that this equation is only valid for $q \ll D$. Upon examining different resonances, it becomes apparent that the order of resonance alone is a poor indicator of the growth of energy. To elucidate this behavior further, let us examine Fig. 3.7, which shows the growth of energy for more general resonances $q = \frac{M}{N}$ with two coprimes M, N (see footnote 11). As it turns out, some of them coincide and have identical spread (for example $q = 1/5$ and $q = 3/5$), while others vary immensely in their spread (for example $q = 1/5$ and $q = 2/5$). Further, there is a dependence on the kicking strength P as well. We can estimate the average growth of kinetic energy using the spinor representation (3.38) of the $t - th$ power of the time-translation operator (3.30)

$$(U_{\sigma\sigma}(k))^t = \left(\sum_{s=1}^N \psi_{s,\sigma}(k) e^{-\epsilon_s(k)} \psi_{s,\sigma}^*(k) \right)^t = \sum_{s=1}^N \psi_{s,\sigma}(k) e^{-t\epsilon_s(k)} \psi_{s,\sigma}^*(k) \quad (3.56)$$

with the eigenstates $\psi_{s,\sigma}(k)$ of $U_{\sigma\sigma'}(k)$. Then, using $m = Nn + \sigma$, the kinetic energy for a state $\phi(t)$ takes the form

$$\begin{aligned} E_{\text{kin}}(t) &= \langle \phi(t) | \hat{L}_z^2 | \phi(t) \rangle = \langle \phi_0 | (U^\dagger)^t \hat{L}_z^2 U^t | \phi_0 \rangle \\ &= \sum_{mm'm''} \phi_{0,m} \phi_{0,m''} (U_{mm'}^\dagger)^t m^2 (U_{m'm''}^t)^t \\ &= \sum_{\substack{\sigma\sigma'\sigma'' \\ nn'n''}} \phi_{0,\sigma}(n) \phi_{0,\sigma''}(n'') (U_{\sigma\sigma'}^\dagger(n' - n))^t (Nn' + \sigma)^2 (U_{\sigma'\sigma''}^t)^t \end{aligned} \quad (3.57)$$

Now, we choose²⁴ $\phi_\sigma^* = \delta_{\sigma,0} \delta_{n,0}$ as the initial state and can remove

²³In the classical kicked rotor [49], the average momentum changes with $\langle H_0 \rangle_t \approx Dt/2$.

²⁴The calculation can possibly also be done with a generic initial state, but it will become very cumbersome.

3.3. Quantum resonance of rotors

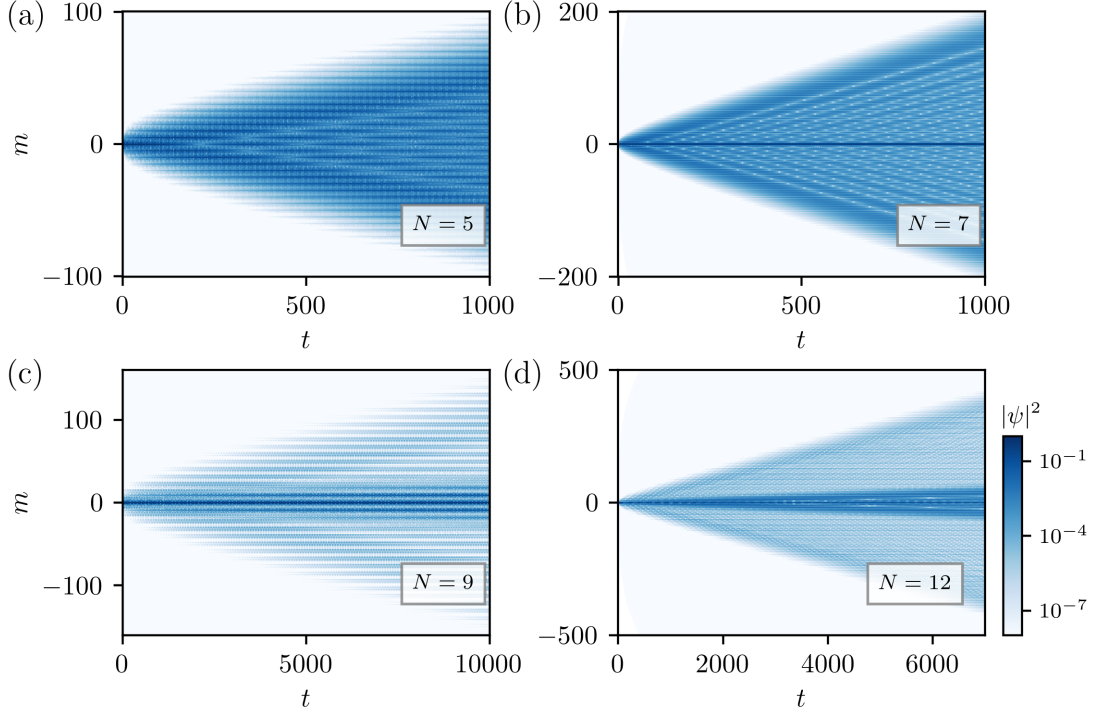


Figure 3.6: Time-evolution for higher quantum resonances. (a-d) The plots show the linear spread of the wavefunction for various resonance orders N . The color scale shows the probability density $|\psi(t)|^2$ as a function of momentum m and time t . The linear nature of the spread is evident across all resonances, although the specific rate of spread varies by orders of magnitude (note the different ranges of the axis). There is a general trend where higher resonances correspond to slower spread. For a more detailed analysis of the energy accumulation see Fig. 3.6.

four of the sums. Factorization in eigenstates becomes

$$\begin{aligned}
 &= \frac{1}{4\pi} \sum_{\sigma, n, s, s'} (Nn + \sigma)^2 \int_0^{2\pi} dk \int_0^{2\pi} dk' e^{-i(n(k'-k) + t(s-s'))} \\
 &\quad \cdot \psi_{s,0}^*(k) \psi_{s,\sigma}(k) \psi_{s',\sigma}(k') \psi_{s',0}^*(k').
 \end{aligned} \tag{3.58}$$

Remarkably, we can derive an identity for $\sum_{n=-\infty}^{\infty} (Nn + \sigma)^2 e^{-in(k'-k)}$,

3. LATTICES OF ANGULAR MOMENTUM

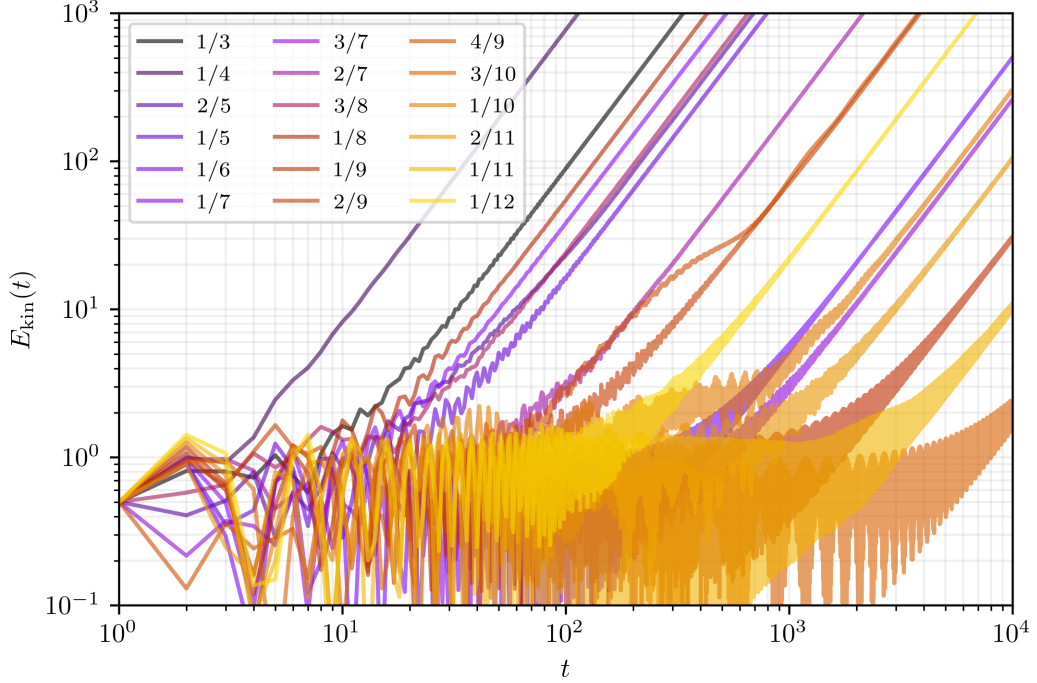


Figure 3.7: Growth of kinetic energy for higher quantum resonances. The plots show the quadratic growth of energy ($P = 1$) for various resonance orders $q = M/N$ with Floquet operator $U = e^{-2\pi i \hat{L}_z^2 M/N} e^{-i \cos(\hat{\theta})}$. First, we confirm that all resonances lead asymptotically, after an initial irregular phase, to quadratic growth t^2 as visible from the slope of the curves. Second, we confirm that overall, for increasing resonances N , the growth rates drop exponentially (with notable exceptions, such as $q = 1/8$).

see²⁵), and remove the infinite sum. With defining

$$\chi_{s\sigma}(k) = e^{-it\epsilon_s(k)} \psi_{s,\sigma}(k) \psi_{s,0}^*(k) \quad (3.59)$$

²⁵After expansion, there are three terms can be written as

$$N^2 \underbrace{\sum_{n=-\infty}^{\infty} n^2 e^{-in\Delta k}}_{-2\pi \sum_{n=-\infty}^{\infty} \delta''(\Delta k - 2\pi n)} + 2N\sigma \underbrace{\sum_{n=-\infty}^{\infty} n e^{-in\Delta k}}_{-2\pi i \sum_{n=-\infty}^{\infty} \delta'(\Delta k - 2\pi n)} + \sigma^2 \underbrace{\sum_{n=-\infty}^{\infty} e^{-in\Delta k}}_{2\pi \sum_{n=-\infty}^{\infty} \delta(\Delta k - 2\pi n)}$$

Clearly, in the infinite sums only $n = 0$ contribute, since $\Delta k \in [0, 2\pi)$. The delta functions then facilitate the integration over k' and by noting that $\partial_{\Delta k} \psi(k) = \partial_k \psi(k)$ we arrive at (3.60).

we find

$$E_{\text{kin}}(t) = \frac{1}{2} \sum_{\sigma, s, s'} \int_0^{2\pi} dk \chi_{s\sigma}^*(k) \left(\sigma^2 \chi_{s'\sigma}(k) - 2iN\sigma \partial_k \chi_{s'\sigma}(k) - N^2 \partial_k^2 \chi_{s'\sigma}(k) \right). \quad (3.60)$$

The expression inside the integral constitutes something like a transport tensor that needs to be integrated over k . Since σ, s, s' all run only from 1 to N , this is something one can evaluate straightforwardly.

3.4 Dynamical localization

What happens when we deviate from perfect resonance conditions? Consider the case where $T = 2\pi q$ with some non-rational number q , for example, $q = \pi^{-1}$. A fascinating phenomenon emerges, known as *dynamical localization*, where the wavefunction becomes localized in angular momentum space [46]. To develop physical intuition, consider a driven oscillator analogy: When kicks occur at intervals incommensurate with the oscillator's natural frequency, they effectively appear as random perturbations rather than coherent driving. Instead of resonant energy absorption, we observe destructive interference effects that inhibit energy growth, creating behavior reminiscent of dissipative processes, though the underlying mechanism is purely quantum mechanical. Figure 3.8 illustrates the time evolution of a rotor in the dynamical localization regime. The system initially exhibits a brief growth phase before settling into a quasi-steady state with bounded random fluctuations. This state persists indefinitely, as demonstrated in panels (b) and (d), with the wavefunction displaying exponential localization. The origin of this phenomenon lies in *Anderson localization* physics. The driving period's incommensurability with the rotational period effectively introduces quasi-random disorder into the system, causing localization in momentum space analogous to Anderson localization in real space lattices. The degree of localization depends critically on the "incommensurability" of q . Figure 3.9 demonstrates this for

3. LATTICES OF ANGULAR MOMENTUM

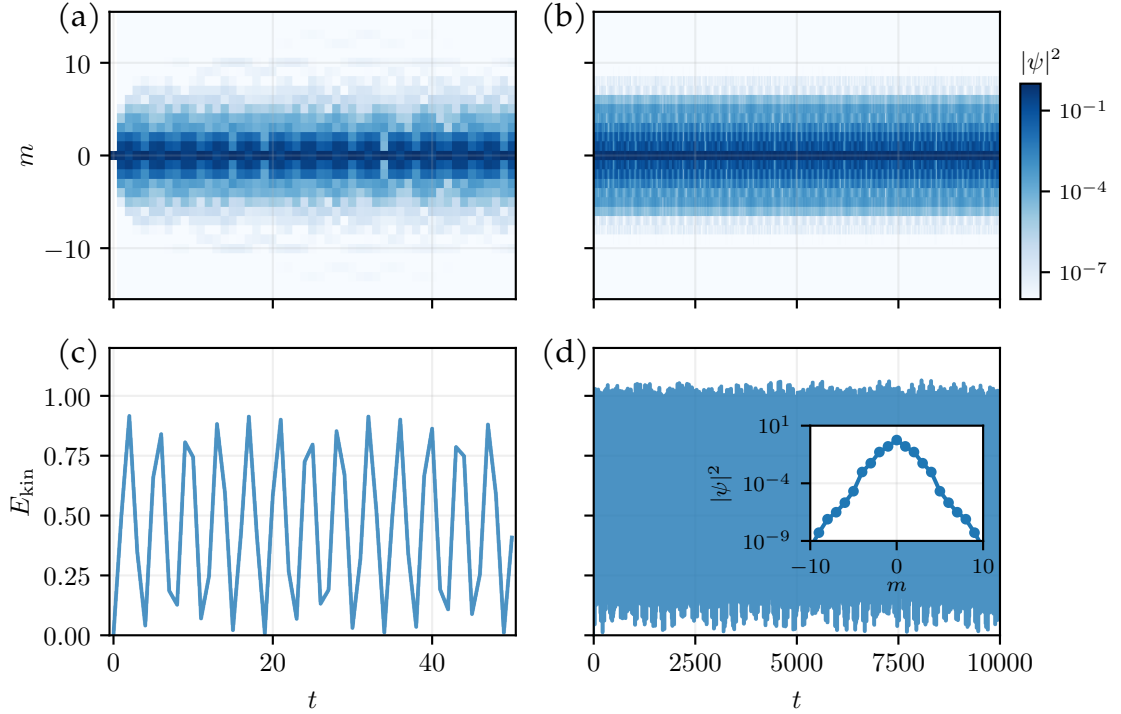


Figure 3.8: Time-evolution demonstrating dynamical localization. All panels show results for $P = 1$ and $T = 1$. The left panels show the short-term evolution over $n = 50$ kicks and the right panels the long time-evolution over $n = 10000$ kicks. In (d) we show the exponentially localized wavepacket at $t = 10^4$. The system exhibits strong localization with the kinetic energy fluctuating chaotically about a mean value. Notably, this localized behavior persists even over long time scales, contrasting sharply with the ballistic spreading observed in resonant cases.

$q = 0.3331$, which lies near the rational value $q = 1/3$. While the system exhibits strong localization, it displays significant kinetic energy fluctuations. These fluctuations, though appearing regular, are fundamentally chaotic and non-repeating. Notably, the energy variations arise primarily from wavefunction phase changes while the probability density remains relatively stable.

For delta-kick potentials \hat{V} , we can establish an exact mapping to a tight-binding model [173]. Given a Floquet operator $U = e^{-iH_0T} e^{-i\hat{V}}$

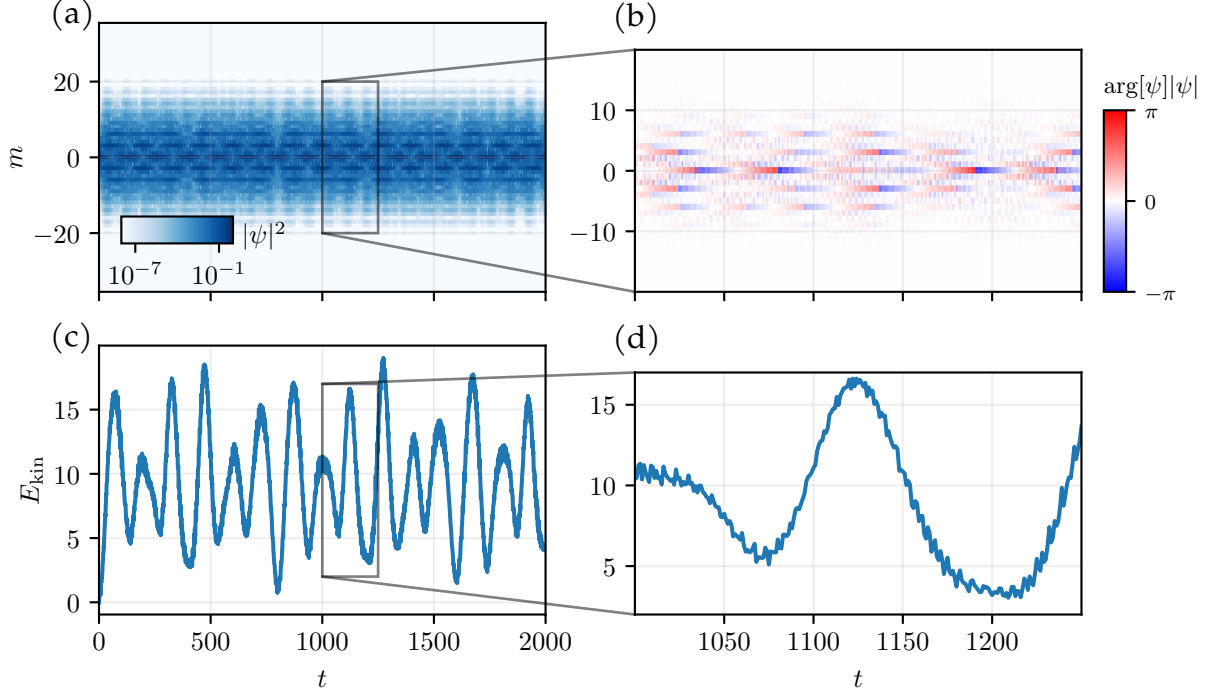


Figure 3.9: Time-evolution near quantum resonance. Here we look at $q = 0.3331$, near the $1/3$ quantum resonance. (a) Time evolution of probability density $|\psi(t)|^2$ and (b) time-evolution of the phase $\arg[\psi]|\psi|$ within a selected time window. (c) Full time evolution of kinetic energy, demonstrating large-scale fluctuations, and (d) selected time window. Despite the nearly constant probability density distribution, the system exhibits dramatic kinetic energy fluctuations up to 80% of the mean value, driven by quantum phase interference effects.

with Floquet mode $U|\psi\rangle = e^{-i\epsilon}|\psi\rangle$, we obtain²⁶:

$$\sum_{m'} (W_{mm'} - \delta_{mm'} Q_{m'}(\epsilon)) \tilde{\psi}_{m'} = 0 \quad (3.61)$$

²⁶First, we use the fact that we can rewrite $e^{-i\hat{V}} = \frac{1+iW}{1-iW}$ with an hermitian operator $W = -\tan[\hat{V}/2]$. Then, $U|\psi\rangle = e^{-i\epsilon}|\psi\rangle$ turns into

$$(1 + e^{-i(\epsilon - H_0 T)})|\psi\rangle + iW(1 - e^{-i\epsilon - H_0 T})|\psi\rangle = 0.$$

Finally, we replace $|\psi\rangle$ by $\tilde{\psi} = 1 - (e^{-i(\epsilon - H_0 T)})|\psi\rangle$ and use the identity $\frac{1 - e^{-i(\epsilon - H_0 T)}}{1 + e^{-i(\epsilon - H_0 T)}} = i \tan[(\epsilon - H_0 T)/2]$ to arrive at (3.61).

3. LATTICES OF ANGULAR MOMENTUM

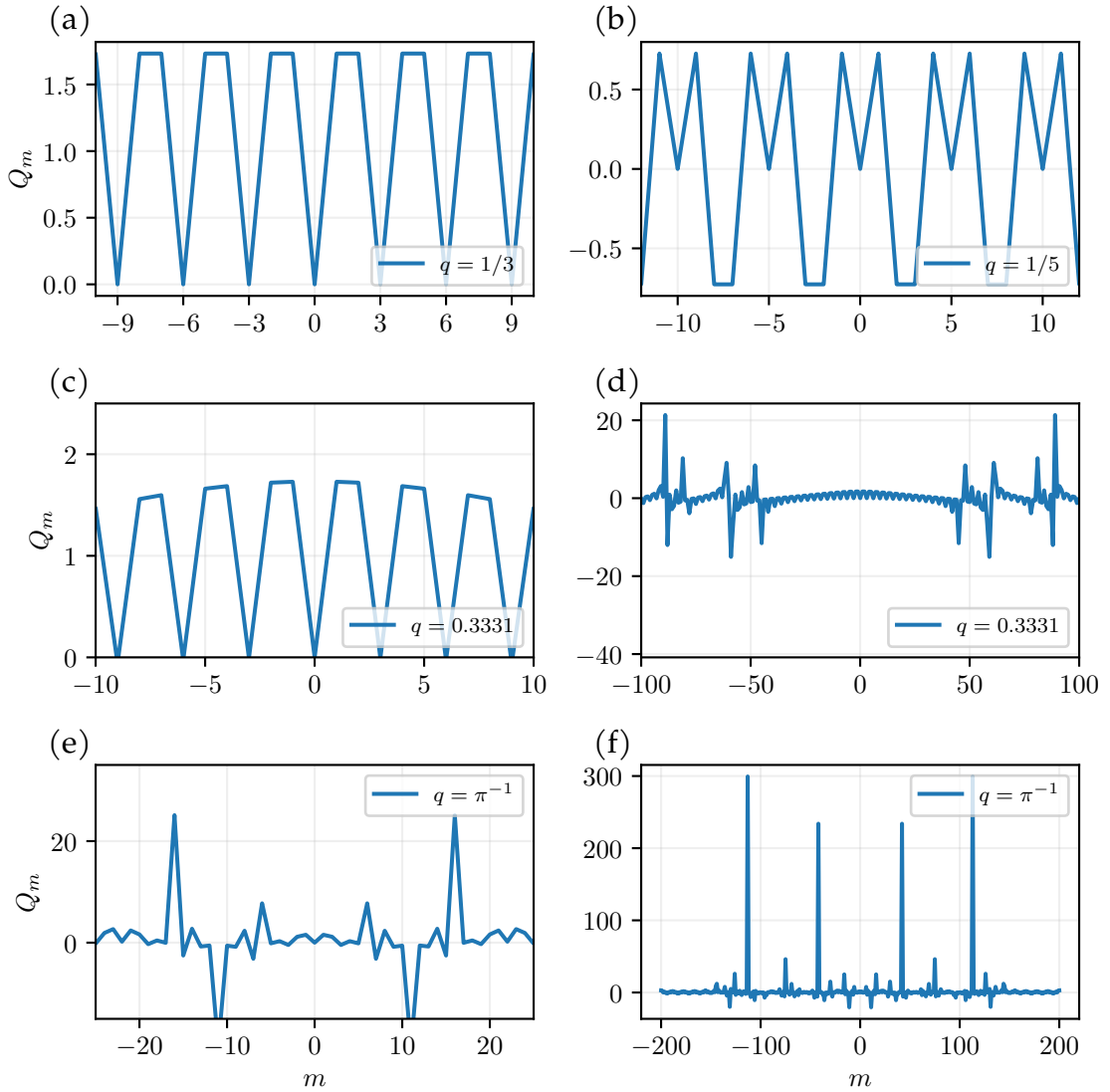


Figure 3.10: On-site potentials for the tight-binding map. Following the definition of on-site potential in (3.61), (a-b) shows cases at quantum resonance, where we understand that the on-site potentials are perfectly periodic, confirming what we already know from the discussion about the periodicity in (3.35). (c-d) is in the dynamical localization regime, but close to the resonance $q = 1/3$, as in Fig. 3.9. (e-f) is far away from any resonance and does not show any periodicity. In contrast, it shows large fluctuations.

where $W_{mm'} = -\langle m | \tan[\hat{V}/2] | m' \rangle$, $Q = \tan((\epsilon - H_0 T)/2)$, and $\tilde{\psi}_n = \langle m | 1 - (e^{-i(\epsilon - H_0 T)}) | \psi \rangle$. While this equation is not directly solvable due to the dependence on ϵ , it provides valuable insights. For moderate coupling, W_{mn} represents regular nearest-neighbor hopping, with system behavior largely determined by the on-site potential Q_m . Compared to our previous expressions of the dynamics, for example the stroboscopic Hamiltonian, this formulation separates the regular hopping potential \hat{V} from the rotational phases $e^{-iH_0 T}$ appearing as on-site terms.

To understand this tight-binding model, we can look at a related model that looks very similar: The *Lloyd model* offers exact solution of the localization length²⁷

$$\psi_{n+1} + v_n \psi_n + \psi_{n-1} = E \psi_n \quad (3.62)$$

with probability distribution

$$p(v_n) = \frac{1}{\sqrt{2\pi}} \frac{w^2}{v_n^2 + w^2}, \quad v_n > 0. \quad (3.63)$$

This model exhibits exponential localization for any non-zero disorder strength w , with localization length ξ_{loc}

$$\xi_{\text{loc}}^{-1} = \text{arcosh} \left[\frac{1}{4} \left(\sqrt{(2+E)^2 + w^2} + \sqrt{(2-E)^2 + w^2} \right) \right] \quad (3.64)$$

For $E = 0$, a Taylor expansion of the localization length yields

$$\xi_{\text{loc}}^{-1} = \text{arcosh}(2) + \frac{w^2}{16} + \frac{w^4}{1024} + O(w^6) \quad (3.65)$$

which leads to the characteristic scaling $\xi_{\text{loc}} \propto 1/w^2$ for small disorder. The divergence of the localization length as $w \rightarrow 0$ signals the localization-delocalization transition at zero disorder, marking the boundary between localized and extended states.

²⁷Following [49] closely.

For our quantum rotor, while not truly random, the terms $Q_m = \tan(\epsilon - m^2 T)/2$ become sufficiently disordered for incommensurate T to induce localization. This disorder-induced localization differs fundamentally from the topological edge states we will encounter in the 3D rotors of the next Section, where boundaries give rise to distinct edge modes of topological origin.

3.5 Periodically driven 3D rotors

In Chapter 2, we extensively discussed the interaction of molecules with off-resonant multi- and few-cycle pulses. The sudden approximation, which we elaborated there, will serve as the basic ingredient for the periodically driven molecule. From now let us assume that we are working in the regime where the sudden approximation is applicable and refer the reader to our previous discussion when questions of validity arise.

Within the sudden approximation, the full Hamiltonian of a linear molecule plus interaction with a train of linearly polarized laser pulses takes the following form of a time-independent Hamiltonian H_0 and a periodic potential

$$\begin{aligned} H_{\text{KR}}(t) &= B\hat{\mathbf{L}}^2 + \left(P_1 \cos(\hat{\theta}) + P_2 \cos^2(\hat{\theta}) \right) \sum_{n=0}^{\infty} \delta(t - nT) \\ &= H_0 + \hat{V} \sum_{n=0}^{\infty} \delta(t - nT). \end{aligned} \quad (3.66)$$

with the effective pulse strengths P_1, P_2 defined in (2.60) and (2.51) and the duration between the pulses T . The terms arising due to finite P_1 we will call orientation pulse (analogous to the orientation signal $\langle \cos(\hat{\theta}) \rangle$) and P_2 we shall call the alignment pulse (analogous to the alignment signal $\langle \cos^2(\hat{\theta}) \rangle$). For other cases such as the symmetric top or elliptical polarization, the effective strength P_i becomes tensor dependent on the different spherical sectors.

The two-dimensional rotor with \hat{L}_z^2 might seem fundamentally different from the full three-dimensional case governed by \hat{L}^2 . Indeed, instead of the simple basis functions $e^{-im\phi}$ we need to consider the more involved spherical harmonics of (2.4), which, at first glance, introduce significant complications. However, as we will see in the following, we can simplify the problem considerably. When we consider linearly polarized pulses (see Section 2.2 for the complete reference system), the matrix elements $\langle l'm'|\hat{V}|lm\rangle$ exhibit a remarkable property: they are proportional to $\delta_{mm'}$ and converge rapidly to constant values for $l, l' \gg 0$. This convergence enables us to extend our Fourier transform techniques and momentum-dependent Floquet states to the three-dimensional rotor, given that we choose the kicking interval to be at a quantum resonance $T = 2\pi/(B \cdot N)$. Instead of a phase factor $\propto m^2$, the phases turn into

$$\zeta_l = e^{-2\pi il(l+1)/N} \quad (3.67)$$

which, nevertheless, possess a period N^{28} . However, a fundamental distinction arises: unlike the two-dimensional case where $m \in \mathbb{Z}$ spans all integers, three-dimensional angular momentum is confined to $l > 0$, creating a half-infinite lattice with a boundary at $l = 0$. This boundary prevents direct application of Fourier methods to states with significant weight near $l = 0$, which will be important for a specific class of edge modes that are of topological origin. While few in number, these boundary-localized states profoundly influence the molecular dynamics under periodic driving. When including additional terms of a real molecule, such as centrifugal distortion, this will lead to an effective maximum l_{\max} of the lattice, framed *Anderson Wall*. We will discuss this phenomenon in Sec. 3.5.2. From now on, when we work with real-space diagonalization, we shall for practical reasons always assume a finite lattice $0 \leq l \leq l_{\max}$ with the possibility of edge states at both boundaries. For bulk states, however,

²⁸As in the 2D rotor, there are special cases; for $N = 2 + 4n, n \in \mathbb{N}_0$, the period is $N/2$ instead of N due to an accidental symmetry. We prove this in the appendix 6.2.

3. LATTICES OF ANGULAR MOMENTUM

the infinite lattice approximation remains remarkably accurate, as we shall demonstrate in the following.

3.5.1 Convergence of matrix elements of the 3D rotor

The asymptotic expressions take the simple form²⁹

$$\langle l' m' | \cos(\theta) | l m \rangle = -\delta_{mm'} C_{lm10}^{l'm} C_{l'010}^{l0} \xrightarrow{l, l' \gg 0} \delta_{mm'} (\delta_{l, l'+1} + \delta_{l, l'-1}) / 2 \quad (3.71)$$

and

$$\begin{aligned} \langle l' m' | \cos^2(\theta) | l m \rangle &= \delta_{mm'} \left(\frac{2}{3} C_{lm20}^{l'm} C_{l'020}^{l0} + \frac{1}{3} \delta_{ll'} \right) \\ &\xrightarrow{l, l' \gg 0} \delta_{mm'} (\delta_{l, l'} + (\delta_{l, l'+2} + \delta_{l, l'-2}) / 2) / 2. \end{aligned} \quad (3.72)$$

For $m = 0$, these coefficients show particularly rapid convergence, as demonstrated in Fig. 3.11. Thus, the behavior of the 3D rotor is

²⁹To prove this asymptotic, one can use the Edmonds asymptotic formula for 3j-symbols [174]

$$\begin{pmatrix} l_1 & l_2 & l_3 \\ m_1 & m_2 & m_3 \end{pmatrix} \xrightarrow{\text{for } l_2, l_3 \gg l_1} (-1)^{l_3+m_3} \frac{d_{m_1, l_3-l_2}^{l_1}(\alpha)}{\sqrt{l_2+l_3+1}} \quad (3.68)$$

with $\cos(\alpha) = \frac{m_2-m_3}{l_2+l_3+1}$, the Wigner function $d_{m, m'}^l(\alpha)$ and 3j-symbols which are related to the Clebsch-Gordan coefficients [175]

$$\langle j_1 m_1 j_2 m_2 | J M \rangle = (-1)^{-j_1+j_2-M} \sqrt{2J+1} \begin{pmatrix} j_1 & j_2 & J \\ m_1 & m_2 & -M \end{pmatrix}. \quad (3.69)$$

For (3.71) this leads to

$$\begin{aligned} C_{lm10}^{l'm} C_{l'010}^{l0} &= (-1)^{-m} \sqrt{(2l'+1)(2l+1)} \begin{pmatrix} 1 & l' & l \\ 0 & m & m \end{pmatrix} \begin{pmatrix} 1 & l & l' \\ 0 & 0 & 0 \end{pmatrix} \\ &\xrightarrow{\text{for } l, l' \gg 0} (-1)^{l+l'} d_{0, l-l'}^1(\pi/2) d_{0, l'-l}^1(\pi/2) \end{aligned} \quad (3.70)$$

where we used that $\alpha = \pi/2$ for both terms. Since the Clebsch-Gordan coefficients allow only $l - l' = \pm 1$ and $d_{0, \pm 1}^1(\pi/2) d_{0, \mp 1}^1(\pi/2) = 1/2$ this leads to the desired relation. For (3.72) this derivation proceeds analogously, with the difference that $d_{0, \pm 2}^2(\pi/2) d_{0, \mp 2}^2(\pi/2) = 3/8$ and $d_{0, \pm 2}^2(\pi/2) d_{0, \mp 2}^2(\pi/2) = 3/8$ and $d_{0, 0}^2(\pi/2) d_{0, 0}^2(\pi/2) = 1/4$, which in total leads to the desired result.

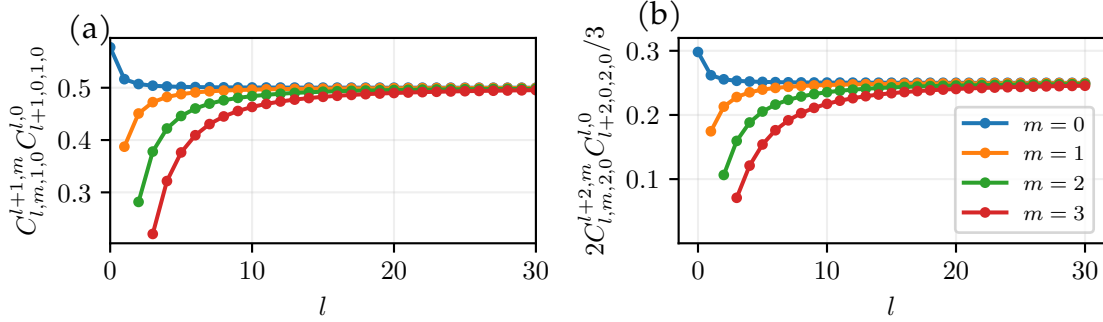
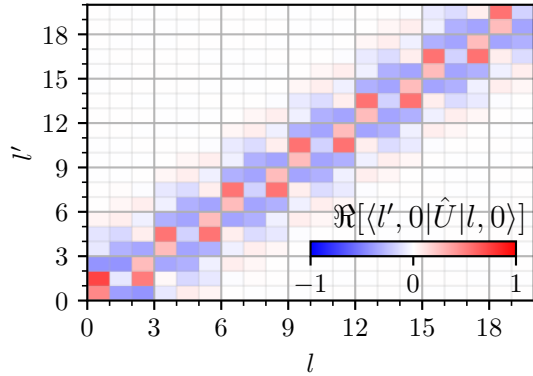


Figure 3.11: Convergence of the off-diagonal Matrix elements. Here we demonstrate that the products of Clebsch-Gordon coefficients that define the relevant transition matrix elements of a laser kick convergence fast for $l \gg 0$ for different m quantum number. (a) for $\cos(\hat{\theta})$ potential, (b) $\cos^2(\hat{\theta})$ potential.

Figure 3.12: One-period time-translation operator for a 3D rotor. Here we show the matrix elements for the time-translation operator with $U = e^{-i2\pi\hat{L}^2/3}e^{-i\hat{V}}$ and $\hat{V} = P_1 \cos(\hat{\theta}) + P_2 \cos^2(\hat{\theta})$ at $P_1 = 1, P_2 = 2, m = 0$. We observe that there is a periodicity of $N = 3$, as we expected, and the deviations around $l = 0$ are very small and barely visible.



well-approximated by assuming constant values for these matrix elements. Even more remarkably, we recover the periodicity from (3.36) that ensures the validity of the Fourier analysis.

Fig. 3.12 illustrates the matrix elements of the time-translation operator for the three-dimensional rotor under a kick described by $U = e^{-2\pi i \hat{L}^2/3} e^{-i \hat{V}}$. Two crucial features emerge from this analysis: First, we observe the expected periodicity of $N = 3$, with deviations near $l = 0$ being remarkably small and barely visible. Second, the rapid convergence of matrix elements, anticipated by (3.71)

and (3.72), is clearly manifest. The matrix structure revealed in Fig. 3.12 suggests that despite the apparent complexity of three-dimensional rotation, the essential physics can be captured by a relatively simple effective model.

Building on our previous analysis, let us now examine the quasi-energies and Floquet states of a periodically driven 3D rotor with $N = 3$ and $m = 0$. Fig. 3.13 shows the results of exact diagonalization, using parameters similar to those that generated the matrix elements in Fig. 3.12. A comparison between real-space and momentum-space diagonalization shows close to perfect agreement for the bulk spectrum and the corresponding Floquet states. Crucially, the real-space method reveals edge states at both boundaries that are inherently absent in the Fourier analysis, as the latter assumes an infinite system. These edge states exhibit exponential decay in angular momentum space.

3.5.2 Anderson wall

While an ideal 3D rotor exhibits the energy spectrum $E_{\text{rot}} = Bl(l+1)$, allowing for driving at quantum resonances, any deviation from a perfect rigid rotor modifies this relation. A prominent example is the centrifugal distortion in non-rigid rotors, which introduces an additional term³⁰

$$\Delta E = D(l(l+1))^2 \tag{3.73}$$

where D is the centrifugal distortion constant. As evident from Table 3.1, D is typically much smaller than the rotational constant B , making this correction negligible for small l [171]. However, its significance grows with increasing l , eventually destroying the N -periodicity of the system. This occurs because the system now exhibits two typically incommensurate timescales, making the resonance condition impossible to satisfy (unless B were an exact multiple of D , which is highly improbable).

³⁰For a detailed derivation, see Sec. 1.1.1 in [171].

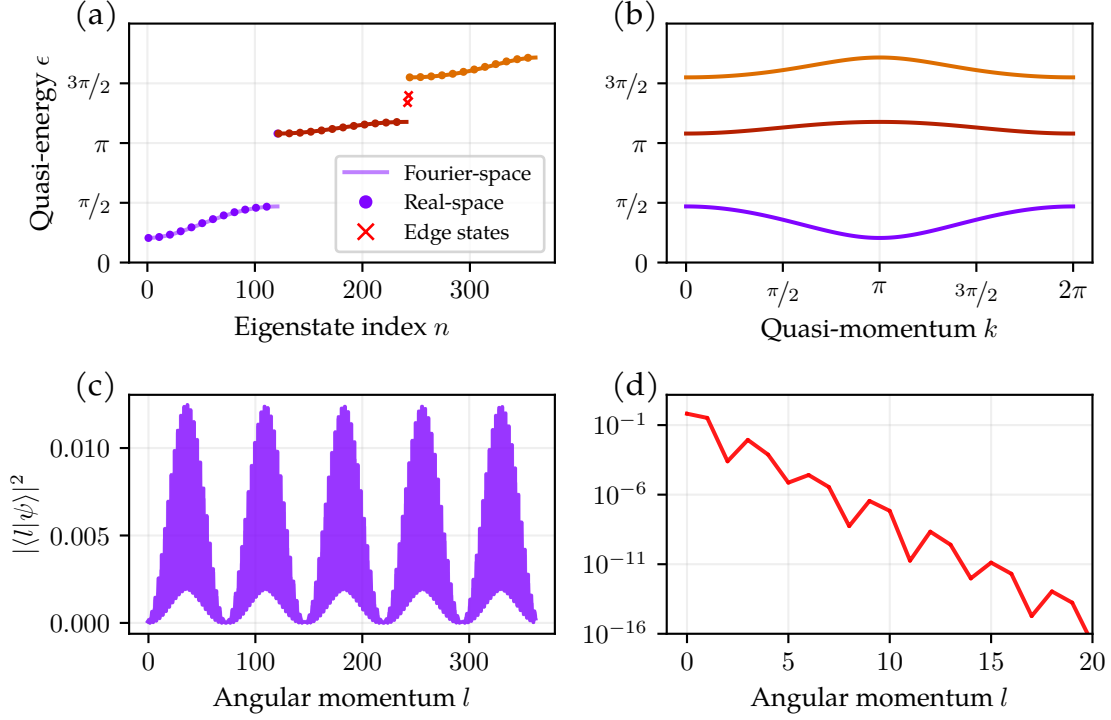


Figure 3.13: Exact diagonalization of the N=3 band model for the driven 3D rotor. (a) Comparison between real-space (dotted) and Fourier-space (solid line) diagonalization at $P_1 = 1, P_2 = 2$. While the bulk spectra show nearly perfect agreement, the real-space calculation reveals additional edge states (red crosses) absent in the Fourier analysis. (b) Spectrum in Fourier space as a function of quasi-momentum k . (c) Representative bulk state wavefunction from real-space diagonalization. (d) Edge state wavefunction showing exponential localization in angular momentum space.

This phenomenon, first identified in [176] and termed the *Anderson wall*, implies that the resonance condition holds only approximately up to some critical momentum l_{\max} . Defining the ratio $g = D/B$, we can approximate this critical angular momentum as³¹

$$l_{\text{crit}} = r/\sqrt[3]{g} \quad (3.74)$$

where r is a constant determined by the acceptable magnitude of

³¹This approximation follows from analyzing the zeros of the tangent function in the tight-binding Hamiltonian derivation from Section 3.4, see [176].

3. LATTICES OF ANGULAR MOMENTUM

deviation. To quantify r , we define a unit-cell matrix norm deviation

$$\Delta U(l) = \frac{1}{N^2} \sum_{\sigma, \sigma'=1}^N |U_{l+\sigma, l+\sigma'} - U_{l+\sigma, l'+\sigma'}|^2. \quad (3.75)$$

Setting a threshold of $\Delta U(l) > 0.1$ yields $r \approx 0.36$, which agrees well with numerical time-evolution simulations of wavepackets which show a change of behavior at that angular momentum (see Fig. 3.14). The results confirm the inverse cubic scaling predicted by Eq. (3.74). The physical manifestation of this effect is striking: without cen-

Molecule	t_{rev} (ps)	$g \cdot 10^6$	Estimated l_{crit}
H ₂	0.281	794	~4
N ₂	8.383	2.90	~25
Cl ₂	68.57	0.765	~39
ICl	146.4	0.354	~51
CO ₂	42.74	0.343	~51
Br ₂	203.5	0.255	~57
OCS	82.22	0.214	~60
I ₂	447.0	0.107	~77

Table 3.1: Effects of centrifugal distortion. Revival times ($t_{\text{rev}} = \pi\hbar/B$), ratio of centrifugal distortion to rotational constants ($g = D/B$), and estimated $l_{\text{crit}} \approx r/\sqrt[3]{g}$ values for various linear molecules, see (3.74). Values of molecules taken from [176].

trifugal distortion, we expect ballistic spreading of the wavefunction. With distortion, this ballistic spread persists only up to l_{crit} , beyond which localization occurs. This effectively creates a finite-size system bounded by $l = 0$ and $l = l_{\text{crit}}$, with wavepacket reflections occurring at both boundaries. For practical purposes, we can set $l_{\text{max}} = l_{\text{crit}}$ and restrict our analysis to $l < l_{\text{crit}}$, as the regime beyond this threshold is only accessible through specific driving protocols, such as high-intensity pulses. Now, having a finite lattice will also lead to a partial failure of the quasi-momentum description. Let us look at this in more detail.

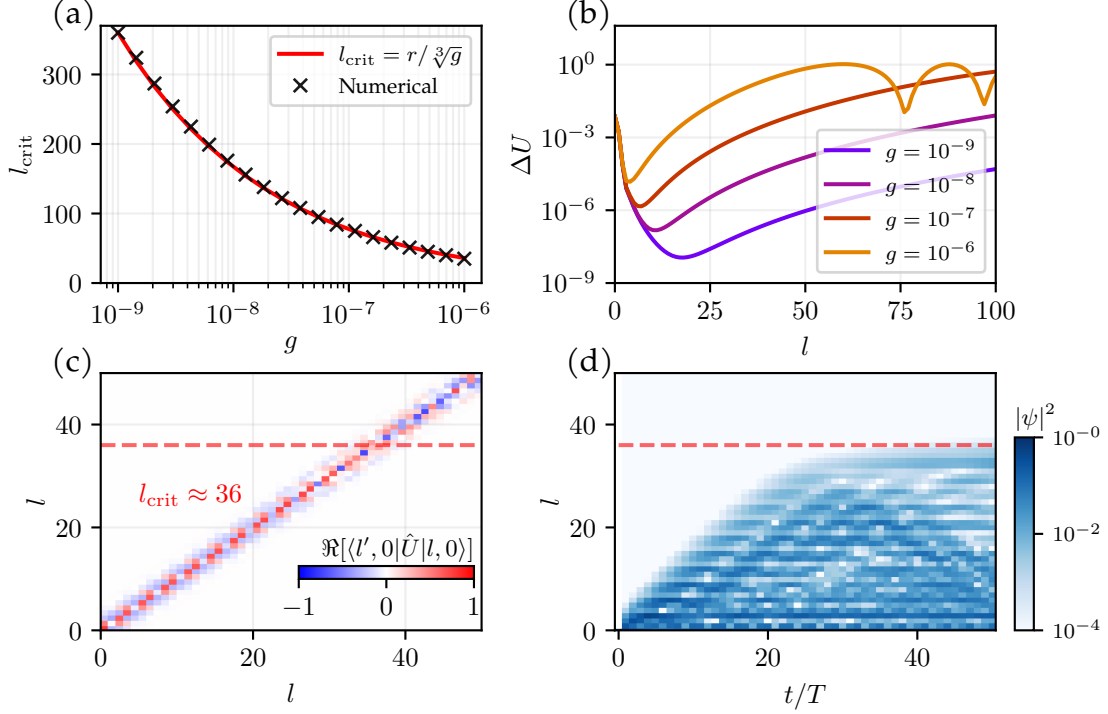


Figure 3.14: Analysis of centrifugal distortion effects in a 3D rotor. Results shown for $P_1 = P_2 = 1$. (a) Critical angular momentum evaluated using the criterion $\Delta U(l) > 10^{-1}$ (Eq. (3.75)) with $r = 0.36$. (b) Matrix norm deviations for various g values. (c) Representative matrix for $g = 10^{-6}$. (d) Exact time-evolution of a wavepacket initially in the rotational ground state at $g = 10^{-6}$.

3.5.3 Limitations of the quasi-momentum description

While not visible in the spectrum, the boundaries at $l = 0$ and $l = l_{\text{max}}$ lead to deviations in the eigenstates of the Hamiltonian. The *fundamental sampling theorem*, as established by Shannon and Nyquist [177], becomes particularly relevant when transforming finite real-space lattice configurations to momentum space and vice versa. For example, the phenomenon of *aliasing* manifests when attempting to represent high-momentum components of wavefunctions, particularly near the Brillouin zone boundaries, leading to spurious folding of bands [178].

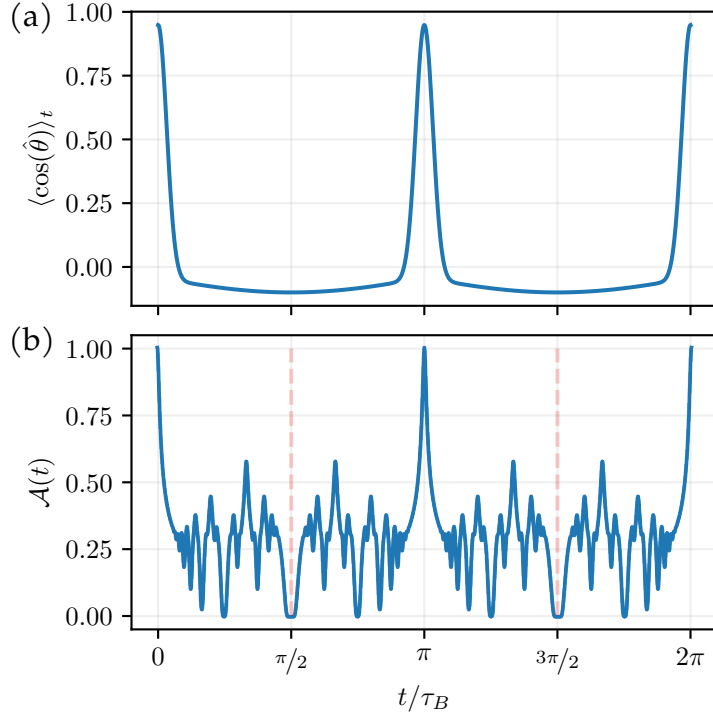
Another aspect is *spectral leakage* [179], which is an issue for all kinds of discrete Fourier transforms and becomes particularly relevant when dealing with localized states. Namely, when the spatial extent of a wavefunction does not perfectly match the periodic boundary conditions, energy contributions can "leak" across multiple k -points. This is why it is important to fine-adjust the Fourier transform parameters (in particular the center in (3.39), which corresponds to the point where we define $n = 0$). Here, the choice of window functions could be another way to approach this issue. However, while windows like Hamming or Blackman can reduce spectral leakage, they simultaneously modify the real-space structure of the wavefunctions [179]. For tight-binding calculations, this introduces artificial spatial correlations that must be carefully accounted for in any physical observable calculations. In this work, we do not use window functions, and instead outline the problems with finite size effects. Edge effects become particularly relevant when studying systems when we investigate the topological edge states.

Then, a challenge is *phase unwrapping*, which emerges when calculating Berry phases or analyzing topological properties of bands. The discrete sampling in momentum space can lead to ambiguities in determining the continuous evolution of wavefunctions across the Brillouin zone, particularly near band degeneracies or touching points [180]. This is particularly important for $k \approx 0$, which corresponds to the infinite wavelength limit and can thus not be resolved in a finite lattice. This will become important in Section 4.4.1, where we use quasi-momentum Floquet states in order to analyze the real-time evolution of a rotating molecule.

3.5.4 Quantum revival pattern for symmetric tops

The quantum dynamics of the 3D rotor exhibits markedly different behavior from its 2D counterpart, primarily due to the distinct phase accumulation described in (3.67) and the restriction to non-negative

Figure 3.15: Revivals of the 3D rotor in a gaussian state. (a) Orientation signal for a gaussian state $\psi(t=0) \propto e^{-\beta l(l+1)^2}$ with $\beta = 10^{-2}$. (b) Autocorrelation function $\mathcal{A}(t)$ of the same state. Unlike the 2D rotor, there is a *grand revival* already at $t = \pi\tau_B$. At $t = \pi\tau_B/2$, we find the anti-revival with zero overlap of the wavepacket with its initial state.



angular momentum quantum numbers ($l \geq 0$). These fundamental differences manifest most clearly in the revival structure, which we previously examined for the 2D case in Fig. 3.2. While the 2D rotor exhibits a revival time of $t_{\text{rev}} = 2\pi$, the revival time of a symmetric top is halved to $t_{\text{rev}} = \pi\tau_B = \pi/B$. This characteristic behavior is demonstrated in Fig. 3.15, where we analyze the evolution of a Gaussian initial state. The revival dynamics can be categorized into three distinct scenarios, each corresponding to different types of kicks. Fig. 3.16 illustrates the case of a pure orientation kick ($P_2 = 0$), revealing a simpler revival structure compared to the 2D rotor. The most striking feature is the appearance of a complete anti-revival at $t = \pi\tau_B/2$, where the wavepacket shows zero overlap with its initial state. This phenomenon, absent in the 2D case, arises from the additional symmetries of the 3D rotation group. For alignment kicks, shown in Fig. 3.17, we observe a more complex revival pattern.

3. LATTICES OF ANGULAR MOMENTUM

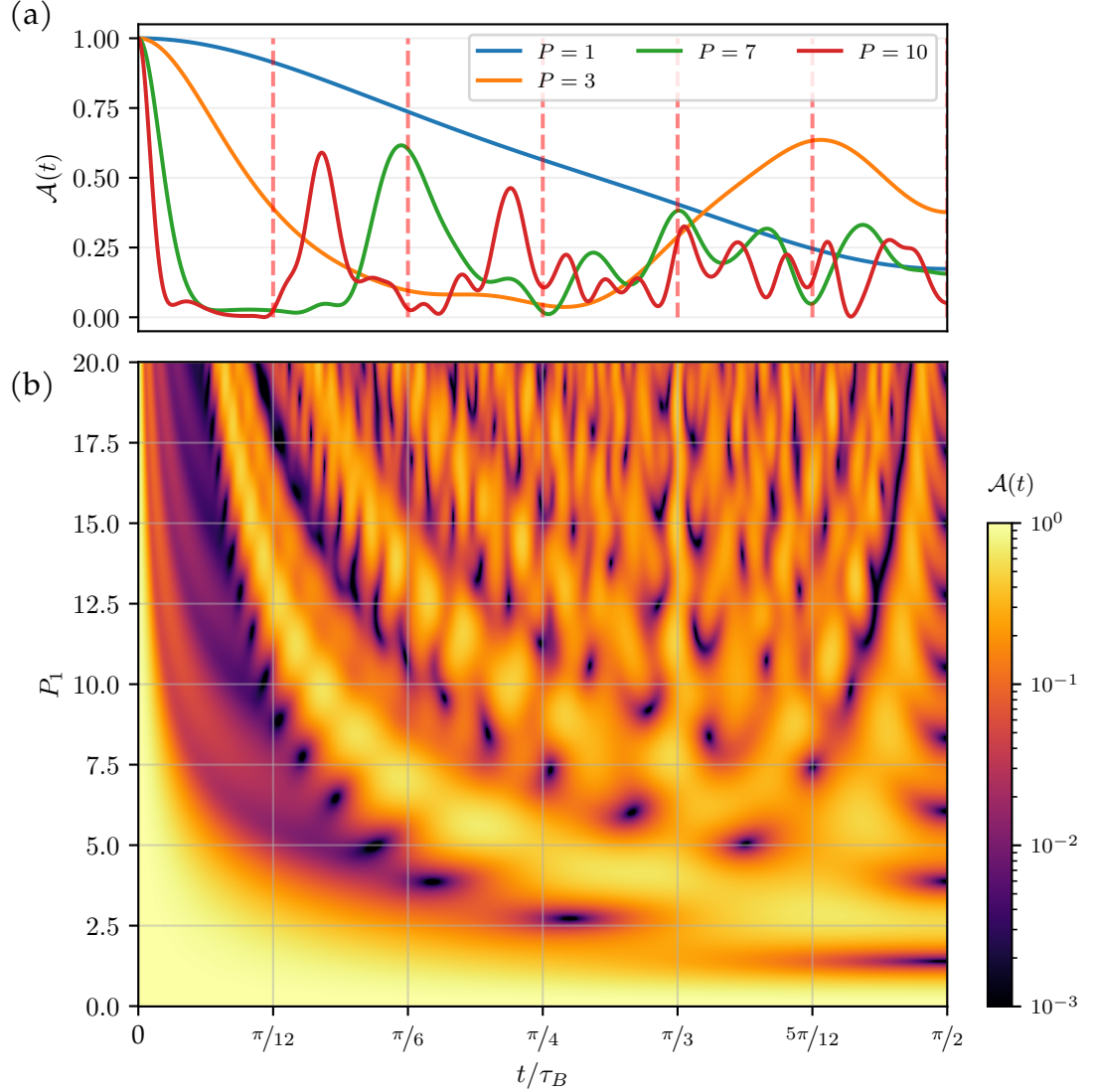


Figure 3.16: Fractional revival pattern for the 3D rotor following a single orientation kick. (a) As in Fig. 3.2, the autocorrelation function $\mathcal{A}(t) = |\langle \psi(t) | \psi(0) \rangle|^2$. The plot is restricted to $0 \leq t/\tau_B \leq \pi/2$ due to symmetry around $t = \pi/2$. (b) Heatmap visualization of $\mathcal{A}(t)$. There are no consistent revivals except at $t = \pi\tau_B$, but characteristic low overlap at $t = \pi/2$ (for $P \gg 0$).

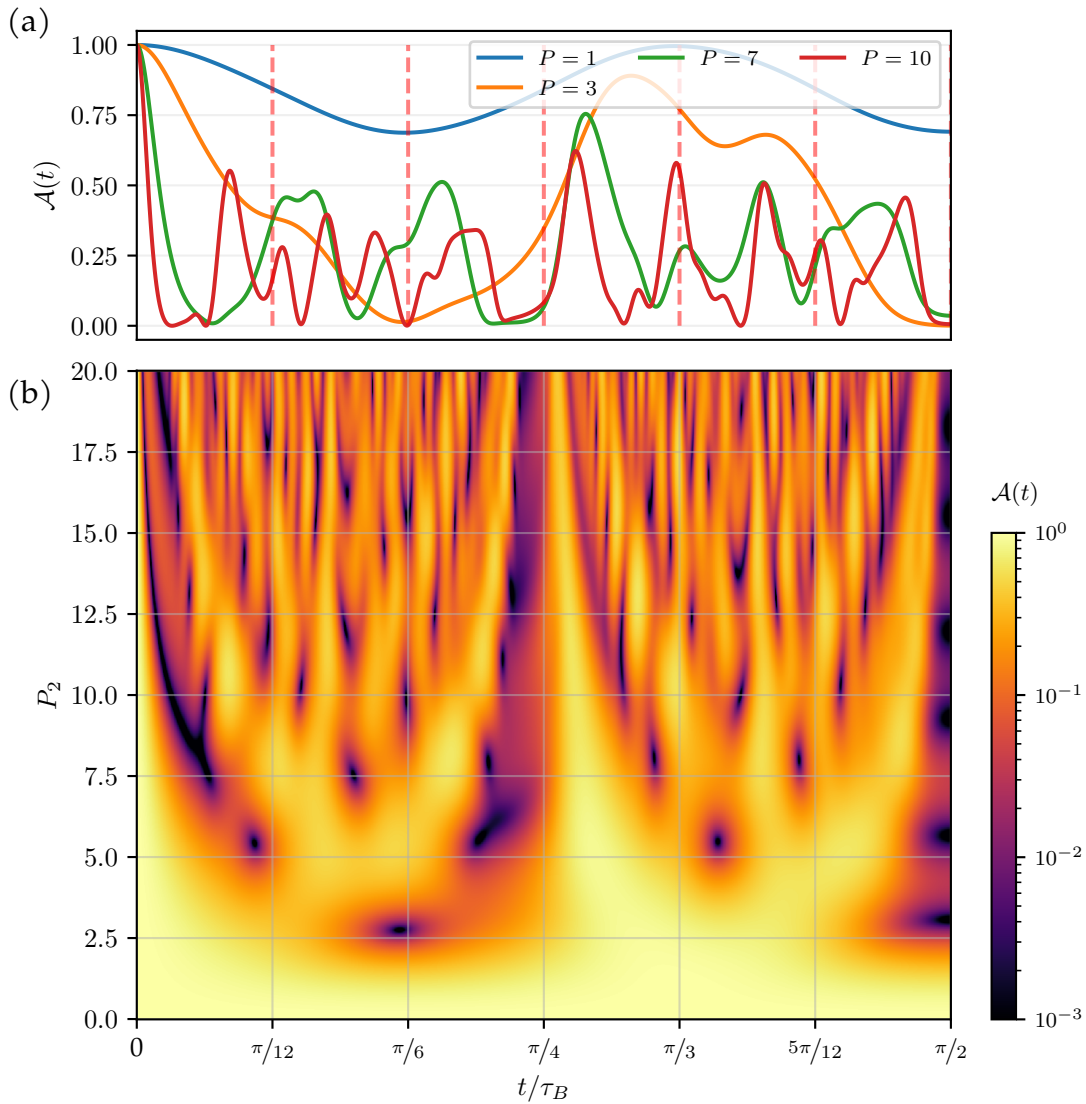


Figure 3.17: Fractional revival pattern for the 3D rotor following a single alignment kick. Similar as in Fig. 3.16. (a) Autocorrelation function $\mathcal{A}(t) = |\langle \psi(t) | \psi(0) \rangle|^2$ and (b) Heatmap visualization the same function for various times t and kicking strengths P . As in for the orientation kick, there is a consistently small autocorrelation function at $t = \tau_B \pi/2$, indicating the anti-resonance. In between, there is a complex revival structure that depends on both kicking strength and time t .

3. LATTICES OF ANGULAR MOMENTUM

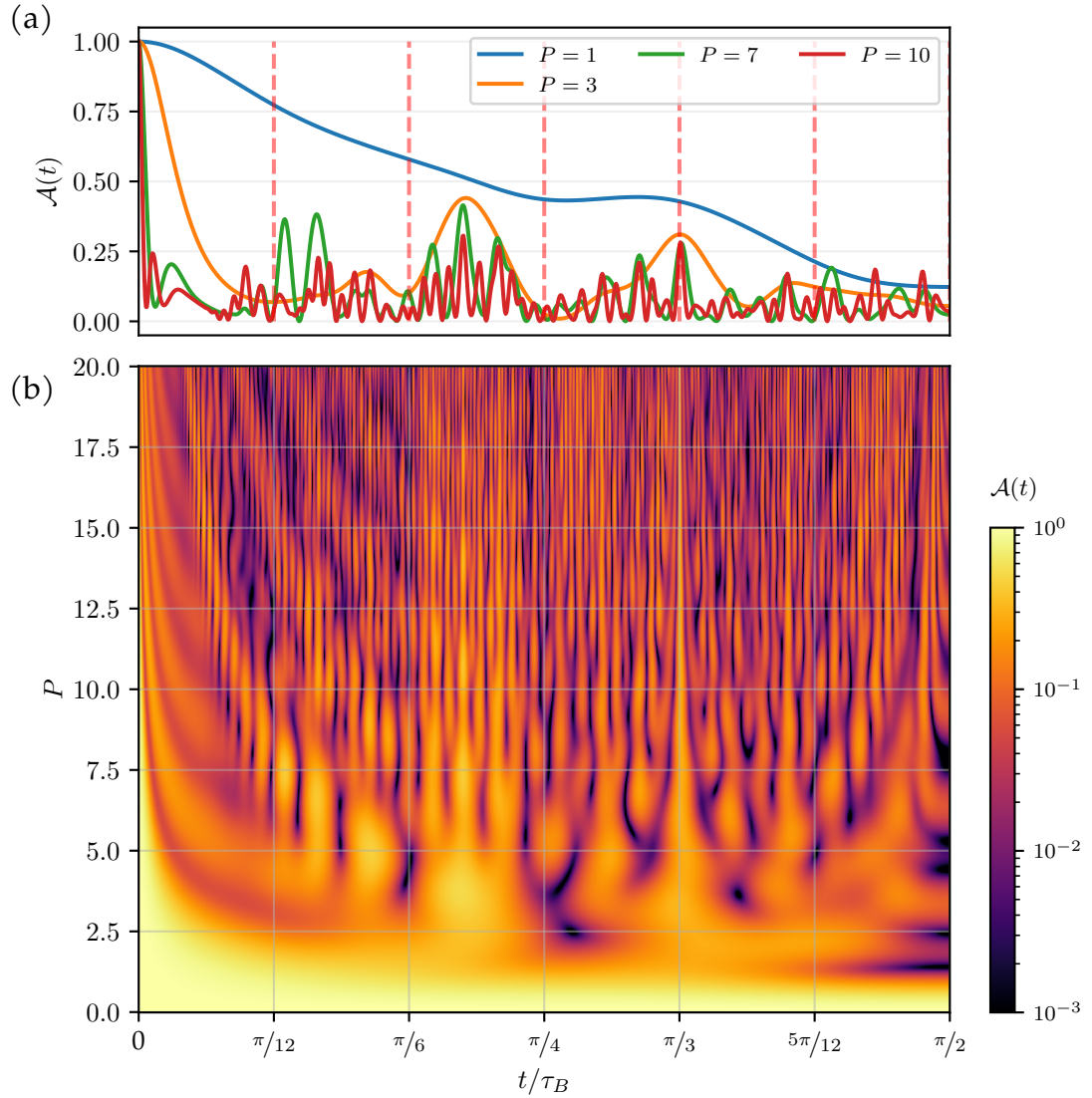


Figure 3.18: Fractional revival pattern for the 3D rotor following a single generic kick. Here we consider a kick with both $P = P_1 = P_2$. (a) Autocorrelation function $\mathcal{A}(t) = |\langle \psi(t) | \psi(0) \rangle|^2$ and its (b) Heatmap visualization as a function of both time t and kicking strength P . We observe consistently low overlap for a wide range of parameters, with many branchings. Unlike the other two cases before, the combination of both an alignment and orientation kick leads to a suppressed phase coherence. Even more surprising it is that after $t = \pi\tau_B$ there will be perfectly revival.

While maintaining the anti-resonance at $t = \pi\tau_B/2$, the intermediate revival structure exhibits rich dynamics that strongly depend on the kick strength P_1 . The branching patterns visible in the heatmap reveal the interplay between the pulse and the rotational degrees of freedom unique to the 3D rotor. Perhaps most intriguingly, Fig. 3.18 presents the case of simultaneous orientation and alignment kicks ($P = P_1 = P_2$). This configuration leads to a surprising suppression of phase coherence across a wide parameter range, manifesting as consistently low overlap values. The complex branching structure in the heatmap suggests a highly non-trivial interplay between the different angular momentum states. Remarkably, despite this apparent chaos, clearly the system still achieves perfect revival at $t = \pi\tau_B$.

3.6 Outlook

With these findings, we conclude our analysis of driven quantum rotors. We established how quantum resonances emerge from the interplay between driving period and rotational revival time—a crucial foundation for what follows. The rich structure of dynamical regimes we uncovered, from perfect transport to complete freezing, reveals striking parallels with condensed matter physics, but now manifesting in angular momentum space rather than position space. As we will see in the next chapter, these dynamics, combined with the symmetries of our Floquet states and their band structure, provide the essential building blocks for understanding topological phenomena in driven quantum rotors.

CHAPTER 4

Geometric phases of driven rotors

In science we like to emphasize the novelty and originality of our ideas. This is harmless enough, provided it does not blind us to the fact that concepts rarely arise out of nowhere. There is always a historical context, in which isolated precursors of the idea have already appeared. What we call "discovery" sometimes looks, in retrospect, more like emergence into the air from subterranean intellectual currents.

– Michael Berry

4.1 Overview

As demonstrated in the previous Chapter, periodic driving can shape the time-evolution of quantum rotors. Section 3.3.6 revealed that quantum resonances enable the engineering of band models with an arbitrary number of bands N ¹. These quantum resonances generate one-dimensional stroboscopic Hamiltonians of the form

$$H_k(P) = \mathbf{d}_k(P) \cdot \Gamma$$

¹While higher-order resonances require considerably longer time evolution to resolve the characteristics of the band model (see Fig. 3.7), $N \gg 2$ remains within experimental reach.

with the generalized Gell-Mann matrices Γ_i of the $\mathfrak{su}(N)$ algebra, the pseudo-momentum k from Section 3.3.2, and $\mathbf{d}_k \in \mathbb{R}^{N^2-1}$. This formulation provides some insight into the dynamics of a rotor after consecutive pulses. By modulating the kicking parameters with each pulse, we can engineer higher-dimensional lattices in synthetic dimensions. Beyond its intrinsic interest for quantum simulation of lattice models and probing quench dynamics of non-trivial states, this approach offers a method for adiabatic preparation, manipulation, and probing of angular momentum states.

Returning to Section 1.2, we argued that topological properties emerge from the geometry of the wavefunctions rather than specific material details. Given the flexibility in engineering lattice models within our framework, we now investigate whether these models can exhibit non-trivial topological properties analogous to those of topological insulators in real materials. Section 4.2 establishes how topological physics emerges from fundamental matrix properties, which is developed through several steps: Section 4.2.1 examines the fundamental origin of geometric phases. Section 4.2.3 explores how symmetries generate topologically protected gapless phases, whose classification extends beyond that of gapped phases. Section 4.2.4 presents the bulk-boundary correspondence, linking topological invariants to non-trivial boundary eigenstates. Section 4.2.5 addresses topological physics in non-hermitian systems, crucial for our strongly-driven, non-energy-conserving system, extending beyond conventional hermitian matter classification.

Building on these foundations, Section 4.3 examines periodically driven rotors. The previously identified symmetries generate topological charges manifesting as Dirac cones. These cones influence the quantum dynamics of the rotor through Landau-Zener transitions and, notably, give rise to topologically protected edge states, as predicted by the bulk-boundary correspondence. Section 4.2.4 traces their emergence and establishes their connection to topological invariants. Section 4.4 explores the translation of topological invariants

into measurable observables, focusing particularly on orientation and alignment signals.

4.2 Geometric phases

The elegance of geometric phases unfolds from a surprisingly simple origin - as Berry showed, even a simple 2x2 matrix contains all the essential physics [82]. Consider the Hamiltonian²

$$H = \begin{pmatrix} E_0 + \Delta & v \\ v & E_0 - \Delta \end{pmatrix}, \quad (4.1)$$

where $E_0, \Delta, v \in \mathbb{R}$. The eigenvalues of H are $E_{\pm} = E_0 \pm r$ with $r = \sqrt{v^2 + \Delta^2}$. A degeneracy occurs at $v = \Delta = 0$, forming a nodal point³ in the (v, Δ, E_0) parameter space (Fig. 4.1 (a)). The normalized eigenvectors take the form

$$|\psi_{\pm}\rangle = \frac{1}{\sqrt{2r(r \pm \Delta)}} \begin{pmatrix} \Delta \pm r \\ v \end{pmatrix} \quad (4.2)$$

with a $U(1)$ gauge freedom $|\psi_{\pm}\rangle \rightarrow e^{i\phi}|\psi_{\pm}\rangle$ that underlies the subsequent phenomena. Consider a circular path of the eigenstate $|\psi_{+}\rangle$ encircling the degeneracy point. Using polar coordinates, we express $v = r \sin k$ and $\Delta = r \cos k$, transforming the eigenstates to⁴

$$|\psi_{+}\rangle = \frac{1}{\sqrt{1 + \cos(k)}} \begin{pmatrix} 1 + \cos k \\ \sin k \end{pmatrix} = \text{sign}[\cos(k/2)] \begin{pmatrix} \cos(k/2) \\ \sin(k/2) \end{pmatrix}. \quad (4.3)$$

This parametrization is discontinuous at $k = \pi$ where $|\psi_{+}\rangle \rightarrow -|\psi_{+}\rangle$. While multiplying by $\text{sign}[\cos(k/2)]$ yields a smooth parametrization,

²This choice of coordinate system (E_0, v, Δ) exemplifies the general case for matrices with symmetries. Adding complex phases on the off-diagonal let us reach the space of all hermitian matrices, but breaks the necessary symmetry, as will be shown later.

³With nodal point we refer from now to a degeneracy of the eigenvalues. Conversely, a nodal line is a 1-dimensional subspace where (at least) a pair of eigenvalues are degenerate.

⁴Using the identities $1 + \cos(k) = 2 \cos^2(k/2)$ and $\sin(k) = 2 \sin(k/2) \cos(k/2)$.

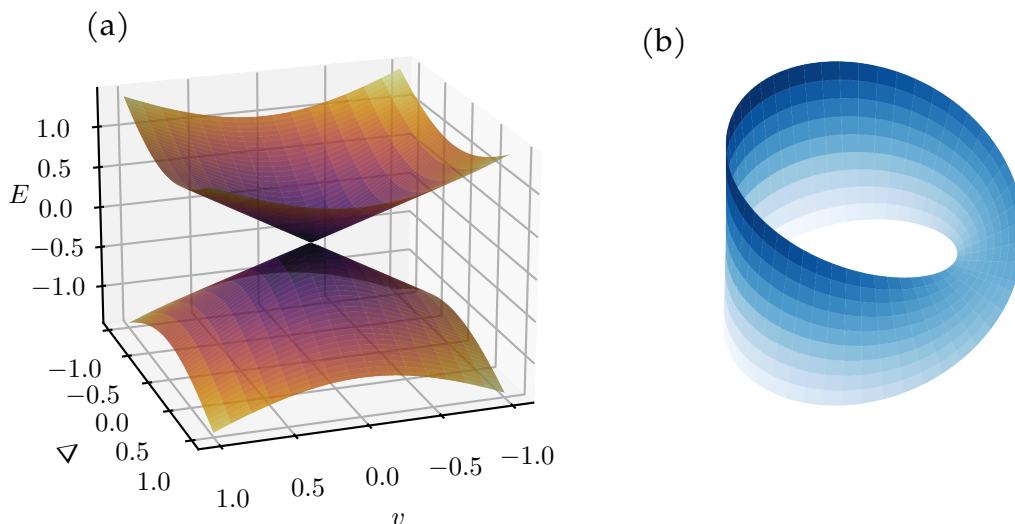


Figure 4.1: Degeneracy and Möbius strip. (a) Linear degeneracy of the energies from (4.1) (b) Möbius strip as an example of a non-orientable surface.

the wavefunction becomes periodic only over $k \in [0, 4\pi]$. Remarkably, no gauge choice enables smooth behavior within $k \in [0, 2\pi]$. Upon completing one circuit, the wavefunction inevitably undergoes a sign inversion: $|\psi_+(0)\rangle = -|\psi_+(2\pi)\rangle$. This sign inversion reveals that $|\psi_+\rangle$ cannot be defined as a continuous, single-valued function over the circle S^1 in the parameter space (v, Δ) without encountering a discontinuity. The nodal line $(v, \Delta, E_0) = (0, 0, E_0)$ represents a singularity where eigenvalues become degenerate and eigenstates are arbitrary. This topological structure parallels the Möbius strip (Fig. 4.1), where traversing the base space once results in a twist⁵.

⁵In differential geometric terms, $\psi_+(k)$ forms a section of a fiber bundle over S^1 . This line bundle, where each fiber contains the eigenstate at a point on S^1 , is nontrivial due to the impossibility of globally defining ψ_+ without discontinuity. The nontrivial line bundle over S^1 is characterized by its first Stiefel-Whitney class [172].

4.2.1 Berry Phase

A deep connection exists between the inability to define a smooth wavefunction on $k \in [0, 2\pi]$ and the phases acquired during adiabatic evolution [76]. To explore this connection, consider a Hamiltonian $H(\mathbf{x})$ dependent on parameters \mathbf{x} . For slowly varying parameters, the instantaneous eigenstates $|\psi(\mathbf{x})\rangle$ and energies $E(\mathbf{x})$ evolve adiabatically according to

$$|\Psi(t)\rangle = e^{i\alpha(t)}|\psi(\mathbf{x}(t))\rangle, \quad (4.4)$$

where $\alpha(t)$ represents the acquired phase. The time-dependent Schrödinger equation $i\partial_t|\Psi(t)\rangle = H(\mathbf{x}(t))|\Psi(t)\rangle$ must be satisfied. Hence, substituting the adiabatic wavefunction and applying the chain rule yields

$$\partial_t\alpha(t) = A_j(\mathbf{x})\frac{\partial\mathbf{x}^j}{\partial t} - E(\mathbf{x}(t)) \quad (4.5)$$

where $A_j(\mathbf{x})$ denotes the *Berry connection* [121]

$$A_j(\mathbf{x}) = i\langle\psi(\mathbf{x})|\nabla|\psi(\mathbf{x})\rangle. \quad (4.6)$$

For sufficiently slow adiabatic evolution along a closed path, the dynamical phases integrate to zero, leaving only the geometric phase, known (among other names, see Section 1.2) as the *Berry phase*

$$\gamma = \oint A_j(\mathbf{x}(t))\frac{\partial\mathbf{x}^j(t)}{\partial t}dt \equiv \oint A_j(\mathbf{x})d\mathbf{x}^j. \quad (4.7)$$

Note that this is actually the proper definition of a line integral, and it exhibits the fundamental properties that are known from classical mechanics [15]. In particular, the parametrization independence reflects that only the path matters, not the rate of traversal. Even more so, the gradient theorem implies that a non-zero geometric phase indicates a non-conservative force field. By the fundamental theorem of vector calculus, every differentiable vector field decomposes into

4. GEOMETRIC PHASES OF DRIVEN ROTORS

irrotational and solenoidal components. In three dimensions⁶, the *Helmholtz decomposition* gives

$$\mathbf{F}(\mathbf{x}) = -\nabla\phi(\mathbf{x}) + \nabla \times A(\mathbf{x}) \quad (4.8)$$

with scalar potential $\phi(\mathbf{x})$, a vector potential $A(\mathbf{x})$ and the field strength $\mathbf{F}(\mathbf{x})$. The Berry connection thus represents the solenoidal component⁷. Returning to (4.1), we can resolve the smoothness problem in (4.2) by choosing the gauge $|\psi_{\pm}\rangle = e^{ik/2}(\cos(k/2), \sin(k/2))^T$. This smooth interpolation allows calculation of the Berry phase

$$\gamma_{\pm} = \frac{1}{2\pi} \int_0^{2\pi} A_{\pm}(k)dk = \pm\frac{1}{2} \quad (4.9)$$

where $A_{\pm}(k) = i\langle\psi_{\pm}(k)|\partial_k\psi_{\pm}(k)\rangle$. The degeneracy at $r = 0$ quantizes this phase⁸. This concept generalizes to arbitrary state spaces and parameter dimensions. The profound insight lies in extracting topological properties from integration of local quantities [76]. This connection between geometry and topology is far from trivial and will be explored in more detail in the next Section. Here, the quantization emerges from symmetry – specifically, the Hamiltonian degeneracy in the $\Delta - v$ plane for all E_0 – which prevents smooth deformation between loops encircling and avoiding the singularity. Thus, the geometric phase is protected by symmetry.

But what is the geometric interpretation for the topology of a 2x2 Hamiltonian (4.1) and how can we understand this in a more general

⁶This generalizes to complex vector fields in arbitrary dimensions through the Hodge decomposition for differential forms on Riemannian manifolds, where any differential form uniquely decomposes into exact, co-exact, and harmonic components [172].

⁷In differential geometry, vector fields correspond to differential *1-forms*. Conservative fields correspond to *exact 1-forms* $d\phi$, while irrotational fields correspond to *closed 1-forms* ω where $d\omega = 0$. The property $d^2 = 0$ ensures every exact form is closed, hence every conservative field is irrotational. For simply connected domains, every closed 1-form is exact [172].

⁸The gauge factor $e^{ik/2}$ proves crucial; without it, the connection would be flat. The central singularity transforms the topology from that of a flat space, previously evident only through the sign function.

framework? The answer lies in examining the space that eigenvalues and eigenvectors of matrices form. Consider a diagonalizable square matrix $H(\mathbf{x}) \in \mathbb{C}^{N \times N}$ that depends on parameters \mathbf{x} . Clearly, the eigenspaces are determined by the zeros of the characteristic polynomial $f_H(\lambda)$

$$f_H(\lambda, \mathbf{x}) = \det(H(\mathbf{x}) - \mathbb{I}\lambda) \quad (4.10)$$

with eigenvalue λ . The eigenvalues define the level sets $\mathcal{M} = f^{-1}(0)$ ⁹, forming a manifold with potentially non-trivial topology. While the matrix structure is linear, the manifold can exhibit rich non-linear features, including curvature and holes. We can characterize the tangent space of this manifold \mathcal{M} through the *implicit function theorem*¹⁰

$$\frac{\partial \lambda(\mathbf{x})}{\partial x_j} = - \left[\frac{\partial f_A(\lambda, \mathbf{x})}{\partial \lambda} \right]^{-1} \frac{\partial f_A(\lambda, \mathbf{x})}{\partial x_j}. \quad (4.11)$$

This formulation will prove invaluable when we employ it as a method of continuation for nodal lines. From a broader perspective, this framework provides a universal approach to understanding topological phase transitions through eigenvalue degeneracies.

Following our discussion in Section 1.2, we can draw a parallel with electrodynamics. Let us look the two-level system as a spin, expressing the Hamiltonian (up to the constant E_0) as

$$H = \Delta \sigma_z + v \cdot \sigma_x = \mathbf{B} \cdot \boldsymbol{\sigma} \quad (4.12)$$

where we identify an effective magnetic field $\mathbf{B} = (v, 0, \Delta)$. This Hamiltonian anti-commutes with σ_y , namely $\sigma_y H \sigma_y = -H$ ¹¹, a

⁹Note that here we really mean $f(\lambda, \mathbf{x}) = 0$, hence the solution of inverse f^{-1} at 0.

¹⁰This holds for some \mathbf{x} with $f_A(\lambda, \mathbf{x}) = 0$, provided $\frac{\partial f_A}{\partial x_j} \neq 0$. In this case, small neighborhoods around \mathbf{x} lead to well-defined flows. Special care must be taken at saddle points and other critical points [181].

¹¹We note that any two Pauli matrices could be chosen, leading to a chiral symmetry of the third matrix. Indeed, we can rotate in that space and select a quantization plane where the geometric phase counts the number of windings around the singularity. This holds even for complex coefficients \mathbf{d} , but departing from the plane breaks the quantization, allowing γ to take any real value [71]

property known as chiral symmetry. This symmetry ensures a $\mathbb{Z}/2$ -valued winding number (the geometric phase) in odd dimensions [71]. The introduction of a σ_y term would break this chiral symmetry, enabling the adiabatic transformation of a loop encircling the singularity into one that does not, thus lifting the quantization condition. However, from electrodynamics we know of a different topological invariant which holds even for systems without symmetries: the charge.

4.2.2 Magnetic monopoles

There are many ways to introduce Chern numbers. Here, we consider an analogy to classical electrodynamics, where we encounter the $U(1)$ gauge symmetry from before. This symmetry manifests through the four-potential \mathcal{A}_μ , a covariant object that unifies the scalar potential ϕ and the vector potential \mathbf{A} . The physical electromagnetic fields emerge from the electromagnetic field tensor [87]

$$\mathcal{F}_{\mu\nu}(x) = \partial_\mu \mathcal{A}_\nu(x) - \partial_\nu \mathcal{A}_\mu(x), \quad (4.13)$$

a covariant tensor defined in arbitrary dimensions¹² for $x \in \mathbb{R}^{d+1}$. The form of this tensor arises from two fundamental principles: gauge invariance and Lorentz invariance. Under gauge transformations, the potential transforms as

$$\mathcal{A}_\mu(x) \rightarrow \mathcal{A}_\mu(x) + \partial_\mu \chi(x), \quad (4.15)$$

with an arbitrary scalar function $\chi(x)$. The anti-symmetric structure of $\mathcal{F}_{\mu\nu}$ ensures invariance under these transformations, as the partial

¹²In 3+1 dimensions, the spatial components $\mathbf{F} = \nabla \times \mathbf{A}$ in the absence of a source field ϕ correspond exactly to the magnetic field. Explicitly, the tensor takes the form:

$$\mathcal{F}_{\mu\nu} = \begin{pmatrix} 0 & -E_1 & -E_2 & -E_3 \\ E_1 & 0 & -B_3 & B_2 \\ E_2 & B_3 & 0 & -B_1 \\ E_3 & -B_2 & B_1 & 0 \end{pmatrix}_{\mu\nu}. \quad (4.14)$$

derivatives in (4.15) cancel in (4.13). Additionally, the tensor must transform appropriately under spacetime rotations¹³. In Maxwell's equations, the covariant form reads

$$\partial_\mu \mathcal{F}^{\mu\nu} = j^\nu, \quad (4.16)$$

where j^ν represents the 4-current. The anti-symmetry of $\mathcal{F}^{\mu\nu}$ leads to Gauss's law for charge conservation

$$\partial_\nu j^\nu = \partial_\nu \partial_\mu \mathcal{F}^{\mu\nu} = 0. \quad (4.17)$$

This conservation law manifests in the total electrical charge Q within a volume \mathcal{V}

$$2\pi Q = \int_{\mathcal{V}} j^0(x) d^3x = \int_{\partial\mathcal{V}} \mathcal{F}^{0,i}(x) dS_i = \int_{\partial\mathcal{V}} \mathbf{E} \cdot d\mathbf{S}, \quad (4.18)$$

where the second expression follows from Stokes' theorem applied to the boundary $\partial\mathcal{V}$ with the surface element $dS_{\mu\nu}$ [87]. The last term represents the special case for $d = 3$. This identity appears in mathematics as the *first Chern number* [71, 172], a topological invariant characterizing compact complex manifolds in even dimensions [76]. The quantization of charge emerges naturally from requiring single-valued fields $\mathcal{F}_{\mu\nu}$, leading to integer-valued topological invariants [87]. This topological protection explains both charge conservation and quantization, independent of specific dynamics.

Maxwell's equations also contain the Bianchi identity

$$\partial_\lambda \mathcal{F}_{\mu\nu} + \partial_\mu \mathcal{F}_{\nu\lambda} + \partial_\nu \mathcal{F}_{\lambda\mu} = 0, \quad (4.19)$$

¹³This is a direction which we will not explore further, but lead to similarly interesting consequences, see [87]. The Lorentz invariance is guaranteed by the correct choice of

contraction rules $\mathcal{A}_\mu = \eta_{\mu\nu} \mathcal{A}^\nu$ with the Minkowski metric $\eta_{\mu\nu} = \begin{cases} -1 & \text{if } \mu = \nu = 0, \\ 1 & \text{if } \mu = \nu > 0 \\ 0 & \text{if } \mu \neq \nu. \end{cases}$

4. GEOMETRIC PHASES OF DRIVEN ROTORS

which prohibits magnetic monopoles. The magnetic flux through a ball S demonstrates this [76]

$$\Phi_S = \int_S \epsilon_{\mu\nu\lambda} \mathcal{F}^{\nu\lambda} dS^\mu = \int_S \mathbf{B} \cdot d\mathbf{S} = 0, \quad (4.20)$$

where the last expression represents the special case for $d = 3$. The vanishing flux holds in all dimensions as a direct consequence of (4.19). However, it is important to note that classical electrodynamics is less general than the effective gauge fields constructed previously, such as the Berry connection in (4.6), allowing both electric and magnetic monopoles. Consider the degeneracy at $\mathbf{d}(\mathbf{x}) = 0$ of a band Hamiltonian

$$H = \mathbf{d}(\mathbf{x}) \cdot \boldsymbol{\sigma}. \quad (4.21)$$

As we will show now, this degeneracy acts as a monopole of an effective magnetic field \mathbf{B} . The Berry-curvature, analogous to (4.13), takes the form

$$F_{ij}(\mathbf{x}) = \partial_i A_j(\mathbf{x}) - \partial_j A_i(\mathbf{x}). \quad (4.22)$$

For a sphere of radius r in parameter space, the surface element reads $d\mathbf{S} = \mathbf{e}_r r^2 \sin(\theta) d\theta d\phi = \mathbf{e}_r dS$. The Chern number becomes

$$2\pi C = \int_S \epsilon_{ijk} F^{ij}(\mathbf{x}) dS^k = \int_S B(\theta, \phi) d\theta d\phi \quad (4.23)$$

where (compare to (4.8), where this term appeared already)

$$B(\theta, \phi) \equiv \partial_\theta A_\phi(\theta, \phi) - \partial_\phi A_\theta(\theta, \phi) = (\nabla \times \mathbf{A}(\theta, \phi))_r. \quad (4.24)$$

For the two-band model (4.21), the Berry-curvature of the states (\pm) takes the form [182]

$$\nabla \times \mathbf{A}_\pm(\mathbf{x}) = \pm \frac{\mathbf{d}(\mathbf{x})}{|\mathbf{d}(\mathbf{x})|} \frac{1}{2|\mathbf{d}(\mathbf{x})|^2}. \quad (4.25)$$

Using (4.23), with a $r = 1$ sphere parametrization $\mathbf{d}(\mathbf{x}) = \mathbf{e}_r(\theta, \phi)$, we find

$$C_\pm = \pm 1, \quad (4.26)$$

confirming the monopole character. This result generalizes to arbitrary parametrizations, where the degeneracy acts as a monopole [71]. We realize that arbitrary integer Chern numbers $C \in \mathbb{Z}$ arise from multiple wrappings around the monopole, and with opposite wrappings we find monopole-antimonopole pairs in parameter space.

4.2.3 Topological invariants for gapless phases

The mathematical framework we have seen here connects directly to topology: the classification of spaces through loops defines the *first homotopy group* π_1 , also known as the fundamental group [172]. When we consider higher-dimensional wrappings, such as spheres or n -th hyperspherical integrals, we obtain the second or the n -th homotopy groups π_n ¹⁴.

The classification of non-interacting Hamiltonians through homotopies rests on a key principle: when we modify the Hamiltonian adiabatically while preserving its fundamental symmetries, certain topological invariants change only when the gap closes¹⁵. We call Hamiltonians that allow smooth transformations between each other without gap closure *homeomorphic*¹⁶ to each other [76].

Our classification scheme for topological phases has relied funda-

¹⁴The sequence of homotopy groups $\pi_n(X)$ of a topological space X forms a fundamental algebraic invariant. For $n = 1$, we consider loops and their deformation classes. For $n = 2$, we examine maps from the 2-sphere S^2 to X , describing how 2-spheres can wrap around holes in X . This pattern continues for higher dimensions. These groups connect through the exact homotopy sequence, which relates the homotopy groups of fiber bundles, base spaces, and total spaces [76, 172].

¹⁵Or one of the gaps, for a multi-band Hamiltonian. The gap closure represents a critical point where the band structure undergoes a topological phase transition, analogous to phase transitions in classical systems [71].

¹⁶A homeomorphism between topological spaces X and Y is a bijective function $f : X \rightarrow Y$ such that both f and its inverse f^{-1} are continuous. More precisely, for any open set $U \subset Y$, the preimage $f^{-1}(U)$ is open in X , and for any open set $V \subset X$, the image $f(V)$ is open in Y . Two spaces are called homeomorphic if there exists a homeomorphism between them (taken from [183]).

mentally on the existence of an energy gap. This raises a conceptual challenge: how can we extend this theory to systems where the gap condition is violated by construction, such as semi-metals with band nodes in their Brillouin zone that persist under parameter variations? As it turns out, the formalism we introduced extends naturally to these gapless phases through the concept of topological defects in momentum space [71]. Here, we must account not only for the symmetries and dimension of the Hamiltonian but also for the dimension of the band nodes, which can appear as points, lines, or surfaces in the Brillouin zone. While this introduces additional complexity, many principles from the classification of gapped phases remain applicable, particularly the role of symmetry-protected topological invariants.

The (anti-)unitary symmetries create specific constraints on the space available for adiabatic transformations, effectively restricting the possible deformations of the Hamiltonian. This framework culminates in the *Altland-Zirnbauer (AZ) tenfold classification of topological insulators and superconductors*, which systematically catalogs topological invariants across different dimensions and (anti-)unitary symmetries [71]. Beyond the fundamental symmetries of particle-hole, time-reversal, and chiral symmetry that shape this classification, crystal symmetries (spatial point-group symmetries) such as inversion can introduce additional constraints, leading to novel states like higher-order topological insulators [184–186]. These additional symmetries enrich the classification by introducing new protected boundary states and topological invariants.

This aspect will become particularly relevant for the periodically driven quantum rotors we are considering, where we will encounter topologically protected nodal lines that come from time-reversal and inversion symmetry. These nodal lines manifest as one-dimensional singular submanifolds in the spectrum where bands touch. We will see that the quantum rotor system exhibits remarkably rich topological physics, including multiple types of topological invariants and

protected boundary states.

4.2.4 Bulk-boundary correspondence

The bulk-boundary correspondence represents a fundamental principle in topological physics that connects the topology of the bulk system to the existence of robust boundary modes¹⁷. While this correspondence has remarkable generality across different dimensions and symmetries, its mathematical foundation often requires sophisticated concepts from differential geometry and K-theory¹⁸. Let us develop a concrete physical picture that captures the essential ideas while setting aside the mathematical machinery for now.

To illustrate these concepts, let us return to the two-band model from (4.12),

$$H_k = r \cos(k) \sigma_x + r \sin(k) \sigma_z. \quad (4.27)$$

When interpreting k as a crystal momentum, the real-space version describes a variant of the Su-Schrieffer-Heeger model (SSH) [182], which captures the physics of polyethylene (among other systems). The specific form of the model is not essential since the topological properties are universal.

¹⁷Here, robustness refers to the stability of these boundary modes against perturbations commonly encountered in real materials, such as structural defects, impurities, and many-body interactions, as long as these perturbations do not destroy the essential symmetries of the Hamiltonian. This does not mean the states are indestructible – strong perturbations that break the protecting symmetries can destroy them. For instance, magnetic impurities can destroy states protected by time-reversal symmetry, and strong electron-electron interactions can break the non-interacting topological classification [71]

¹⁸At its core, K-theory works with vector bundles over topological spaces and their equivalence classes. The so-called ‘K’ groups capture stable equivalence classes of these bundles – ‘stable’ meaning that we can add trivial bands without changing the topological classification. K-theory unifies different approaches from vector bundles, cohomology theories, and index theorems. As it turned out, this machinery proves particularly useful when understanding both strong and weak topological invariants, as well as crystalline topological phases [187].

Taking the continuum limit corresponds to focusing on modes with wavelengths much larger than the lattice constant (i. e. $k \rightarrow 0$), we can substitute $k = -i\partial_x$ in real-space to obtain for (4.27)

$$H(x) \approx -ir\sigma_z\partial_x + r\sigma_x. \quad (4.28)$$

This represents a simplified version of the Jackiw-Rebbi model¹⁹. Due to chiral symmetry, we expect the system to have a symmetric spectrum with extended states at finite energies. By symmetry arguments, any non-propagating bound state $\psi(x)$ must occur at zero energy. Solving $H(x)\psi(x) = 0$ using (4.28) yields

$$\partial_x\psi(x) = \sigma_y\psi(x) \quad (4.29)$$

which admits the exact solution²⁰ $\psi(x) \propto e^{-x}(i, 1)^T$. One can demonstrate that this state exists only when the path exhibits non-trivial topology – with an associated topological invariant. Surprisingly, this result does not hold only for localized modes at open boundaries, but extends to all kinds of defects, phase boundaries and lattice dislocations²¹.

As we will see in the following, this concept goes beyond Hermitian matrices. For the periodically driven molecules we study, we cannot speak of closed systems – energy conservation breaks down as

¹⁹The Jackiw-Rebbi model, introduced in quantum field theory [188], describes fermions interacting with a topological defect. It provides one of the earliest examples of fractionalization, where excitations carry quantum numbers that are fractions of the fundamental ones. The model has found applications far beyond its original context, appearing in condensed matter physics and quantum computation [71].

²⁰We can solve this by noting that the eigenvectors of σ_y are $\phi_{\pm} = (\pm i, 1)^T$ with eigenvalues ± 1 . A general solution takes the form $\psi(x) = \psi_+(x)\phi_+ + \psi_-(x)\phi_-$ with coefficients $\psi_{\pm}(x)$. From (4.29) we find $\partial_x\psi_{\pm}(x) = \mp\psi_{\pm}(x)$. Hence, we obtain two solutions (for each boundary) when applying appropriate boundary conditions. The physical solution must be normalizable, so we need to take the exponentially decaying solution.

²¹This generalization is known as the defect classification of topological phases. Defects can be viewed as lower-dimensional topological phases embedded in a higher-dimensional system [71].

the pulses can add significant energy over time. This necessitates extending our discussion to non-hermitian topology.

4.2.5 Non-hermitian topology

Research has long focused on topological invariants of hermitian matrices, specifically on classifications based on gap closings of the energy bands. In contrast, driven and dissipative systems cannot generally be described by a single hermitian matrix. The interplay between gain and loss can lead to new properties. Several frameworks exist to describe such systems, including Liouvillian superoperators and the Keldysh formalism for non-equilibrium quantum fields [189]. In some special cases, we can derive an effective non-hermitian Hamiltonian to describe the behavior of the system. While this offers significant simplification compared to the theories mentioned before, it introduces complex instead of real eigenvalues λ . This formalism has been applied successfully to a wide range of driven-dissipative systems, encompassing classical optical systems with decay channels, electrical circuits, mechanical systems, and driven-dissipative quantum materials [190].

While early works by Parachatnam were basically non-hermitian by construction [88], Hatano Naomichi realized in 1996 that non-hermitian couplings can lead to similar topological physics as in the static case, with topological invariants, bulk-boundary correspondence and edge modes [191]. This effect, now known as the *non-hermitian skin effect*, demonstrates how topological concepts of hermitian physics extend to the non-hermitian case. Moreover, new phenomena emerge, which relate to the so-called *exceptional points* or *exceptional nodal lines* [192]. However, for the description of periodically driven systems with unitary symmetries, we can concentrate on a subclass of non-hermitian topology concerning the classification of Floquet Hamiltonians [164, 193–195]. When we examine the effective Hamiltonian H_{eff} with $U_T = e^{-iH_{\text{eff}}}$, it often suffices to consider

static topological invariants of H_{eff} , and the discussion of the last section remains fully valid. However, there are cases where this approach proves insufficient, and the periodicity of the quasi-energy plays an important role; these are called *anomalous Floquet phases*, that is, anomalous when compared with the static setup. This occurs precisely when we examine topology that arises due to band-node closings of both the usual gap and the π -gap. We will explore this case in detail in Section 5.4. Another case emerges when we examine non-abelian gauge groups of periodically driven rotors, which we will discuss in Chapter 5. In that case, we can create a non-abelian anomalous phase. Let us first examine the simple case of band nodes that appear in periodically driven molecules and their influence on the dynamics of the system.

4.3 Dirac cones and topological charges

Building upon our previous understanding of how eigenvalue degeneracies can lead to geometric phases, we now return to periodically driven molecules with a finite, one-dimensional angular momentum lattice introduced in Section 3.5, bounded by $l = 0$ and $l = l_{\text{max}}$ ²². Certainly, there are also topological invariants for 2D rotors, but unlike the 3D rotor there are no natural boundaries. We examine the model defined by (3.66) with $N = 3$, which exhibits three bands²³. With three bands come three gaps (including the π -gap). Fig. 4.2(a) shows the phase space of the model in terms of band degeneracies. The degeneracies form nodal lines arranged in a regular grid-like pattern. As emphasized earlier in Section 3.3.3, two fundamental symmetries protect these nodal points: time-reversal symmetry and inversion symmetry. These symmetries cause the nodal points to extend into nodal lines and place the model in the class AI [71]. As a

²²Here, we present extended and refined results from our paper [2].

²³For $N = 1$, there exists only one band, for $N = 2$ the map shows perfect revival, thus we select $N = 3$ as the smallest N with non-trivial behavior.

consequence, while the Berry curvature vanishes at all momenta, the band nodes transform into *topological charged Dirac cones*. These can only disappear through symmetry breaking or through annihilation of two Dirac cones with opposite charges. The symmetries define a conserved topological charge under adiabatic parameter changes. In Fig. 4.2(b-c), we present the spectrum along a specific path through parameter space as a function of $s \in [0, 1]$. Each value of s corresponds to one model $U_k(P_1, P_2)$ with specific kicking strengths²⁴.

Due to the symmetries, gap closings occur either at $k = 0, k = \pi$ or at momentum pairs $(k, -k)$. Fig. 4.3 reveals the momentum-space dependence of the quasi-energies and demonstrates this behavior for the two paths from Fig. 4.2. In this case, the gap closing of the first two bands appears at $k = 0$, while the closing of the second gap occurs at $k = \pi$. We also examine a path²⁵ crossing a $(-k, k)$ nodal line in Fig. 4.2. While the nodal lines at $P_2 = 4n\pi/3 \pm 2P_1$ appear at $k = 0$ and $k = \pi$, the other nodal lines emerge at momentum pairs $(-k, k)$, as shown in (c) and (f) of Fig. 4.3.

4.3.1 Engineering synthetic dimensions with adiabatic paths

Let us now examine how tuning the kicking strengths leads to topological phase transitions at band touching points, transforming the system from a regime without topological edge states to one where edge states emerge. While Fig. 4.2 displays only the minimum of gaps, all three gaps exhibit closings. We can create a two-dimensional model by tuning the parameters periodically with $\alpha \in [0, 2\pi]$ such that

$$\alpha \mapsto f(\alpha) = (P_1, P_2), \quad f(0) = f(2\pi), \quad (4.30)$$

thereby engineering a momentum space torus – a compact manifold.

²⁴The two paths are parametrized as following: For the two paths, we choose $(P_1, P_2) = r_0(2\pi s + \pi/2, 4\pi(1 \pm s))/3$ with $r_0 = \pi/3$.

²⁵Here we choose $(P_1, P_2) = r_0(2\pi s/6 + 7\pi/3, 4\pi(1 - s/6)/3)$.

4. GEOMETRIC PHASES OF DRIVEN ROTORS

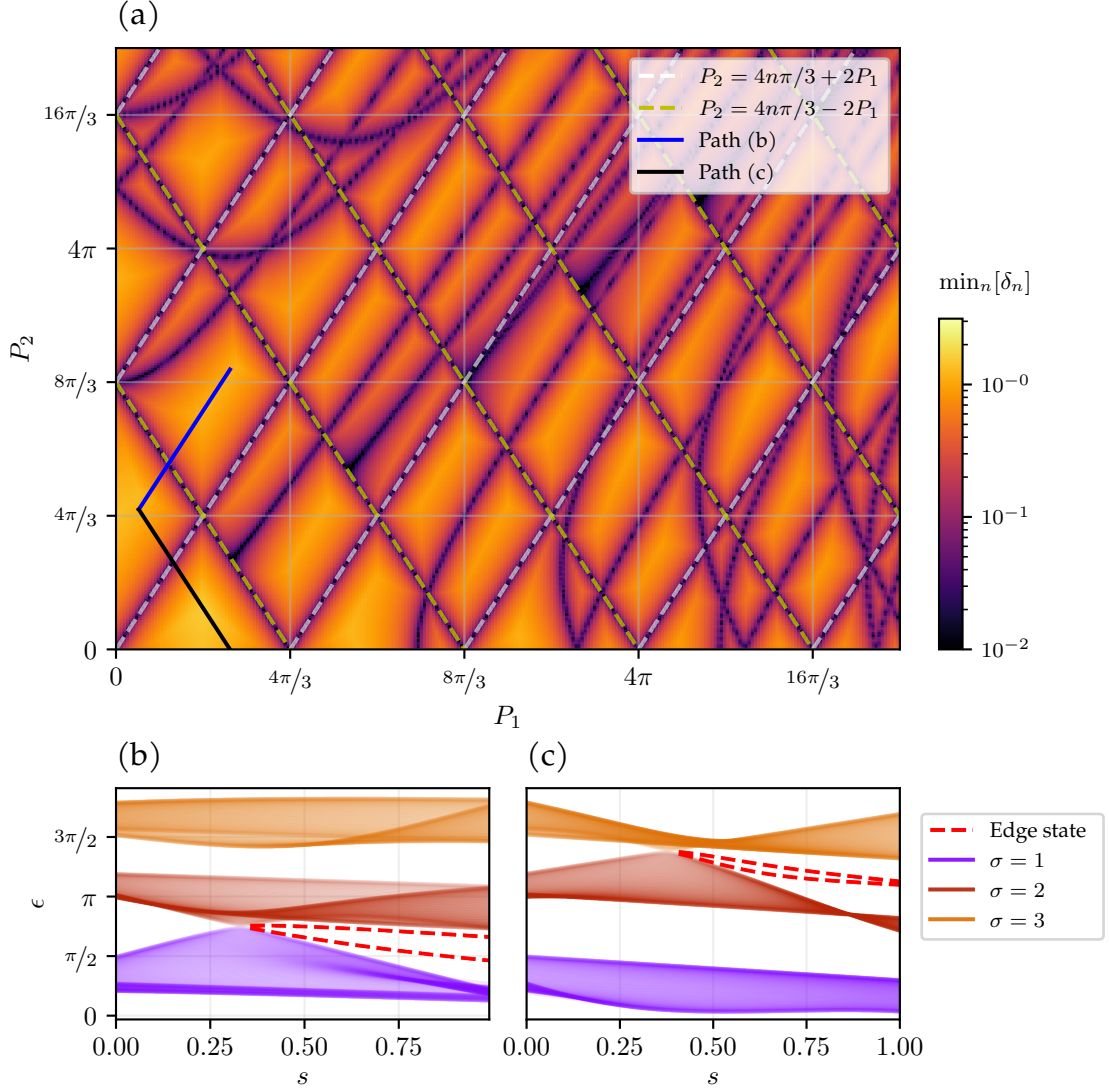


Figure 4.2: Phase diagram for $N = 3$ of the periodically driven 3D rotor. (a) The minimal band gap as a function of driving strengths P_1 and P_2 . The phase diagram reveals a grid of nodal lines where the bandgap δ_n vanishes. There are straight lines at $k \in \{0, \pi\}$ and curved lines forming $(-k, k)$ rings. (b) Path across the nodal line of the first gap, indicated by the blue line in (a). (c) Path across the nodal line of the second gap. Edge states (red dashed) emerge when crossing either nodal line, arising from the topological charge of the effective Dirac cone.

Following our previous discussion, the degeneracy of the bands

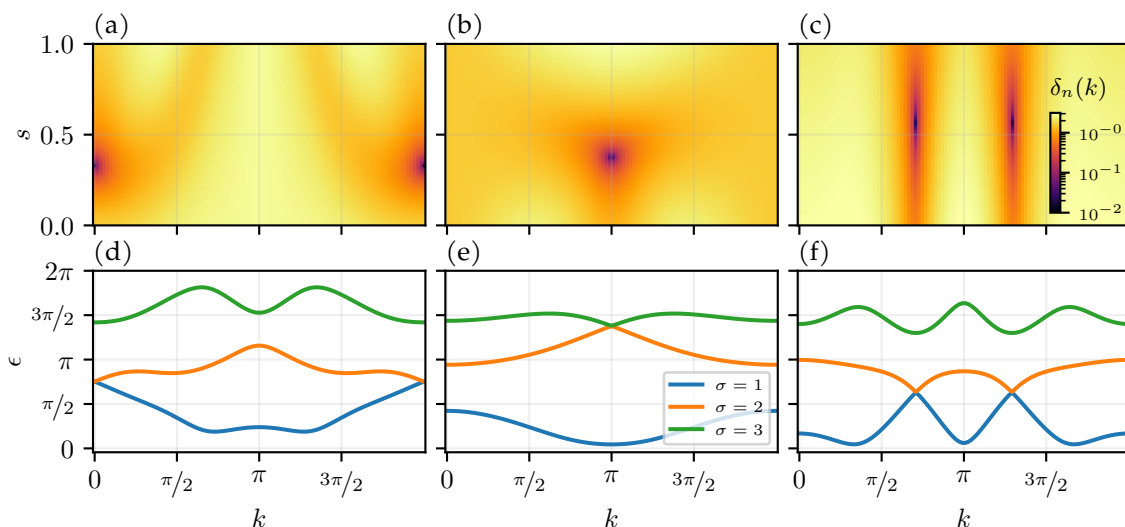


Figure 4.3: Band nodes at k -symmetric points. (a) The band gap of the first path of Fig. 4.2 (b) the band gap of the second path, (c) band gap of a path going over a $(-k, k)$ nodal line. All three as a function of the parameter s and momentum k . (d-f) The corresponding spectra with at their critical values $s = s_{\text{crit}}$ and (d) $k = 0$, (e) $k = \pi$, and (f) with $k \approx \pm 0.7\pi$.

should lead to a characteristic signature in the wavefunction, manifesting as a Berry phase. In Fig. 4.5, we show the results for a circular path²⁶. By construction, since the nodal lines at $k = 0$ or $k = \pi$ are linear in the $P_1 - P_2$ plane, every circular path must cross them twice. Thus, models of this construction always exhibit an even number of nodal points. This property extends to the curved nodal lines with $(-k, k)$, as each point (P_1, P_2) contains at least two nodal points, ensuring an even total number for any circular path.

As we have already seen in Fig. 3.13 in the last chapter, for a finite system there are localized eigenstates. However, now we identify them as a result of the topological phase transition at the two nodal points. This is an important result, because this shows that they are connected to the topological charge of the nodal points. Once created by the first nodal point, these states can only vanish by merging with

²⁶Here we choose $(P_1, P_2) = (0.6 \sin(\alpha) + 1.0, 1.8 \cos(\alpha) + 2.2)$.

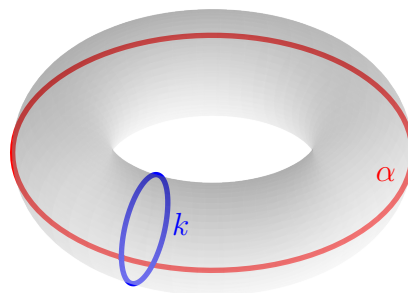


Figure 4.4: Engineering synthetic dimensions. By adiabatically changing the kicking parameters of the driven model with time t , we can simulate higher-dimensional models. By choosing circular paths $\alpha \in [0, 2\pi]$ we effectively create another momentum dimension, which can lead to the simulation of a two-dimensional band model. When doing this adiabatically, we expect that the Floquet eigenstates stay in their band. We will see later how this could be probed experimentally.

the second nodal point (which, as we will show, carries opposite charge). The topological edge states behave analogously to field lines in the space of wave functions between the two degeneracies. In Chapter 5, we will demonstrate the possibility of annihilating the two nodal points in the opposite direction of their creation, generating topological modes disconnected from the bulk. The two-dimensional momentum vector becomes

$$\mathbf{k} = (k, \alpha). \quad (4.31)$$

To calculate the geometric phase around a path encircling the nodal points, we use (4.31) and (4.9) to obtain

$$\gamma_\sigma = \frac{1}{2\pi} \oint A_{j\sigma}(\mathbf{k}) dk^j, \quad (4.32)$$

4.3. Dirac cones and topological charges

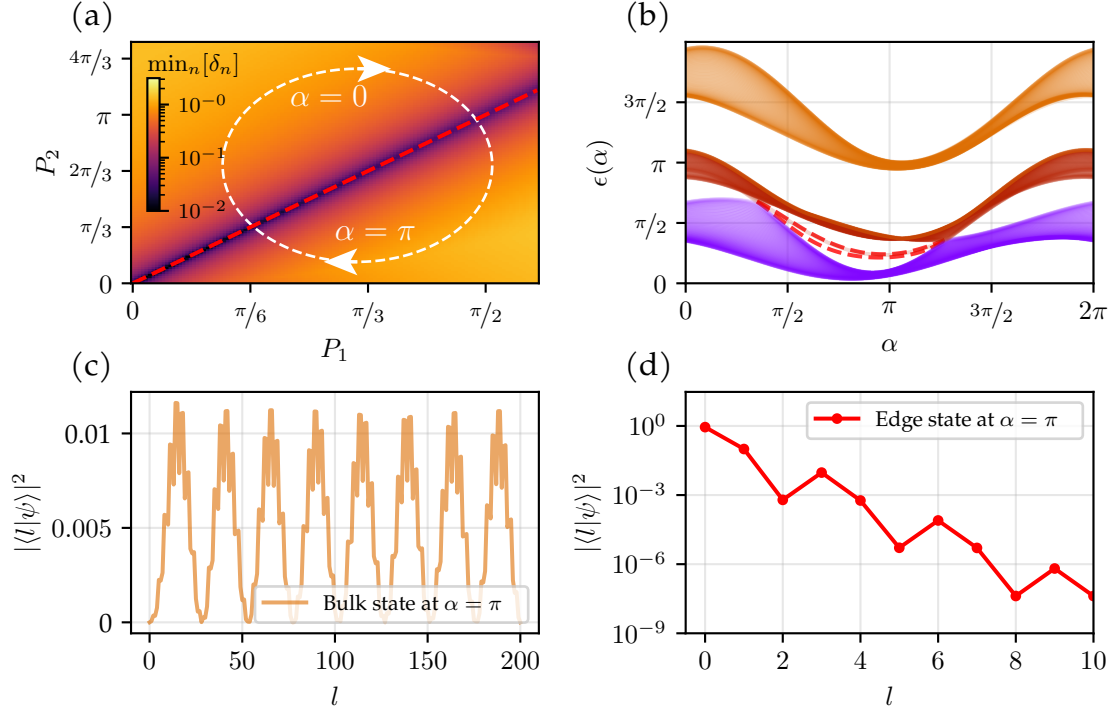
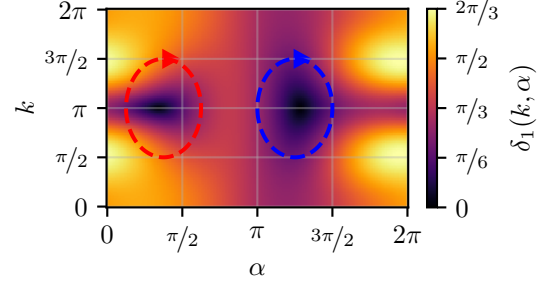


Figure 4.5: Nodal lines as topological phase transitions. As in Fig. 4.2 we look at the results of periodically driven molecule at $N = 3$. In (a) we show the phase space for this section, including the circular path whose spectrum is shown in (b). As before, we understand how the nodal lines give rise to the gap closings and the corresponding topological edge states. In (c), we show a regular bulk state, as compared to (d) with a topological edge state, both evaluated at $\alpha = \pi$.

with $A_{j\sigma}(\mathbf{k}) = i\psi_\sigma^\dagger(\mathbf{k})\partial_j\psi_\sigma(\mathbf{k})$ and the partial derivative with respect to \mathbf{k} . We can evaluate²⁷ the phases for the two nodal points. The red path evaluates to $\gamma_1 = 1/2$, and the blue one to $\gamma_1 = -1/2$ (note that for the second band, i. e. γ_2 , we would find the opposite result); as expected, the total charge sums to zero.

²⁷Therefore, we use the method introduced in [196], which uses the logarithm of the scalar products to avoid the random phases of numerical diagonalization.

Figure 4.6: Topological charges of the Dirac cones. As a heatmap we show the energy difference between the first and the second band of Fig 4.5. Further there are the contours taken in (4.32) for the two nodal points, i. e. Dirac cones, in order to evaluate their topological charges.



4.4 Experimental signatures of Dirac cones

At this point the question arises whether this has any experimental signatures. Apart from measuring energy or angular momentum states directly (which are typically difficult to measure) the orientation signal $\langle \cos(\hat{\theta}) \rangle$ and the alignment signal $\langle \cos^2(\hat{\theta}) \rangle$ can give good indications what is happening in the system. In the limit where both of them are translationally invariant, we can evaluate them fully in momentum space using (3.40) and (3.41) for different Floquet states $\psi_\sigma(k, \alpha)$ with

$$\langle \cos(\hat{\theta}) \rangle_k = \psi_\sigma^\dagger(k, \alpha) (\cos(\hat{\theta}))_k \psi_\sigma(k, \alpha) \quad (4.33)$$

$$\langle \cos^2(\hat{\theta}) \rangle_k = \psi_\sigma^\dagger(k, \alpha) (\cos^2(\hat{\theta}))_k \psi_\sigma(k, \alpha) \quad (4.34)$$

where $\cos(\hat{\theta})_k$ and $\cos^2(\hat{\theta})_k$ are $N \times N$ matrices (here: $N = 3$), respectively. In Fig. 4.7 we show the results for the Floquet states of a circular path from the last section (Fig. 4.5). We observe that the two signals are not close to 0 to begin with; we see that the eigenstates have significant alignment for a wide range of parameters. This occurs because the eigenstates of these two operators are delocalized in angular momentum space²⁸. Even more so, we see that the alignment strongly depends on the position of the band nodes. We

²⁸Trivially, both have the angle state $|\pm\theta\rangle$ with $\theta \in [0, 2\pi]$ as eigenstates, whose matrix elements are the spherical harmonics $\langle lm | \pm\theta, \phi \rangle = Y_{lm}(\pm\theta, \phi)$.

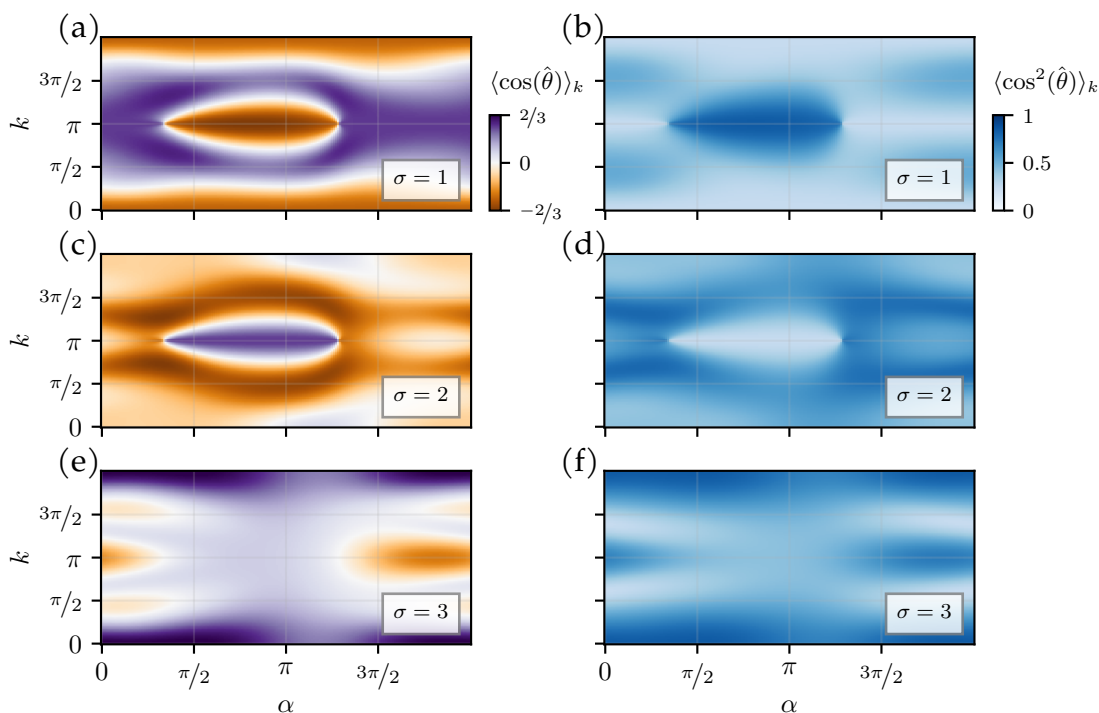


Figure 4.7: Alignment and orientation signatures of band nodes. As in Fig. 4.5 we look at a circular path $\alpha \in [0, 2\pi]$ of periodically driven molecule at $N = 3$. In (a,c,e) we show the orientation signal and in (b,d,f) we show the alignment signal; each for the three bands σ . We see that the band nodes at $\alpha \approx 1$ and $\alpha \approx 4$ lead to an inversion of these signals respectively.

realize that the band node has a clear interpretation in terms of these signals; it marks exactly the position where a positively oriented Floquet state of the first band transforms into the negatively oriented Floquet state of the second band. Note, though, that this description does not include the edge states, which evade a momentum-space based description.

4.4.1 Adiabatic time-evolution

Despite the elegance of this band description, we must verify its applicability to full exact diagonalization. As we mentioned in Sec-

tion 3.5.3, working with finite lattices presents well-known challenges in discrete Fourier transforms. Surprisingly, the band description of the driven rotor proves more accurate than initially anticipated. Even when approximating the synthetic α -dimension with just a few kicks and considering states of small total energy and few angular momentum components (states potentially achievable in experiment), the band model and particularly the Dirac cones provide remarkable insight into the system dynamics. Let us begin by considering a Floquet state $\psi_\sigma(k, \alpha) \in \mathbb{C}^N$ of band σ as initial state. The time-translation operator conserves momentum since $U(k, \alpha)\psi_\sigma(k, \alpha) = e^{-i\epsilon_\sigma(k, \alpha)}\psi_\sigma(k, \alpha)$. This momentum conservation proves to be an excellent approximation. For a change $\alpha \rightarrow \alpha + \delta\alpha$ in the next kick (at fixed k),

$$U(\alpha + \delta\alpha)\psi_\sigma(\alpha) = \sum_{\sigma'=1}^N e^{-i\epsilon_{\sigma'}(\alpha + \delta\alpha)}\psi_{\sigma'}(\alpha + \delta\alpha)\langle\psi_{\sigma'}(\alpha + \delta\alpha)|\psi_\sigma(\alpha)\rangle. \quad (4.35)$$

For a series of kicks,

$$\phi(t) = U_t(\alpha_t)U_{t-1}(\alpha_{t-1}) \dots U_1(k, \alpha_1)\phi(t = 0), \quad (4.36)$$

with a path $\alpha_t \dots \alpha_0$. Let us first assume suppressed interband transitions $\sigma \rightarrow \sigma'$. Then, for an expectation value of a translation-invariant operator \hat{A} , all phases cancel out²⁹ and we find

$$\langle\phi(t)|\hat{A}|\phi(t)\rangle = \langle\psi_\sigma(\alpha_t)|\hat{A}|\psi_\sigma(\alpha_t)\rangle \quad (4.37)$$

For an adiabatic path α_t , we expect interband transitions to scale inversely with both the quasi-energy difference and the magnitude of changes $\delta\alpha = \alpha_t - \alpha_{t-1}$. However, a pure quasi-momentum state presents two challenges: it is completely delocalized in angular momentum with infinite energy (making experimental preparation

²⁹Clearly, the quasi-energy terms $e^{-i\epsilon_\sigma(\alpha_t)}$ cancel out. The overlaps are related to the Berry connection (compare to (4.5)) since $\lim_{\delta\alpha \rightarrow 0} (\langle\psi_\sigma(\alpha)|\psi_\sigma(\alpha + \delta\alpha)\rangle - 1) / \delta\alpha = \langle\psi_\sigma(\alpha)|\partial_\alpha|\psi_\sigma(\alpha)\rangle$ and cancel out as well.

difficult) and impossible to achieve in a finite lattice. Therefore, we turn our attention to states localized in both quasi-momentum and angular momentum. For a band with small bandwidth, not only pure states $\phi(0) \propto \psi_\sigma(k, \alpha)$ follow the band adiabatically, but also superpositions of eigenstates. States with identical quasi-energy but different momenta evolve in parallel, maintaining their shape due to decoupled quasi-momentum sectors. For different energies, the wavepacket shape evolution follows the bandwidth, determined by quasi-energy differences across occupations. Since the Fourier transform of a Gaussian state is also a Gaussian state, we choose a superposition of eigenstates of some band with an approximately Gaussian profile³⁰ with width σ_k , centered around some chosen momentum $k_0 \in [0, 2\pi]$ such that

$$\phi(t=0) \propto e^{-\frac{(k-k_0)^2}{2\sigma_k^2}} \psi_\sigma(k, \alpha_0) \quad (4.38)$$

and evaluate the orientation and alignment signal for this state when choosing path $\alpha(t)$ that quenches over the Dirac cone established in Fig. 4.5. We choose a momentum that is close but not identical to $k = \pi$ in order to resolve the nodal point structure shown in Fig. 4.7. The results are shown in Fig. 4.8. Indeed, we can confirm that the quasi-momentum description works extremely well, even in this scenario of changing kick parameters α . The state keeps its shape both in angular momentum and quasi-momentum space almost perfectly over the series of kicks (note that this would be

³⁰In fact, the method to find such a state is numerically more involved. First, we generate a Gaussian state according to (4.38). Then, we Fourier transform this state back to real-space using the second expression in (3.39) at some l_0 as reference point for Δn . However, due to finite size effects, this state is not only occupying the σ -band, so we construct a projector \mathcal{P}_σ using the real-space states of that band and project out the other bands with $\mathcal{P}_\sigma|\phi\rangle$. This projection leads to a slight delocalization, hence we regularize this state with a real-space Gaussian $e^{-(l-l_0)^2/(2\sigma_l^2)}$ and repeat the projection - regularization until the state is converged. This method leads to a perfect occupation in the σ -band, and both localization in angular momentum and quasi-momentum space, even though the latter is slightly perturbed by the method. However, numerics show that it works surprisingly well.

4. GEOMETRIC PHASES OF DRIVEN ROTORS

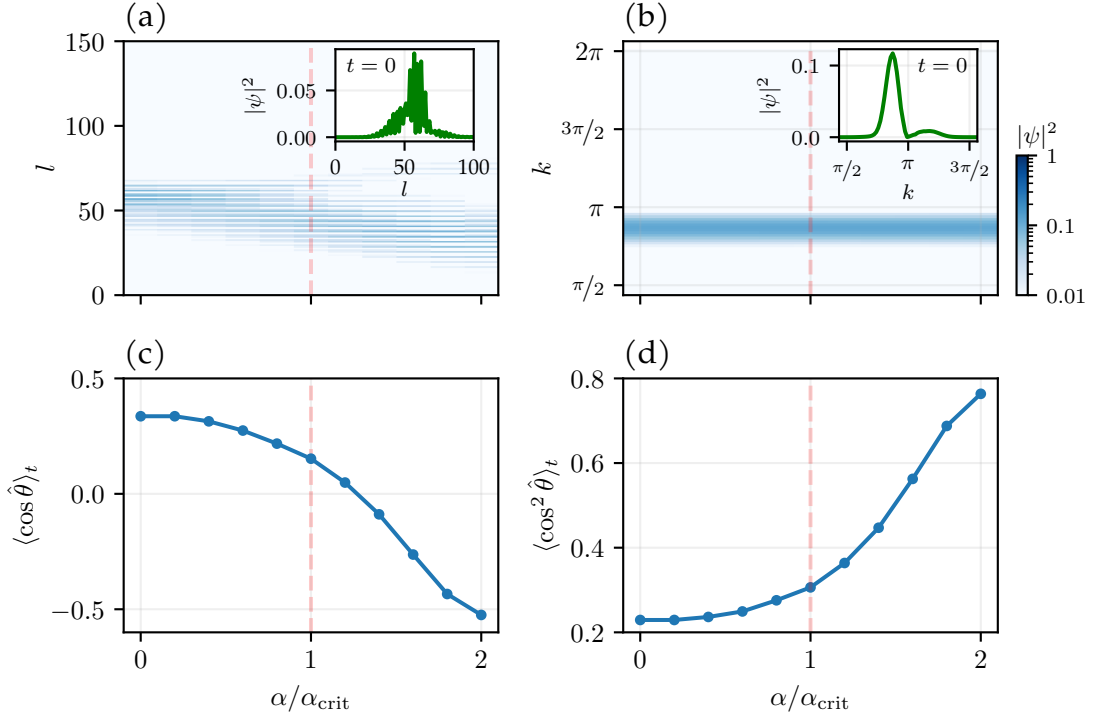


Figure 4.8: Quench dynamics of a Gaussian state. Here we show the results of exact diagonalization with $N_t = 10$ kicks for the same parameters as in Fig. 4.5 and with $\alpha(t) = 2t/N_t$. The upper panels show $|\psi|^2$ in (a) angular-momentum space and (b) quasi-momentum space. The wavefunction is approximately localized in both spaces at $t = 0$ (see inset figures) and throughout the time-evolution (note that there is a drift towards $l = 0$ though in angular momentum space). In (c) we show the orientation and in (d) the alignment signal. Both show a drastic change due to the Dirac cone at $\alpha_{\text{crit}} \approx 1$. The state is constructed with $k_0 = \pi, \sigma_k = 0.45, l_0 = 55, \sigma_l = 15$, see footnote 30 for the technical details of the state construction. Note that the state construction leads to the intended shift towards smaller momentum k , even though we started with $k_0 = \pi$.

different if the wavepacket would come close to the boundary $l = 0$, at which the periodicity condition is broken and quasi-momentum is not conserved. However, what happens is that at the boundary quasi-momentum is inverted from $k \rightarrow -k$). Further, even though there is no visible change in the wavefunction (apart from a drift towards lower l , which is insignificant for this analysis. The same

results can be achieved for a wavepacket towards higher l ; after some fine-tuning one could possibly find a state with no drift at all), there is a drastic change in the orientation and alignment signal. Note that both change corresponding to what we expect from the analysis of the Floquet states in quasi-momentum from Fig. 4.7. Hence, the results of these expectation values are more closely related to the relative phases (and hence, the berry connection) than the absolute occupations, which are predicted not to change considerably.

4.5 Outlook

As we conclude this chapter, let us outline its significance for our subsequent exploration of non-abelian topology. Our analysis revealed how degeneracies in spectrum of even simple matrices give rise to a rich variety of phenomena, whose classification depends fundamentally on the symmetries. For simple cases of the periodically driven rotors, we showed that the two-band hermitian topological classification suffices, as the Floquet operator manifests precisely these simple classes through the stroboscopic Hamiltonian. However, in the next chapter, we will see how this framework extends to reveal the non-abelian character of the topological charges. Most intriguingly, the non-equilibrium nature of our system will lead us to discover an anomalous Dirac-string phase – a phenomenon unique to driven systems that transcends conventional hermitian topology. Understanding this phase requires careful analysis of the full Floquet operator, drawing us into the fascinating frontier of multi-band Floquet topology.

CHAPTER 5

Non-abelian topological phases

The greatest strategy is doomed if it's implemented badly.
– Bernhard Riemann

5.1 Overview

The exploration of band degeneracies in the preceding chapter revealed how topological invariants emerge through single-band integrals of the Berry connection. The Berry phase stands as a fundamental quantity underpinning our understanding of topological insulators and topological semimetals. While this single-band framework has driven substantial advances in topological materials [184–186, 197–203], recent developments have highlighted the rich physics arising from multi-band interactions and their associated non-abelian topological characteristics. These phenomena extend beyond conventional solid-state systems, manifesting in photonic crystals, mechanical metamaterials, ultracold atoms, and driven quantum systems [204–207].

The study of multi-band topological phenomena, particularly under constraints imposed by combinations of (anti-)unitary and crystalline symmetries, has generated universal classification schemes [199,

200]. These schemes unveil the intricate relationship between momentum space constraints and real space properties. Our focus lies on such symmetry-constrained multi-gap topology, where collective band behavior reveals phenomena unattainable in single-gap systems [208–215]. The field has expanded rapidly across diverse physical platforms: from phononic [216, 217] and electronic systems [209, 218, 219] to magnetic materials [220], metamaterials [221–223], and out-of-equilibrium phenomena [224–229], including an anomalous variant requiring periodic driving [226].

Systems with $N \geq 3$ bands featuring real Hamiltonians due to \mathcal{PT} symmetry¹ present a compelling example. Band singularities in these systems carry non-abelian frame charges [208, 209, 230], and their braiding between adjacent band pairs modifies these charges, leading to topologically protected nodes characterized by the Euler invariant. Building on our previous discussion of periodically kicked quantum rotors and their Floquet topological phases, we note that these driven systems offer distinct advantages over solid-state implementations. Their well-controlled parameters and tunable band number N provide an ideal platform for exploring novel multi-band topological phenomena in non-equilibrium settings.

In section 4.3, we demonstrated how periodic driving induces time evolution in quantum rotors that can host single-gap topological charges. These charges develop distinctive properties under additional symmetries. We now examine how maintaining time-reversal symmetry (\mathcal{T}) in kicked quantum rotors allows topological singularities to acquire non-abelian properties for $N \geq 2$ [208, 209, 230]. Systems with \mathcal{PT} symmetry reveal a rich structure through the lens of the Euler class. Multi-band topological physics transcends the conventional Chern classification of topological insulators: The fundamental distinction arises from band closings (degeneracies) or nodes, which exhibit non-commutative behavior. This non-commutativity

¹Other combinations of symmetries also generate real hamiltonians, for example $\mathcal{C}_2\mathcal{T}$ with the n -fold rotational symmetry \mathcal{C}_n [210].

generates exotic braiding phenomena, leading to novel topological phases including Euler insulators and anomalous Dirac string phases in periodically driven systems. The 2π periodicity of the Floquet spectrum allows gap closings in the π -gap between bands $n = 1$ and $n = N$, generating anomalous Floquet topologies without equilibrium analogues [204, 205, 226, 231–233].

Our investigation proceeds as follows. We examine the non-abelian braiding of topological singularities through periodically kicked quantum rotors. By modulating laser pulse intensity, we demonstrate how band node non-abelian charges transform through mutual circulation during rotor evolution. This manipulation realizes an anomalous Dirac string phase [226], where topological singularities in all gaps, including the anomalous π -gap, participate in the braiding process. Zero-angular-momentum edge states serve as definitive signatures of these multi-gap phases.

The structure of the chapter is as follows: Section 5.2 examines the phenomenon of orientability in detail, beginning with the Stiefel-Whitney class in Section 5.2.1. We then introduce non-abelian charges in Section 5.2.2 and demonstrate the emergence of Dirac strings across different gaps in Section 5.2.3.

Section 5.3 applies these concepts to periodically driven quantum rotors through the triple-kicked rotor model. Section 5.3.1 demonstrates how the Euler class captures the braiding process, generating non-abelian topological invariants, including the multi-gap Euler number. These invariants characterize the Dirac string braiding process and its classification.

Section 5.4 introduces the anomalous Dirac-string phase, a novel state emerging from the interplay between multi-gap topology and periodic driving that transcends static system classification schemes. We conclude in Section 5.5 with a review of our findings and highlight the distinctive achievements of this work.

5.2 Non-Orientability and Dirac-strings

5.2.1 The Stiefel-Whitney Class

To understand how these non-abelian properties emerge, we must first examine the fundamental role of symmetry in our system. The combination of inversion \mathcal{P} and time-reversal symmetry \mathcal{T} enables us to work in a gauge where the effective Hamiltonian becomes real². This reality condition extends naturally to the eigenvectors, i. e.

$$H(\mathbf{k})\psi_\sigma(\mathbf{k}) = \epsilon_\sigma(\mathbf{k})\psi_\sigma(\mathbf{k}), \quad (5.1)$$

where $\psi_\sigma(\mathbf{k}) \in \mathbb{R}^N$. We can express this more compactly through an orthogonal transformation

$$H(\mathbf{k}) = R(\mathbf{k})\text{diag}[\epsilon(\mathbf{k})]R^T(\mathbf{k}), \quad (5.2)$$

with the orthogonal group $R(\mathbf{k}) \in O(N)$. The crucial observation is that when there is only one gap, which is positioned between bands $\sigma = p$ and $\sigma = p + 1$, we can continuously deform the spectrum while preserving the essential topological features [234]. This deformation process, known as spectral flattening³, relies on the homotopy equivalence between Hamiltonians with the same gap structure [71]. Specifically, we can define a continuous path of Hamiltonians $H_t(\mathbf{k})$ for $t \in [0, 1]$ such that

$$H_t(\mathbf{k}) = R(\mathbf{k})\text{diag}[f_t(\epsilon_1(\mathbf{k})), \dots, f_t(\epsilon_N(\mathbf{k}))]R^T(\mathbf{k}), \quad (5.3)$$

where $f_t(x)$ smoothly interpolates between the original spectrum ($t = 0$) and the flattened spectrum ($t = 1$)

$$f_t(x) = (1 - t)x + t \text{sign}(x). \quad (5.4)$$

²See footnote 19.

³The flattening procedure is well-defined as long as the gap remains open throughout the deformation. This is guaranteed by the continuity of eigenvalues with respect to perturbations, a consequence of the implicit function theorem, see (4.11).

This homotopy preserves the gap, ensuring that no eigenvalue becomes degenerate during the deformation. The endpoint of this deformation is the flattened Hamiltonian $Q(\mathbf{k})$

$$Q(\mathbf{k}) = R(\mathbf{k}) \text{diag}[\underbrace{(-1, \dots, -1)}_p, \underbrace{(1, \dots, 1)}_{N-p}] R^T(\mathbf{k}). \quad (5.5)$$

After flattening, the Hamiltonian $Q(\mathbf{k})$ exhibits degeneracies of $O(p)$ symmetry in the lower bands and $O(N - p)$ symmetry in the upper bands⁴. The classifying space of such a system is naturally described by the real Grassmannian [210]

$$\text{Gr}_{p,N}^{\mathbb{R}} = O(N)/[O(p) \times O(N - p)], \quad (5.6)$$

which parametrizes all possible ways to split an N -dimensional real vector space into orthogonal subspaces of dimensions p and $N - p$.

While complex vector bundles are characterized by integer-valued Chern classes $c_n \in \mathbb{Z}$, real vector bundles exhibit a fundamentally different topology through the Stiefel-Whitney classes $\omega_n \in \mathbb{Z}_2$ [172]. The distinction between \mathbb{Z} and \mathbb{Z}_2 invariants reflects the different nature of orientability in real and complex spaces⁵. Additionally, the Euler class $\chi \in \mathbb{Z}$, emerges as a fragile topological invariant⁶, which we will consider in Section 5.3.1.

The physical meaning of the Stiefel-Whitney class becomes clear when considering the Berry-phase along non-contractible paths in the Brillouin zone (for example, in k or α direction). The first Stiefel-Whitney class manifests as a geometric phase accumulated when transporting states along such paths. When this class is non-zero,

⁴These degeneracies arise from the freedom to perform orthogonal transformations within each eigenspace while preserving the spectral flattening.

⁵In complex vector bundles, phases can wind continuously, leading to integer classifications. In real vector bundles, only sign changes are possible, resulting in \mathbb{Z}_2 classifications.

⁶The Euler class is "fragile" because, unlike the Stiefel-Whitney classes, it can be destroyed by adding trivial bands [210].

it becomes impossible to define $R(\mathbf{k})$ consistently throughout the Brillouin zone – attempting to do so results in a sign ambiguity $R(\mathbf{k}) \rightarrow -R(\mathbf{k})$ upon completing certain closed paths (this is in direct correspondence to the scenario in Section 4.2). This mathematical obstruction directly reflects the non-orientability of the vector bundle, analogous to the twist in a Möbius strip⁷.

Now, let us consider again the case of non-degenerate Hamiltonians [230]. Each eigenvector can be multiplied with ± 1 (which corresponds to $O(1)$), hence the space of Hamiltonians is just the coset space $O(N)/O(1)^N$.

5.2.2 Non-abelian charges

Already for $N = 3$ the implications of the preceding discussion lead to non-trivial aspects. The space of Hamiltonians turns into

$$O(3)/O(1)^3 = O(3)/\mathbb{Z}_2^3 = SO(3)/D_2, \quad (5.7)$$

with the Dihedral group D_2 ⁸. The band nodes in this system carry topological charges that extend beyond the usual \mathbb{Z}_2 classification. These charges manifest through the first homotopy group

$$\pi_1(SO(3)/D_2) = \mathbb{Q}, \quad (5.8)$$

where \mathbb{Q} is the non-abelian quaternion group [230]

$$\mathbb{Q} = \{1, \pm \mathbf{i}, \pm \mathbf{j}, \pm \mathbf{k}, -1\}. \quad (5.9)$$

satisfying

$$\mathbf{i}^2 = \mathbf{j}^2 = \mathbf{k}^2 = \mathbf{ijk} = -1. \quad (5.10)$$

⁷Just as one cannot define a continuous normal vector field on a Möbius strip, one cannot define continuous real wavefunctions globally when the first Stiefel-Whitney class non-zero $\omega_1 \neq 0$.

⁸See p.34 in [235].

The quaternions form a non-abelian group, sharing this property with the more familiar $SU(2)$ group of Pauli matrices. This connection becomes precise through a one-to-one correspondence

$$\mathbf{i} = -i\sigma_1, \quad \mathbf{j} = -i\sigma_2, \quad \mathbf{k} = -i\sigma_3. \quad (5.11)$$

From this mapping or directly from (5.10), we find that any two different elements $a, b \in \mathbb{Q}$ anticommute with $ab = -ba$.

The physical significance of these quaternion charges can be understood through individual Berry phases. When encircling a band node, each band σ accumulates a Berry phase $\gamma_\sigma \in \{\pm 1/2\}$, see (4.32), that maps directly to a specific element of the quaternion group. We can see this by looking at the rotation matrix $R(\mathbf{k})$ defined in (5.5), where the rotation matrix can be written [230] in terms of rotation matrices L_σ with $\sigma \in \{x, y, z\}$ such that

$$R(k) = \exp[(k + \pi)L_\sigma/2] \quad (5.12)$$

where the charges $\mathbf{i}, \mathbf{j}, \mathbf{k}$ correspond now to clockwise rotations around σ , i. e. the three band indices respectively. While the Berry phase indicates whether a nodal line is encircled, the quaternionic charge specifies the eigenframe rotation axis.

This mapping reveals a profound consequence: since band nodes of different bands correspond to distinct quaternion elements, they must be non-commutative, just as rotations. Specifically, when two band nodes of different gaps exchange positions - a process we call braiding - they can flip their associated \mathbb{Z}_2 frame charges⁹. These braiding rules mirror the familiar non-commutative nature of spin rotations in quantum mechanics [209]. This non-commutativity has profound implications for our physical system. When we braid band nodes carrying quaternion charges, their order matters - braiding node A around node B produces a different result than braiding B

⁹We call them frame charges, because they are gauge-dependent, since there is a higher gauge symmetry than just $U(1)$.

around A . The anti-commutation relations directly determine how the frame charges transform under braiding operations [209].

The non-abelian nature of these charges leads to a remarkable phenomenon: Consider a pair of nodes (of the same gap) with $(+1)$, (-1) frame charge. The sign of one of the node's frame charge can be reversed through braiding with a node hosted in either adjacent gaps (i. e. the gap directly above or below). Afterwards, the two band nodes (of the same gap) cannot annihilate each other, since they both carry the same \mathbb{Z}_2 frame charge, which reflects the anticommuting algebra of the quaternion elements [209, 210, 226]. This property distinguishes our system from conventional topological insulators, where braiding typically results in Abelian phase factors.

The connection between the geometric phases we studied in Section 5.2 and these non-abelian charges becomes clear: the impossibility of defining a global frame (non-orientability) manifests as discrete quaternion charges that cannot be continuously deformed into one another. This discrete nature, combined with the anticommuting property of quaternions, ensures the robustness of the non-abelian braiding operations.

However, to make this analogy precise and explain what we mean by "commutation" of band nodes, we must first introduce the concept of *Dirac strings* in the next Section.

5.2.3 Dirac strings of topological charges

In systems with magnetic monopoles (and hence topological charges, see Section 4.2.2), we observe the physical manifestation of Dirac strings – mathematical objects that have drawn significant attention since Dirac's foundational work [236] and which we will explain in detail below. While these strings remain elusive in fundamental physics despite intensive searches [237], our system provides a

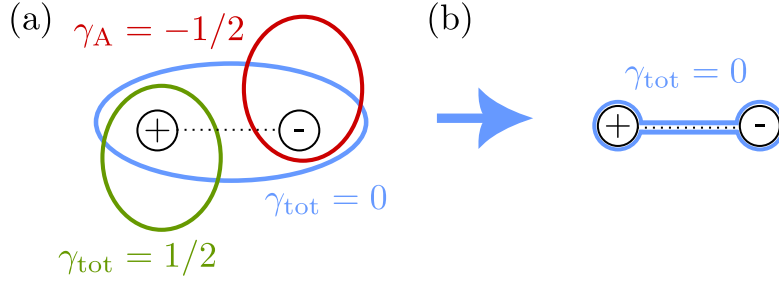


Figure 5.1: Dirac strings between nodal points. (a) A large contour (blue) encircling two band nodes yields zero total Berry phase, while individual contours (red and green) around each node reveal opposite charges ($\pm 1/2$). (b) When continuously shrinking the blue contour, the phase must discontinuously jump from $+1/2$ to $-1/2$ between the nodes through a Dirac string. The band nodes prevent the contour from being reduced to a point, creating an unavoidable obstruction. This structure is classified by the first Stiefel-Whitney class ω_1 , which captures the impossibility of choosing consistent signs for real wavefunctions across the region.

platform where these theoretical constructs become tangible and measurable [75].

The existence of these Dirac strings in our system follows from basic topological arguments. In Section 4.3.1, we established how band nodes form and relate to topological charges. Consider a pair of band nodes of the same gap with opposite charges $\gamma_A = 1/2, \gamma_B = -1/2$, as shown in Fig. 5.1. A large contour \mathcal{C} encircling both nodes yields zero total Berry phase

$$\gamma_{\text{total}} = \frac{1}{2\pi} \oint_{\mathcal{C}} A(\mathbf{k}) \cdot d\mathbf{k} = 0. \quad (5.13)$$

When we continuously deform this contour to decrease its radius, we cannot shrink it to a point - the two band nodes act as obstructions, each contributing $\pm 1/2$ to the Berry phase. This requires a sign change from $+\pi$ to $-\pi$ between the nodes, manifesting as a line of discontinuity - the *Dirac string* - connecting the two nodes where the phase flips sign. While the string's position depends on gauge choice, its endpoints remain fixed at the band nodes, making them physically observable through various experimental techniques. When

5. NON-ABELIAN TOPOLOGICAL PHASES

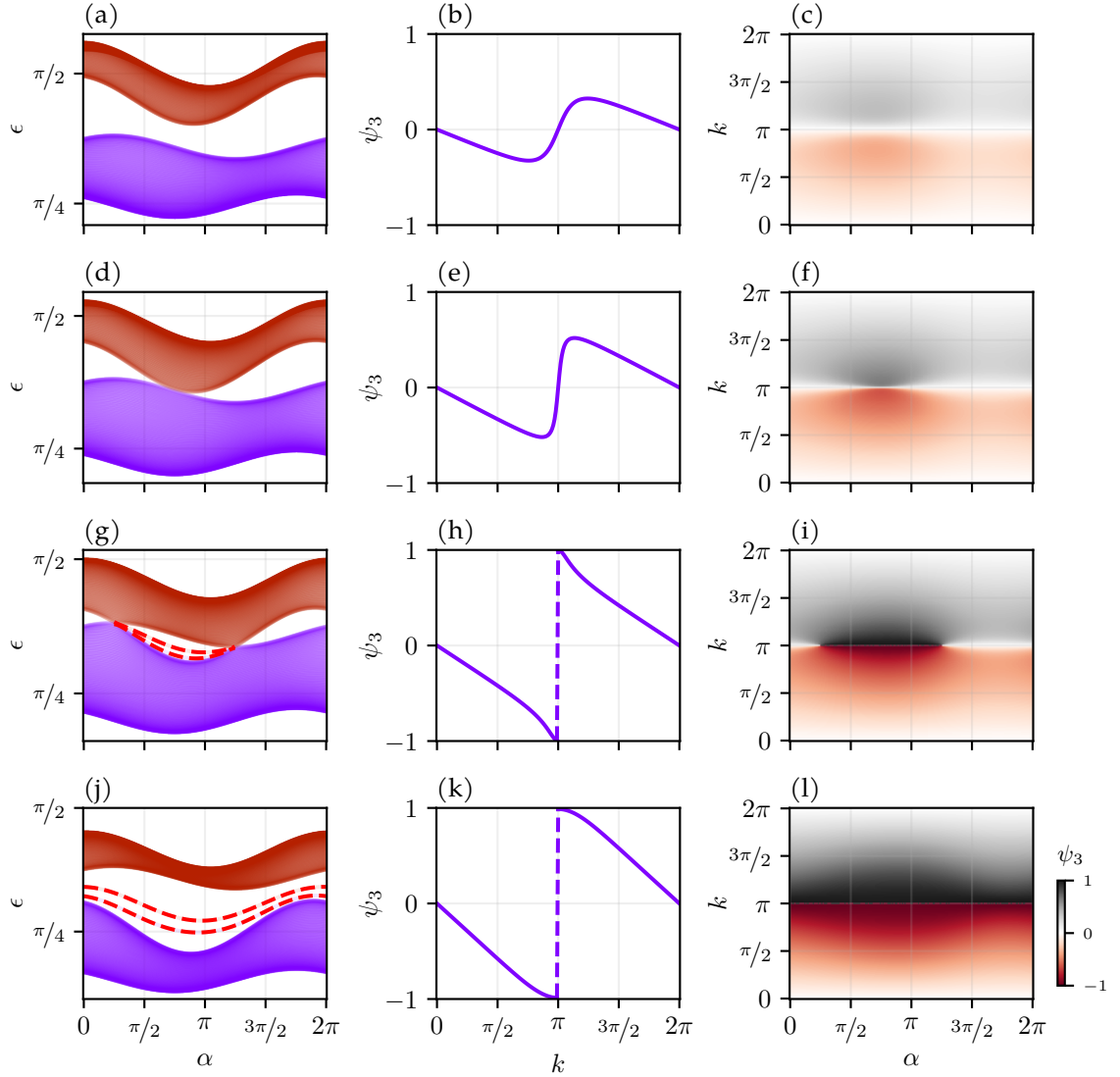


Figure 5.2: Creation of a lone Dirac string. Kicked 3D rotor system as in Fig. 4.6. Each row shows: quasi-energies for lower two bands (left), wavefunction component ψ_3 (of first band) at $\alpha = \pi$ (middle), and as a function of both k, α (right). Evolution from top to bottom: no nodes/strings (a-c), quadratic node appears (d-f), splits into two linear nodes (g-i), and after node annihilation at the boundary, a lone Dirac string remains (j-l). While the Dirac string's shape is gauge-dependent, its endpoints are fixed by band nodes when present. In (j-l), the sole existence of the string (connecting left to right) is protected by the Stiefel-Whitney class ω_1 .

band nodes annihilate across the periodic boundary, they create a particularly interesting state: a persistent Dirac string protected by the inability to smoothly transform it away. In Fig. 5.2, we examine this process in our kicked rotor system with $N = 3$ ¹⁰. The system evolves through several distinct phases: First, we create a quadratic node, which splits into two linear (Dirac) nodes, and finally these nodes annihilate across the periodic boundary. This process leaves behind a Dirac string that remains stable against gauge transformations and small perturbations. While the band nodes are visible in the band structure, they also manifest in the wavefunction. To analyze this, we examine the third component ψ_3 of the first band's wavefunction¹¹ as a function of momentum. Band nodes emerge as phase vortices with non-zero contour integrals. In the second column, we show the wavefunction component ψ_3 at $\alpha = \pi$, which visualizes the Dirac string as a discontinuous jump from -1 to $+1$. In fact, the non-zero Berry phases around individual nodes can be understood as a direct consequence of this Dirac string.

The node annihilation at the periodic boundary ($\alpha = 0$) creates a persistent Dirac string, ensuring a non-zero Berry phase in the k -direction across all α (this is sometimes also called *Zak-phase*, since it's around a non-contractible direction of the Brillouin zone). This provides another interpretation of the bulk-boundary correspondence: the topological phase with edge states arises from node creation and annihilation, resulting in a non-trivial first Stiefel-Whitney class ω_1 . Thus, we conclude that the process of nodal point annihilation across periodic boundaries in k -space naturally leads to a non-trivial Berry phase in the α -direction.

The phenomena we have discussed here – band nodes, their Dirac

¹⁰We use $(P_1, P_2) = (0.1 \sin(\alpha) + 0.5r, 0.2 \cos(\alpha) + (2 - r))$ where r controls the topological regime: $r < 0.85$ trivial, $r > 1.15$ topological, with a gapless phase between. Parameters: (a-c) $r = 0.70$, (d-f) $r = 0.85$, (g-i) $r = 1.0$, (j-l) $r = 1.3$.

¹¹We examine ψ_3 in a gauge where $\psi_1 \geq 0$, achieved via $\tilde{\psi}_\sigma(\mathbf{k}) = \psi_\sigma(\mathbf{k}) \text{sign}[\psi_1(\mathbf{k})]$, ensuring wavefunction smoothness everywhere except at the Dirac string, where this non-smoothness cannot be removed by any gauge choice.

strings, and their annihilation – can occur in simple two-band abelian systems. The concept of Dirac strings, however, proves essential for understanding the deeper implications of non-abelian band nodes. With this foundation, we can now analyze how the non-commutative nature of multi-band systems leading to the braiding of band nodes that we introduced in Section 5.2.2. The nodal lines shown in the phase diagram in Fig. 4.2 play a central role in this analysis. Non-abelian braiding of band nodes requires specific crossings of nodal lines between different bands. Each nodal line carries both a \mathbb{Z}_2 frame charge and a quaternionic charge, with the latter depending on the exchange order with other nodal lines. The non-commutative nature emerges when nodal lines of different gaps encircle each other [209, 210, 230], with the specific behavior determined by the encircling path.

Although this physics might be accessible in the simple kicked rotor for very high kicking strengths, we now turn to a slightly more complex model where these effects arise naturally even at small kicking strength.

5.3 The triple-kicked rotor

Let us construct a system that manifests the non-abelian phenomena we discussed in the previous section at experimentally accessible kicking strengths¹². We combine three kicked rotors into a single Floquet operator that preserves both time-reversal and inversion symmetry¹³

$$U_{\text{TKR}}(\mathbf{P}) = U_{\text{KR}}(P_1, P_2)U_{\text{KR}}(P_3, P_4)U_{\text{KR}}(P_1, P_2). \quad (5.14)$$

This triple-kicked rotor, parametrized by $\mathbf{P} = (P_1, P_2, P_3, P_4)$, extends our previous analysis of Dirac strings and band nodes to a

¹²This section is based on our recent submitted paper [5].

¹³See footnote 17.

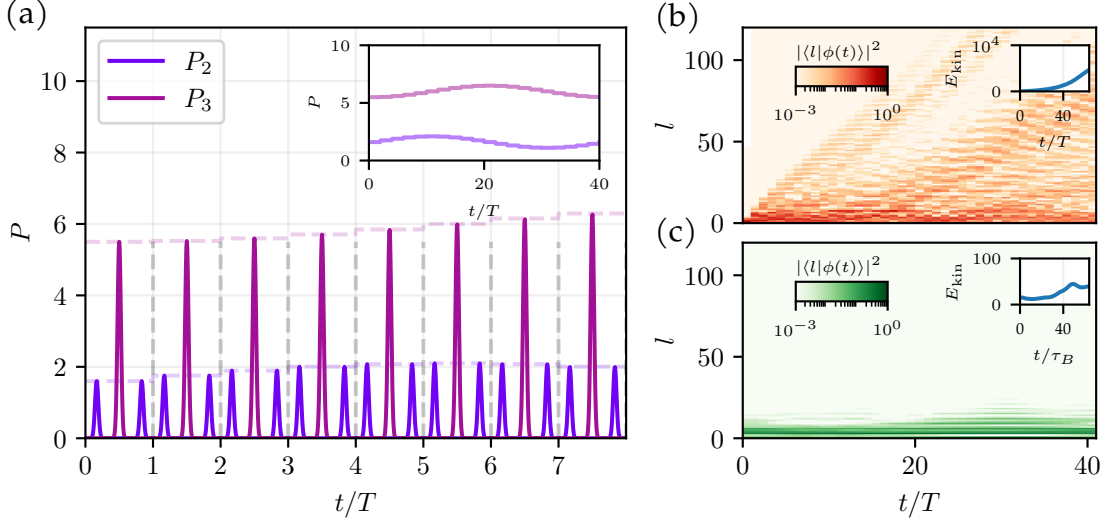


Figure 5.3: Triple-kicked rotor (5.14). We use $P_2 = P_3 = 0$, which reduces the protocol to two infrared pulses and one terahertz pulse within each Floquet period. We vary the pulse strengths stroboscopically on a circular path (see main text). In (a) we show the Pulse sequence, the inset shows the variation of pulse strengths over the entire protocol, spanning $N_\gamma = 40$ iterations with three pulses per sequence within each of which α is adjusted as $\alpha_n = 2\pi n/N_\gamma$. In (b) and (c) we show the full time evolution of a driven rotor under this protocol, see Section 4.4.1. (b) Starting with typical thermal state (with $\pi/(\tau_B k_B T) = 0.17$), we observe resonant energy absorption ($E_{\text{kin}} = \langle \hat{\mathbf{L}}^2 \rangle \approx 5 \cdot 10^3$), as expected for a generic initial state in this system. Conversely, (c) showcases an edge state (with the same initial energy) that persists throughout the protocol and absorbs little energy ($\langle \hat{\mathbf{L}}^2 \rangle \approx 50$). Significantly, this is an anomalous π -gap topological edge state, which we will later show is a witness of the anomalous Dirac String phase and exists even though all Berry phases are zero.

regime where non-abelian effects emerge naturally. As shown in Fig. 5.3, we can implement this protocol¹⁴ using linear molecules driven by a sequence of infrared and terahertz laser pulses (see Chapter 2 for the molecular physics details). The time evolution in Fig. 5.3(b,c) already reveals two distinct behaviors: generic states show delocalization dynamics, while an edge states of the π -gap

¹⁴The pulse strengths vary as $(P_2, P_3) = (1.6 + \sin(\alpha)/2, 6.0 - \cos(\alpha)/2)$ with synthetic dimension $\alpha \in [0, 2\pi]$.

5. NON-ABELIAN TOPOLOGICAL PHASES

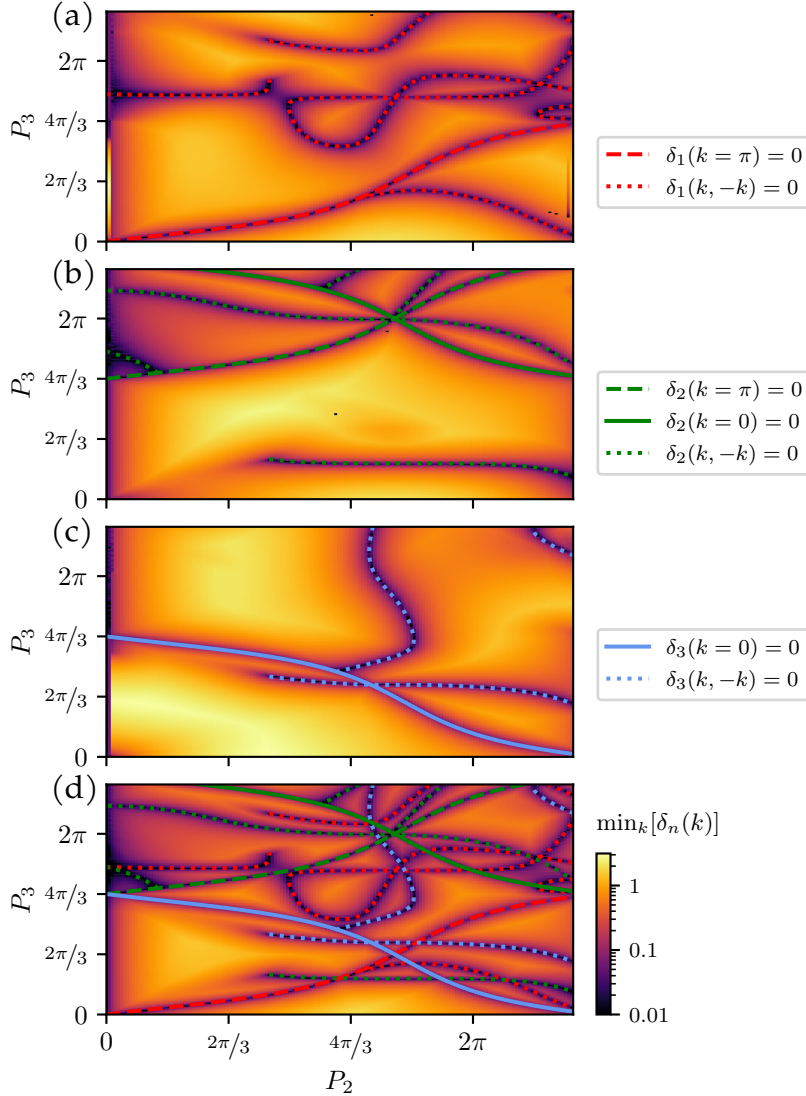


Figure 5.4: Nodal lines of the triple-kicked rotor. Gap functions δ_n between adjacent bands: (a) δ_1 , (b) δ_2 , and (c) δ_3 (which corresponds to the π -gap). Panel (d) shows the minimal gap $\min_n(\delta_n)$. Colors mark nodal lines of different gaps at $k = \pi$ (dashed), $k = 0$ (solid) and $(k, -k)$ pairs (dotted).

remains localized even though the Berry phases are zero— a direct consequence of the system’s topological structure, as we will see later. The phase diagram in Fig. 5.4 reveals how our previous single-

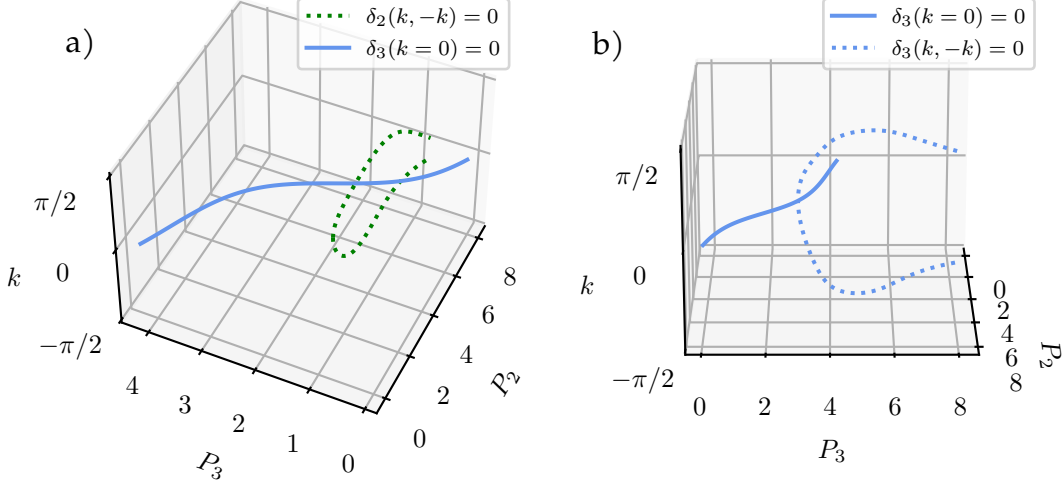


Figure 5.5: Dispersing nodal lines of the triple-kicked rotor. Non-abelian braiding in (k, P_2, P_3) space using parameters from Fig. 5.4. (a) A nodal line in the second gap (green) winds around a nodal line in the third gap (blue), demonstrating their non-abelian braiding. (b) Formation of a $(k, -k)$ nodal line pair encircling a $k = 0$ nodal line. Additional nodal lines omitted for clarity.

gap nodal lines transform¹⁵ in this multi-gap system. These lines emerge from symmetric points $k = 0$ and $k = \pi$, extending through parameter space under the control of the kicking strengths. The two-dimensional projections suggest that nodal lines from different gaps intersect. However, Fig. 5.5 shows their actual three-dimensional structure: lines from different gaps pass by each other at distinct quasi-momenta k . We also observe how a single nodal line at $k = 0$ generates a pair of $(k, -k)$ nodal lines. As we will see in the following, this three-dimensional arrangement of nodal line crossings enables non-abelian braiding: when nodal lines of different gaps cross, their associated topological charges interact non-commutatively, manifesting the quaternionic algebra we derived in Section 5.2.2.

¹⁵Here, we have evaluated all nodal lines by numerical homotopy continuation, see [238].

5.3.1 Euler class and non-abelian braiding

Let us now introduce the mathematical structure that captures the topological obstruction against annihilating band nodes¹⁶. Consider two adjacent bands n and $n + 1$ within a patch D of the Brillouin zone. The obstruction is quantified by the path Euler class [210]

$$\chi_{n,n+1}^D = \frac{1}{2\pi} \left(\oint_D \text{Eu}(\mathbf{k}) \, dk \wedge d\alpha - \oint_{\partial D} A_{n,n+1}(\mathbf{k}) \cdot d\mathbf{k} \right) \in \mathbb{Z}, \quad (5.15)$$

which consists of two terms. The first involves the Euler two-form

$$\text{Eu}(\mathbf{k}) = \langle \partial_k \psi_n | \partial_\alpha \psi_{n+1} \rangle - \langle \partial_\alpha \psi_n | \partial_k \psi_{n+1} \rangle, \quad (5.16)$$

measuring how the wavefunctions $\psi_n(\mathbf{k})$ and $\psi_{n+1}(\mathbf{k})$ twist relative to each other as we move through the Brillouin zone. The second term involves the non-abelian Berry connection

$$A_{n,n+1}(\mathbf{k}) = \langle \psi_n(\mathbf{k}) | \nabla \psi_{n+1}(\mathbf{k}) \rangle, \quad (5.17)$$

which captures the interband geometric phase accumulated along the boundary of the patch. When band nodes are created in pairs from the vacuum, they naturally carry opposite charges, resulting in a vanishing patch Euler class. However, this can change when we consider the case when band nodes of adjacent gaps exchange positions with these nodes, since this exhibits non-abelian behavior. To demonstrate this, let us examine a sequence of manipulations in our kicked rotor system¹⁷, illustrated in Fig. 5.6.

Starting with a single pair of band nodes (first column) with opposite charges, yielding a zero Euler class within the corresponding patch.

¹⁶The concepts presented in this section build upon additional mathematical foundations beyond the scope of our current discussion. For a comprehensive understanding, we recommend consulting the referenced literature.

¹⁷The parameter evolution follows $f(x, y, \beta) = (0.7 + \frac{3\beta}{4}(y + 1), (1 + 5\beta(x + 1), 0.7 + \frac{3\beta}{2}(y + 1)), 0.4 + 2\beta(x + 1))$ with $\beta = 0.15$ (first column), $\beta = 0.21$ (second column), $\beta = 0.3$ (third column), though the phenomenon is robust across different parameter choices.

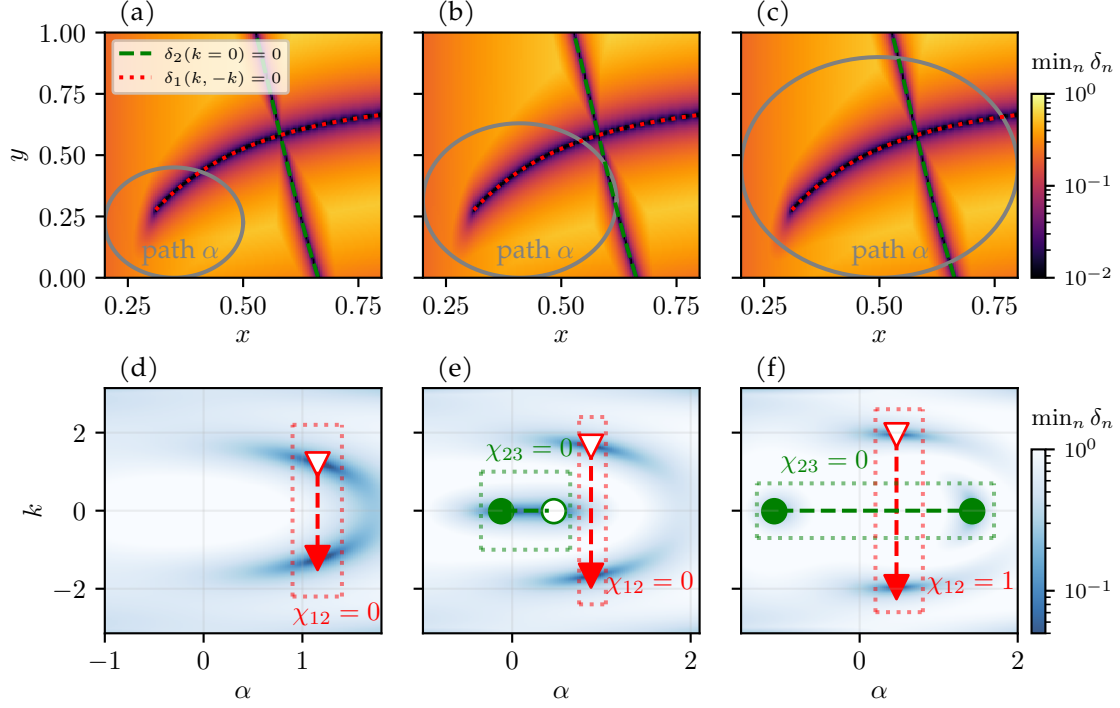


Figure 5.6: Non-abelian braiding demonstrated in the triple-kicked rotor. The columns show three different parameter configurations, with the upper row displaying the paths through parameter space and the corresponding nodal lines (red and green), while the lower row shows the resulting gap functions of the corresponding paths. (a,d) A path crossing the red nodal line, creating an oppositely charged pair. (b,e) Additional crossing of the green nodal line, creating a second pair while maintaining trivial Euler classes. (c,f) Path showing the green node having crossed the Dirac string of the red pair, altering the charge structure, see main text. Note that fundamentally, the origin of this behavior is the crossing of the red and green nodal line in phase space.

Then (second column) we create a second pair of nodes, marked by intersections with the nodal line of the second gap (green line in Fig. 5.6(b)). At this stage, both patches maintain trivial Euler classes, as expected for nodes created from vacuum.

The non-abelian nature of the system reveals itself when we move the green band node through the Dirac string of the red pair (third column). This braiding operation alters the charge structure: we end

up with two equally charged green band nodes. While the total Euler class remains zero due to the Dirac string contribution, the patch containing the band nodes of the other gap now carries an Euler class of one. This transformation demonstrates how frame charges can be modified through braiding, creating topological obstructions that prevent node annihilation unless their charges are realigned through further braiding operations.

5.4 Anomalous Dirac-String phase

The \mathbb{Z}_2 Berry phases alone cannot fully capture the rich non-equilibrium topological phenomena in our system [226, 228]. This limitation arises from a unique feature of the periodically-kicked quantum rotor: it can support a nodal line in the anomalous π -gap (δ_3), a direct consequence of the 2π -periodicity of quasienergies.

Fig. 5.7 reveals this richness through a phase diagram where we track both nodal lines and Berry phases. Following the marked path from the trivial phase (gray area), we encounter a sequence of topological transitions. Remarkably, after crossing nodal lines in each gap, we arrive at another phase with vanishing Berry phases. Despite sharing the same Berry phases, these phases are topologically distinct— one cannot transform between them without closing gaps [228]. This novel state, termed the anomalous Dirac string phase [226], emerges from the system's non-equilibrium nature and manifests through nodal lines in all quasienergy gaps. Its topological character becomes evident in Fig. 5.8(c), where we observe edge states in every gap, including the anomalous π -gap.

A crucial aspect here is that it's possible to align pairs of Dirac strings through smooth gauge transformations, leading to mutual cancellation. The Berry phase γ_n thus only indicates the parity of Dirac strings along a path. Each nodal line fixed at $k = 0$ or $k = \pi$ marks a phase boundary where the Berry phases (in k -direction) of the corre-

5.4. Anomalous Dirac-String phase

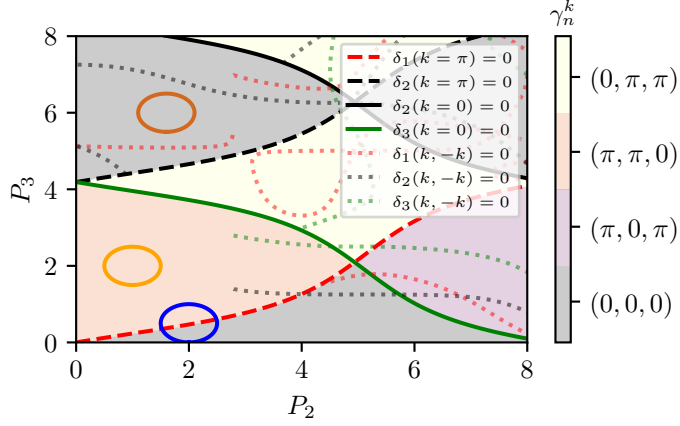


Figure 5.7: Phase diagram for triple kicked rotor. Same as Fig. 5.3, but here with Berry phases γ in k -direction for all bands. Nodal lines as before. Additionally, the three paths for Fig. 5.8 (below) are shown as blue, orange, and brown solid lines.

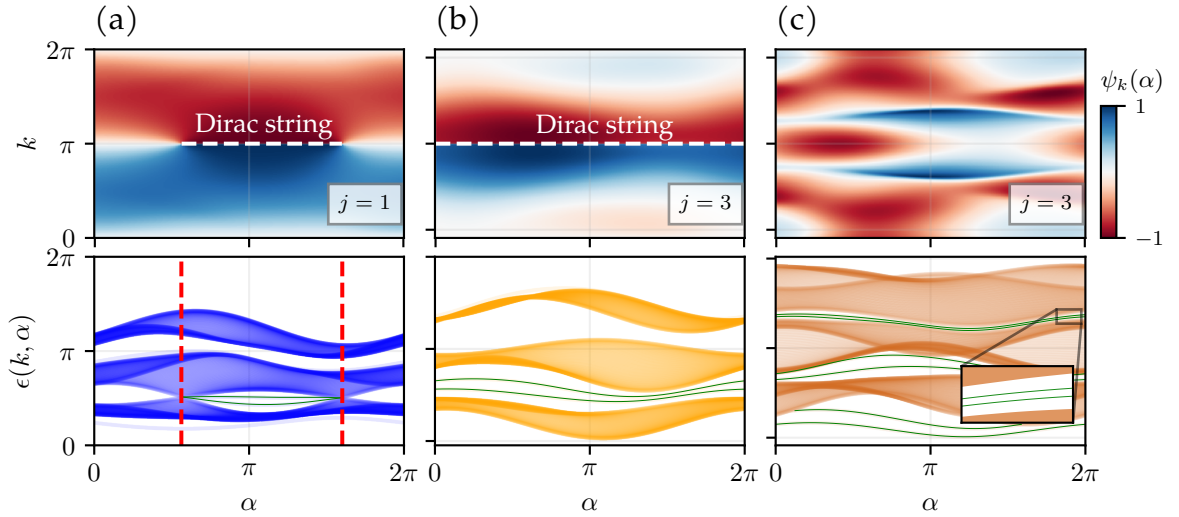


Figure 5.8: Anomalous Dirac string phase. Evolution of the system along paths marked in Fig. 5.7. Upper panels show the j th component of the $n = 2$ eigenstate, while lower panels display the corresponding quasienergy spectrum. (b) Annihilation of two nodal points over the periodic boundary leaves their Dirac string, changing Berry phases to $\gamma_1^k = \gamma_2^k = \pi$ and inducing edge states. (c) After crossing two additional nodal lines, the Berry phase of each band returns to zero due to the nodal line in the anomalous gap (δ_3), enabled by periodic kicking—a signature of the anomalous Dirac string phase with edge modes in each gap.

sponding bands switch between 0 and π . For instance, a nodal line between the first and second band at $k = \pi$ (i. e. with $\delta_1(k = \pi, P) = 0$), shown as a red dashed line, triggers such a Berry phase transition in both bands.

5.5 Outlook

The exploration of non-abelian topology in driven quantum systems reveals a rich landscape of phenomena that transcend conventional static classifications. We have seen how the patch Euler class, (5.15), provides a mathematical framework for real systems that allows us to understand topological obstructions in band node manipulation, leading to non-abelian braiding behavior when nodal lines of adjacent gaps exchange positions. This braiding manifests through the modification of frame charges, creating topological constraints that prevent arbitrary node annihilation unless specific braiding operations realign their charges.

Most remarkably, the combination of this non-abelian character with the periodic nature of the quasi-energies in Floquet systems gives rise to novel topological phases without static analogues. The anomalous Dirac string phase exemplifies this uniqueness – it harbors edge states in all gaps despite displaying trivial Berry phases, demonstrating how traditional band invariants fail to capture the full richness of driven quantum matter. This phase emerges from the intricate interplay between periodic quasienergies, multiple band gaps, and the manipulation of Dirac strings.

CHAPTER 6

Conclusion

All success cloaks a surrender.

– Simone de Beauvoir

6.1 Summary

As we close this inquiry into driven quantum rotors¹, our work shows how linear molecules under strong periodic pulses become elegant platforms for probing fundamental physics. Our studies demonstrate that quantum rotation – typically related to molecular spectroscopy – gives rise to mathematical structures and topological phenomena that persist even at room temperature.

This story began with a deceptively simple question: How does a molecule respond to ultrashort laser pulses? Pursuing this question led us to reexamine the foundations of laser-molecule interactions, where we identified subtle quantum interference effects hidden beneath the standard sudden approximation. These effects, while significant in their own right, opened an unexpected direction. By applying multiple pulses in sequence, we found that molecular rota-

¹For structured summary of the chapters, please refer to Section 1.4 of the introduction.

6. CONCLUSION

tions could be transformed into a synthetic crystal – not in physical space, but in the abstract space of angular momentum.

This crystalline structure in angular momentum exhibited novel properties beyond our expectations: The intrinsic symmetries of the system, combined with periodic driving, generated topological properties previously observed only in few solid-state materials. Dirac cones emerged naturally in our system, their topological charges protected by the very symmetries from which they arose. An important finding occurred when we extended our model to include three or more bands; then these Dirac cones showed their nature as non-abelian entities.

The manifestation of non-abelian physics in such a conceptually accessible system is closely linked to fundamental physics. The same Dirac strings that continue to elude particle physicists in their search for magnetic monopoles appear naturally in our driven molecules, where they can be studied and manipulated through specifically chosen laser pulses. Through our triple-kicked rotor protocol, we demonstrated the braiding of these non-abelian charges, uncovering an anomalous Dirac string phase unique to driven systems – a phase hosting topological edge modes in every gap despite vanishing Berry phases.

While these abstract phenomena translate into measurable molecular alignment signals at room temperature, the implications extend well beyond molecular physics. Quantum rotors now appear across diverse physical systems: driven Bose-Einstein condensates, nanorotors, and as quasiparticles – rotational states of excitons, polaritons, the recently characterized angulons, and Laughlin quasi-holes. Each manifestation provides insights into fundamental physics, showing connections between seemingly disparate phenomena.

Our work establishes quantum rotors as versatile platforms for investigating topological phenomena. The ability to precisely engineer band structures in experiment offers distinct advantages over con-

ventional solid-state systems, particularly for exploring non-abelian multi-band topology. Their experimental accessibility makes them valuable both for learning about fundamental aspects such as Dirac strings, but also as potential building blocks in emerging quantum technologies.

6.2 Future directions

The exploration of periodically-driven quantum rotors suggests several research directions, spanning from practical applications in physical chemistry to fundamental questions in quantum theory. Here, we outline several directions that follow up on the theoretical foundations established in this thesis.

At the most immediate level, our understanding of quantum resonances and periodic driving indicates novel approaches to chemical reaction control. The ability to manipulate molecular rotation with laser pulses, combined with our understanding of the non-abelian nature of rotational dynamics, presents new possibilities for controlling quantum states of linear molecules and their orientation and alignment signals [27, 33]. This control, particularly in regard to going beyond the traditional picture of conical intersections, becomes instrumental for selective bond manipulation – a critical component for engineering chemical reactions and synthesis [116].

The connection to many-body physics presents an intriguing direction, such as rotational impurities in quantum baths – the recently-discovered angulon quasiparticles [33, 239] – subjected to periodic driving. Earlier work indicates that bath-impurity coupling leads to collective quantum states, potentially creating controlled non-abelian excitations analogous to those in fractional quantum Hall systems [35]. We propose probing and controlling these states through periodic pulses, potentially leading to topological phase transitions and novel intermediate regimes. This connection extends to lattices

6. CONCLUSION

of ultracold molecules in optical tweezers [240], where periodic driving could generate topologically protected many-body states [241].

Beyond atomic and molecular physics, our findings suggest innovative approaches to materials science. Driven rotational impurities in solid-state systems, when populated into topological states, could modify material properties in controllable ways. Recent research indicates that polaronic rotational states enhance photovoltaic efficiency in lead-halide perovskites [242, 243]. Through specific driving protocols, it may become possible to control these rotational states and develop new mechanisms for quantum transport. The ability to influence material properties through topological control of molecular rotation suggests promising directions for materials design and optimization.

These directions represent both extensions of our current work and gateways to novel areas of study. As we hope to have demonstrated, the driven quantum rotor – whether manifesting as a molecule, quasiparticle, or abstract mathematical structure – bridges topology with quantum dynamics in ways that extend far beyond traditional approaches. This connection offers unique opportunities to explore fundamental or applied physics with exceptional control over system parameters. As this field evolves, quantum rotors could become exemplary platforms where theoretical insights converge with experimental accessibility.

Bibliography

- [1] Volker Karle, Maksym Serbyn, and Alexios A. Michailidis. “Area-Law Entangled Eigenstates from Nullspaces of Local Hamiltonians”. In: *Physical Review Letters* 127 (2021), p. 060602. DOI: [10.1103/PhysRevLett.127.060602](https://doi.org/10.1103/PhysRevLett.127.060602).
- [2] Volker Karle, Areg Ghazaryan, and Mikhail Lemeshko. “Topological charges of periodically kicked molecules”. In: *Physical Review Letters* 130.10 (2023), p. 103202. DOI: [10.1103/PhysRevLett.130.103202](https://doi.org/10.1103/PhysRevLett.130.103202).
- [3] Volker Karle and Mikhail Lemeshko. “Die faszinierende Topologie rotierender Quanten: Rotierende Moleküle in starken Feldern”. In: *Physik in unserer Zeit* 55.1 (2024), pp. 28–33. DOI: [10.1002/piuz.202301690](https://doi.org/10.1002/piuz.202301690).
- [4] Volker Karle and Mikhail Lemeshko. “Modeling laser pulses as δ kicks: Reevaluating the impulsive limit in molecular rotational dynamics”. In: *Physical Review A* 109 (2024), p. 023101. DOI: [10.1103/PhysRevA.109.023101](https://doi.org/10.1103/PhysRevA.109.023101).
- [5] Volker Karle, Mikhail Lemeshko, Adrien Bouhon, Robert-Jan Slager, and F. Nur Ünal. *Anomalous multi-gap topological phases in periodically driven quantum rotors*. 2024. arXiv: [2408.16848](https://arxiv.org/abs/2408.16848).
- [6] Marlan O Scully and M Suhail Zubairy. *Quantum optics*. Cambridge University Press, 1997. DOI: [10.1017/CB09780511813993](https://doi.org/10.1017/CB09780511813993).

- [7] Asger Aaboe. "Scientific astronomy in antiquity". In: *Philosophical Transactions of the Royal Society of London. Series A , Mathematical and Physical Sciences* 276.1257 (1974), pp. 21–42. DOI: <https://doi.org/10.1098/rsta.1974.0007>.
- [8] Alexander Raymond Jones. *Ptolemaic system*. Encyclopedia Britannica. Accessed 25 November 2024. Aug. 2024. URL: <https://www.britannica.com/science/Ptolemaic-system>.
- [9] J. Freely. *Light from the East: How the Science of Medieval Islam Helped to Shape the Western World*. Bloomsbury Academic, 2015. ISBN: 9781784531386. URL: <https://books.google.at/books?id=JNQZCAAQBAJ>.
- [10] George Saliba. *Islamic science and the making of the European renaissance*. Mit Press, 2007. DOI: [10.7551/mitpress/3981.001.0001](https://doi.org/10.7551/mitpress/3981.001.0001).
- [11] Otto Neugebauer. "A History of Ancient Mathematical Astronomy". In: *Journal for the History of Astronomy, Vol. 9, p. 201* 9 (1978), p. 201. DOI: [10.1007/978-3-642-61910-6](https://doi.org/10.1007/978-3-642-61910-6).
- [12] Leonhard Euler. *Theoria motus corporum solidorum seu rigidorum*. Latin. 1st ed. Vol. 3. Opera Mechanica. Rostochii et Gryphiswaldiae: Rostochium, 1765, p. 520.
- [13] ARP Rau. "The asymmetric rotor as a model for localization". In: *Reviews of Modern Physics* 64.2 (1992), p. 623. DOI: [10.1103/RevModPhys.64.623](https://doi.org/10.1103/RevModPhys.64.623).
- [14] Lev D. Landau and Evgeny M. Lifshitz. *Mechanics*. 3rd ed. Vol. 1. Course of Theoretical Physics. Butterworth-Heinemann, 1976. ISBN: 9780750628969.
- [15] Herbert Goldstein, Charles P. Poole, and John L. Safko. *Classical Mechanics*. 3rd. Addison Wesley, 2002, pp. 150–152.

-
- [16] Yue Ma, Kiran E. Khosla, Benjamin A. Stickler, and M. S. Kim. “Quantum Persistent Tennis Racket Dynamics of Nanorotors”. In: *Physical Review Letters* 125 (5 July 2020), p. 053604. DOI: [10.1103/PhysRevLett.125.053604](https://doi.org/10.1103/PhysRevLett.125.053604).
- [17] Sabin Rizescu, Alexandru Bolcu, and Leonard Marius Ciurezu-Gherghe. “Adding Some Remarks Concerning the Dzahanibekov Effect”. In: *International Conference of Mechanical Engineering (ICOME-2022)*. Atlantis Press, 2023, pp. 115–121. DOI: [10.2991/978-94-6463-152-4_13](https://doi.org/10.2991/978-94-6463-152-4_13).
- [18] Max Planck. “On the law of distribution of energy in the normal spectrum”. In: *Annalen der physik* 4.553 (1901), p. 1.
- [19] Steven Weinberg. *Lectures on quantum mechanics*. Cambridge University Press, 2015. DOI: [10.1017/CB09781316276105](https://doi.org/10.1017/CB09781316276105).
- [20] James Edward Baggott. *The quantum story: a history in 40 moments*. Oxford University Press, 2011. ISBN: 9780198784777.
- [21] Max Born and Pascual Jordan. “Zur Quantenmechanik”. In: *Zeitschrift für Physik* 34.1 (1925), pp. 858–888.
- [22] J. von Neumann. “Mathematische Begründung der Quantenmechanik”. In: *Nachrichten von der Gesellschaft der Wissenschaften zu Göttingen, Mathematisch-Physikalische Klasse* 1927 (1927), pp. 1–57. URL: <http://eudml.org/doc/59215>.
- [23] Kristian Camilleri. *Heisenberg and the Interpretation of Quantum Mechanics: The Physicist as Philosopher*. Cambridge University Press, 2009.
- [24] Steven Weinberg. *The quantum theory of fields*. Vol. 2. Cambridge University Press, 1995. DOI: [10.1017/CB09781139644167](https://doi.org/10.1017/CB09781139644167).
- [25] Edward Uhler Condon and George Hiram Shortley. *The theory of atomic spectra*. Cambridge University Press, 1935.
- [26] Lawrence C Biedenharn and James D Louck. *Angular momentum in quantum physics: theory and application*. Cambridge University Press, 1984. DOI: [10.1017/CB09780511759888](https://doi.org/10.1017/CB09780511759888).

- [27] Christiane P. Koch, Mikhail Lemeshko, and Dominique Sugny. “Quantum control of molecular rotation”. en. In: *Reviews of Modern Physics* 91.3 (Sept. 2019), p. 035005. ISSN: 0034-6861, 1539-0756. DOI: [10.1103/RevModPhys.91.035005](https://doi.org/10.1103/RevModPhys.91.035005).
- [28] Aage Bohr. “On the Quantization of Angular Momenta in Heavy Nuclei”. In: *Physical Review* 81 (1 Jan. 1951), pp. 134–138. DOI: [10.1103/PhysRev.81.134](https://doi.org/10.1103/PhysRev.81.134). URL: <https://link.aps.org/doi/10.1103/PhysRev.81.134>.
- [29] Benjamin A. Stickler, Björn Schrintski, and Klaus Hornberger. “Rotational Friction and Diffusion of Quantum Rotors”. In: *Physical Review Letters* 121 (4 July 2018), p. 040401. DOI: [10.1103/PhysRevLett.121.040401](https://doi.org/10.1103/PhysRevLett.121.040401).
- [30] Julien Chabé, Gabriel Lemarié, Benoit Grémaud, Dominique Delande, Pascal Szriftgiser, and Jean Claude Garreau. “Experimental Observation of the Anderson Metal-Insulator Transition with Atomic Matter Waves”. In: *Physical Review Letters* 101 (25 Dec. 2008), p. 255702. DOI: [10.1103/PhysRevLett.101.255702](https://doi.org/10.1103/PhysRevLett.101.255702). URL: <https://link.aps.org/doi/10.1103/PhysRevLett.101.255702>.
- [31] Andreas Buchleitner, Dominique Delande, and Jakub Zakrzewski. “Non-dispersive wave packets in periodically driven quantum systems”. In: *Physics reports* 368.5 (2002), pp. 409–547. DOI: [10.1016/S0370-1573\(02\)00270-3](https://doi.org/10.1016/S0370-1573(02)00270-3).
- [32] R. Blümel, A. Buchleitner, R. Graham, L. Sirko, U. Smilansky, and H. Walther. “Dynamical localization in the microwave interaction of Rydberg atoms: The influence of noise”. In: *Physical Review A* 44 (7 Oct. 1991), pp. 4521–4540. DOI: [10.1103/PhysRevA.44.4521](https://doi.org/10.1103/PhysRevA.44.4521).
- [33] Mikhail Lemeshko. “Quasiparticle Approach to Molecules Interacting with Quantum Solvents”. In: *Physical Review Letters* 118 (9 Feb. 2017), p. 095301. DOI: [10.1103/PhysRevLett.118.095301](https://doi.org/10.1103/PhysRevLett.118.095301).

- [34] Y. Nozue, N. Miyahara, S. Takagi, and M. Ueta. “Rotational and vibrational states of excitonic molecules in CuBr studied by the two-photon-resonant Raman scattering”. In: *Solid State Communications* 38.12 (1981), pp. 1199–1202. ISSN: 0038-1098. DOI: [https://doi.org/10.1016/0038-1098\(81\)90987-X](https://doi.org/10.1016/0038-1098(81)90987-X).
- [35] E. Yakaboylu, A. Ghazaryan, D. Lundholm, N. Rougerie, M. Lemeshko, and R. Seiringer. “Quantum impurity model for anyons”. In: *Physical Review B* 102 (14 Oct. 2020), p. 144109. DOI: [10.1103/PhysRevB.102.144109](https://doi.org/10.1103/PhysRevB.102.144109).
- [36] R. B. Laughlin. “Anomalous Quantum Hall Effect: An Incompressible Quantum Fluid with Fractionally Charged Excitations”. In: *Physical Review Letters* 50 (18 May 1983), pp. 1395–1398. DOI: [10.1103/PhysRevLett.50.1395](https://doi.org/10.1103/PhysRevLett.50.1395).
- [37] Daniel Arovas, J. R. Schrieffer, and Frank Wilczek. “Fractional Statistics and the Quantum Hall Effect”. In: *Physical Review Letters* 53 (7 Aug. 1984), pp. 722–723. DOI: [10.1103/PhysRevLett.53.722](https://doi.org/10.1103/PhysRevLett.53.722).
- [38] Jérémy Bert, Emilien Prost, Ilia Tutunnikov, Pierre B éjot, Edouard Hertz, Franck Billard, Bruno Lavorel, Uri Steinitz, Ilya Sh Averbukh, and Olivier Faucher. “Optical imaging of coherent molecular rotors”. In: *Laser & Photonics Reviews* 14.5 (2020), p. 1900344. DOI: [10.1002/lpor.201900344](https://doi.org/10.1002/lpor.201900344).
- [39] Kang Lin, Qiying Song, Xiaochun Gong, Qinying Ji, Haifeng Pan, Jingxin Ding, Heping Zeng, and Jian Wu. “Visualizing molecular unidirectional rotation”. In: *Physical Review A* 92.1 (2015), p. 013410. DOI: [10.1103/PhysRevA.92.013410](https://doi.org/10.1103/PhysRevA.92.013410).
- [40] Kenta Mizuse, Romu Fujimoto, Nobuo Mizutani, and Yasuhiro Ohshima. “Direct imaging of laser-driven ultrafast molecular rotation”. In: *Journal of visualized experiments: JoVE* 120 (2017). DOI: [10.3791/2F54917](https://doi.org/10.3791/2F54917).

- [41] Evangelos T. Karamatskos, Sebastian Raabe, Terry Mullins, Andrea Trabattoni, Philipp Stammer, Gildas Goldsztejn, Rasmus R. Johansen, Karol Długołęcki, Henrik Stapelfeldt, Marc J. J. Vrakking, Sebastian Trippel, Arnaud Rouzee, and Jochen Küpper. “Molecular movie of ultrafast coherent rotational dynamics of OCS”. In: *Nature Communications* 10.1 (Dec. 2019), p. 3364. ISSN: 2041-1723. DOI: [10.1038/s41467-019-11122-y](https://doi.org/10.1038/s41467-019-11122-y).
- [42] Hirofumi Sakai, C. P. Safvan, Jakob Juul Larsen, Karen Marie Hilligso/e, Kasper Hald, and Henrik Stapelfeldt. “Controlling the alignment of neutral molecules by a strong laser field”. In: *The Journal of Chemical Physics* 110.21 (June 1999), pp. 10235–10238. ISSN: 0021-9606, 1089-7690. DOI: [10.1063/1.478039](https://doi.org/10.1063/1.478039).
- [43] Stefan Pabst, Phay J. Ho, and Robin Santra. “Computational studies of x-ray scattering from three-dimensionally-aligned asymmetric-top molecules”. In: *Physical Review A* 81.4 (Apr. 2010), p. 043425. ISSN: 1050-2947, 1094-1622. DOI: [10.1103/PhysRevA.81.043425](https://doi.org/10.1103/PhysRevA.81.043425).
- [44] Ming Zhang, Shuqiao Zhang, Yanwei Xiong, Hankai Zhang, Anatoly A Ischenko, Oriol Vendrell, Xiaolong Dong, Xiangxu Mu, Martin Centurion, Haitan Xu, et al. “Quantum state tomography of molecules by ultrafast diffraction”. In: *Nature communications* 12.1 (2021), p. 5441. DOI: [10.1038/s41467-021-25770-6](https://doi.org/10.1038/s41467-021-25770-6).
- [45] Anders S Mouritzen and Klaus Mølmer. “Quantum state tomography of molecular rotation”. In: *The Journal of chemical physics* 124.24 (2006). DOI: [10.1063/1.2208351](https://doi.org/10.1063/1.2208351).
- [46] Giulio Casati, BV Chirikov, FM Izraelev, and Joseph Ford. “Stochastic behavior of a quantum pendulum under a periodic perturbation”. In: *Stochastic behavior in classical and quantum Hamiltonian systems*. Springer, 1979, pp. 334–352. DOI: [10.1007/BFb0021757](https://doi.org/10.1007/BFb0021757).

-
- [47] Giulio Casati, Italo Guarneri, and D. L. Shepelyansky. “Anderson Transition in a One-Dimensional System with Three Incommensurate Frequencies”. In: *Physical Review Letters* 62 (4 Jan. 1989), pp. 345–348. DOI: [10.1103/PhysRevLett.62.345](https://doi.org/10.1103/PhysRevLett.62.345).
- [48] P. W. Anderson. “Absence of Diffusion in Certain Random Lattices”. In: *Physical Review* 109 (5 Mar. 1958), pp. 1492–1505. DOI: [10.1103/PhysRev.109.1492](https://doi.org/10.1103/PhysRev.109.1492).
- [49] Giulio Casati and Boris Chirikov. *Quantum chaos: between order and disorder*. Cambridge University Press, 2006. ISBN: 9780521031660.
- [50] Victor V. Albert, Jacob P. Covey, and John Preskill. “Robust Encoding of a Qubit in a Molecule”. In: *Physical Review X* 10 (3 Sept. 2020), p. 031050. DOI: [10.1103/PhysRevX.10.031050](https://doi.org/10.1103/PhysRevX.10.031050).
- [51] Erik Urban, Neil Glikin, Sara Mouradian, Kai Krimmel, Boerge Hemmerling, and Hartmut Haeffner. “Coherent Control of the Rotational Degree of Freedom of a Two-Ion Coulomb Crystal”. In: *Physical Review Letters* 123 (13 Sept. 2019), p. 133202. DOI: [10.1103/PhysRevLett.123.133202](https://doi.org/10.1103/PhysRevLett.123.133202).
- [52] Ryutaro Ohira, Takashi Mukaiyama, and Kenji Toyoda. “Breaking rotational symmetry in a trapped-ion quantum tunneling rotor”. In: *Physical Review A* 101 (2 Feb. 2020), p. 022106. DOI: [10.1103/PhysRevA.101.022106](https://doi.org/10.1103/PhysRevA.101.022106).
- [53] Jens Koch, Terri M. Yu, Jay Gambetta, A. A. Houck, D. I. Schuster, J. Majer, Alexandre Blais, M. H. Devoret, S. M. Girvin, and R. J. Schoelkopf. “Charge-insensitive qubit design derived from the Cooper pair box”. In: *Physical Review A* 76 (4 Oct. 2007), p. 042319. DOI: [10.1103/PhysRevA.76.042319](https://doi.org/10.1103/PhysRevA.76.042319).
- [54] Jens Koch, Terri M. Yu, Jay Gambetta, A. A. Houck, D. I. Schuster, J. Majer, Alexandre Blais, M. H. Devoret, S. M. Girvin, and R. J. Schoelkopf. “Charge-insensitive qubit design derived

- from the Cooper pair box". In: *Physical Review A* 76 (4 Oct. 2007), p. 042319. DOI: [10.1103/PhysRevA.76.042319](https://doi.org/10.1103/PhysRevA.76.042319).
- [55] Loic Anderegg, Lawrence W Cheuk, Yicheng Bao, Sean Burchesky, Wolfgang Ketterle, Kang-Kuen Ni, and John M Doyle. "An optical tweezer array of ultracold molecules". In: *Science* 365.6458 (2019), pp. 1156–1158. DOI: [10.1126/science.aax1265](https://doi.org/10.1126/science.aax1265).
- [56] L. R. Liu, J. D. Hood, Y. Yu, J. T. Zhang, K. Wang, Y.-W. Lin, T. Rosenband, and K.-K. Ni. "Molecular Assembly of Ground-State Cooled Single Atoms". In: *Physical Review X* 9 (2 May 2019), p. 021039. DOI: [10.1103/PhysRevX.9.021039](https://doi.org/10.1103/PhysRevX.9.021039).
- [57] Victor V. Albert, Eric Kubischta, Mikhail Lemesko, and Lee R. Liu. *Topology and entanglement of molecular phase space*. 2024. arXiv: [2403.04572](https://arxiv.org/abs/2403.04572) [quant-ph]. URL: <https://arxiv.org/abs/2403.04572>.
- [58] Shubham P Jain, Joseph T Iosue, Alexander Barg, and Victor V Albert. "Quantum spherical codes". In: *Nature Physics* (2024), pp. 1–6. DOI: [10.1038/s41567-024-02496-y](https://doi.org/10.1038/s41567-024-02496-y).
- [59] Johannes Floß and Ilya Sh. Averbukh. "Quantum resonance, Anderson localization, and selective manipulations in molecular mixtures by ultrashort laser pulses". In: *Physical Review A* 86 (2 Aug. 2012), p. 021401. DOI: [10.1103/PhysRevA.86.021401](https://doi.org/10.1103/PhysRevA.86.021401).
- [60] R. Blümel, S. Fishman, and U. Smilansky. "Excitation of molecular rotation by periodic microwave pulses. A testing ground for Anderson localization". In: *The Journal of Chemical Physics* 84.5 (1986), pp. 2604–2614. DOI: [10.1063/1.450330](https://doi.org/10.1063/1.450330).
- [61] Jiao Wang and Jiangbin Gong. "Proposal of a cold-atom realization of quantum maps with Hofstadter's butterfly spectrum". In: *Physical Review A* 77.3 (2008), p. 031405. DOI: [10.1103/PhysRevA.77.031405](https://doi.org/10.1103/PhysRevA.77.031405).

- [62] S. Zhdanovich, C. Bloomquist, J. Floß, I. Sh. Averbukh, J. W. Hepburn, and V. Milner. “Quantum Resonances in Selective Rotational Excitation of Molecules with a Sequence of Ultrashort Laser Pulses”. In: *Physical Review Letters* 109 (4 July 2012), p. 043003. DOI: [10.1103/PhysRevLett.109.043003](https://doi.org/10.1103/PhysRevLett.109.043003).
- [63] M. Bitter and V. Milner. “Experimental Observation of Dynamical Localization in Laser-Kicked Molecular Rotors”. In: *Physical Review Letters* 117.14 (Sept. 2016), p. 144104. ISSN: 0031-9007, 1079-7114. DOI: [10.1103/PhysRevLett.117.144104](https://doi.org/10.1103/PhysRevLett.117.144104).
- [64] Martin Bitter and Valery Milner. “Experimental demonstration of coherent control in quantum chaotic systems”. In: *Physical Review Letters* 118.3 (2017), p. 034101. DOI: [10.1103/PhysRevLett.118.034101](https://doi.org/10.1103/PhysRevLett.118.034101).
- [65] M. Bitter and V. Milner. “Control of quantum localization and classical diffusion in laser-kicked molecular rotors”. In: *Physical Review A* 95 (1 Jan. 2017), p. 013401. DOI: [10.1103/PhysRevA.95.013401](https://doi.org/10.1103/PhysRevA.95.013401).
- [66] Johannes Floß, Shmuel Fishman, and Ilya Sh. Averbukh. “Anderson localization in laser-kicked molecules”. en. In: *Physical Review A* 88.2 (Aug. 2013), p. 023426. ISSN: 1050-2947, 1094-1622. DOI: [10.1103/PhysRevA.88.023426](https://doi.org/10.1103/PhysRevA.88.023426).
- [67] Johannes Floß and Ilya Sh. Averbukh. “Edge states of periodically kicked quantum rotors”. In: *Physical Review E* 91 (5 May 2015), p. 052911. DOI: [10.1103/PhysRevE.91.052911](https://doi.org/10.1103/PhysRevE.91.052911).
- [68] Alexandra Bakman, Hagar Veksler, and Shmuel Fishman. “Edge states of a three dimensional kicked rotor”. In: *The European Physical Journal B* 92.10 (2019), p. 236. DOI: [10.1140/epjb/e2019-100174-8](https://doi.org/10.1140/epjb/e2019-100174-8).
- [69] Steven M Girvin and Kun Yang. *Modern Condensed Matter Physics*. Cambridge University Press, 2019. DOI: [10.1017/9781316480649](https://doi.org/10.1017/9781316480649).

- [70] B Andrei Bernevig. *Topological insulators and topological superconductors*. Princeton University Press, 2013. doi: [10.1515/9781400846733](https://doi.org/10.1515/9781400846733).
- [71] Ching-Kai Chiu, Jeffrey C. Y. Teo, Andreas P. Schnyder, and Shinsei Ryu. "Classification of topological quantum matter with symmetries". In: *Rev. Mod. Phys.* 88 (3 Aug. 2016), p. 035005. doi: [10.1103/RevModPhys.88.035005](https://doi.org/10.1103/RevModPhys.88.035005).
- [72] Elizabeth Gibney and Davide Castelvecchi. "Physics of 2D exotic matter wins Nobel". In: *Nature* 538.7623 (2016). doi: [10.1038/nature.2016.20722](https://doi.org/10.1038/nature.2016.20722).
- [73] Klaus Von Klitzing. "Developments in the quantum Hall effect". In: *Philosophical Transactions of the Royal Society A: Mathematical, Physical and Engineering Sciences* 363.1834 (2005), pp. 2203–2219. doi: [10.1098/rsta.2005.1640](https://doi.org/10.1098/rsta.2005.1640).
- [74] G. Landwehr. "25 Years quantum Hall effect: how it all came about". In: *Physica E: Low-dimensional Systems and Nanostructures* 20.1 (2003). Proceedings of the International Symposium "Quantum Hall Effect: Past, Present and Future, pp. 1–13. ISSN: 1386-9477. doi: [10.1016/j.physe.2003.09.015](https://doi.org/10.1016/j.physe.2003.09.015).
- [75] M. Z. Hasan and C. L. Kane. "Colloquium: Topological insulators". In: *Rev. Mod. Phys.* 82 (4 Nov. 2010), pp. 3045–3067. doi: [10.1103/RevModPhys.82.3045](https://doi.org/10.1103/RevModPhys.82.3045).
- [76] Gregory L Naber and Gregory L Naber. *Topology, geometry, and gauge fields*. Springer, 1997. doi: [10.1007/978-1-4419-7254-5](https://doi.org/10.1007/978-1-4419-7254-5).
- [77] David J. Thouless, Mahito Kohmoto, M. Peter Nightingale, and Marcel den Nijs. "Quantized Hall Conductance in a Two-Dimensional Periodic Potential". In: *Physical Review Letters* 49.6 (1982), p. 405. doi: [10.1103/PhysRevLett.49.405](https://doi.org/10.1103/PhysRevLett.49.405).

- [78] F. Duncan M. Haldane. “Nonlinear Field Theory of Large-Spin Heisenberg Antiferromagnets: Semiclassically Quantized Solitons of the One-Dimensional Easy-Axis Néel State”. In: *Physical Review Letters* 50.15 (1983), p. 1153. DOI: [10.1103/PhysRevLett.50.1153](https://doi.org/10.1103/PhysRevLett.50.1153).
- [79] F. Duncan M. Haldane. “Model for a Quantum Hall Effect without Landau Levels: Condensed-Matter Realization of the “Parity Anomaly””. In: *Physical Review Letters* 61.18 (1988), p. 2015. DOI: [10.1103/PhysRevLett.61.2015](https://doi.org/10.1103/PhysRevLett.61.2015).
- [80] Pierre Delplace and Antoine Venaille. “From the geometry of Foucault pendulum to the topology of planetary waves”. en. In: *Comptes Rendus. Physique* 21.2 (2020), pp. 165–175. DOI: [10.5802/crphys.28](https://doi.org/10.5802/crphys.28).
- [81] Vladimir Igorevich Arnol’d. *Mathematical methods of classical mechanics*. Vol. 60. Springer Science & Business Media, 2013. DOI: [10.1007/978-1-4757-2063-1](https://doi.org/10.1007/978-1-4757-2063-1).
- [82] Michael Berry et al. “Anticipations of the geometric phase”. In: *Physics Today* 43.12 (1990), pp. 34–40. DOI: [10.1063/1.881219](https://doi.org/10.1063/1.881219).
- [83] Patrik Öhberg Jonas Larson Erik Sjöqvist. *Conical Intersections in Physics: An Introduction to Synthetic Gauge Theories*. Vol. 965. Lecture Notes in Physics. Springer, 2020. DOI: [10.1007/978-3-030-34882-3](https://doi.org/10.1007/978-3-030-34882-3).
- [84] B. J Hiley. *The Early History of the Aharonov-Bohm Effect*. 2013. arXiv: [1304.4736](https://arxiv.org/abs/1304.4736) [physics.hist-ph]. URL: <https://arxiv.org/abs/1304.4736>.
- [85] Kenneth G. Wilson. “Confinement of quarks”. In: *Physical Review D* 10 (8 Oct. 1974), pp. 2445–2459. DOI: [10.1103/PhysRevD.10.2445](https://doi.org/10.1103/PhysRevD.10.2445).

- [86] Franz J Wegner. “Duality in generalized Ising models and phase transitions without local order parameters”. In: *Journal of Mathematical Physics* 12.10 (1971), pp. 2259–2272. DOI: [10.1063/1.1665530](https://doi.org/10.1063/1.1665530).
- [87] Eberhard Zeidler. *Quantum Field Theory III: Gauge Theory: A Bridge between Mathematicians and Physicists*. Springer Science & Business Media, 2011. DOI: [10.1007/978-3-642-22421-8](https://doi.org/10.1007/978-3-642-22421-8).
- [88] Eliahu Cohen, Hugo Larocque, Frédéric Bouchard, Farshad Nejadshattari, Yuval Gefen, and Ebrahim Karimi. “Geometric phase from Aharonov–Bohm to Pancharatnam–Berry and beyond”. In: *Nature Reviews Physics* 1.7 (2019), pp. 437–449.
- [89] J. Zak. “Berry’s phase for energy bands in solids”. In: *Physical Review Letters* 62 (23 June 1989), pp. 2747–2750. DOI: [10.1103/PhysRevLett.62.2747](https://doi.org/10.1103/PhysRevLett.62.2747).
- [90] Joseph Samuel. “Geometry and quantum interference”. In: *Nature India* (2024). DOI: [10.1038/d44151-023-00171-4](https://doi.org/10.1038/d44151-023-00171-4).
- [91] Shiing-shen Chern. “Characteristic classes of Hermitian manifolds”. In: *Annals of Mathematics* 47.1 (1946), pp. 85–121. DOI: [10.2307/1969037](https://doi.org/10.2307/1969037).
- [92] Hung-hsi Wu. “Shiing-shen Chern: 1911–2004”. In: *Bulletin of the American Mathematical Society* 46.2 (2009), pp. 327–338. DOI: [10.1090/S0273-0979-08-01219-6](https://doi.org/10.1090/S0273-0979-08-01219-6).
- [93] Alexander Altland and Ben D Simons. *Condensed matter field theory*. Cambridge University Press, 2010. DOI: [10.1017/CB09780511789984](https://doi.org/10.1017/CB09780511789984).
- [94] Michael F Atiyah and Isadore M Singer. “The index of elliptic operators on compact manifolds”. In: *Bulletin of the American Mathematical Society* 69.3 (1963), pp. 422–433.
- [95] Xiao-Liang Qi and Shou-Cheng Zhang. “Topological insulators and superconductors”. In: *Reviews of Modern Physics* 83.4 (2011), p. 1057. DOI: [10.1103/RevModPhys.83.1057](https://doi.org/10.1103/RevModPhys.83.1057).

-
- [96] NP Armitage, EJ Mele, and Ashvin Vishwanath. “Weyl and Dirac semimetals in three-dimensional solids”. In: *Reviews of Modern Physics* 90.1 (2018), p. 015001. DOI: [10.1103/RevModPhys.90.015001](https://doi.org/10.1103/RevModPhys.90.015001).
- [97] Masatoshi Sato and Yoichi Ando. “Topological superconductors: a review”. In: *Reports on Progress in Physics* 80.7 (2017), p. 076501. DOI: [10.1088/1361-6633/aa6ac7](https://doi.org/10.1088/1361-6633/aa6ac7).
- [98] Takashi Oka and Sota Kitamura. “Floquet engineering of quantum materials”. In: *Annual Review of Condensed Matter Physics* 10.1 (2019), pp. 387–408. DOI: [10.1146/annurev-conmatphys-031218-013423](https://doi.org/10.1146/annurev-conmatphys-031218-013423).
- [99] Gaston Floquet. “Sur les équations différentielles linéaires à coefficients périodiques”. In: *Annales scientifiques de l’École normale supérieure*. Vol. 12. 1883, pp. 47–88. DOI: [10.24033/asens.220](https://doi.org/10.24033/asens.220).
- [100] George William Hill. “On the part of the motion of the lunar perigee which is a function of the mean motions of the sun and moon”. In: (1886). DOI: [10.1007/bf02417081](https://doi.org/10.1007/bf02417081).
- [101] Wilhelm Magnus and Stanley Winkler. *Hill’s equation*. Courier Corporation, 2004.
- [102] MSP Eastham and ML Thompson. “On the limit-point, limit-circle classification of second-order ordinary differential equations”. In: *The Quarterly Journal of Mathematics* 24.1 (1973), pp. 531–535. DOI: [10.1093/qmath/24.1.531](https://doi.org/10.1093/qmath/24.1.531).
- [103] Peter A Kuchment. *Floquet theory for partial differential equations*. Vol. 60. Birkhäuser, 2012. DOI: [10.1007/978-3-0348-8573-7](https://doi.org/10.1007/978-3-0348-8573-7).
- [104] Robert Hofstadter, Marvin Chodorow, Arthur L. Schawlow, and J. Dirk Walecka. *Memorial Resolution: Felix Bloch (1905-1983)*. Memorial Resolution. Stanford University Faculty Senate Memorial Resolution for Felix Bloch , presented by Robert

- Hofstadter (Chair), Marvin Chodorow, Arthur L. Schawlow, and J. Dirk Walecka. Stanford University, 1984. URL: <https://wayback.archive-it.org/all/20170311100004/https://physics.stanford.edu/sites/default/files/BlochF.pdf>.
- [105] David Bohm. “Note on a theorem of Bloch concerning possible causes of superconductivity”. In: *Physical Review* 75.3 (1949), p. 502.
- [106] Jon H. Shirley. “Solution of the Schrödinger Equation with a Hamiltonian Periodic in Time”. In: *Physical Review* 138 (4B May 1965), B979–B987. DOI: [10.1103/PhysRev.138.B979](https://doi.org/10.1103/PhysRev.138.B979). URL: <https://link.aps.org/doi/10.1103/PhysRev.138.B979>.
- [107] Hermann Haken. “Eine modellmäßige Behandlung der Wechselwirkung zwischen einem Elektron und einem Gitteroszillator”. In: *Zeitschrift für Physik* 135.4 (1953), pp. 408–430. DOI: [10.1007/BF01337667](https://doi.org/10.1007/BF01337667).
- [108] L Brillouin. “Interactions between Electrons and Waves”. In: *Proceedings of the National Academy of Sciences* 41.6 (1955), pp. 401–415.
- [109] S. R. Barone, M. A. Narcowich, and F. J. Narcowich. “Floquet theory and applications”. In: *Physical Review A* 15 (3 Mar. 1977), pp. 1109–1125. DOI: [10.1103/PhysRevA.15.1109](https://doi.org/10.1103/PhysRevA.15.1109).
- [110] Milena Grifoni and Peter Hänggi. “Driven quantum tunneling”. In: *Physics Reports* 304.5-6 (1998), pp. 229–354. DOI: [10.1016/S0370-1573\(98\)00022-2](https://doi.org/10.1016/S0370-1573(98)00022-2).
- [111] Luca Gammaitoni, Peter Hänggi, Peter Jung, and Fabio Marchesoni. “Stochastic resonance”. In: *Rev. Mod. Phys.* 70 (1 Jan. 1998), pp. 223–287. DOI: [10.1103/RevModPhys.70.223](https://doi.org/10.1103/RevModPhys.70.223). URL: <https://link.aps.org/doi/10.1103/RevModPhys.70.223>.

- [112] Michael Berry. “Quantum chaology, not quantum chaos”. In: *Physica Scripta* 40.3 (1989), p. 335. DOI: [10.1088/0031-8949/40/3/013](https://doi.org/10.1088/0031-8949/40/3/013).
- [113] P. Cvitanović, R. Artuso, R. Mainieri, G. Tanner, and G. Vattay. *Chaos: Classical and Quantum*. Copenhagen: Niels Bohr Inst., 2016. URL: <http://ChaosBook.org/>.
- [114] Shmuel Fishman, D. R. Grempel, and R. E. Prange. “Chaos, Quantum Recurrences, and Anderson Localization”. In: *Physical Review Letters* 49 (8 Aug. 1982), pp. 509–512. DOI: [10.1103/PhysRevLett.49.509](https://doi.org/10.1103/PhysRevLett.49.509).
- [115] Fritz Haake. “Quantum signatures of chaos”. In: *Quantum Coherence in Mesoscopic Systems*. 4th ed. Springer, 2018, pp. 583–595. DOI: [10.1007/978-3-319-97580-1](https://doi.org/10.1007/978-3-319-97580-1).
- [116] H. Stapelfeldt and T. Seideman. “Colloquium: Aligning molecules with strong laser pulses”. In: *Reviews of Modern Physics* 75.2 (2003), p. 543. DOI: [10.1103/RevModPhys.75.543](https://doi.org/10.1103/RevModPhys.75.543).
- [117] Venkataraman Balakrishnan. *Mathematical Physics: Applications and Problems*. Springer Nature, 2020. DOI: [10.1007/978-3-030-39680-0](https://doi.org/10.1007/978-3-030-39680-0).
- [118] Subhankar Khatua and R Ganesh. “Berry phase in the rigid rotor: Emergent physics of odd antiferromagnets”. In: *Physical Review B* 105.18 (2022), p. 184401. DOI: [10.1103/PhysRevB.105.184401](https://doi.org/10.1103/PhysRevB.105.184401).
- [119] Ilya G. Ryabinkin, Loic Joubert-Doriol, and Artur F. Izmaylov. “Geometric Phase Effects in Nonadiabatic Dynamics near Conical Intersections”. In: *Accounts of Chemical Research* 50.7 (July 2017), pp. 1785–1793. DOI: [10.1021/acs.accounts.7b00220](https://doi.org/10.1021/acs.accounts.7b00220).

- [120] Nimrod Moiseyev, Milan Šindelka, and Lorenz S Cederbaum. “Laser-induced conical intersections in molecular optical lattices”. In: *Journal of Physics B* 41.22 (Nov. 2008), p. 221001. DOI: [10.1088/0953-4075/41/22/221001](https://doi.org/10.1088/0953-4075/41/22/221001).
- [121] Gábor J. Halász, Ágnes Vibók, Milan Šindelka, Nimrod Moiseyev, and Lorenz S. Cederbaum. “Conical intersections induced by light: Berry phase and wavepacket dynamics”. In: *Journal of Physics B* 44.17 (Aug. 2011), p. 175102. DOI: [10.1088/0953-4075/44/17/175102](https://doi.org/10.1088/0953-4075/44/17/175102).
- [122] Longwen Zhou and Jiangbin Gong. “Recipe for creating an arbitrary number of Floquet chiral edge states”. In: *Physical Review B* 97.24 (2018), p. 245430. DOI: [10.1103/PhysRevB.97.245430](https://doi.org/10.1103/PhysRevB.97.245430).
- [123] Derek Y.H. Ho and Jiangbin Gong. “Quantized adiabatic transport in momentum space”. In: *Physical review letters* 109.1 (2012), p. 010601. DOI: [10.1103/PhysRevLett.109.010601](https://doi.org/10.1103/PhysRevLett.109.010601).
- [124] R. N. Zare. “Laser Control of Chemical Reactions”. In: *Science* 279.5358 (Mar. 1998), pp. 1875–1879. ISSN: 00368075, 10959203. DOI: [10.1126/science.279.5358.1875](https://doi.org/10.1126/science.279.5358.1875).
- [125] Xinhua Xie, Katharina Doblhoff-Dier, Huailiang Xu, Stefan Roither, Markus S. Schöffler, Daniil Kartashov, Sonia Erattupuzha, Tim Rathje, Gerhard G. Paulus, Kaoru Yamanouchi, Andrius Baltuška, Stefanie Gräfe, and Markus Kitzler. “Selective Control over Fragmentation Reactions in Polyatomic Molecules Using Impulsive Laser Alignment”. In: *Physical Review Letters* 112 (16 Apr. 2014), p. 163003. DOI: [10.1103/PhysRevLett.112.163003](https://doi.org/10.1103/PhysRevLett.112.163003).
- [126] D. Mitra, K. H. Leung, and T. Zelevinsky. “Quantum control of molecules for fundamental physics”. In: *Physical Review A* 105 (4 Apr. 2022), p. 040101. DOI: [10.1103/PhysRevA.105.040101](https://doi.org/10.1103/PhysRevA.105.040101).

- [127] W Demtröder and *Molecules Atoms. An Introduction to Atomic-, Molecular-and Quantum Physics (Graduate Texts in Physics)*. Springer, Heidelberg, 2010. doi: [10.1007/978-3-662-55523-1](https://doi.org/10.1007/978-3-662-55523-1).
- [128] Stefan Ulf Pabst. “New theoretical approaches to atomic and molecular dynamics triggered by ultrashort light pulses on the atto-to picosecond time scale”. In: (2013). doi: [10.1140/epjst/e2013-01819-x](https://doi.org/10.1140/epjst/e2013-01819-x).
- [129] Tamar Seideman. “Shaping molecular beams with intense light”. In: *The Journal of chemical physics* 107.24 (1997). Publisher: American Institute of Physics, pp. 10420–10429. doi: [10.1063/1.474206](https://doi.org/10.1063/1.474206).
- [130] Peter F Bernath. *Spectra of atoms and molecules*. Oxford university press, 2020. doi: [10.1080/00107514.2017.1291731](https://doi.org/10.1080/00107514.2017.1291731).
- [131] J. Ortigoso, M. Rodriguez, M. Gupta, and B. Friedrich. “Time evolution of pendular states created by the interaction of molecular polarizability with a pulsed nonresonant laser field”. In: *The Journal of Chemical Physics* 110.8 (Feb. 1999), pp. 3870–3875. ISSN: 0021-9606. doi: [10.1063/1.478241](https://doi.org/10.1063/1.478241).
- [132] L. Cai, J. Marango, and B. Friedrich. “Time-Dependent Alignment and Orientation of Molecules in Combined Electrostatic and Pulsed Nonresonant Laser Fields”. In: *Physical Review Letters* 86 (5 Jan. 2001), pp. 775–778. doi: [10.1103/PhysRevLett.86.775](https://doi.org/10.1103/PhysRevLett.86.775).
- [133] L. Cai and B. Friedrich. “Recurring molecular alignment induced by pulsed nonresonant laser fields”. In: *Collection of Czechoslovak Chemical Communications* 66.7 (2001), pp. 991–1004.
- [134] C.M. Dion, A. Keller, and O. Atabek. “Orienting molecules using half-cycle pulses”. In: *The European Physical Journal D-Atomic, Molecular, Optical and Plasma Physics* 14.2 (2001), pp. 249–255. doi: [10.1007/s100530170223](https://doi.org/10.1007/s100530170223).

- [135] M. Leibscher, I. S. Averbukh, and H. Rabitz. "Molecular alignment by trains of short laser pulses". In: *Physical review letters* 90.21 (2003), p. 213001. DOI: [10.1103/PhysRevLett.90.213001](https://doi.org/10.1103/PhysRevLett.90.213001).
- [136] S. Fleischer, Y. Khodorkovsky, Y. Prior, and I. S. Averbukh. "Controlling the sense of molecular rotation". In: *New Journal of Physics* 11.10 (2009), p. 105039. DOI: [10.1088/1367-2630/11/10/105039](https://doi.org/10.1088/1367-2630/11/10/105039).
- [137] T. Seideman. "Revival structure of aligned rotational wave packets". In: *Physical Review Letters* 83.24 (1999), p. 4971. DOI: [10.1103/PhysRevLett.83.4971](https://doi.org/10.1103/PhysRevLett.83.4971).
- [138] N. Owschimikow, B. Schmidt, and N. Schwentner. "State selection in nonresonantly excited wave packets by tuning from nonadiabatic to adiabatic interaction". In: *Physical Review A* 80.5 (2009), p. 053409. DOI: [10.1103/PhysRevA.80.053409](https://doi.org/10.1103/PhysRevA.80.053409).
- [139] M. Mirahmadi, B. Schmidt, M. Karra, and B. Friedrich. "Dynamics of polar polarizable rotors acted upon by unipolar electromagnetic pulses: From the sudden to the adiabatic regime". In: *The Journal of Chemical Physics* 149.17 (Nov. 2018), p. 174109. ISSN: 0021-9606. DOI: [10.1063/1.5051591](https://doi.org/10.1063/1.5051591).
- [140] M. Mirahmadi, B. Schmidt, and B. Friedrich. "Quantum dynamics of a planar rotor driven by suddenly switched combined aligning and orienting interactions". In: *New Journal of Physics* 23.6 (June 2021), p. 063040. DOI: [10.1088/1367-2630/ac00d6](https://doi.org/10.1088/1367-2630/ac00d6).
- [141] M. Lemeshko and B. Friedrich. "Probing Weakly Bound Molecules with Nonresonant Light". In: *Physical Review Letters* 103 (5 July 2009), p. 053003. DOI: [10.1103/PhysRevLett.103.053003](https://doi.org/10.1103/PhysRevLett.103.053003).

- [142] M. Lemeshko and B. Friedrich. “Fine-Tuning Molecular Energy Levels by Nonresonant Laser Pulses”. In: *The Journal of Physical Chemistry A* 114.36 (Sept. 2010), pp. 9848–9854. doi: [10.1021/jp1032299](https://doi.org/10.1021/jp1032299).
- [143] A. Lugovskoy and I. Bray. “Sudden perturbation approximations for interaction of atoms with intense ultrashort electromagnetic pulses”. In: *The European Physical Journal D* 69.12 (2015), p. 271. doi: [10.1140/epjd/e2015-60471-2](https://doi.org/10.1140/epjd/e2015-60471-2).
- [144] A. Matos-Abiague, A. S. Moskalenko, and J. Berakdar. “Ultrafast Dynamics of Nano and Mesoscopic Systems Driven by Asymmetric Electromagnetic Pulses”. In: *Current Topics in Atomic, Molecular and Optical Physics*. 0. WORLD SCIENTIFIC, Oct. 2006, pp. 1–20. doi: [10.1142/97898127725100001](https://doi.org/10.1142/97898127725100001).
- [145] A. S. Moskalenko, Z.-G. Zhu, and J. Berakdar. “Charge and spin dynamics driven by ultrashort extreme broadband pulses: A theory perspective”. In: *Physics Reports* 672 (2017). Charge and spin dynamics driven by ultrashort extreme broadband pulses: a theory perspective, pp. 1–82. ISSN: 0370-1573. doi: <https://doi.org/10.1016/j.physrep.2016.12.005>.
- [146] R. Tehini and D. Sugny. “Field-free molecular orientation by nonresonant and quasi-resonant two-color laser pulses”. In: *Physical Review A* 77 (2 Feb. 2008), p. 023407. doi: [10.1103/PhysRevA.77.023407](https://doi.org/10.1103/PhysRevA.77.023407).
- [147] C. M. Dion, A. Ben Haj-Yedder, E. Cancès, C. Le Bris, A. Keller, and O. Atabek. “Optimal laser control of orientation: The kicked molecule”. In: *Physical Review A* 65 (6 June 2002), p. 063408. doi: [10.1103/PhysRevA.65.063408](https://doi.org/10.1103/PhysRevA.65.063408).
- [148] R. M. Arkhipov, M. V. Arkhipov, A. V. Pakhomov, P. A. Obraztsov, and N. N. Rosanov. “Unipolar and Subcycle Extremely Short Pulses: Recent Results and Prospects (Brief Review)”. In: *JETP Letters* 117.1 (2023), pp. 8–23. doi: [10.1134/S0021364022602652](https://doi.org/10.1134/S0021364022602652).

- [149] N. Rosanov, D. Tumakov, M. Arkhipov, and R. Arkhipov. “Criterion for the yield of micro-object ionization driven by few- and subcycle radiation pulses with nonzero electric area”. In: *Physical Review A* 104 (6 Dec. 2021), p. 063101. DOI: [10.1103/PhysRevA.104.063101](https://doi.org/10.1103/PhysRevA.104.063101).
- [150] A. Pakhomov, M. Arkhipov, N. Rosanov, and R. Arkhipov. “Ultrafast control of vibrational states of polar molecules with subcycle unipolar pulses”. In: *Physical Review A* 105 (4 Apr. 2022), p. 043103. DOI: [10.1103/PhysRevA.105.043103](https://doi.org/10.1103/PhysRevA.105.043103).
- [151] J. Rauch and G. Mourou. “The time integrated far field for Maxwell’s and d’Alembert’s equations”. In: *Proceedings of the American Mathematical Society* 134.3 (2006), pp. 851–858. DOI: [10.1090/S0002-9939-05-08140-2](https://doi.org/10.1090/S0002-9939-05-08140-2).
- [152] A. B. Plachenov and N. N. Rozanov. “Pulses of the Electromagnetic Field with a Non-Zero Electric Area”. In: *Radio-physics and Quantum Electronics* (2023), pp. 1–11. DOI: [10.1007/s11141-023-10267-7](https://doi.org/10.1007/s11141-023-10267-7).
- [153] R. Arkhipov, M. Arkhipov, A. Pakhomov, I. Babushkin, and N. Rosanov. “Half-cycle and unipolar pulses (Topical Review)”. In: *Laser Physics Letters* 19.4 (2022), p. 043001. DOI: [10.1088/1612-202X/ac5522](https://doi.org/10.1088/1612-202X/ac5522).
- [154] I. Barth, L. Serrano-Andrés, and T. Seideman. “Nonadiabatic orientation, toroidal current, and induced magnetic field in BeO molecules”. In: *The Journal of chemical physics* 129.16 (2008), p. 164303. DOI: [10.1063/1.2994737](https://doi.org/10.1063/1.2994737).
- [155] K. Tanaka, H. Ito, K. Harada, and T. Tanaka. “CO₂ and CO laser microwave double resonance spectroscopy of OCS: Precise measurement of dipole moment and polarizability anisotropy”. In: *The Journal of Chemical Physics* 80.12 (June 1984), pp. 5893–5905. DOI: [10.1063/1.446693](https://doi.org/10.1063/1.446693).

- [156] S. Fleischer, Y. Zhou, R. W. Field, and K. A. Nelson. “Molecular Orientation and Alignment by Intense Single-Cycle THz Pulses”. In: *Physical Review Letters* 107 (16 Oct. 2011), p. 163603. DOI: [10.1103/PhysRevLett.107.163603](https://doi.org/10.1103/PhysRevLett.107.163603).
- [157] W. Magnus. “On the exponential solution of differential equations for a linear operator”. In: *Communications on pure and applied mathematics* 7.4 (1954), pp. 649–673. DOI: [10.1002/cpa.3160070404](https://doi.org/10.1002/cpa.3160070404).
- [158] R. Graham, M. Schlautmann, and P. Zoller. “Dynamical localization of atomic-beam deflection by a modulated standing light wave”. en. In: *Physical Review A* 45.1 (Jan. 1992), R19–R22. ISSN: 1050-2947, 1094-1622. DOI: [10.1103/PhysRevA.45.R19](https://doi.org/10.1103/PhysRevA.45.R19).
- [159] F. L. Moore, J. C. Robinson, C. Bharucha, P. E. Williams, and M. G. Raizen. “Observation of Dynamical Localization in Atomic Momentum Transfer: A New Testing Ground for Quantum Chaos”. en. In: *Physical Review Letters* 73.22 (Nov. 1994), pp. 2974–2977. ISSN: 0031-9007. DOI: [10.1103/PhysRevLett.73.2974](https://doi.org/10.1103/PhysRevLett.73.2974).
- [160] R. Blümel, A. Buchleitner, R. Graham, L. Sirko, U. Smilansky, and H. Walther. “Dynamical localization in the microwave interaction of Rydberg atoms: The influence of noise”. en. In: *Physical Review A* 44.7 (Oct. 1991), pp. 4521–4540. ISSN: 1050-2947, 1094-1622. DOI: [10.1103/PhysRevA.44.4521](https://doi.org/10.1103/PhysRevA.44.4521).
- [161] FM Izrailev and Dmitrii L’vovich Shepelyanskii. “Quantum resonance for a rotator in a nonlinear periodic field”. In: *Theoretical and Mathematical Physics* 43.3 (1980), pp. 553–561.
- [162] MS Santhanam, Sanku Paul, and J Bharathi Kannan. “Quantum kicked rotor and its variants: Chaos, localization and beyond”. In: *Physics Reports* 956 (2022), pp. 1–87.
- [163] Sandro Wimberger. *Nonlinear dynamics and quantum chaos*. Vol. 10. Springer, 2014.

- [164] Rahul Roy and Fenner Harper. “Periodic table for Floquet topological insulators”. In: *Physical Review B* 96 (15 Oct. 2017), p. 155118. DOI: [10.1103/PhysRevB.96.155118](https://doi.org/10.1103/PhysRevB.96.155118).
- [165] Nico M Temme. *Special functions: An introduction to the classical functions of mathematical physics*. John Wiley & Sons, 2011. DOI: [10.1119/1.18604](https://doi.org/10.1119/1.18604).
- [166] Michael S. Chapman, Christopher R. Ekstrom, Troy D. Hammond, Jörg Schmiedmayer, Bridget E. Tannian, Stefan Wehinger, and David E. Pritchard. “Near-field imaging of atom diffraction gratings: The atomic Talbot effect”. In: *Physical Review A* 51 (1 Jan. 1995), R14–R17. DOI: [10.1103/PhysRevA.51.R14](https://doi.org/10.1103/PhysRevA.51.R14).
- [167] M. Leibscher, I. Sh. Averbukh, P. Rozmej, and R. Arvieu. “Semiclassical catastrophes and cumulative angular squeezing of a kicked quantum rotor”. In: *Physical Review A* 69 (3 Mar. 2004), p. 032102. DOI: [10.1103/PhysRevA.69.032102](https://doi.org/10.1103/PhysRevA.69.032102).
- [168] M. Mirahmadi. “Spectra and Dynamics of Driven Linear Quantum Rotors”. PhD thesis.
- [169] Martina Abb, Italo Guarneri, and Sandro Wimberger. “Pseudoclassical theory for fidelity of nearly resonant quantum rotors”. In: *Physical Review E* 80 (3 Sept. 2009), p. 035206. DOI: [10.1103/PhysRevE.80.035206](https://doi.org/10.1103/PhysRevE.80.035206).
- [170] R.W. Robinett. “Quantum wave packet revivals”. In: *Physics Reports* 392.1 (2004), pp. 1–119. ISSN: 0370-1573. DOI: <https://doi.org/10.1016/j.physrep.2003.11.002>.
- [171] Helene Lefebvre-Brion and Robert W Field. *The Spectra and Dynamics of Diatomic Molecules: Revised and Enlarged Edition*. Elsevier, 2004. DOI: [10.1016/B978-0-12-441455-6.X5000-8](https://doi.org/10.1016/B978-0-12-441455-6.X5000-8).
- [172] Mikio Nakahara. *Geometry, topology and physics*. CRC press, 2018. DOI: [10.1201/9781315275826](https://doi.org/10.1201/9781315275826).

- [173] D.L. Shepelyansky. “Localization of diffusive excitation in multi-level systems”. In: *Physica D: Nonlinear Phenomena* 28.1 (1987), pp. 103–114. ISSN: 0167-2789. DOI: [10.1016/0167-2789\(87\)90123-0](https://doi.org/10.1016/0167-2789(87)90123-0).
- [174] James PM Flude. “The Edmonds asymptotic formulas for the 3j and 6j symbols”. In: *J. Math. Phys.* 39.7 (1998), pp. 3906–3915. DOI: [10.1063/1.532474](https://doi.org/10.1063/1.532474).
- [175] D. A. Varshalovich, A. N. Moskalev, and V. K. Khersonskii. *Quantum theory of angular momentum*. World Scientific, 1988. DOI: [10.1142/0270](https://doi.org/10.1142/0270).
- [176] Johannes Floß and Ilya Sh. Averbukh. “Anderson Wall and Bloch Oscillations in Molecular Rotation”. In: *Physical Review Letters* 113.4 (2014), p. 043002. DOI: [10.1103/PhysRevLett.113.043002](https://doi.org/10.1103/PhysRevLett.113.043002).
- [177] Claude Elwood Shannon. “Communication in the presence of noise”. In: *Proceedings of the IRE* 37.1 (1949), pp. 10–21.
- [178] Neil W Ashcroft, N David Mermin, and Sergio Rodriguez. “Solid state physics”. In: *American Journal of Physics* 46.1 (1978), pp. 116–117.
- [179] Douglas A Lyon. “The discrete fourier transform, part 4: spectral leakage”. In: *Journal of object technology* 8.7 (2009). DOI: [10.5381/jot.2009.8.7.c2](https://doi.org/10.5381/jot.2009.8.7.c2).
- [180] David Vanderbilt. *Berry phases in electronic structure theory: electric polarization, orbital magnetization and topological insulators*. Cambridge University Press, 2018.
- [181] Susan J. Colley. *Vector Calculus*. 4th ed. Pearson, 2012. ISBN: 9780321780652.
- [182] János K Asbóth, László Oroszlány, and András Pályi. “A short course on topological insulators”. In: *Lecture notes in physics* 919.1 (2016). DOI: [10.1007/978-3-319-25607-8](https://doi.org/10.1007/978-3-319-25607-8).

- [183] Dušan Repovš and Pavel V Semenov. “Continuous selections of multivalued mappings”. In: *Recent progress in general topology III* (2013), pp. 711–749. doi: [10.2991/978-94-6239-024-9_17](https://doi.org/10.2991/978-94-6239-024-9_17).
- [184] Jorrit Kruthoff, Jan de Boer, Jasper van Wezel, Charles L. Kane, and Robert-Jan Slager. “Topological Classification of Crystalline Insulators through B and Structure Combinatorics”. In: *Physical Review X* 7 (4 Dec. 2017), p. 041069. doi: [10.1103/PhysRevX.7.041069](https://doi.org/10.1103/PhysRevX.7.041069).
- [185] Robert-Jan Slager, Andrej Mesáros, Vladimir Juričić, and Jan Zaanen. “The space group classification of topological band-insulators”. In: *Nat. Phys.* 9 (Jan. 2013), p. 98.
- [186] Liang Fu. “Topological Crystalline Insulators”. In: *Physical Review Letters* 106 (10 Mar. 2011), p. 106802. doi: [10.1103/PhysRevLett.106.106802](https://doi.org/10.1103/PhysRevLett.106.106802).
- [187] Guo Chuan Thiang. “On the K-theoretic classification of topological phases of matter”. In: *Annales Henri Poincaré*. Vol. 17. Springer. 2016, pp. 757–794. doi: [10.1007/s00023-015-0418-9](https://doi.org/10.1007/s00023-015-0418-9).
- [188] R. Jackiw and C. Rebbi. “Solitons with fermion number $\frac{1}{2}$ ”. In: *Physical Review D* 13 (12 June 1976), pp. 3398–3409. doi: [10.1103/PhysRevD.13.3398](https://doi.org/10.1103/PhysRevD.13.3398).
- [189] Emil J Bergholtz, Jan Carl Budich, and Flore K Kunst. “Exceptional topology of non-Hermitian systems”. In: *Reviews of Modern Physics* 93.1 (2021), p. 015005.
- [190] Ramy El-Ganainy, Konstantinos G Makris, Mercedeh Khajavikhan, Ziad H Musslimani, Stefan Rotter, and Demetrios N Christodoulides. “Non-Hermitian physics and PT symmetry”. In: *Nature Physics* 14.1 (2018), pp. 11–19. doi: [10.1038/nphys4323](https://doi.org/10.1038/nphys4323).

-
- [191] Naomichi Hatano and David R. Nelson. “Localization Transitions in Non-Hermitian Quantum Mechanics”. In: *Physical Review Letters* 77 (3 July 1996), pp. 570–573. doi: [10.1103/PhysRevLett.77.570](https://doi.org/10.1103/PhysRevLett.77.570).
- [192] Zongping Gong, Yuto Ashida, Kohei Kawabata, Kazuaki Takasan, Sho Higashikawa, and Masahito Ueda. “Topological phases of non-Hermitian systems”. In: *Physical Review X* 8.3 (2018), p. 031079.
- [193] Dominic V. Else and Chetan Nayak. “Classification of topological phases in periodically driven interacting systems”. In: *Physical Review B* 93 (20 May 2016), p. 201103. doi: [10.1103/PhysRevB.93.201103](https://doi.org/10.1103/PhysRevB.93.201103).
- [194] Andrew C. Potter, Takahiro Morimoto, and Ashvin Vishwanath. “Classification of Interacting Topological Floquet Phases in One Dimension”. In: *Physical Review X* 6 (4 Oct. 2016), p. 041001. doi: [10.1103/PhysRevX.6.041001](https://doi.org/10.1103/PhysRevX.6.041001).
- [195] Takuya Kitagawa, Erez Berg, Mark Rudner, and Eugene Demler. “Topological characterization of periodically driven quantum systems”. In: *Physical Review B* 82 (23 Dec. 2010), p. 235114. doi: [10.1103/PhysRevB.82.235114](https://doi.org/10.1103/PhysRevB.82.235114).
- [196] Takahiro Fukui, Yasuhiro Hatsugai, and Hiroshi Suzuki. “Chern numbers in discretized Brillouin zone: efficient method of computing (spin) Hall conductances”. In: *Journal of the Physical Society of Japan* 74.6 (2005), pp. 1674–1677.
- [197] Xiao-Liang Qi and Shou-Cheng Zhang. “Topological insulators and superconductors”. In: *Rev. Mod. Phys.* 83 (4 Oct. 2011), pp. 1057–1110. doi: [10.1103/RevModPhys.83.1057](https://doi.org/10.1103/RevModPhys.83.1057).
- [198] M. Z. Hasan and C. L. Kane. “Colloquium: Topological Insulators”. In: *Rev. Mod. Phys.* 82 (4 Nov. 2010), pp. 3045–3067. doi: [10.1103/RevModPhys.82.3045](https://doi.org/10.1103/RevModPhys.82.3045).

- [199] Hoi Chun Po, Ashvin Vishwanath, and Haruki Watanabe. “Symmetry-based indicators of band topology in the 230 space groups”. In: *Nat. Commun.* 8.1 (2017), p. 50. doi: [10.1038/s41467-017-00133-2](https://doi.org/10.1038/s41467-017-00133-2).
- [200] Barry Bradlyn, L. Elcoro, Jennifer Cano, M. G. Vergniory, Zhijun Wang, C. Felser, M. I. Aroyo, and B. Andrei Bernevig. “Topological quantum chemistry”. In: *Nature* 547 (July 2017), p. 298.
- [201] Robert-Jan Slager. “The translational side of topological band insulators”. In: *J. Phys. Chem. Solids* 128 (2019). Spin-Orbit Coupled Materials, pp. 24–38. ISSN: 0022-3697. doi: [10.1016/j.jpcs.2018.01.023](https://doi.org/10.1016/j.jpcs.2018.01.023).
- [202] Ken Shiozaki and Masatoshi Sato. “Topology of crystalline insulators and superconductors”. In: *Physical Review B* 90 (16 Oct. 2014), p. 165114. doi: [10.1103/PhysRevB.90.165114](https://doi.org/10.1103/PhysRevB.90.165114).
- [203] N. P. Armitage, E. J. Mele, and Ashvin Vishwanath. “Weyl and Dirac semimetals in three-dimensional solids”. In: *Rev. Mod. Phys.* 90 (1 Jan. 2018), p. 015001. doi: [10.1103/RevModPhys.90.015001](https://doi.org/10.1103/RevModPhys.90.015001).
- [204] Takuya Kitagawa, Erez Berg, Mark Rudner, and Eugene Demler. “Topological characterization of periodically driven quantum systems”. In: *Physical Review B* 82 (23 Dec. 2010), p. 235114. doi: [10.1103/PhysRevB.82.235114](https://doi.org/10.1103/PhysRevB.82.235114).
- [205] Mark S. Rudner, Netanel H. Lindner, Erez Berg, and Michael Levin. “Anomalous Edge States and the Bulk-Edge Correspondence for Periodically Driven Two-Dimensional Systems”. In: *Physical Review X* 3 (3 July 2013), p. 031005. doi: [10.1103/PhysRevX.3.031005](https://doi.org/10.1103/PhysRevX.3.031005).
- [206] Rahul Roy and Fenner Harper. “Periodic table for Floquet topological insulators”. In: *Physical Review B* 96 (15 Oct. 2017), p. 155118. doi: [10.1103/PhysRevB.96.155118](https://doi.org/10.1103/PhysRevB.96.155118).

- [207] F. Nur Ünal, André Eckardt, and Robert-Jan Slager. “Hopf characterization of two-dimensional Floquet topological insulators”. In: *Physical Review Research* 1 (2 Sept. 2019), p. 022003. DOI: [10.1103/PhysRevResearch.1.022003](https://doi.org/10.1103/PhysRevResearch.1.022003).
- [208] Junyeong Ahn, Sungjoon Park, and Bohm-Jung Yang. “Failure of Nielsen-Ninomiya Theorem and Fragile Topology in Two-Dimensional Systems with Space-Time Inversion Symmetry: Application to Twisted Bilayer Graphene at Magic Angle”. In: *Physical Review X* 9 (2 Apr. 2019), p. 021013. DOI: [10.1103/PhysRevX.9.021013](https://doi.org/10.1103/PhysRevX.9.021013).
- [209] Adrien Bouhon, QuanSheng Wu, Robert-Jan Slager, Hongming Weng, Oleg V. Yazyev, and Tomáš Bzdušek. “Non-Abelian reciprocal braiding of Weyl points and its manifestation in ZrTe”. In: *Nature Physics* 16.11 (2020), pp. 1137–1143. DOI: [10.1038/s41567-020-0967-9](https://doi.org/10.1038/s41567-020-0967-9).
- [210] Adrien Bouhon, Tomas Bzdusek, and Robert-Jan Slager. “Geometric approach to fragile topology beyond symmetry indicators”. In: *Physical Review B* 102 (11 Sept. 2020), p. 115135. DOI: [10.1103/PhysRevB.102.115135](https://doi.org/10.1103/PhysRevB.102.115135).
- [211] Adrien Bouhon, Annica M. Black-Schaffer, and Robert-Jan Slager. “Wilson loop approach to fragile topology of split elementary band representations and topological crystalline insulators with time-reversal symmetry”. In: *Physical Review B* 100 (19 Nov. 2019), p. 195135. DOI: [10.1103/PhysRevB.100.195135](https://doi.org/10.1103/PhysRevB.100.195135).
- [212] Wojciech J. Jankowski, Arthur S. Morris, Zory Davoyan, Adrien Bouhon, F. Nur Ünal, and Robert-Jan Slager. “Non-Abelian Hopf-Euler insulators”. In: *Physical Review B* 110 (7 Aug. 2024), p. 075135. DOI: [10.1103/PhysRevB.110.075135](https://doi.org/10.1103/PhysRevB.110.075135).
- [213] Junyeong Ahn and Bohm-Jung Yang. “Symmetry representation approach to topological invariants in $C_{2z}T$ -symmetric

- systems". In: *Physical Review B* 99 (23 June 2019), p. 235125. DOI: [10.1103/PhysRevB.99.235125](https://doi.org/10.1103/PhysRevB.99.235125).
- [214] Zory Davoyan, Wojciech J. Jankowski, Adrien Bouhon, and Robert-Jan Slager. "Three-dimensional \mathcal{PT} -symmetric topological phases with a Pontryagin index". In: *Physical Review B* 109 (16 Apr. 2024), p. 165125. DOI: [10.1103/PhysRevB.109.165125](https://doi.org/10.1103/PhysRevB.109.165125).
- [215] Hyeongmuk Lim, Sunje Kim, and Bohm-Jung Yang. "Real Hopf insulator". In: *Physical Review B* 108 (12 Sept. 2023), p. 125101. DOI: [10.1103/PhysRevB.108.125101](https://doi.org/10.1103/PhysRevB.108.125101).
- [216] Bo Peng, Adrien Bouhon, Bartomeu Monserrat, and Robert-Jan Slager. "Phonons as a platform for non-Abelian braiding and its manifestation in layered silicates". In: *Nature Communications* 13.1 (2022), p. 423. DOI: [10.1038/s41467-022-28046-9](https://doi.org/10.1038/s41467-022-28046-9).
- [217] Bo Peng, Adrien Bouhon, Robert-Jan Slager, and Bartomeu Monserrat. "Multigap topology and non-Abelian braiding of phonons from first principles". In: *Physical Review B* 105 (8 Feb. 2022), p. 085115. DOI: [10.1103/PhysRevB.105.085115](https://doi.org/10.1103/PhysRevB.105.085115).
- [218] Viktor Könye, Adrien Bouhon, Ion Cosma Fulga, Robert-Jan Slager, Jeroen van den Brink, and Jorge I. Facio. "Chirality flip of Weyl nodes and its manifestation in strained MoTe_2 ". In: *Physical Review Research* 3 (4 Nov. 2021), p. L042017. DOI: [10.1103/PhysRevResearch.3.L042017](https://doi.org/10.1103/PhysRevResearch.3.L042017).
- [219] Siyu Chen, Adrien Bouhon, Robert-Jan Slager, and Bartomeu Monserrat. "Non-Abelian braiding of Weyl nodes via symmetry-constrained phase transitions". In: *Physical Review B* 105 (8 Feb. 2022), p. L081117. DOI: [10.1103/PhysRevB.105.L081117](https://doi.org/10.1103/PhysRevB.105.L081117).
- [220] Adrien Bouhon, Gunnar F. Lange, and Robert-Jan Slager. "Topological correspondence between magnetic space group representations and subdimensions". In: *Physical Review B*

- 103 (24 June 2021), p. 245127. DOI: [10.1103/PhysRevB.103.245127](https://doi.org/10.1103/PhysRevB.103.245127).
- [221] Bin Jiang, Adrien Bouhon, Zhi-Kang Lin, Xiaoxi Zhou, Bo Hou, Feng Li, Robert-Jan Slager, and Jian-Hua Jiang. “Experimental observation of non-Abelian topological acoustic semimetals and their phase transitions”. In: *Nature Physics* 17.11 (2021), pp. 1239–1246. DOI: [10.1038/s41567-021-01340-x](https://doi.org/10.1038/s41567-021-01340-x).
- [222] Bin Jiang, Adrien Bouhon, Shi-Qiao Wu, Ze-Lin Kong, Zhi-Kang Lin, Robert-Jan Slager, and Jian-Hua Jiang. “Observation of an acoustic topological Euler insulator with meronic waves”. In: *Science Bulletin* 69.11 (2024), pp. 1653–1659. ISSN: 2095-9273. DOI: <https://doi.org/10.1016/j.scib.2024.04.009>.
- [223] Tianshu Jiang, Qinghua Guo, Ruo-Yang Zhang, Zhao-Qing Zhang, Biao Yang, and C. T. Chan. “Four-band non-Abelian topological insulator and its experimental realization”. In: *Nature Communications* 12.1 (2021), p. 6471. DOI: [10.1038/s41467-021-26763-1](https://doi.org/10.1038/s41467-021-26763-1).
- [224] F. Nur Ünal, Adrien Bouhon, and Robert-Jan Slager. “Topological Euler Class as a Dynamical Observable in Optical Lattices”. In: *Physical Review Letters* 125 (5 July 2020), p. 053601. DOI: [10.1103/PhysRevLett.125.053601](https://doi.org/10.1103/PhysRevLett.125.053601).
- [225] W. -D. Zhao, Y. -B. Yang, Y. Jiang, Z. -C. Mao, W. -X. Guo, L. -Y. Qiu, G. -X. Wang, L. Yao, L. He, Z. -C. Zhou, Y. Xu, and L. -M. Duan. *Observation of topological Euler insulators with a trapped-ion quantum simulator*. 2022. DOI: [10.48550/arXiv.2201.09234](https://doi.org/10.48550/arXiv.2201.09234). arXiv: [2201.09234](https://arxiv.org/abs/2201.09234).
- [226] Robert-Jan Slager, Adrien Bouhon, and F. Nur Ünal. “Non-Abelian Floquet braiding and anomalous Dirac string phase in periodically driven systems”. In: *Nature Communications* 15.1 (2024), p. 1144. DOI: [10.1038/s41467-024-45302-2](https://doi.org/10.1038/s41467-024-45302-2).

- [227] T. Li and H. Hu. “Floquet non-Abelian topological insulator and multifold bulk-edge correspondence”. In: *Nature Communications* 14 (2023), p. 6418. DOI: [10.1038/s41467-023-42139-z](https://doi.org/10.1038/s41467-023-42139-z).
- [228] Robert-Jan Slager, Adrien Bouhon, and F. Nur Ünal. “Comment on “Floquet non-Abelian topological insulator and multifold bulk-edge correspondence””. In: *arXiv:2310.12782* (2023). URL: <https://arxiv.org/abs/2310.12782>.
- [229] Oliver Breach, Robert-Jan Slager, and F. Nur Ünal. *Interferometry of non-Abelian band singularities and Euler class topology*. 2024. arXiv: [2401.01928](https://arxiv.org/abs/2401.01928) [[cond-mat.quant-gas](https://arxiv.org/abs/2401.01928)].
- [230] QuanSheng Wu, Alexey A. Soluyanov, and Tomáš Bzdušek. “Non-Abelian band topology in noninteracting metals”. In: *Science* 365.6459 (2019), pp. 1273–1277. ISSN: 0036-8075. DOI: [10.1126/science.aau8740](https://doi.org/10.1126/science.aau8740).
- [231] Karen Wintersperger, Christoph Braun, F. Nur Ünal, Andre Eckardt, Marco Di Liberto, Nathan Goldman, Immanuel Bloch, and Monika Aidelsburger. “Realization of an anomalous Floquet topological system with ultracold atoms”. In: *Nat. Phys.* 16 (2020), p. 1058. DOI: [10.1038/s41567-020-0949-y](https://doi.org/10.1038/s41567-020-0949-y).
- [232] Paraj Titum, Erez Berg, Mark S. Rudner, Gil Refael, and Netanel H. Lindner. “Anomalous Floquet-Anderson Insulator as a Nonadiabatic Quantized Charge Pump”. In: *Physical Review X* 6 (2 May 2016), p. 021013. DOI: [10.1103/PhysRevX.6.021013](https://doi.org/10.1103/PhysRevX.6.021013).
- [233] Frederik Nathan, Dmitry Abanin, Erez Berg, Netanel H. Lindner, and Mark S. Rudner. “Anomalous Floquet insulators”. In: *Physical Review B* 99 (19 May 2019), p. 195133. DOI: [10.1103/PhysRevB.99.195133](https://doi.org/10.1103/PhysRevB.99.195133).

- [234] Alexei Kitaev. “Periodic table for topological insulators and superconductors”. In: *AIP conference proceedings*. Vol. 1134. 1. American Institute of Physics. 2009, pp. 22–30. DOI: [10.1063/1.3149495](https://doi.org/10.1063/1.3149495).
- [235] H Kurzweil. *The Theory of Finite Groups: An Introduction*. Springer, 2004. DOI: [10.1007/b97433](https://doi.org/10.1007/b97433).
- [236] Paul Adrien Maurice Dirac. “Quantised singularities in the electromagnetic field”. In: *Proceedings of the Royal Society of London. Series A, Containing Papers of a Mathematical and Physical Character* 133.821 (1931), pp. 60–72. DOI: [10.1098/rspa.1931.0130](https://doi.org/10.1098/rspa.1931.0130).
- [237] Kimball A Milton. “Theoretical and experimental status of magnetic monopoles”. In: *Reports on Progress in Physics* 69.6 (2006), p. 1637. DOI: [10.1088/0034-4885/69/6/R02](https://doi.org/10.1088/0034-4885/69/6/R02).
- [238] JC Alexander and James A Yorke. “The homotopy continuation method: numerically implementable topological procedures”. In: *Transactions of the American Mathematical Society* 242 (1978), pp. 271–284. DOI: [10.1090/S0002-9947-1978-0478138-5](https://doi.org/10.1090/S0002-9947-1978-0478138-5).
- [239] Richard Schmidt and Mikhail Lemeshko. “Rotation of Quantum Impurities in the Presence of a Many-Body Environment”. In: *Physical Review Letters* 114 (20 May 2015), p. 203001. DOI: [10.1103/PhysRevLett.114.203001](https://doi.org/10.1103/PhysRevLett.114.203001).
- [240] Bhuvanesh Sundar, Bryce Gadway, and Kaden RA Hazzard. “Synthetic dimensions in ultracold polar molecules”. In: *Scientific reports* 8.1 (2018), pp. 1–7. DOI: [10.1038/s41598-018-21699-x](https://doi.org/10.1038/s41598-018-21699-x).
- [241] Pieter W. Claeys, Mohit Pandey, Dries Sels, and Anatoli Polkovnikov. “Floquet-Engineering Counterdiabatic Protocols in Quantum Many-Body Systems”. In: *Physical Review Letters* 123 (9 Aug. 2019), p. 090602. DOI: [10.1103/PhysRevLett.123.090602](https://doi.org/10.1103/PhysRevLett.123.090602).

- [242] Florian Kluibenschedl, Georgios M. Koutentakis, Ragheed Alhyder, and Mikhail Lemeshko. *Domain-Wall Ferroelectric Polarons in a two-dimensional Rotor Lattice Model*. 2024. arXiv: 2407.19993 [cond-mat.mes-hall]. URL: <https://arxiv.org/abs/2407.19993>.
- [243] Georgios M. Koutentakis, Areg Ghazaryan, and Mikhail Lemeshko. "Rotor lattice model of ferroelectric large polarons". In: *Physical Review Res.* 5 (4 Oct. 2023), p. 043016. DOI: [10.1103/PhysRevResearch.5.043016](https://doi.org/10.1103/PhysRevResearch.5.043016).
- [244] M. Artin. *Algebra: Pearson New International Edition*. Pearson Education, 2013. ISBN: 9781292051741. URL: <https://books.google.at/books?id=UzSpBwAAQBAJ>.

Appendix

Integrals

We want to calculate the matrix element $\langle l'm' | e^{iP \cos(\hat{\theta})} | lm \rangle$. We expand in spherical harmonics

$$\begin{aligned} &= \int_{-1}^1 d \cos(\theta) \int_0^{2\pi} d\phi Y_{lm}^*(\theta, \phi) Y_{l'm'}(\theta, \phi) e^{iP \cos(\theta)} \\ &= 2\pi \delta_{mm'} N_{lm} N_{l'm} \int_{-1}^1 d \cos(\theta) e^{iP \cos(\theta)} P_l^*(\cos(\theta)) P_l(\cos(\theta)) \end{aligned} \quad (1)$$

where we used $Y_{lm}(\theta, \phi) = N_{lm} P_l(\cos(\theta)) e^{im\phi}$ and the associated Legendre polynomials $P_l(\cos(\theta))$. Hence, with $x = \cos(\theta)$ we are only left with the integral

$$I = \int_{-1}^1 e^{iPx} P_l(x) P_{l'}(x) dx. \quad (2)$$

The exponential term e^{iPx} can be expanded in terms of Legendre polynomials as

$$e^{iPx} = \sum_{n=0}^{\infty} (2n+1) i^n j_n(P) P_n(x) \quad (3)$$

where $j_n(P)$ is the spherical Bessel function of order n . Hence, the integral becomes

$$I = \sum_{n=0}^{\infty} (2n+1) i^n j_n(P) \int_{-1}^1 P_n(x) P_l(x) P_{l'}(x) dx \quad (4)$$

We can evaluate the integral of the product of three Legendre polynomials using Gaunt's formula

$$\int_{-1}^1 P_n(x)P_l(x)P_{l'}(x) dx = \frac{2}{2s+1} \begin{pmatrix} l & l' & s \\ 0 & 0 & 0 \end{pmatrix}^2 \quad (5)$$

where $\begin{pmatrix} l & l' & s \\ 0 & 0 & 0 \end{pmatrix}$ is the Wigner 3j-symbol, and $s = l + l' + n$. Note that Gaunt's formula is only valid if the two conditions are satisfied: First, the triangular condition with $|l - l'| \leq s \leq l + l'$ and second the parity condition that $l + l' + s$ must be even. Then, the integral turns into

$$I = 2 \sum_{s=|l-l'|}^{l+l'} i^s j_s(P) \begin{pmatrix} l & l' & s \\ 0 & 0 & 0 \end{pmatrix}^2. \quad (6)$$

with these conditions.

Periodicity proofs

In this section we provide the proofs that guarantee the periodicity of the lattice for arbitrary quantum resonances $T = 2\pi M/N$. The first lemma will deal with the rotational phases of the 2D rotor, and the second lemma with the rotational phases of the 3D rotor. We will make use of some nomenclature of algebra [244].

Lemma 1. *Let M and N be coprime positive integers. For any integer m , the smallest positive integer q satisfying*

$$\exp\left(-2\pi i \frac{M(m+q)^2}{N}\right) = \exp\left(-2\pi i \frac{Mm^2}{N}\right) \quad (7)$$

is exactly

$$q = \begin{cases} N/2 & \text{if } N \text{ is divisible by } 4, \\ N & \text{otherwise.} \end{cases} \quad (8)$$

Proof. The equality in (7) holds if and only if

$$\frac{M((m+q)^2 - m^2)}{N} = \frac{M(2mq + q^2)}{N} \in \mathbb{Z}. \quad (9)$$

Since M and N are coprime, M , the condition simplifies to

$$2mq + q^2 \equiv 0 \pmod{N}. \quad (10)$$

For the equality to hold for all integers m , the coefficient of m must be congruent to zero modulo N

$$2q \equiv 0 \pmod{N} \quad (11)$$

which implies that N divides $2q$. So we need to satisfy both (11) and (10).

Case 1: N is even.

Let $N = 2n$ for some positive integer n . Now, it turns out we need to differentiate between the cases of N divisible by 4 and N not divisible by 4.

Subcase 1.1: n is even (N is divisible by 4).

Then $n = 2k$ for some integer k , so $N = 4k$. From (11), N divides $2q$, so

$$2q \equiv 0 \pmod{4k} \implies q \equiv 0 \pmod{2k}.$$

We can choose $q = 2k = N/2$. Let us check the constant term in (10)

$$q^2 \equiv 0 \pmod{N} \implies (2k)^2 = 4k^2 \equiv 0 \pmod{4k}.$$

Since $4k^2$ is divisible by $4k$, the condition is satisfied.

Subcase 1.2: n is odd ($N \equiv 2 \pmod{4}$).

In this case, $N = 2n$ with n odd. From (11),

$$2q \equiv 0 \pmod{2n} \implies q \equiv 0 \pmod{n}.$$

Let us set $q = n = N/2$. The constant term yields

$$q^2 = n^2 \equiv n^2 \pmod{2n}.$$

However, since n^2 is odd and $2n$ is even, n^2 is not divisible by $2n$, so $q^2 \not\equiv 0 \pmod{N}$. The condition is not satisfied with $q = N/2$. Hence, we must take $q = N$, which is the smallest q possible.

Case 2: N is odd.

Since N is odd and $\gcd(N, 2) = 1$, from (11) it follows that N divides q . Therefore, the smallest positive integer q is $q = N$. \square

Lemma 2. *Let M and N be coprime positive integers. The smallest positive integer q satisfying*

$$\exp\left(-2\pi i \frac{M(l+q)(l+q+1)}{N}\right) = \exp\left(-2\pi i \frac{Ml(l+1)}{N}\right) \quad (12)$$

for all integers l is

$$q = \begin{cases} N/2 & \text{if } N \equiv 2 \pmod{4}, \\ N & \text{otherwise.} \end{cases} \quad (13)$$

Proof. The equality in (12) holds if and only if

$$\frac{M((l+q)(l+q+1) - l(l+1))}{N} = \frac{M(2lq + q^2 + q)}{N} \in \mathbb{Z}. \quad (14)$$

Since M and N are coprime, we can simplify the condition to

$$2lq + q^2 + q \equiv 0 \pmod{N}. \quad (15)$$

For the equality to hold for all integers l , the coefficient of l must satisfy

$$2q \equiv 0 \pmod{N}, \quad (16)$$

which means N divides $2q$. Since l can be arbitrary, the constant term must also satisfy

$$q^2 + q \equiv 0 \pmod{N}. \quad (17)$$

Case 1: N is odd.

Since $\gcd(N, 2) = 1$, from (16) it follows that N divides q , so $q = N$. The constant constant becomes

$$q^2 + q = N^2 + N \equiv 0 \pmod{N}.$$

Thus, both conditions are satisfied.

Case 2: N is even.

Let $N = 2n$ for some positive integer n .

Subcase 2.1: n is odd ($N \equiv 2 \pmod{4}$).

From (16):

$$2q \equiv 0 \pmod{2n} \implies q \equiv 0 \pmod{n}.$$

Let us set $q = n = N/2$. The constant becomes

$$q^2 + q = n^2 + n = n(n + 1).$$

Since n is odd, $(n + 1)$ is even, so $n(n + 1)$ is divisible by $2n = N$. Therefore, $q^2 + q \equiv 0 \pmod{N}$ and hence $q = N/2$ is the smallest number that satisfies (14).

Subcase 2.2: n is even ($N \equiv 0 \pmod{4}$).

From (16):

$$2q \equiv 0 \pmod{2n} \implies q \equiv 0 \pmod{n}.$$

Let us set $q = n$. The constant term yields

$$q^2 + q = n^2 + n = n(n + 1).$$

Since n is even, n and $(n + 1)$ are consecutive, one even and one odd. However, $n(n + 1)$ is divisible by n but not necessarily by $2n$ or $4n$. Therefore, $q^2 + q$ may not be divisible by $N = 2n$ or $N = 4n$. Thus, $q = N$ is the smallest positive integer satisfying both conditions. \square

List of Figures

1.1	Illustration of topology.	9
2.1	Euler angles of the rotating molecule.	22
2.2	Results for a Gaussian pulse.	37
2.3	Sudden approximation for Gaussian pulses.	38
2.4	Relative error r_2	38
2.5	Parametrization of a half-cycle pulse.	40
2.6	Behavior of a finite-width half-cycle pulse.	41
2.7	Outcomes for half-cycle pulses in the <i>Gaussian</i> limit.	42
2.8	Results for half-cycle pulses for the <i>oscillating</i> limit.	43
2.9	Behavior for an arbitrary value of ξ	44
2.10	Numerical simulation of wave-packet time-evolution for an OCS molecule.	46
2.11	Wave-packet time-evolution in the intermediate regime with $\xi = 0.1$	47
2.12	Wave-packet time-evolution for longer pulses.	48
2.13	Wave-packet time-evolution in the oscillatory regime.	49
3.1	Revivals of the 2D rotor in a gaussian state.	65
3.2	Fractional revival pattern for the 2D rotor following a single kick.	66
3.3	Dynamics of a quantum rotor at full resonance ($N=1$) with $P=1$	73
3.4	Dynamics of a quantum rotor at half resonance ($N=2$) with $P=10$	75
3.5	Quasi-energy spectrum at the triadic resonance $N = 3$	77
3.6	Time-evolution for higher quantum resonances.	79

LIST OF FIGURES

3.7	Growth of kinetic energy for higher quantum resonances.	80
3.8	Time-evolution demonstrating dynamical localization.	82
3.9	Time-evolution near quantum resonance.	83
3.10	On-site potentials for the tight-binding map.	84
3.11	Convergence of the off-diagonal Matrix elements. . .	89
3.12	One-period time-translation operator for a 3D rotor. .	89
3.13	Exact diagonalization of the N=3 band model for the driven 3D rotor.	91
3.14	Analysis of centrifugal distortion effects in a 3D rotor.	93
3.15	Revivals of the 3D rotor in a gaussian state.	95
3.16	Fractional revival pattern for the 3D rotor following a single orientation kick.	96
3.17	Fractional revival pattern for the 3D rotor following a single alignment kick.	97
3.18	Fractional revival pattern for the 3D rotor following a single generic kick.	98
4.1	Degeneracy and Möbius strip.	104
4.2	Phase diagram of the periodically driven 3D rotor. . .	118
4.3	Band nodes at k -symmetric points.	119
4.4	Engineering synthetic dimensions.	120
4.5	Nodal lines as topological phase transitions.	121
4.6	Topological charges of the Dirac cones.	122
4.7	Alignment and orientation signatures of band nodes.	123
4.8	Quench dynamics of a Gaussian state.	126
5.1	Dirac strings between nodal points.	137
5.2	Creation of a lone Dirac string.	138
5.3	Triple-kicked rotor	141
5.4	Nodal lines of the triple-kicked rotor.	142
5.5	Dispersing nodal lines of the triple-kicked rotor. . . .	143
5.6	Non-abelian braiding.	145
5.7	Phase diagram for triple kicked rotor.	147
5.8	Anomalous Dirac string phase.	147